University of Alberta

An Automated Substructuring Framework with Application to Multiphysics & MEMS Design Problems

by

Khaled Sadek

A thesis submitted to the Faculty of Graduate Studies and Research

in partial fulfillment of the requirements for the degree of

Doctor of Philosophy

Department of Mechanical Engineering

Edmonton, Alberta

Spring 2007

Your file Votre référence
ISBN: 978-0-494-29732-2
Our file Notre référence
ISBN: 978-0-494-29732-2

Abstract

This thesis objective is to develop and apply an automated substructuring framework to solve sequentially one-way and two-way coupled multiphysics finite element (FE) problems, such as those experienced in the design and reliability analysis of Micro-Electro-Mechanical Systems (MEMS). The backbone of the developed framework is a novel algorithm, developed in this thesis, referred to as the Major Vector, which consider the substructuring process as a graph partitioning problem, where, spectral techniques are utilized to automatically isolate the linear regions from a graphical representation of the FE mesh. Verification and application of the developed framework was carried out in two different multiphysics FE problems. The first one involved a MEMS microheater based-gas sensor with complicated geometry, whereas the second one involved a Radio Frequency (RF) MEMS switch with simpler geometry and, relatively, more complicated coupled physics. With the utilization of the Major Vector algorithm in the automated substructuring framework, the nonlinear regions in the models of tested MEMS devices are isolated from the substructured linear regions. Higher isolation speed factors (*I.S.F*) has been achieved in the range of 19-37, compared to the traditional manual-substructuring technique. As a result, higher speed factors (S) ratios, up to 4.4, were also achieved using the developed automated substructuring framework. The benefit of this substructuring framework was then utilized in studying the reliability of both MEMS devices, where improvements on the microfabrication parameters for the microheater and geometry optimization of the RF MEMS switch are achieved.

Acknowledgements

I would like to express my deepest gratitude to my advisor Dr. Walied Moussa for the tremendous amount of sound advice he has given me during the course of my research work. It has been his dynamic personality that has inspired me in much of my work. I am also deeply grateful for the full financial support from the University of Alberta.

It was the smiling faces of my wife Doaa, my daughter Farah and my son Amr that have fueled me throughout this work. Special thanks to my dear parents for their prayers, love and care.

Table of Contents

List of Tables

List of Figures

List of Symbols

f,	Scaling Factor
g_0,	Air Gap Length
$h_{\max}$, $h_{\min}$,	Largest and Smallest Distances Between any Two Nodal Indices of an Element, respectively
k,	Thermal Conductivity
k_m,	Thermal Conductivity of the Switch Membrane Material.
k_{Air},	Thermal Conductivity of Air
l_m,	Length of Switch Membrane
m',	Number of Zero Eigenvalues
n_{total},	Total Number of Runs
p,	Deposition Pressure
q,	Heat Flux
r,	AR Threshold Pre-Identified Value
$r_{res}(T)$	Electrical Resistance per Unit Area
t_e,	Electrode Thickness
t_m,	Switch Membrane Thickness

t_s,	Substructuring Time
t_{s_M}	Linear-Zones Isolation Overhead Time Using the Traditional Manual-Substructuring
$t_{s_{MV}}$,	Linear-Zones Isolation Overhead Time Using the MajorVector Algorithm
t_C,	Corrugations Thickness
t_{Cpu},	CPU Time
t_{Cpu_R}	Percentage Reduction in the Total Computational Cost of the Runs Conducted in the Parametric Study
$t_{Cpu_{Total}}$,	Total Computational Cost
$u_{B,}$,	Displacements at Boundary Nodes of a Substructure
$u_{I,}$,	Displacements at Internal Nodes of a Substructure
w_i,	Arbitrary Weight Values
x , h,	Cardinality of Vertices and Edges Sets
x, y, z,	Cartesian Coordinates
2y,	Order of PDE
z_{max},	Maximum Deflection at beam Center
Adj (C),	Adjacency Matrix
A_{eff},	Effective Area
B,	Magnetic Field Strength;

$C\ (N, E)$,	Graph Set
D,	Flexural Rigidity
$Deg\ (C)$,	Degree Matrix
D_m,	Membrane Deflection
D_R,	Deposition Rate.
E,	Electrical Field Strength
$\overline{E_m}$,	Effective Young's Modulus
$E\ \{e_1, e_2, e_3 \ldots e_n\}$,	Edges Set
F_1, F_2,	Stress State Factors
F_B,	Forces at Boundary Nodes of a Substructure
$\left[\overline{F_e}\right]_j$	Substructure's Reduced Load Vector
F_{ij},	The View Factor between Surfaces (i) and (j)
F_I,	Forces at Internal Nodes of a Substructure
G,	SiH_2Cl_2/NH_3 Ratio
H_{max}, H_{min},	Largest and Smallest Distances Between Two Consecutive Interface Nodes on the Substructure Boundary, Respectively.
J,	Current Density

K_{eff},	Effective Beam Stiffness
$\left[\overline{K_e}\right]_j$,	Substructure's Reduced Stiffness Matrix
K_{II}, K_{IB}, K_{BI}, K_{BB},	Substructure Stiffness Sub Matrices
L,	Lorentz Number
$L(C)$,	Laplacian
M,	Dimension of Laplace Matrix
ML_1, ML_2, ML_3, ML_{Layer},	Thickness of the Bottom, Upper SiO_2, Middle Si_3N_4 and Total Insulation Layer, Respectively.
N,	Number of Cycles to Failure
N $\{n_1, n_2, n_3 ... n_n\}$,	Vertices Set
N_B,	Number of Boundary Nodes
N_C,	Number of Corrugations
N_p,	Number of Processors
N_s,	Number of Substructures
P,	Applied Pressure
R,	Electrical Resistance
S,	Speed Factor
S_M,	Substructuring with Traditional Manual Substructuring

S_{ut},	Fracture Strength
S_{MV},	Substructuring with Major Vector Algorithm
T,	Deposition Temperature
T_L,	Linearity
T_O,	Nominal Temperature
T_r,	Reference Temperature
T_s,	Surface Temperature
T_{Actual},	Actual Maximum Temperature
V,	Voltage Distribution
V_i,	Eigenvectors Corresponding to Zero Eigenvalues
V_{PI},	Pull in Voltage
W_m,	Width of Switch Membrane

Greek Symbols

α_T,	Thermal Response Factor
β_e, β_E,	Ratios Between the Actual and Nominal Values of the Coefficient of Thermal Expansion and Young's Modulus, Respectively
β_{PI}^{CC},	Effective Area Correction Factor

β_σ,	Stress Factor
δ_A,	Deflection at Point A
ε,	Percentage Error
ε_{cr},	Critical Buckling Strain
ε_r,	Emissivity
$\varepsilon_{th,x}$	Thermally Induced Axial Strain
γ_{PtTi},	Resistivity Tolerance for Pt/Ti
λ_1,	First Eigenvalue
λ_2,	Second Eigenvalue
κ_p,	Tolerance Applied on Thermal Conductivity
μ_H,	Ligament Efficiency
μ_o,	Permittivity of Free Space.
Ω,	Finite Element Domain
Ω_0,	Nonlinear Domain
$\Omega_1,...\Omega_j,\Omega_{j+1}$,	Localized Linear Zones
ψ,	Actual GDS
ψ_O,	Nominal GDS

ψ_{sen},	GDS Factor
σ_{a},	Alternating Stress
$\sigma_a^{eqv.}$,	Equivalent Alternating Stress
σ_{m},	Mean Stress
σ_{res},	Residual Stress
$\sigma_{th,x}$,	Thermally Induced Axial Stress
σ_Y,	Yield Stress
$\sigma_{A_{\max}}$,	Actual Maximum Stress
$\sigma_{Gr}(z)$,	Gradient Residual Stress
σ_M,	Mean Residual Stress
$\sigma_{N_{\max}}$,	Nominal Maximum Stress
σ_{SB},	Stefan Boltzmann Constant
ν_m,	Poisson's Ratio
τ,	Thickness Tolerance
ω,	Operational Frequency

Abbreviations

ANP,	Al-Nasra and Nguyen's Partitioning Algorithm
AR,	Aspect Ratio
BCs,	Boundary Conditions
BE,	Boundary Element
CAD,	Computer Aided Design
CG,	Communications Graph
3D,	Three Dimensional
DD,	Domain Decomposition
DFM,	Design for Manufacturing
DG,	Dual Graph
DOF,	Degrees of Freedom
EBEM,	Electron Beam Evaporization Method
FD,	Finite Difference
FE,	Finite Element
GDS,	Gas Detection Sensitivity
GR,	Greedy Algorithm

ICs,	Integrated Circuits
I.S.F,	Isolation Speed Factor
LPCVD,	Low-Pressure Chemical Vapor Deposition
MEMS,	Micro-Electro-Mechanical Systems
NG,	Nodal Graph
ORM	Oxygen Radical Assisted Electron Beam Evaporization Method
PDEs,	Partial Differential Equations
PECVD,	Plasma Enhanced Convention Vapor Deposition
Pt/Ti,	Platinum/Titanium Alloy
RCB,	Recursive Coordinate Bisection Algorithm
RGB,	Recursive Graph Bisection Algorithm
RF,	Radio Frequency
RMS,	Root Mean Square Error
RNAS,	Reduced Non-Linear Analysis Strategy
RSB,	Recursive Spectral Bisection Algorithm
RSS,	Recursive Spectral Sequential Cut
RST,	Recursive Two-Way Algorithm

Si_3N_4,	Silicon Nitride
SiO_2,	Silicon Dioxide
TNAS	Total Non-Linear Analysis Strategy
UV,	Ultra Violet

Chapter 1

Introduction

Coupled-Field finite element (FE) problems are frequently encountered more often in the design, development cycle and reliability studies of Microelectromechanical Systems (MEMS), Jensen *et al.* (2003), Zhu *et al.* (2004), Sadek and Moussa (2005). In these problems, the coupling between different physical fields is conducted sequentially either as one-way or two-way sequential coupling, Wang *et al.* (2006). A typical example for a one-way sequentially coupled analysis is shown in a thermal-structural coupled field problem, where the temperature field introduces thermal strains in the structural field, but the structural strains generally do not affect the temperature distribution. Thus, in one-way sequentially coupled FE analysis, there is no need to iterate between the two field solutions. More complicated cases involve two-way sequentially coupled FE analysis. For example, a piezoelectric analysis handles the interaction between the structural and electric fields; it solves for the voltage distribution due to the applied displacements, or vice versa. Therefore, this problem requires iterations between the two physics fields to reach convergence.

The computational cost to solve these types of coupled-field interactions is usually very expensive, Wang *et al.* (2006), Sadek and Moussa (2005). Accordingly,

to solve these problems more efficiently, FE analysts usually resort to various computational saving techniques, such as domain decomposition (DD), substructuring and global-local modeling, as a standard practice to reduce the model size of these problems, Hsieh *et al.* (1995), Simon (1991). Among these techniques, various DD algorithms are considered to be the most popular to partition a complicated FE model into several, more manageable, interconnected smaller problems on parallel processors, Farhat (1988), Farhat and Lesoinne (1991), Escaig and Martin (1999), Roux (1989). However, parallel processing tasks can not be utilized with all currently available FE solvers, ANSYS Theory Manual (2005). Moreover, the required resources for parallel processing are not always available for all FE analysts and designers in industrial environments. Therefore, it is important to consider different alternatives for solving coupled-field FE models on single processors.

Alternatively, conventional substructuring techniques do offer a promising route to conduct large scale nonlinear multiphysics FE analysis on single processors Sadek and Moussa (2005). In these techniques, a structure is divided into a number of linear and localized nonlinear zones. The linear zones are then condensed to form a number of substructures to be used later in the FE analysis. During an incremental/iterative analysis for the complete structure, only the stiffness of the nonlinear zones needs to be updated, based on the change of the stress state, which considerably reduce the computational cost of the analysis. In the current state however, the overhead cost involved in the preprocessing stage of the substructuring is expensive because of the

extensive manual-user interaction involved. This renders these techniques unfeasible in solving sequentially coupled multiphysics FE problems. In addition, at the processing stage, the substructures linearity state need to be systematically checked and updated. Moreover, an efficient procedure should be implemented to transfer the loads between the overlapping substructures of the interacting physical domains.

1.1 Research Objective

The current proposed research is directed to develop an automated substructuring framework, to improve on the use of the substructuring technique, in solving sequentially coupled multiphysics FE problems. The main philosophy of the current research is to develop an automated FE modeling framework that is used to eliminate most of the difficulties encountered in implementing substructuring techniques in its current state. The proposed automated substructuring framework is constructed from an algorithm, written in MATLAB © Code, which is utilized in the preprocessing and processing stage of the multiphysics FE analysis. This automated substructuring framework is then tested and verified into different multiphysics FE problems. The first problem involved a MEMS microheater based-gas sensor with complicated geometry involving multi layers of thin films, irregular sensor/heater geometrical configuration and high geometrical aspect ratio. The second problem involved a RF switch with simpler geometry and more complicated physics coupling. The benefit of the automated substructuring framework was then show cased in studying the

reliability of both MEMS devices. The developed automated substructuring framework is implemented as follows:

(a) Major Vector Algorithm; this algorithm is mainly utilized at the preprocessing stage of the multiphysics FE analysis. The substructuring at this stage is treated as a graph partitioning problem. A graphical representation is conducted for the FE mesh and spectral techniques are utilized to automatically extract the linear zones from the global linear domain database. These linear zones are then condensed into substructures to be later used at the processing stage of the multiphysics FE analysis. A modified version of the recursive spectral algorithm (RSB) is also developed and utilized to assess and modify the generated substructures aspect ratio (*AR*). This algorithm is utilized to split the generated substructures with unacceptable aspect ratio based on a pre-specified aspect ratio threshold value set by the FE user.

(b) Load Vector Mapping Procedure; this procedure is mainly utilized at the processing stage of the multiphysics FE analysis to transfer the loads between the interface nodes of the overlapping substructures in the interacting physical domains. The load vector mapping is implemented by conducting an expansion pass to calculate the results at the interior nodes of the substructures at one physical domain. The results at the interior nodes are then used to

transfer the loads at the interface nodes of the substructures generated in the interacting physical field using the developed Major Vector algorithm.

(c) Substructures Update Procedure; this procedure is utilized at the processing stage of the multiphysics FE analysis. This procedure is used to check the linearity state of the elements belonging to the generated substructures at pre-identified load steps in the FE analysis. If the nonlinearity reaches any of these elements, it is reassigned to the nonlinear domain. Next, the developed Major Vector algorithm is utilized to update the substructures previously used at the earlier load steps. This algorithm maximizes the computational efficiency of the substructuring process, because larger linear zones are allowed to be substructured at earlier stages of loading.

1.2 Thesis Outline

The next chapter contains a review of the literature related to the computational saving techniques utilized to solve sequentially coupled multiphysics FE problems. The literature survey also includes a review on MEMS technology and the multiphysics analysis problems, encountered in the design, development and reliability studies of MEMS. Some comments on the use of the computational saving techniques in solving these types of problems are also presented.

In Chapter 3, a detailed explanation of the proposed automated substructuring framework that has been developed in the current thesis research work is presented. This framework eliminates many difficulties encountered on the use of the substructuring process in solving sequentially coupled multiphysics FE problems, by automating the substructures generation process at the preprocessing and processing stages. The algorithm and procedures utilized in the process of linear regions isolation, substructures aspect ratio assessment/modification, load vector mapping and substructures updating were described. This is then followed by a discussion of some structural analysis test cases to validate and compare the proposed substructuring framework with other computational saving techniques reported in literature.

Chapter 4 presents the validation results of the proposed automated substructuring framework in sequentially coupled multiphysics FE problems. The framework is implemented in two complicated multiphysics FE cases in MEMS. The first case discusses the implementation of the proposed substructuring framework to model a two-way sequentially coupled electro-thermal FE analysis for a microheater-based MEMS gas sensor. This case represents a MEMS modeling case that involve geometric complications and a large mesh size with a relatively simple sequential physics coupling. The second case represents the application of the proposed framework to analyze a multi-field coupled FE analysis of RF MEMS switches. This case presents relatively simpler model geometry, where more sophisticated physical

coupling analysis is investigated. The substructured multiphysics analysis results are validated with experimental, analytical and numerical results, reported in previous studies found in the available literature. The computational benefits from the application of the proposed substructuring framework in analyzing these multiphysics test cases is also shown, where comparison of the computational performance results to the traditional manual-substructuring ones is carried out.

In Chapter 5, the automated substructuring framework is utilized to study the reliability of microheater-based MEMS gas sensors. In this reliability study, a total of 625 analysis runs were needed to investigate the effect of the uncertainties generated at various stages of the microfabrication process on the gas detection sensitivity (GDS) performance and the onset of thermal fatigue failure in the gas sensor. Therefore, the application of the developed automated substructuring framework was essential to reduce the computational cost of the parametric analysis runs. Whenever applicable, a correlation between the deposition parameters and the studied design variables of the gas sensor is established.

Chapter 6 presents the utilization of the substructuring framework in analyzing the reliability of RF MEMS switches. To complete this reliability study a total of 100 analysis runs are needed. Two failure mechanisms are discussed in the reliability study, mainly the switch membrane stiction at higher pull-in voltages and the switch buckling at higher operational frequencies. The effect of the switch dimensions, operational frequency and residual stresses generated during microfabrication on the

long term reliability of these switches are discussed. Finally some design modifications are suggested to reduce the reliability problems caused by the studied failure mechanisms.

Chapter 7 presents the conclusion drawn from the work that is accomplished in this thesis. The achieved contributions and some suggestions for future work are also presented.

Chapter 2

Literature Survey

This chapter contains a review of the literature pertaining to the computational-cost reduction techniques utilized in large-scale FE analysis and the role of these techniques in the development and reliability analysis of MEMS. In Section (2.1), a review of the computational-cost reduction techniques, which can be utilized to solve sequentially coupled multiphysics FE problems emerging in the design of MEMS, are discussed. The next section, presents a brief introduction to the history of MEMS and the technology used in their design and fabrication. Section (2.3) summarizes the development cycle of MEMS from conceptual design to microfabrication. In Section (2.4) a discussion of the reliability assessment factors involved in MEMS design and the role of FE simulation and parametric analysis in increasing the durability and operational life of these devices is introduced. Finally, some concluding remarks are given in Section (2.5).

2.1 Computational Cost Reduction Techniques in FE Analysis

2.1.1 Domain Decomposition Techniques

Domain Decomposition (DD) techniques take advantage of distributed memory parallel processing in finite element (FE) analysis. The domain is usually partitioned or decomposed into a number of sub-domains, which are distributed among parallel processors. The computation load for each one of these sub-domains is carried out by a separate processor, Farhat and Lesoinne (1991). The main problems of these approaches are to partition the domain to achieve a well balanced (load balancing) work load between the processors; and to minimize the interface cut of the sub-domains to minimize the inter-processor communications requirement.

Since the FE meshes may be large and generic (irregular shapes, including multiply connected and/or branched domains), manual partitioning of the domains may be difficult and time consuming. Simon (1991) has shown that visual perception alone may not be sufficient for the task of partitioning large three dimensional (3D) structures. Therefore, automatic DD algorithms are generally required.

Several automatic partitioning algorithms have been proposed in the literature. Most of these algorithms may be classified as follows, Hsieh *et al.* (1997).

Topology-based vs. geometry based: The topology-based algorithms partition a FE mesh using topological information of the mesh or its associated graphical representation. Examples of topology-based algorithm include the greedy (GR)

algorithm, Farhat (1988), the reduced bandwidth decomposition (RBD) algorithm, Malone (1988), (1990), the recursive graph bisection (RGB) algorithm, Simon (1991) and the recursive spectral bisection (RSB) algorithms, Simon (1991), Hseih *et al.* (1995). On the other hand, the geometry-based algorithms partition a mesh using geometrical information. Examples are the recursive coordinate bisection (RCB) algorithm, Simon (1991) and the inertial algorithms, Farhat and Lesoinne (1991). In addition, some existing algorithms use both topological and geometrical information for partitioning. For example, Al-Nasra and Nguyen's partitioning (ANP) algorithm, Al-Nasra and Nguyen (1991), the combination algorithm, Rodriguez and Sun (1992) and the algorithm by Miller *et al.* (1992).

Spectral vs. non spectral: Spectral algorithms are based on algebraic properties of a graphical representation associated with the FE mesh. These algorithms use the global properties of the FE graphical representation to perform the partitioning, i.e. a spectral analysis is conducted to compute the separators based on eigenvector components of the graph. This is opposed to most of the non-spectral algorithms that only use the local information of the graph, such as the neighboring information of a vertex. Several spectral algorithms are proposed in the literature. Simon (1991) proposed the RSB algorithm for hypercube architectures, which consists an even number of processors. Hendrickson and Leland (1993) extended this technique to allow for partitioning of a domain into 4 or 8 sub-domains at each stage of recursive decomposition. Hsieh (1993) and Hseih *et al.* (1995) presented the recursive two-way

(RST) and recursive spectral sequential cut (RSS) algorithms to generalize the RSB algorithms to an arbitrary number of processors. All of the spectral algorithms are based on the spectral properties of the Laplacian matrix of a graph associated with the mesh.

Recursive vs. non-recursive (sequential): The partitioning algorithms are either recursive, such as GR, RCB, RGB, RSB and RST algorithms or non-recursive such as RBD algorithm. It is reported that the sequential versions tend to produce strip-wise partitions with longer boundaries but fewer neighbors. On the other hand, recursive algorithms often generate domain-wise partitions with smaller aspect ratios, shorter boundaries but more neighbors, Hseih *et al.* (1995).

2.1.2 Substructuring

The substructuring technique was invented by aerospace engineers back in the 1960s, to carry out a first level break down of complex systems such as a complete airplane. In this technique, a structure is divided into a number of linear and localized nonlinear zones. The linear zones are then condensed to form a number of substructures to be used later in the FE analysis. During an incremental/iterative analysis for the complete structure, only the stiffness of the nonlinear zones needs to be updated based on the change of the stress state.

The substructuring technique has been used extensively by many researchers to conduct nonlinear structural static and dynamic analysis. For example, Dodds and

Lopez (1980) reported a review study for the substructuring application in linear and nonlinear analysis. Owen and Goncalves (1982) discussed the utilization of different substructuring techniques in material nonlinear analysis. Also, Han and Abel (1985) proposed the self adaptive substructuring algorithm to solve nonlinear FE analysis with localized material nonlinearities. In this technique, the sizes and locations of the substructures is dependent on the spread of the plasticity during loading. Powel *et al.* (1997), Jonsson *et al.* (1995), proposed the recursive and constrained substructuring techniques for buckling and dynamic analysis of structural systems.

As discussed in the literature, Noor *et al.* (1978), the mathematical formulation of the substructuring problem can be summarized as follows: (I) a Finite element domain Ω is divided into a nonlinear domain Ω_0 and a number of scattered substructured zones (must be linear) $\Omega_1,...\Omega_j,\Omega_{j+1}$; (II) the degrees of freedom (DOF) of the substructures are classified either as internal or boundary DOF, where the boundary DOF are at the nodes connecting one substructure to other adjacent parts and/or substructures within the FE model. Therefore, the force equilibrium equations for the j^{th} substructure are written in matrix form as follows

$$\begin{bmatrix} K_{II} & K_{IB} \\ K_{BI} & K_{BB} \end{bmatrix}_j \begin{bmatrix} u_I \\ u_B \end{bmatrix}_j = \begin{bmatrix} F_I \\ F_B \end{bmatrix}_j \tag{2.1}$$

where, u_I, u_B, F_I *and* F_B are the displacements and the external forces at the internal nodes and the boundary nodes, respectively, as shown in Fig (2.1). Therefore, by rearranging the overall stiffness matrix for this substructure, the stiffness sub-matrices

can then be rearranged as K_{II}, K_{IB}, K_{BI} and K_{BB}. Using Equation (2.1), the internal and boundary DOF are expressed by Equations (2.2) and (2.3), respectively, as follows.

$$[u_I]_j = [K_{II}]_j^{-1} ([F_I]_j - [K_{IB}]_j [u_B]_j) \tag{2.2}$$

$$[u_B]_j = [K_{BB}]_j^{-1} ([F_B]_j - [K_{BI}]_j [u_I]_j) \tag{2.3}$$

By substituting Equation (2.2) in Equation (2.3), the internal DOF are omitted from Equation (2.3) to obtain the reduced substructure equilibrium equations in terms of u_B in the following form

$$[\overline{K_e}]_j [u_B]_j = [\overline{F_e}]_j \tag{2.4}$$

where, $[\overline{K_e}]_j$ and $[\overline{F_e}]_j$ are the reduced stiffness matrix and load vector, respectively, for the j^{th} substructure and are given by Equations (2.5) and (2.6) as follows

$$[\overline{K_e}]_j = [K_{BB}]_j - [K_{BI}]_j [K_{II}]_j^{-1} [K_{IB}]_j \tag{2.5}$$

$$[\overline{F_e}]_j = [F_B]_j - [K_{BI}]_j [K_{II}]_j^{-1} [F_I]_j \tag{2.6}$$

After the full analysis is done, the internal displacements can be determined, if needed, by back substitution using Equation (2.2).

The advantages of utilizing the substructuring technique in FE problems in terms of the computational cost and the computer storage requirements have been discussed extensively in literature, Powel *et al.* (1997), Jonsson *et al.* (1995), Han and Abel (1985), Dodds and Lopez (1980). This significant savings are mainly due to the fact that substructures in the FE analysis are dealt with as superelements that are only

represented by the boundary DOF, after the elimination of the internal DOF in the condensation phase, as depicted in Equations (2.2), (2.3) and (2.4). This phase results in a reduced system with a lower number of DOF, which lead to a significant reduction in the in-core memory requirement, Owen and Goncalves (1982). Moreover, the stiffness of the substructured linear regions of the FE model does not require updating with all equilibrium iterations, which significantly reduces the computational cost of the FE analysis.

Despite these advantages, the use of substructuring techniques has been limited for many years due to the extensive manual user-interaction required throughout the whole FE analysis process. The most extensive part in this process is the identification of the linear zones of the analyzed FE model. This problem is far more costly when analyzing large scale models, which might have thousands or even millions of DOF. Even with the help of interactive computer graphics, the manual implementation of FE substructuring is extremely tedious and time consuming process. To improve on the use of the substructuring techniques in FE analysis, an automated framework should be developed to reduce the overhead cost for different tasks involved in the substructuring process.

2.2 MEMS Technology

MEMS technology is used to produce complex structures and devices on the micrometers scale. Nowadays, many unique MEMS specific micromachining

processes are being developed, Gad El Hak (2001). In MEMS, a variety of transduction mechanisms can be used to convert signals from one form of energy to another, thus enabling many microsystems, microsensors and microactuators. Despite only partial standardization, a maturing of MEMS computer aided design (CAD) technology and a narrow database, complex and sophisticated MEMS devices have been produced.

The integration of integrated circuits (ICs) with MEMS can improve performance, but at the price of higher development costs, greater complexity and a longer development time. A growing appreciation of MEMS has prompted many efforts to commercialize a wide variety of novel MEMS products. In addition, MEMS have potential applications in space exploration and thus will play a major role in future missions to Mars and beyond, Judy (2001).

The history of MEMS is dependent on the development of micromachining processes. Early lithographic for defining and etching sub-mm features was developed as early as 1500 A.C. However the greatest impact of micromachining has been derived by the development of pure semiconductors in the 1940s. In the year of 1949, the ability to grow single-crystal silicon significantly improved the performance of semiconductor transistors. In 1959, in his historical lecture 'There's plenty of room at the bottom', Professor Feynman first described the enormous amount of space available on the microscale. In his talk, he challenged the world to fabricate a motor with a volume less than 1/64 of an inch a side, Feynman (1992). It

was not until the year of 1964, when the first engineered batch fabricated MEMS device was produced by Nathenson at Westinghouse, Nathenson *et al.* (1967). In the 1970s and 1980s, the commercialization of MEMS was started by several companies that produced parts for the automotive industry (e.g., IC Transducers and IC Sensors). Since then MEMS have found and are still finding increased applications in a variety of industrial and medical fields, Gad El Hak (2000).

2.3 MEMS Development Cycle

The field of MEMS is so rich and varied, that it would be challenging to emphasize all the elements, which illustrate the development of the technology in one section. In general, all MEMS devices undergo the development cycle shown in Fig (2.2). The concept of any MEMS device is driven either by market demand or technology demonstrations, Senturia (2004). A commercial design is a one where the need for a specific capability is well understood, and the next step is to search for concepts and corresponding fabrication methods that can realize the desired functionality. On the other hand, a technology driven design is one, where a specific technology development have been realized and a search is made for device concepts that can use the new technology. The MEMS device then enters to different levels during its development varying from conceptual design to modeling and prototyping, microfabrication, packaging and testing before it can be returned to the market.

2.3.1 MEMS Design and Modeling

The design of MEMS is a complicated issue that requires several different levels of description and detail. First, the designer should investigate the need and specifications of the proposed MEMS device and the outcome of different alternatives for microfabrication. At the next level, the system should be partitioned into components that can be analyzed individually. After that comes the stage of materials selection, identifying fabrication sequence for each individual component, methods of packaging, and means to assure device uniformity in manufacturing.

Modeling can play a major role in the design process by permitting the evaluation of the device performance prior to the actual microfabrication stage. This would enable the troubleshooting of the proposed design and evaluation of failure mechanisms prior to a device entering manufacturing. Modeling and simulation are involved at all development levels of MEMS. Senturia (2004) identifies four different modeling levels, which are system, device, physical and process. Each modeling level is linked to the next by double headed arrows, which symbolizes the iterative exchange of information between them.

At the top of the modeling levels is the system, in which block diagram or lumped element circuit models can be used to describe the dynamic behavior of the system. At the bottom is the process level, in which the process sequence and photomask designs are created. At this level the designer usually uses computer aided design

(CAD) tools to predict the geometry from the masks and process sequence, Giridharan *et al.* (2001).

The physical level is used to address the physical behavior of the device in 3-D continuums. The governing equations are typically partial differential equations (PDEs). The physical modeling of PDEs usually requires approximate analytical solutions or highly meshed numerical analysis. Numerical tools available include finite element (FE), boundary element (BE), finite difference (FD), or a mix of these techniques.

At the device level, a designer usually uses macro models or in other words, reduced order models in order to capture the essential behavior of a component of the whole system. The reduced order models are usually analytical rather than numerical. An important feature of macro models is to capture all essential device behavior in a way that permits rapid calculation and provide a valid preliminary input to a system level simulator.

2.3.2 Micromachining

Many of the microfabrication techniques and materials used in MEMS are originally borrowed from the IC industry. However, the evolution of the microsystems technology has also driven the development of other micromachining processes and materials. Conventional IC processes include photolithography, thermal oxidation, dopant diffusion, low-pressure chemical vapor deposition (LPCVD), plasma

enhanced convention vapor deposition (PECVD), evaporation, sputtering, wet etching, plasma etching, reactive ion etching and ion milling.

Additional processes used in MEMS include anisotropic wet etching, deep reactive ion etching, X-ray lithography, electro plating, low-stress LPCVD films, thick film resist, spin casting, micromolding and batch microassembly, Madou (2002). Photolithography is the most important process that enables ICs and MEMS to be produced with microscopic dimensions in high volumes.

The photolithographic process starts by selecting a substrate material and geometry. The substrate is then coated by a photosensitive photoresist. A mask consisting of a transparent supporting medium with precisely patterned opaque regions is then used to cast a highly detailed shadow on the photoresist. The regions receiving an exposure of ultra violet (UV) light are chemically altered. After the exposure process, the photoresist is immersed in a solution that chemically removes the exposed regions or the unexposed regions. The wafer is then dried and the mask can be used for a subsequent deposition or etching process.

Methods used to integrate multiple patterned materials together to fabricate a completed MEMS device are as important as the individual processes. Two general methods for MEMS integration are described below.

- Surface Micromachining

Surface micromachining is a method for producing MEMS by depositing, patterning and etching a sequence of thin films, typically from 1-100 μm. One of the most

important processing steps required is the selective removal of an underlying film referred to as the sacrificial layer, Bustillo *et al.* (1998). Surface micromachining is used to produce a wide variety of MEMS devices for many different applications. The variety of surface micromachining processes and materials make it impossible to discuss them in sufficient detail. A thorough treatment of these processes is presented in the book by Madou (2002).

- Bulk Micromachining

In bulk micromachining, the substrate material, which is usually single crystal silicon, is patterned and shaped to form an important functional component of the MEMS device. Exploiting the predictable anisotropic etching characteristics of single crystal silicon, high precision complex three dimensional (3D) shapes can be formed. These shapes might include V grooves, channels, membranes and nozzles, Peterson (1982) and Kovacs (1998).

2.4 Reliability Assessment Factors in MEMS Design

A failure of a MEMS component or system occurs when it fails to perform its expected function. Poor reliability is generally due to failures accentuated by environmental factors and operational stresses. In situations where redundancy and repair are impractical, reliability becomes the central indicator of quality.

The quantification of reliability in terms of probability to failure, usually involve the utilization of statistical methods because of the uncertainties associated with the

useful life of the product. Because the sources of these uncertainties are both human and material, the statistical treatment has to deal with the behavior of the device or product resulting from an unlikely interaction of parameters that perhaps is not well understood. This is especially true in the case of MEMS, where the lack of a clear understanding of the material behaviors at the micron scale and the utilization of novel microfabrication techniques, generate deviations in these devices performance at actual operation from the expected design target values.

At the design stage of MEMS, many factors should be taken in to consideration for the reliability assessment of these products. These factors, shown in Fig (2.3), are classified into two major categories, mainly the scaling and the microfabrication factors.

2.4.1 Scaling Factors

When miniaturizing any device or system, it is critical to have a good understanding of the scaling properties of the transduction mechanism, the overall design and the material characterization. The scaling properties of any one of these components could present a difficult barrier to adequate performance. Due to the powerful scaling practices in MEMS, the previous experience at various macroscale phenomena and design might not transfer directly to the microscale. Therefore, the scaling factor has a significant impact on the constitutive equations used to predict the behavior of microsystems.

For example, in fluidic systems, the Reynolds's number is a function of the scale of the system. The fluid flow in micro fluidic systems is almost dominated by laminar flow conditions. Therefore, because of this behavior, it is very difficult to accomplish thorough mixing in micro fluidic systems. Also, in mechanical systems, when the linear dimensions are reduced by a certain scaling factor (f), the volume and mass of this object is reduced by f^3, while the stiffness of this component is only reduced by a factor of f.

The material characterization in MEMS is greatly affected by the scaling factors. The properties of thin film are often different from their bulk or macroscale form. Much of this disparity arises from the fact that the assumption of homogeneity, which is commonly used with high accuracy for bulk materials, become unreliable when used to model devices in the microscale. Therefore, local changes in grain size and other characteristics can significantly alter the performance of MEMS from the design target values. However, one potential advantage of scaling MEMS to densities approaching the defect density of the material is the lower probability to produce products with a high count of local defects. Therefore, fracture strength values are usually greater at the microscale than its counterparts at the macroscale, Striker and Spearing (2003). In fact, the yield strengths of thin metal films can exceed bulk values by up to an order of magnitude, Nix (1989). Accordingly, in MEMS design, bulk values can be used as conservative limits for the yield and fracture strength. However, the uncertainties in the characterization of other thin film material

properties, such as Young's modulus, Poisson's ratio, thermal conductivity etc, introduce a major problem in modeling the behavior of MEMS devices.

Stiction and adhesion of contacting surfaces are mainly controlled by four mechanisms, mainly capillary forces, hydrogen bridging, electrostatic and van der Waals forces, Tas *et al.* (1996). These mechanisms are usually insignificant in the design of macroscale devices. However, at the microscale, because of the high surface to volume ratios and the smoothness of contacting surfaces, these mechanisms are more dominant in controlling the stiction and adhesion of thin films. Malfunctioning due to stiction of moving components, present one of the major reliability concerns in the design of some of MEMS devices, such as radio frequency (RF) MEMS switches and comb drives. The stiction is usually associated with the charge build up at the contacting surfaces with the application of higher actuation voltages. Therefore, utilizing different approaches to reduce the actuation voltages is highly desirable in the design practice of these devices in order to increase their long term operational reliability.

2.4.2 Microfabrication Factors

For many microelectronics thin films, uncertainties are introduced at various stages of microfabrication. For example, the characterization of thin film material properties depends strongly on the details of the deposition process and the growth conditions. In addition, some properties may depend on the post deposition thermal processing,

refereed to as annealing. For example, Wrbaneck and Kimala (2005), report a significant variation in the resistivity of platinum thin films with the change in the annealing time. Furthermore, Uma *et al.* (2001), report the dependence of the thermal conductivity of doped polysilicon layers on layer deposition temperature. In addition, the same study indicates that the annealing conditions might alter the thermal conductivity by a factor that can reach up to 40%. Also, uncertainties are introduced in the dimensional parameters of thin films. The dimensional tolerance in the thickness of thin films is dependent on the type of the deposition process and the deposition parameters. To examine the significance of the dimensional uncertainty, Zappa and Einstein (2002), calculated the variation of the resonant frequency of a micro resonator with a 10% relative tolerance in linear dimensions of etched features. This study reports an uncertainty of 15% in the value of the resonant frequency with the applied dimensional tolerance. Also, Paul and Baltes (1993) report a ±17 % variation in measured value of the thermal conductivity for SiO_2 thin films with a ± 20% variation in the thickness of these films.

The uncertainties generated at the microfabrication of thin films are not only limited to the variations in material properties and dimensional tolerance. A very important parameter, extensively studied is the generated residual stresses. Nearly all thin films exhibit a state of residual stress due to mismatch in the coefficient of thermal expansion, non uniform plastic deformation, interstitial impurities and growth processes. The residual stresses generated in the thin films are usually categorized as

either intrinsic or extrinsic. The intrinsic stresses develop during the film nucleation. Extrinsic stresses are imposed by unintended external factors, such as temperature gradients or sensor package induced stresses. They arise either in a structure with inhomogeneous thermal expansion coefficients subjected to a uniform temperature change or in a homogeneous material exposed to a thermal gradient. Intrinsic stresses in thin films are usually larger than extrinsic stresses. They usually arise as a result of the non equilibrium nature of thin film deposition.

The stress developing in a film during the initial phases of a deposition may be compressive, causing buckling or delamination. Alternatively, thin films may be in tensile stress, which may lead to cracking if forces are high enough to exceed the fracture strength of the film material. Therefore the elimination of microfabrication residual stresses is often a standard practice in surface micromachining processes. However, in some cases, controlled values of residual stresses might be desirable. For, example in RF MEMS switches, a controlled value of tensile residual stresses in the switch membrane, might be useful to counteract the compressive stresses induced with high operational temperatures generated at high operational frequencies, thus reducing the probability of buckling failure in the switch.

Extensive efforts have been conducted by many researchers to measure the value of intrinsic and extrinsic residual stresses, either experimentally or by utilizing a mix of experimental measurements and numerical modeling. For example, Leplan *et al.* (1995) developed a correlation between the residual stresses generated in evaporated

SiO_2 thin films and deposition parameters. In this study, residual stresses were determined by measurements of the radius of curvature of Si and Ge substrates. Kim and Allen (1999) measured the residual stresses in polyimide thin films by correlating the variation in the resonant frequency of a polyamide string with the state of stress in the thin film. Also, Min and Kim (2000) reported a new technique for measuring residual stresses, using composite- layered cantilevers. In their study, the residual stress of an additional thin film is obtained by comparing the deflections of the composite cantilever before and after the deposition of the additional film. Seok *et al.* (2002) proposed a new electrical residual stress characterization method using bent beam actuators. Also, Chen *et al.* (2002) developed a residual stress measurement method, in which the stress distribution is determined by matching the thermal deflections from a finite element (FE) model to measured deflections of a thin fixed-fixed beam structure.

2.4.3 Modeling Scaling and Microfabrication Induced Variations

The variations generated as a result of MEMS scaling factors and uncertainties in the microfabrication process have prompted MEMS manufacturers to undergo a lengthy and costly cycle of prototyping and experimentation. To date, only a few MEMS-based products have crossed the threshold of prototype volumes into large scale volume productions. Even the most successful MEMS products in the market, such as piezoresistive pressure sensors and inertial sensors lasted in average between 4-15

years from concept to final volume production and market insertion. Using a build and test approach, inherent in such a traditional approach, lead to the fact that engineering of the product will take a much longer and costly time cycle.

Building a robust design for manufacturing (DFM) methodology for MEMS at the pre-microfabrication stage, is thus a very important factor in reducing the costly process, currently utilized in the development of MEMS devices. This methodology for DFM will likely be based on a combination of a robust industrial information database and efficient numerical modeling tools. The modeling of the MEMS device can play a vital role in predicting the device performance in response to the variations in the material characteristics, dimensional parameters and generated residual stresses. However, accurate MEMS models usually involve nonlinear 3D multiphysics interactions, which are computationally very expensive and requires a high level of expertise. Also, the high aspect ratio of MEMS devices, usually contribute to the expensive computational cost of their analysis. Therefore, it is important to investigate various techniques to reduce the computational expenses involved in the modeling process of MEMS.

2.5 Concluding Remarks

MEMS devices are currently modeled using weak analytical tools, which results in a relatively inaccurate prediction of performance behaviors. The MEMS design process is usually performed in a trial-and-error fashion, which requires several iterations

before the performance requirements of a given device are finally satisfied. This non-ideal design methodology combined with the length of time and high costs associated with MEMS prototyping results in a very inefficient and ineffective scenario for commercial product development.

In this sense, developing efficient multiphysics analysis tools to model the MEMS device performance, in response to different design parameters variations, is urgently needed. However, the computational cost for solving coupled multiphysics analysis problems is very expensive. Therefore, a survey of the literature related to different computational cost reduction techniques has been conducted. The following conclusions can be drawn:

(i) None of the existing domain decomposition algorithms guarantees optimal solutions or produces partitions that generally satisfy all the needs of various numerical solution strategies.

(ii) Domain decomposition techniques are highly dependent on the available computational resources. These resources might not be usually available in industrial environments.

(iii) The selection of a domain decomposition technique is highly dependent on the physical nature of the problem, which might introduce a great disadvantage in solving multiphysics analysis problems.

(iv) Domain decomposition algorithms address the distribution of the work load balance among processors, only by the number of elements assigned to each processor. This feature of the DD algorithms might introduce some problems in analyzing nonlinear FE models.

(v) The substructuring technique shows less dependence on the computing resources used in the FE analysis.

(vi) The substructuring technique is less sensitive to the type of the physical problem analyzed, compared to DD algorithms. However the accuracy of the results is more dependent on the expertise level of the FE analyst in setting nonlinearity criterions for the substructuring process.

(vii) The extensive manual user interaction involved at the preprocessing/processing stages of the substructuring process, in its current state, presents a great disadvantage to this technique.

Based on the conclusions presented above, an automated substructuring framework will be developed in this study to solve sequentially coupled multiphysics FE analysis problems, emerging in the design of MEMS. The developed framework should satisfy the following requirements:

(a) Reduce the overhead cost involved in the preprocessing/processing stages of the substructuring process

(b) The developed framework should be generic in nature to offer more flexibility in analyzing various multiphysics modeling cases.

(c) The substructuring framework should include an algorithm to assess and modify the substructures aspect ratios.

(d) The developed framework should include a methodology to transfer the loads between the substructures generated in the interacting physical domains, which might be overlapping.

(e) The developed framework should include a procedure to update the substructures with the spread of nonlinearity at different loading stages during a nonlinear FE analysis.

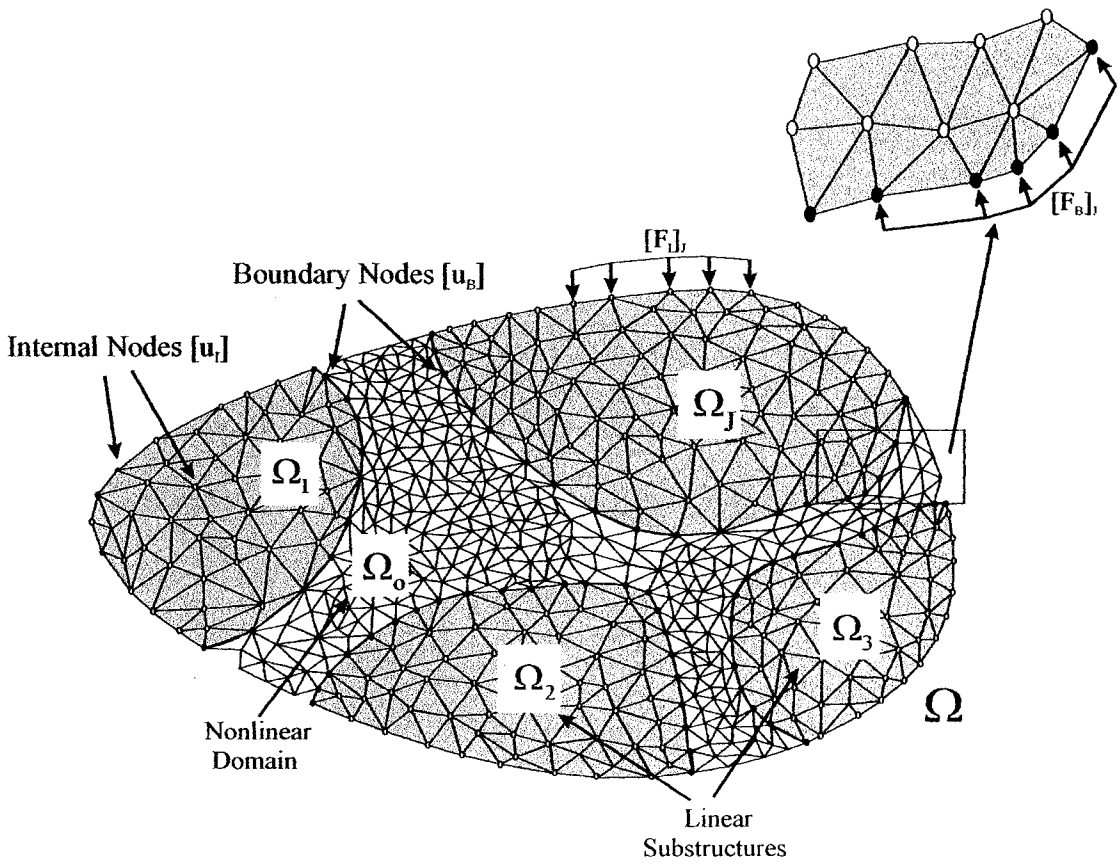

Figure 2.1: Schematic representation of types of forces and degrees of freedom in substructures

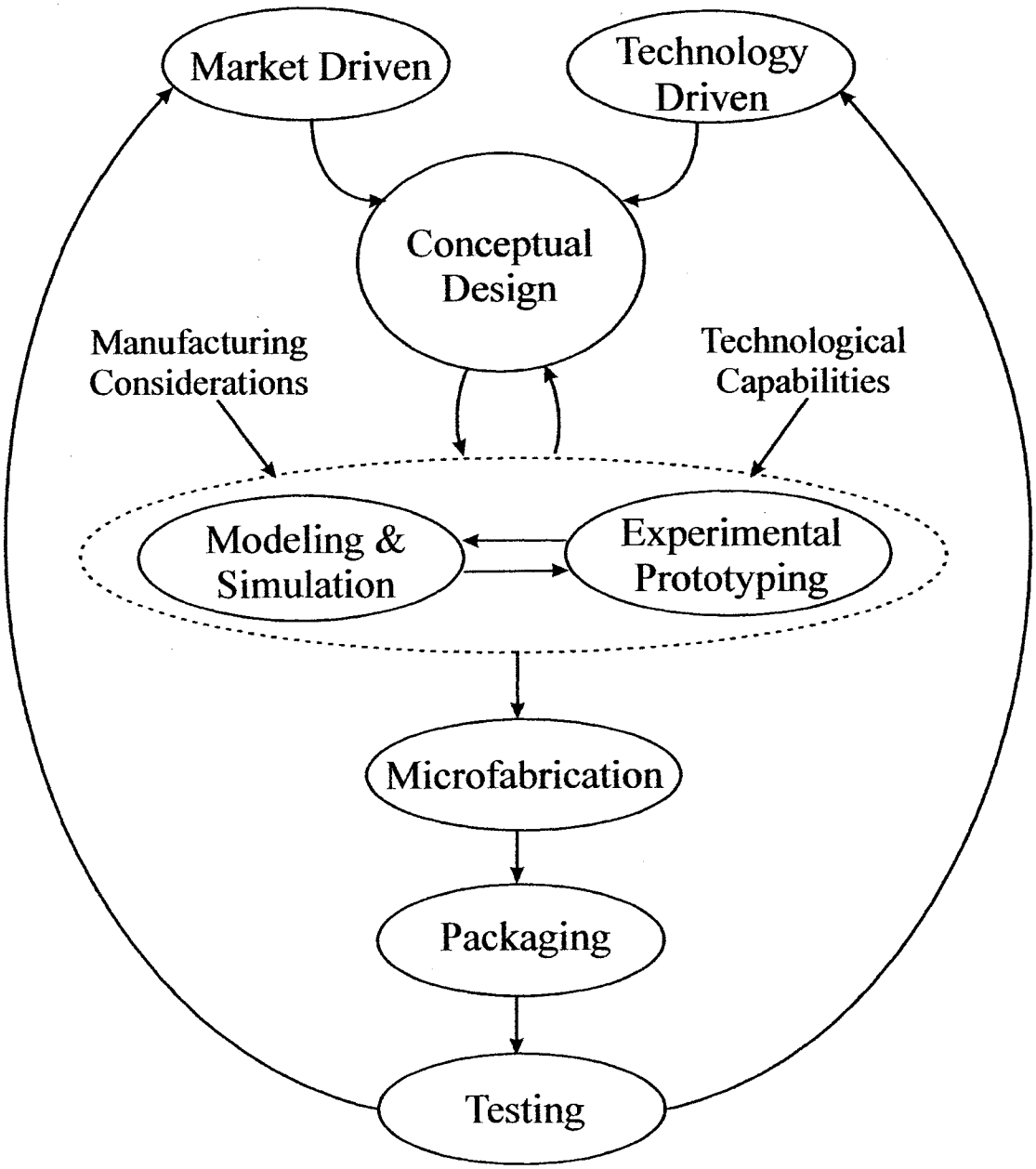

Figure 2.2: MEMS development cycle.

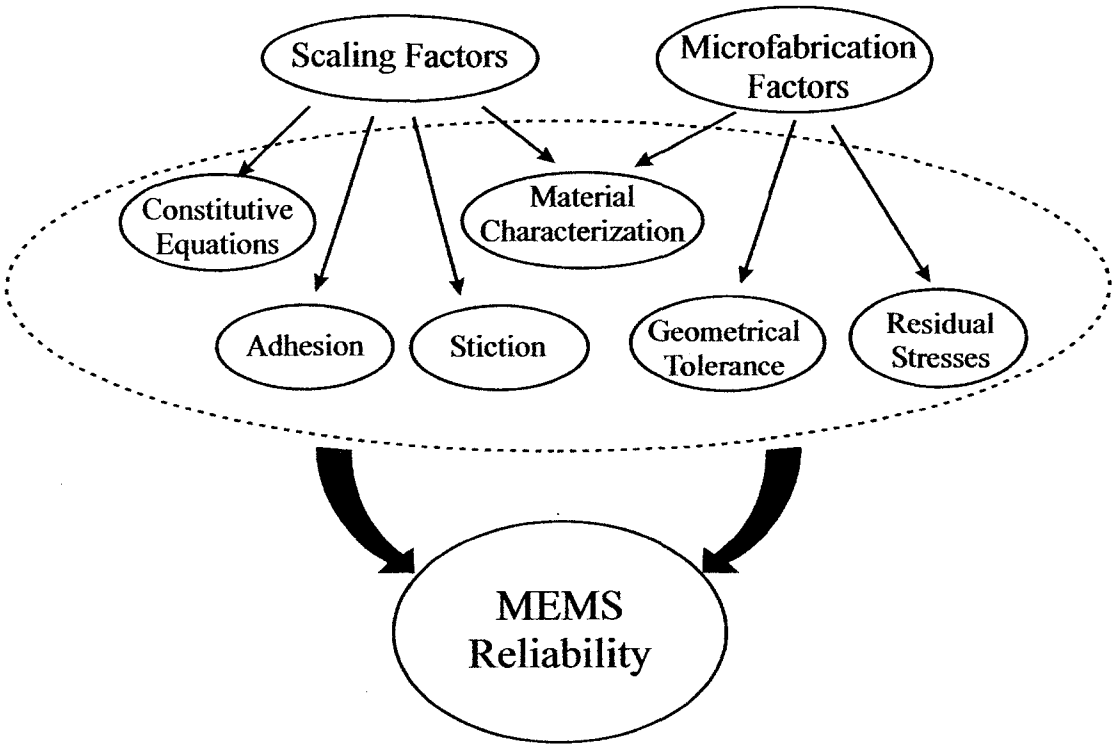

Figure 2.3: Reliability assessment factors in MEMS design

Chapter 3

Automated Substructuring Framework for Sequentially Coupled Nonlinear Multiphysics FE Analysis

This Chapter presents the development process of an automated substructuring framework to solve sequentially coupled multiphysics FE problems, emerging in the design and development cycle of MEMS. In these problems, the locations of the substructures are dependent on nonlinearity criterions, set by the FE analyst, for the studied physical fields. Therefore, the substructures generated in each physical domain might be overlapping with the substructures generated in the interacting physical field(s). Moreover, load transfer between the interface nodes of these overlapping substructures, considerably increases the overhead time of the multiphysics substructuring analysis. In addition, within each physical analysis, the sizes and locations of the linear zones might change, according to the stage of loading. Therefore, the generated substructures must be consistently checked at

certain loading stages, and updated, once the nonlinearity reaches elements previously assigned to the linear zones, at earlier load steps.

In order to reduce the overhead cost of the substructuring process in sequentially coupled multiphysics FE analysis, the automated substructuring framework, proposed in this study, is implemented by developing an algorithm, referred to as the Major Vector, which is utilized to automatically extract the linear zones, in each physical domain, and to assess/modify the substructures aspect ratio (*AR*). Section (3.1) will discuss the full details of the Major Vector algorithm. Next a methodology is utilized to conduct the load vector transfer between the interface nodes of the overlapping substructures in the interacting physical fields. Full details of this methodology will be discussed in Section (3.2). Finally a procedure, discussed in Section (3.3), is followed to check the linearity state, and update the substructures within the loading stages of each physical analysis. The automated substructuring framework was implemented using a developed MATLAB © code and utilized with ANSYS © 10.1 indirect multiphysics solver to solve multiphysics FE analysis problems.

The automated substructuring framework is validated and compared with another computational saving technique, referred to as the adaptive substructuring technique developed by Han (1984), as will be shown in Section (3.4). Finally, some concluding remarks on the automated substructuring framework are presented in Section (3.5).

3.1 Major Vector Algorithm

A flow chart of the Major Vector algorithm is shown in Fig (3.1). The algorithm is implemented through four consecutive phases. In the first phase, elements of the FE mesh are assigned into linear and nonlinear zones, based on nonlinearity criterions set by the FE analyst. Then, a graphical representation of the global linear domain is conducted in the second phase. The Laplacian of the FE mesh graphical representation is calculated and a spectral analysis of this Laplacian is conducted at the third phase to identify the connectivity and locations of the linear zones. The calculated linear zones are then condensed into substructures. In the final phase, the aspect ratios (AR) of the generated substructures are assessed and modified automatically using a modified version of the recursive spectral bisection (RSB) algorithm. The modified substructures are then utilized in the FE analysis.

In a traditional manual-substructuring process, the FE analyst has to be involved in phases 2, 3 and 4, mentioned above, through direct manual-user interaction. Alternatively, the Major Vector algorithm offers a number of features to FE users at different stages of the analysis process. The first feature is incorporated at the pre-processing stage, where the manual user-interaction is completely eliminated during the substructures generation phase and the substructures aspect ratio (AR) assessment/modification phase. The second feature is shown at the processing stage; since the overhead cost of the substructuring process is considerably reduced, the

Major Vector algorithm can be directly applied to systematically check the linearity state and update the used substructures, more efficiently, as will be shown in Section (3.4). The third feature of the Major Vector algorithm is its generic nature; since it mainly deals with a graphical representation of the FE mesh, once the nonlinearity criterions for isolating linear and nonlinear zones have been set by the analyst. Therefore, various cases of nonlinear multiphysics FE problems can be analyzed. Furthermore, this algorithm can be connected to any available commercial FE solver or research code as a separate design module. Since phase 1 depends on the specific nonlinearity criterion defined by the FE user for a specific physical analysis, i.e. problem dependent, it will be discussed separately in Chapter 4. Detailed description of the Major Vector algorithm for phases 2, 3 and 4 will be discussed next.

3.1.1 Graphical Representation of FE Mesh

In this phase, the FE mesh is considered as a graph *C (N, E)* consisting of a set of vertices $N\{n_1, n_2, n_3 \ldots n_n\}$ and a set of edges $E\{e_1, e_2, e_3 \ldots e_n\}$, which are unordered pairs of separate values that form $N; E = \{(n_i, n_j) | n_i \in N, n_j \in N, i \neq j\}$. The cardinality of the sets *N* and *E* are defined as *x* and *h,* respectively, Haemers (1980), Deo (1974), Harary (1972). These cardinality values, determine the selection of the graphical representation type for the FE mesh. For example, consider the FE mesh with twelve 3-node triangle (T3) elements and twelve nodes shown in Fig (3.2-A). A

graph representation of this FE mesh is conducted using the nodal graph (NG) or the dual graph (DG). The nodal graph, shown in Fig (3.2-B), represents the connectivity of the nodes. The vertices in this NG represent the nodes in the original FE mesh, while the edges represent the connectivity of adjacent nodes sharing the same elements. The dual graph represents the connectivity of the elements in a topological sense, as shown in Fig (3.2-C). The vertices in this DG represent the elements in the original FE mesh, while the edges represent the connectivity of adjacent elements that share a common boundary in the original mesh.

The choice of the FE graph representation type is based on the database size (i.e. if the number of elements in the database is greater than the number of nodes, the algorithm is automatically directed to construct an NG representation, and vice versa). Next, the Laplacian matrix *L(C)* for the NG and DG is constructed as shown in Fig (3.2-D) and Fig (3.2-E), respectively. The Laplacian matrix *L(C)* is a symmetric matrix of order $M \times M$, where M refer to the number of vertices in the graph. The Laplacian matrix is obtained from the degree matrix *Deg (C)*, and the adjacency matrix *Adj (C)*, as follows, Kaveh and Davaran (1999), Deo (1974).

$$L_{ij} = Deg_{ij} + Adj_{ij} \quad ,\forall\ i, j \tag{3.1}$$

$$Deg_{ij} = \begin{cases} -\sum_{j=1}^{M} Adj_{ij} & ,i = j \\ 0 & ,i \neq j \end{cases} \tag{3.2}$$

$$Adj_{ij} = \begin{cases} -1 & if \{n_i, n_j\} \in E \\ 0 & if \{n_i, n_j\} \notin E \end{cases} \tag{3.3}$$

3.1.2 Spectral Identification of Linear Zones

In this phase, the automated identification of the linear zones is carried out after the construction of *L(C)*. The spectral properties of *L(C)* are of special interest in the current work, since the eigenvectors can be used to isolate the linear regions in the proposed automated substructuring process. Starting from the first eigenvalue (λ_1), the number of zero eigenvalues corresponds to the number of linear zones in the global linear domain. To identify the elements in each linear zone, the corresponding eigenvectors are multiplied by arbitrary weight values and summed to construct a special vector, refereed to as the MajorVector as follows

$$\text{MajorVector} = \sum_{i=1}^{m'} w_i V_i \tag{3.4}$$

where, m', w_i, and V_i refer to the number of zero eigenvalues, the arbitrary weight values and the corresponding eigenvectors, respectively. This MajorVector is then utilized to extract the information of the linear zones to be later condensed into

substructures. The addition of the eigenvectors is carried out in Equation 3.1 because some null eigenvectors might be present in the spectral analysis, which does not clearly identify the locations of the elements forming a certain linear zone. Also, the multiplication of all eigenvectors by arbitrary weight values is carried out in Equation 3.1 because some eigenvectors may contain similar non-zero cell values, at different indices. The values of the arbitrary weights are randomly calculated (preferred to be a fraction of two decimal points and distinct).

A simple example that demonstrates the application of the linear zones spectral identification phase is shown in Fig (3.3). In this example, the linear regions are pre-identified (gray regions) in an arbitrary FE mesh of twenty four T3 elements, as shown in Fig (3.3-A). The global linear domain database consists of elements 1-8, 13-16, and 21-24. Fig (3.3-B) demonstrates the DG representation of the global linear domain. This is followed by the calculation of *L(C),* as shown in Fig (3.3-C). Prior to *L(C) calculation,* a pseudo numbering scheme is applied to the global linear domain to minimize the size of *L(C)*. Spectral analysis shows that the number of zero eigenvalues is three, which corresponds to the number of linear zones in the generic FE mesh. The corresponding eigenvectors contains more information regarding the elements belonging to each linear zone. Since there is no null eigenvectors or eigenvectors of similar nonzero cell values, the arbitrary weights were chosen to be one (only for this special case example). The multiplication of the corresponding

eigenvectors by the arbitrary weights and the summation of this multiplication, represent the condensed result of the spectral identification of the linear zones, as shown in Fig (3.3-D). In the current example, the first eight cells in the MajorVector have the same value (-0.3536) and they correspond to the first linear zone information (elements 1-8). The same result is noticed for the second and the third linear zones.

Similar information is extracted, in this example, from individual eigenvectors (i.e. with no need to construct the MajorVector). However, for a complicated FE mesh with a large linear domain database, the case is different. The user cannot simply locate the substructures locations as in this example. Therefore, the use of arbitrary weight values and the construction of the MajorVector are crucial to guarantee an accurate extraction of the linear regions information.

To prove this argument, consider the example shown in Fig (3.4). In this example, the global linear domain database, shown in Fig (3.4-A), consists of three scattered linear zones; $\Omega_1\{E;$ 1, 3, 4, 5, 7, 9, 11 and 16$\}$, $\Omega_2\{E;$ 2, 6, 8and 10$\}$ and $\Omega_3\{E;$ 12, 13, 14 and 15$\}$. The Dual graph representation of the global linear domain and the calculated Laplacian matrix *L(C)*, for this example are shown in Fig (3.4-B) and Fig (3.4-C), respectively. Spectral analysis shows that the number of zero eigenvalues is three, which corresponds to the number of linear zones in this example. The corresponding eigenvectors, shown Fig (3.4-D), are multiplied by arbitrary weight values ($w_i = 1, i = 1, 2, 3$), and added to construct the MajorVector. In

contrast to the example depicted in Fig (3.3), the eigenvectors, in the current example does not directly provide information about the linear zones of the arbitrary FE mesh. Alternatively, the MajorVector clearly identifies the elements belonging to each linear zone by unique cell values, as shown in Fig (3.4-E). Cell indices 1, 3, 4, 5, 7, 9, 11 and 16, in the MajorVector have the same value of 0.2634, which indicates that element numbers equivalent to these indices are connected to form one of the three linear zones. The same outcome can be noticed for the other two linear zones. It is clearly shown in this example that in general, individual eigenvectors can not be solely used to extract the linear zones information from the global linear database.

3.1.3 Modified Recursive Spectral Bisection (RSB) Algorithm

For a given FE mesh, the aspect ratio (AR) for an element is defined as h_{max}/ h_{min}, where, h_{max} and h_{min} are the largest and smallest distances between any two nodal indices in this element, respectively Farhat and Lesoinne (1991). The condition number of the stiffness matrix is directly proportional to $(h_{max}/ h_{min})^{2y-1}$, where 2y is the order of the partial differential equation describing the analyzed physics. Bad element aspect ratio ($AR \gg 1$) results in poor conditioning of the global stiffness matrix. The same concept also applies to substructures, which are considered superelements. Therefore, substructures with (AR) largely greater than one, have ill conditioned stiffness matrices and can generate local problems that are difficult to

solve iteratively. Accordingly, substructures with bad aspect ratios should be generally avoided, especially when a local or interface problem is solved with an iterative algorithm, Farhat (1988). The aspect ratio for a substructure is defined by Equation (3.5) as follows

$$AR = \frac{H_{max}}{H_{min}} \tag{3.5}$$

where, H_{max}, and H_{min} denote the largest and smallest distances between two interface nodes on the substructure boundary, respectively.

The Major Vector algorithm incorporates a modified version of the RSB algorithm for assessment and modification of the generated substructures aspect ratios. The RSB is mainly applied in spectral DD techniques, to partition a large 3D FE mesh among parallel processors, Kaveh and Davaran (1999). This algorithm uses the special properties of the second eigenvalue (λ_2) and the corresponding second eigenvector (Fiedler vector) to ensure load balancing (almost equal number of DOF) among processors with minimum inter-processor communication requirements. This work, however, is focused on solving complete FE models on a single processor; therefore, in the modified RSB algorithm, the load balancing requirement is not essential. The main focus of the modified RSB algorithm is to rather ensure minimum splitting of substructures with bad (AR) to minimize the interface problem, or in other words the number of boundary nodes (N_B).

A flowchart for the modified RSB algorithm is shown in Fig (3.5). The algorithm starts by checking the aspect ratio of a substructure (parent substructure Ω_n) against a predefined threshold value (r). Substructures with bad (AR) are split using RSB into two balanced substructures Ω_{n_1} and Ω_{n_2}. The same procedure is done recursively for the newly generated substructures to check their AR. The new substructures with acceptable (AR) are combined one by one according to their connectivity, to minimize N_B, subject to the condition that the new (AR) for the combined substructures is less than or equal to (r). The application of the modified RSB algorithm on a simple substructure is demonstrated in Fig (3.6).

3.2 Methodology for Substructures Load Vector Mapping

In a substructured sequentially coupled multiphysics FE analysis, the loads or data communication between the interacting physical domains should be directly transferred to the master nodes at the interface of the utilized substructures. Since, in multiphysics analysis, the nonlinearity criterions are selected according to the type of each studied physical domain, the substructures generated for different physical domains might be overlapping. Therefore, a methodology should be implemented to guarantee an accurate load vector coupling between these substructures. In this study, a procedure for substructures load vector mapping was followed. A flowchart

illustrating the procedure steps of this methodology, on a hypothetical case of two interacting physical domains 1 and 2, is shown in Fig (3.7). After solving for the substructured FE analysis of physical domain 1, an expansion pass is conducted to calculate the displacements at the internal degrees of freedom of the substructures. At step 2, these displacements are applied as loads on physical domain 2. Next, the Major Vector algorithm is utilized to check for the linearity state of the substructures in physical domain 2, and to update these substructures, if necessary. The load vectors are then recalculated in the next step and applied to the generated substructures. Finally, the solver starts the FE analysis for physical domain 2.

For one-way sequentially coupled multiphysics FE analysis, the load vector mapping procedure is utilized only once after the analysis of physical domain 1 is fully conducted. Alternatively, in two-way sequentially coupled multiphysics FE cases, this procedure should be applied in all interactions between the interacting physical domains.

3.3 Substructures Updating Procedure

In many nonlinear physical analyses, the nonlinearity zone(s) may expand at later stages of the loading process, Han (1984). Therefore, to maximize the benefit from the substructuring, the zones, which are expected to reach nonlinearity at a later stage of loading, can be treated as substructures at earlier load steps. However, if the

nonlinearity occurs in these substructures, the analysis must stop and a re-substructuring process should be conducted, as shown in Fig (3.8); otherwise, inaccurate results are obtained. In traditional manual-substructuring, the overhead cost of the substructuring process is very expensive. Therefore, this process of substructures updating, might alter the computational efficiency of the substructuring analysis. Accordingly, FE analysts, utilizing the traditional manual-substructuring techniques, usually resort to either one of two different strategies to solve this problem. In the first strategy, a large nonlinear zone is assumed at the beginning of the analysis to avoid the spread of nonlinearity in the generated substructures. In the second strategy, the substructures updating process is only conducted at certain load steps, predicted using a user defined criterion. While the first strategy may reduce the efficiency of the substructuring analysis, the second strategy is more dependable on the expertise of the FE user and might require a number of trial and error iterations until satisfactory solution accuracy is achieved.

Alternatively, the automation process and the considerable reduction in the overheat time cost of the substructuring process, achieved with the Major Vector algorithm, allows the substructuring updating process to be done more efficiently. In this study a procedure that utilizes the Major Vector technique is utilized to conduct the substructures updating during the physical analysis. A flowchart of this procedure is shown in Fig (3.9). At certain load steps, the linearity state is checked at the

interface nodes and the elements located at the boundaries of the existing substructures. If the nonlinearity did not reach the existing substructure (s), the condensed stiffness matrices and the load vectors are saved and used for the next loading stages. Otherwise, if the nonlinearity reaches one or more of the elements belonging to one of the existing substructures, an expansion pass is conducted and these elements are reassigned to the nonlinear zone. Next a spectral analysis is conducted to check the connectivity of the remaining linear elements by evaluating the second eigenvalue. If the second eigenvalue is greater than zero, this means that the remaining linear elements are perfectly connected and can be re-condensed into a single substructure. In this case, the aspect ratio of the new substructure is assessed using the modified RSB algorithm. On the other hand, if the second eigenvalue is evaluated at zero, this means that the remaining linear elements belong to one or more unconnected linear zones. In this case the Major Vector algorithm is applied to generate the new substructures. Next, the new substructures are used in the FE analysis. In the next section, the validation of the Major Vector algorithm on structural analysis cases is presented. In Chapter 4, the validation of the Major Vector algorithm is conducted on multiphysics analysis of MEMS

3.4 Major Vector Algorithm Validation

Two structural analysis cases are presented in this Section to validate the Major Vector algorithm. These two cases (pressurized axisymmetric pressure vessel and welded tension plates) are used to check the accuracy of the proposed methodology in comparison to experimental and numerical results available in the literature. In both cases, a comparison is conducted between the performance of the Major Vector algorithm and the adaptive substructuring algorithm proposed by Han in 1984. As far as the author knows, the adaptive substructuring algorithm developed by Han in 1984 was the only attempt to introduce automation to the substructuring process on single processors to the current date.

3.4.1 Structural Analysis of Axisymmetric Pressure Vessel

The pressure vessel is constructed from a cylindrical and spherical shell welded together along the junction line. The problem description is shown in Fig (3.10). The pressure vessel is loaded with an internal pressure that varies from 0 to 8 MPa. The FE model of the pressure vessel is meshed and analyzed using 10500 3D 8-noded tetrahedral solid elements. A comparison of the numerically calculated stress values from the Major Vector algorithm, Han (1984) and Zienkiewicz (1977) is shown in Fig (3.11). The calculated deflection using the Major Vector algorithm was also validated

with the experimental deflection reported by Dino and Gill (1965) for the same case, as shown in Fig (3.12); where, P and δ_A refer to the applied pressure and the corresponding deflection at point A, shown in Fig (3.10). Both comparisons show good agreement between the Major Vector algorithm and the reported numerical/experimental results.

An analysis of the CPU time (t_{Cpu}), speed factor (S) and percentage computational savings is listed in Table (3.1) for the axisymmetric pressure vessel problem. The efficiency of the Major Vector algorithm is compared with the adaptive substructuring algorithm reported by Han (1984). The direct analysis (D-A) in Table (3.1), refer to the solution of the model without the use of substructuring. A speed factor of 3.18, which corresponds to a 68.5 percent computational savings, was achieved with the Major Vector algorithm, compared to only 1.07 speed factor and 6 percent computational saving with the adaptive substructuring algorithm, Han (1984).

3.4.2 Welded Tension Plates

In this case, two sets of tension plates are welded to a connection plate, as shown in Fig (3.13). The tension plates are loaded with a tension force, which is equal to 0.4 the yield load of the plates. The FE model is meshed using 8500 3D 8-noded tetrahedral solid elements. The values for S and percentage of computational savings

are listed in Table (3.2). These values are compared with the one obtained using the adaptive substructuring method by Han (1984). A higher speed factor of 2.82, which corresponds to a 64.6 percent computational savings, was achieved with the Major Vector algorithm compared to 2.01 speed factor and 49 percent computational saving achieved with the adaptive substructuring algorithm, Han (1984).

3.5 Concluding Remarks

An automated substructuring framework has been developed to improve on the use of the substructuring technique in multiphysics FE analysis. The main focus of this framework is to reduce the overhead time cost of the substructuring process. This reduction in the overhead time cost is mainly experienced in the following substructuring steps:

(i) Linear zones isolation and substructures aspect ratio assessment/modification.

(ii) Load vector mapping between overlapping substructures in multiphysics analysis.

(iii) Substructures updating process within every studied physical analysis.

The backbone of the proposed automated substructuring framework is the Major Vector algorithm presented in Section (3.1). Due to the important role of this algorithm, the automated substructuring framework will be referred to as the Major Vector algorithm in the remaining chapters of this thesis. Several cases have been presented to validate the proposed framework with another computational saving technique published in the literature. In the next chapter, the validation of the Major Vector algorithm will be presented in more detail on a two complicated coupled multiphysics FE analysis cases for MEMS gas sensors and RF MEMS switches.

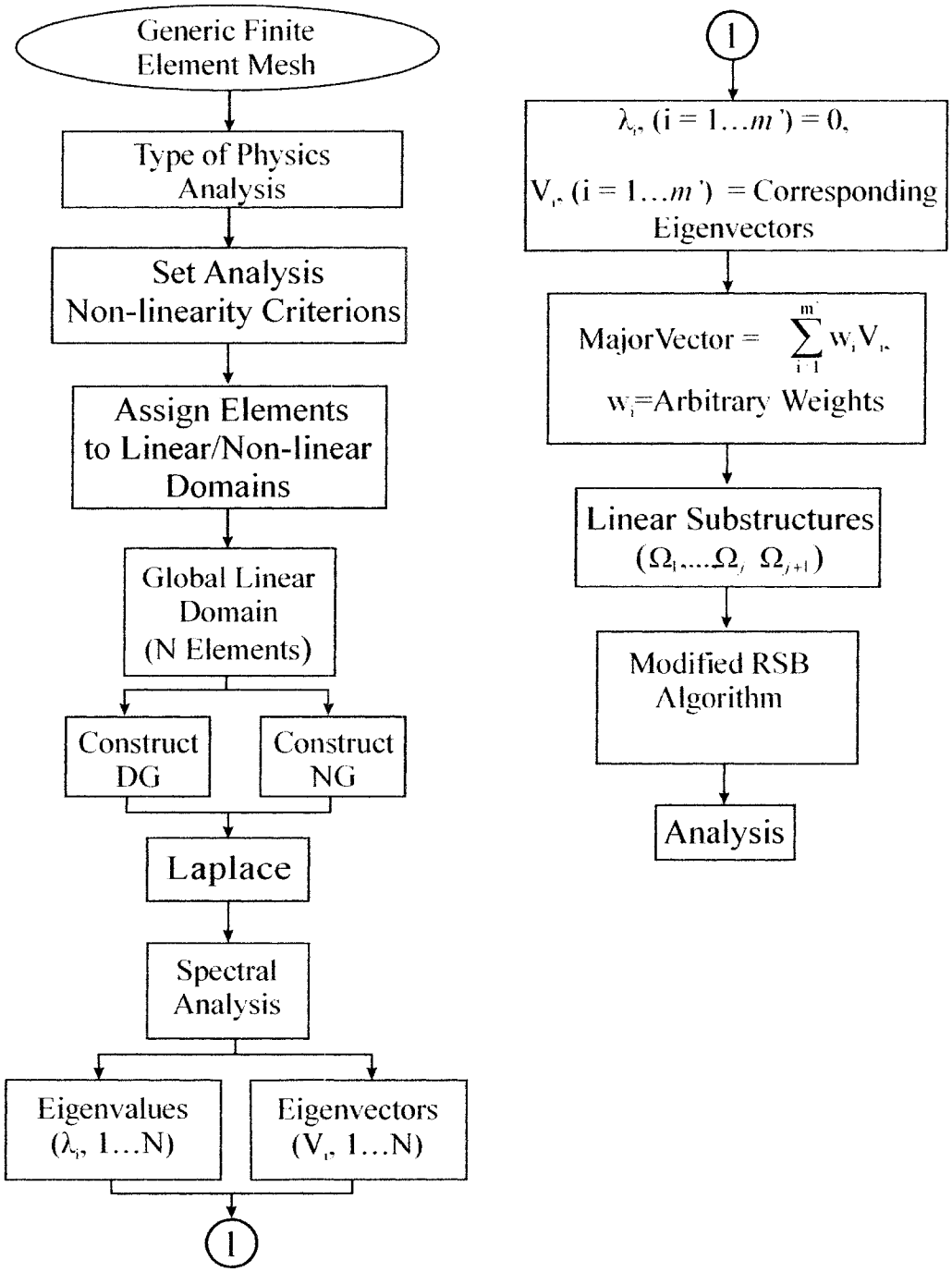

Figure 3.1: Flowchart of the Major Vector algorithm

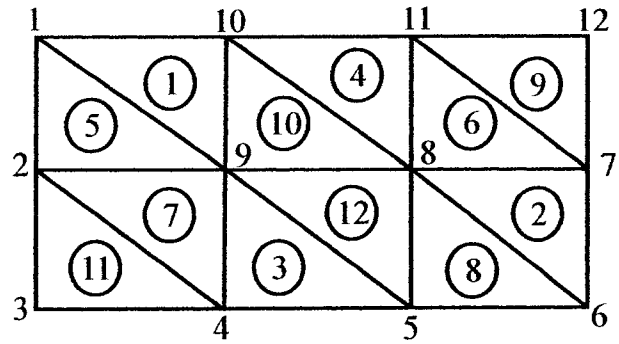

A) Finite element mesh

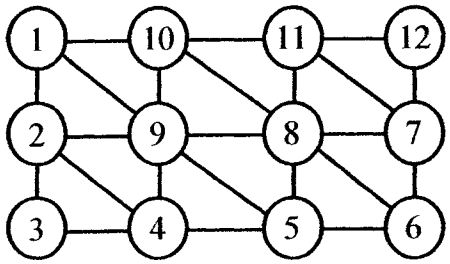

B) Nodal graph (NG)

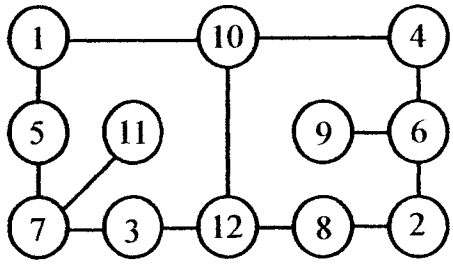

C) Dual graph (DG)

$$\begin{bmatrix}
3 & -1 & 0 & 0 & 0 & 0 & 0 & 0 & -1 & -1 & 0 & 0 \\
-1 & 4 & -1 & -1 & 0 & 0 & 0 & 0 & -1 & 0 & 0 & 0 \\
0 & -1 & 2 & -1 & 0 & 0 & 0 & 0 & 0 & 0 & 0 & 0 \\
0 & -1 & -1 & 4 & -1 & 0 & 0 & 0 & -1 & 0 & 0 & 0 \\
0 & 0 & 0 & -1 & 4 & -1 & 0 & -1 & -1 & 0 & 0 & 0 \\
0 & 0 & 0 & 0 & -1 & 3 & -1 & -1 & 0 & 0 & 0 & 0 \\
0 & 0 & 0 & 0 & 0 & -1 & 4 & -1 & 0 & 0 & -1 & -1 \\
0 & 0 & 0 & 0 & -1 & -1 & -1 & 6 & -1 & -1 & -1 & 0 \\
-1 & -1 & 0 & -1 & -1 & 0 & 0 & -1 & 6 & -1 & 0 & 0 \\
-1 & 0 & 0 & 0 & 0 & 0 & 0 & -1 & -1 & 4 & -1 & 0 \\
0 & 0 & 0 & 0 & 0 & 0 & -1 & -1 & 0 & -1 & 4 & -1 \\
0 & 0 & 0 & 0 & 0 & 0 & -1 & 0 & 0 & 0 & -1 & 2
\end{bmatrix}$$

D) Laplace of NG

$$\begin{bmatrix}
2 & 0 & 0 & 0 & -1 & 0 & 0 & 0 & 0 & -1 & 0 & 0 \\
0 & 2 & 0 & 0 & 0 & -1 & 0 & -1 & 0 & 0 & 0 & 0 \\
0 & 0 & 2 & 0 & 0 & 0 & -1 & 0 & 0 & 0 & 0 & -1 \\
0 & 0 & 0 & 2 & 0 & -1 & 0 & 0 & 0 & -1 & 0 & 0 \\
-1 & 0 & 0 & 0 & 2 & 0 & -1 & 0 & 0 & 0 & 0 & 0 \\
0 & -1 & 0 & -1 & 0 & 3 & 0 & 0 & -1 & 0 & 0 & 0 \\
0 & 0 & -1 & 0 & -1 & 0 & 3 & 0 & 0 & 0 & -1 & 0 \\
0 & -1 & 0 & 0 & 0 & 0 & 0 & 2 & 0 & 0 & 0 & -1 \\
0 & 0 & 0 & 0 & 0 & -1 & 0 & 0 & 1 & 0 & 0 & 0 \\
-1 & 0 & 0 & -1 & 0 & 0 & 0 & 0 & 0 & 2 & 0 & -1 \\
0 & 0 & 0 & 0 & 0 & 0 & -1 & 0 & 0 & 0 & 1 & 0 \\
0 & 0 & -1 & 0 & 0 & 0 & 0 & -1 & 0 & -1 & 0 & 2
\end{bmatrix}$$

E) Laplace of DG

Figure 3.2: Types of graph representations of a generic FE mesh

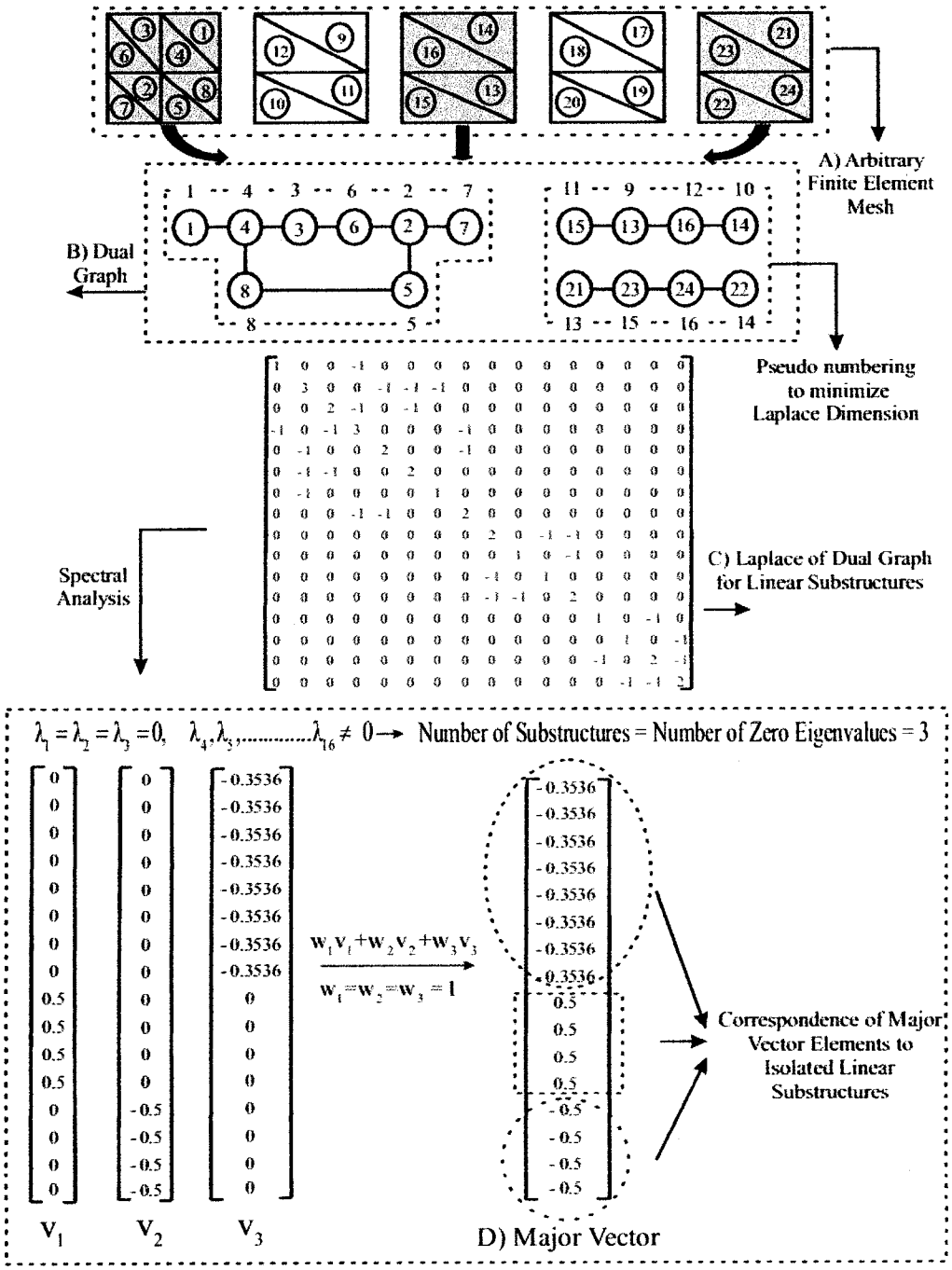

Figure 3.3: A simplified Example of linear substructures identification using spectral analysis

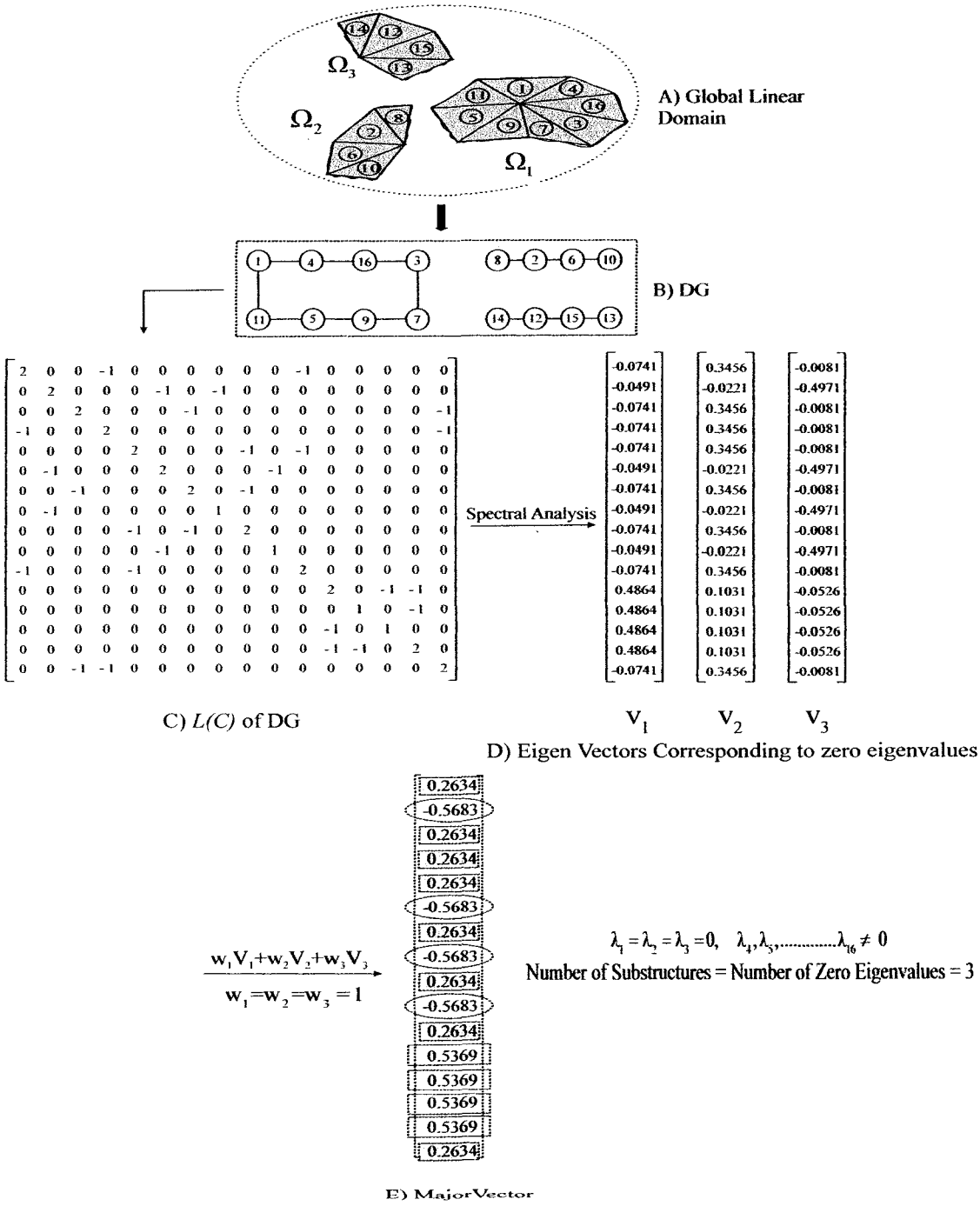

Figure 3.4: A simplified example to clarify importance of MajorVector in spectral identification of substructures

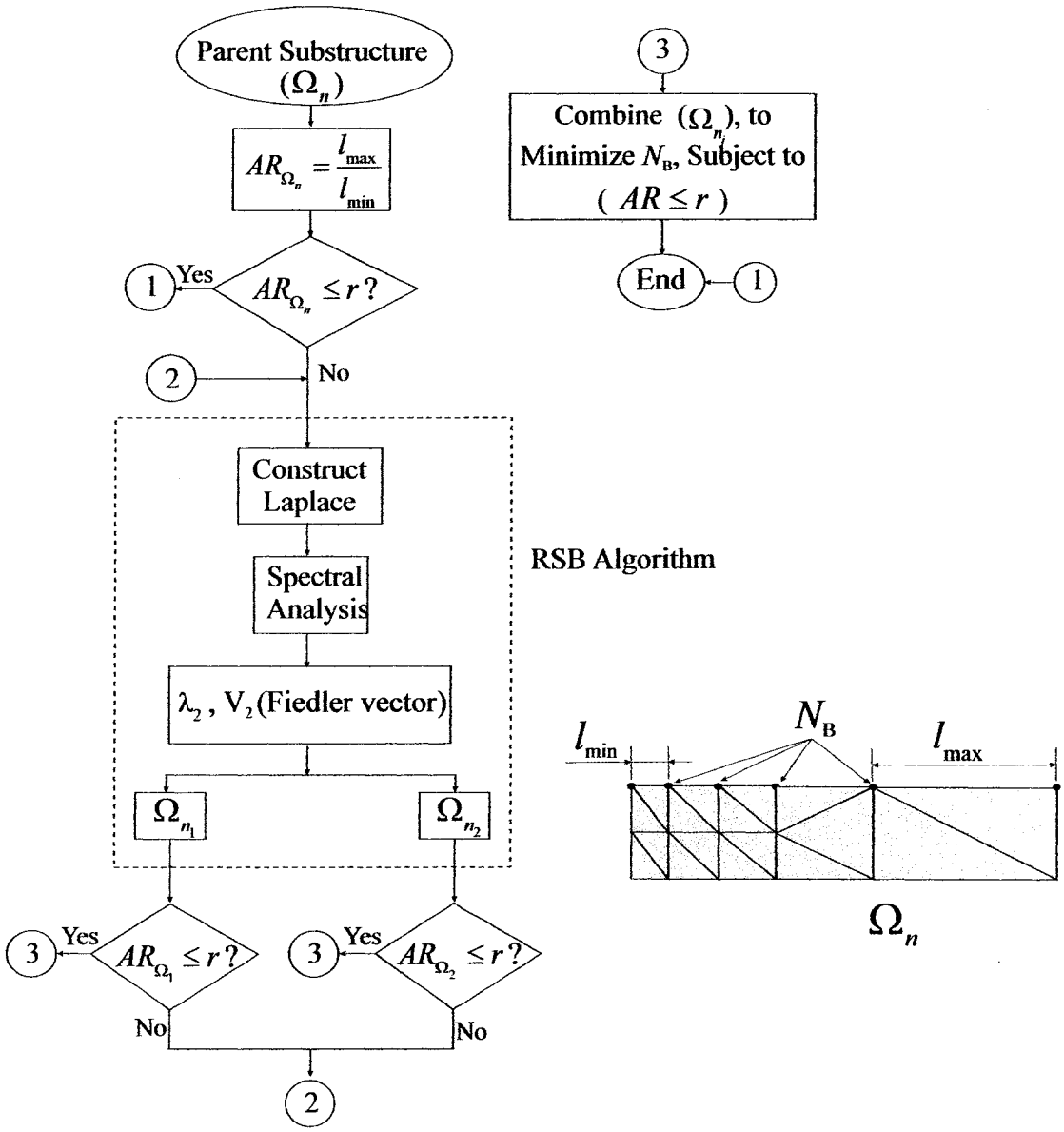

Figure 3.5: Modified RSB algorithm

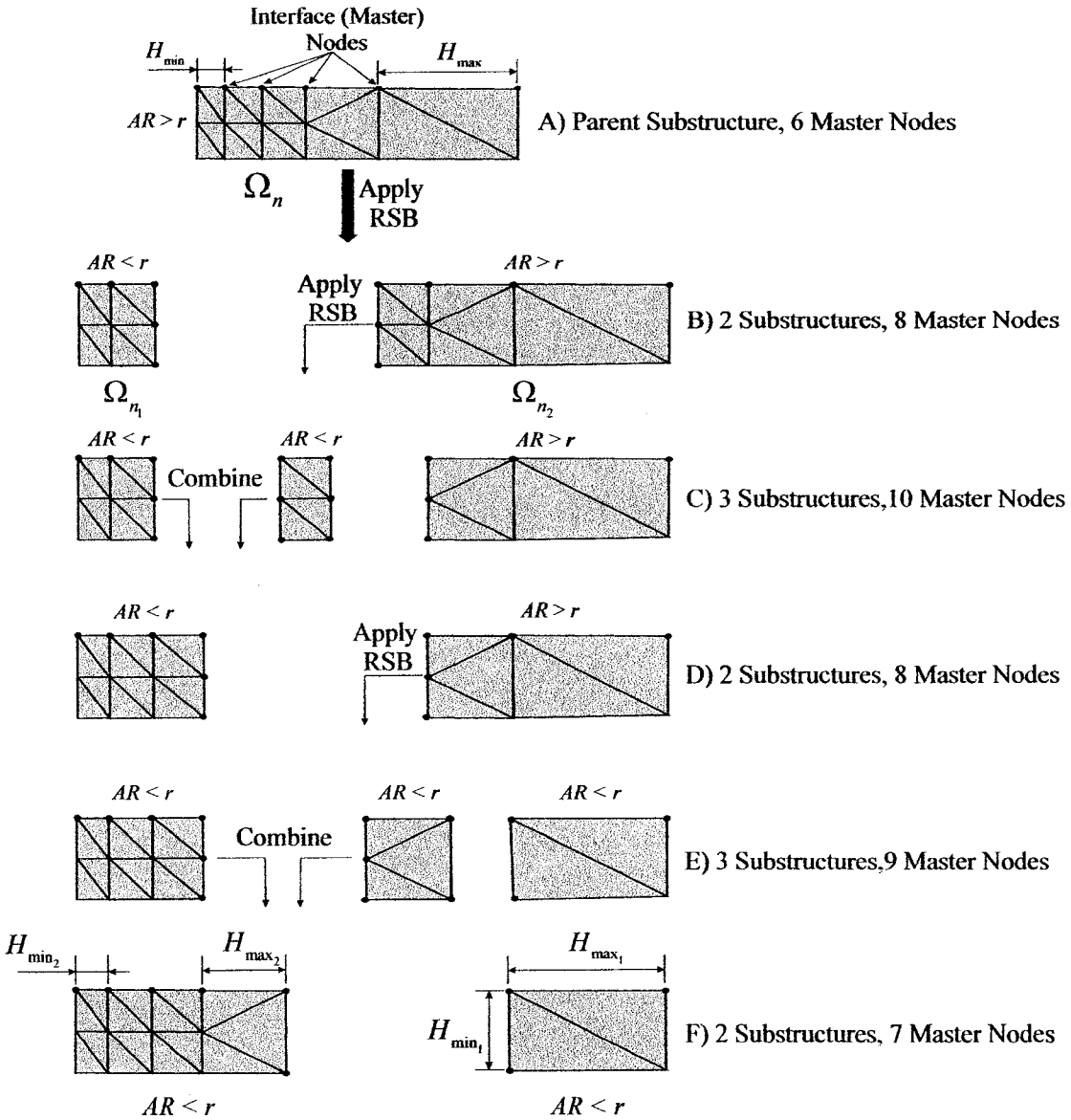

Figure 3.6: A simple example of modified RSB algorithm implementation

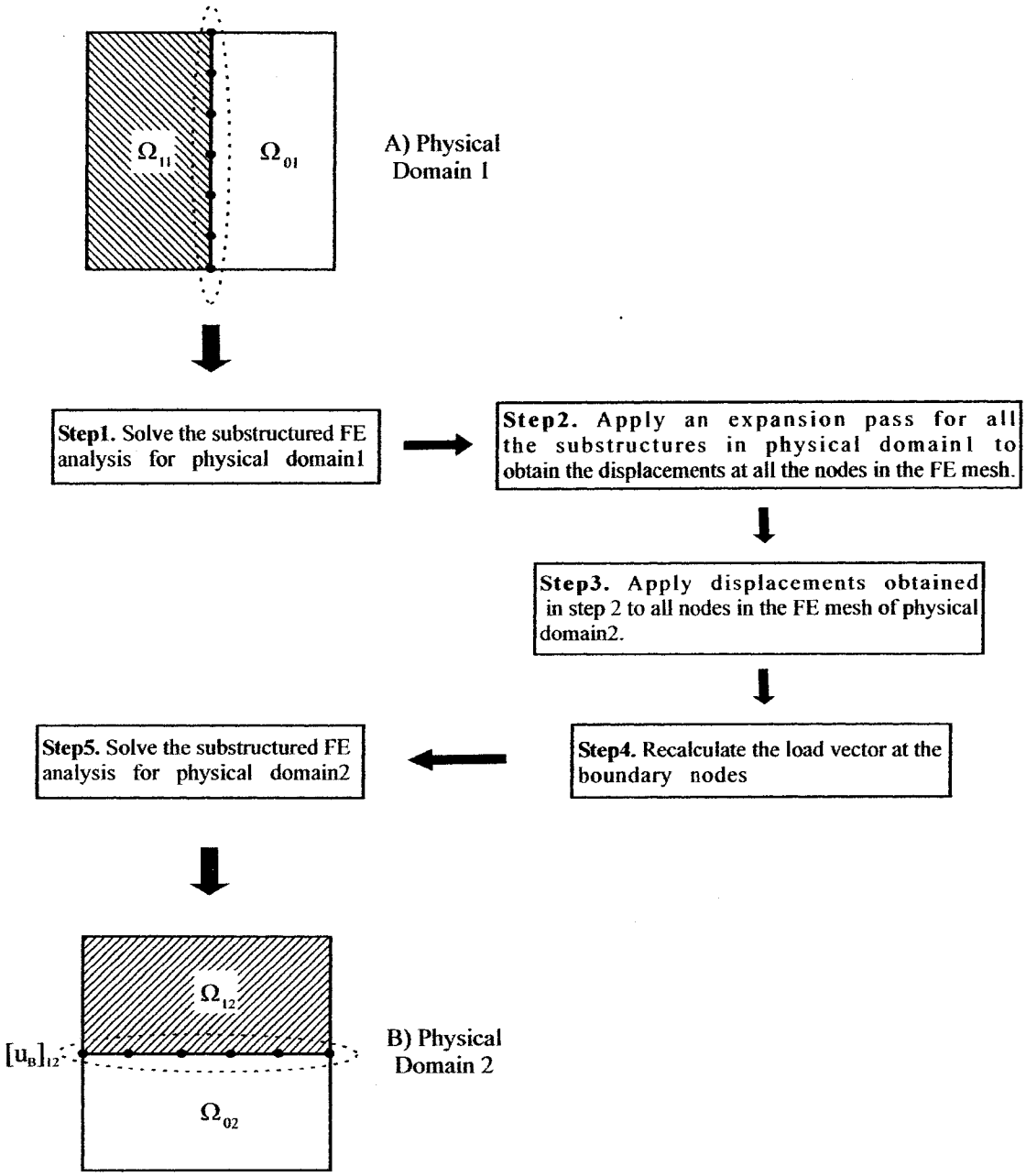

Figure 3.7: Load transfer methodology for substructures in interacting physical domains

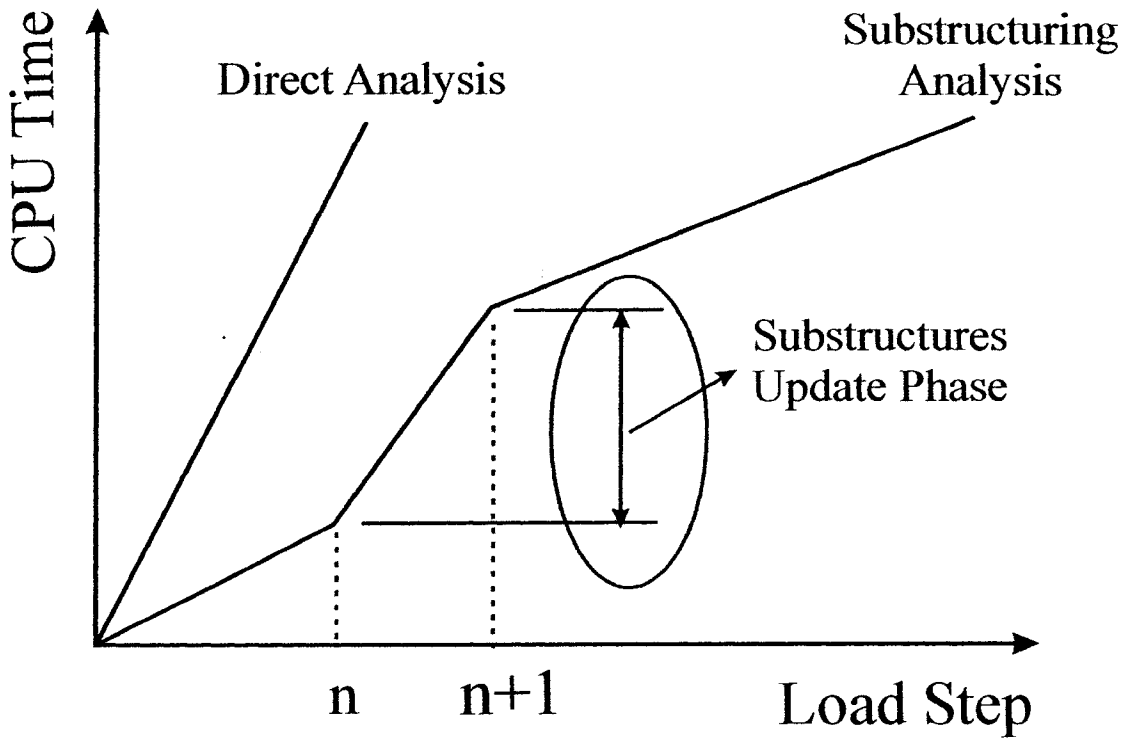

Figure 3.8: Substructures updating within a single physics analysis loading

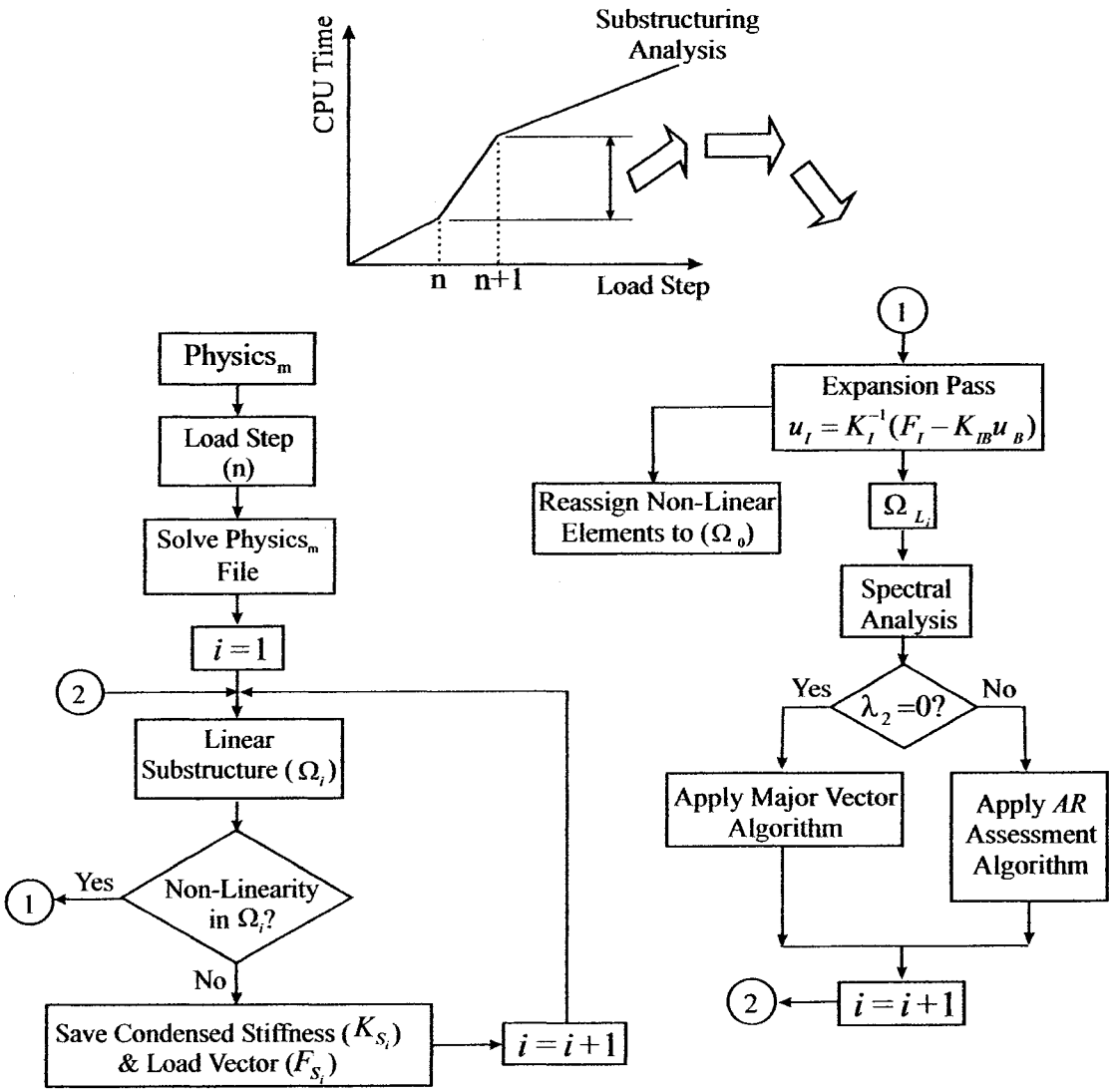

Figure 3.9: Procedure for substructures updating

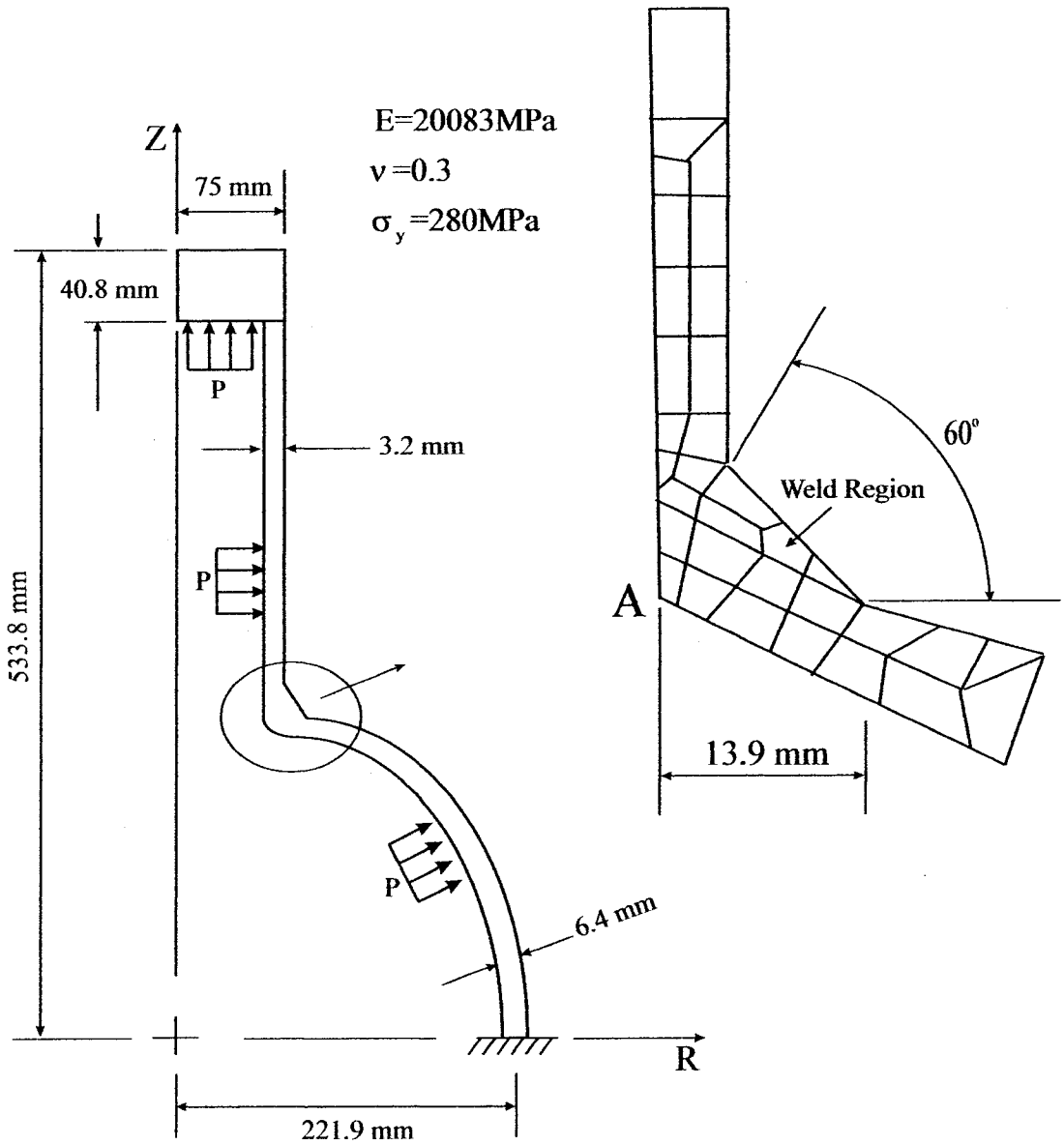

Figure 3.10: Axisymmetric pressure vessel, Han (1984)

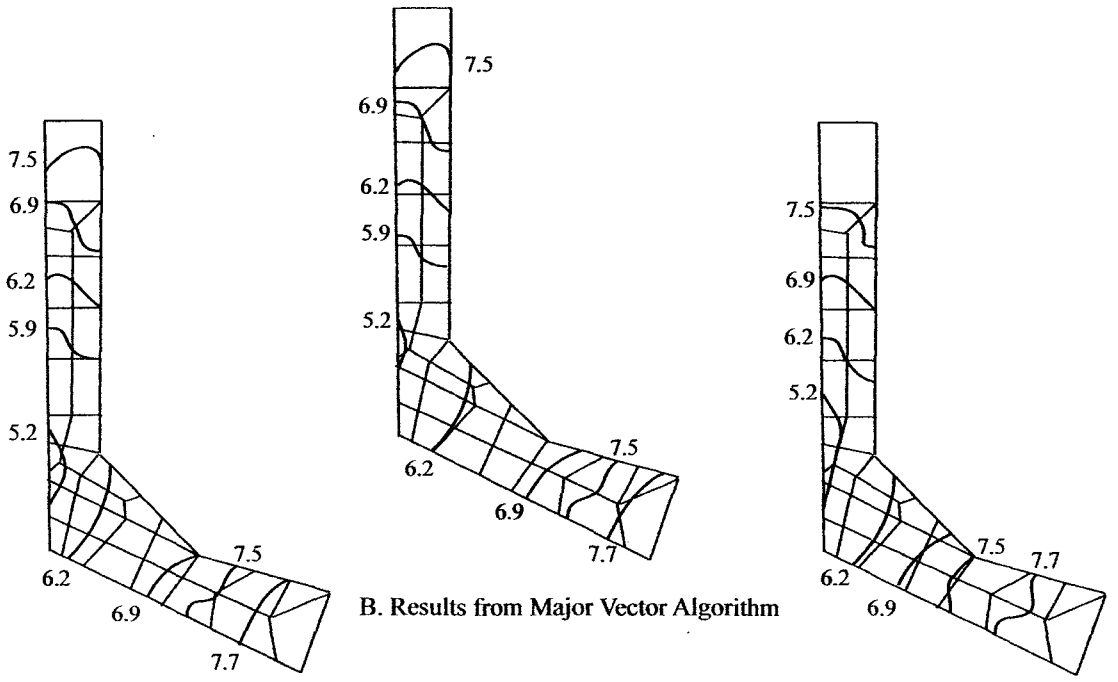

A. Results from Zienkiewicz (1977)

B. Results from Major Vector Algorithm

C. Results from Han (1984)

Figure 3.11: Spread of plastic zones (labels on contours indicate plastification limits at designated pressure in MPa).

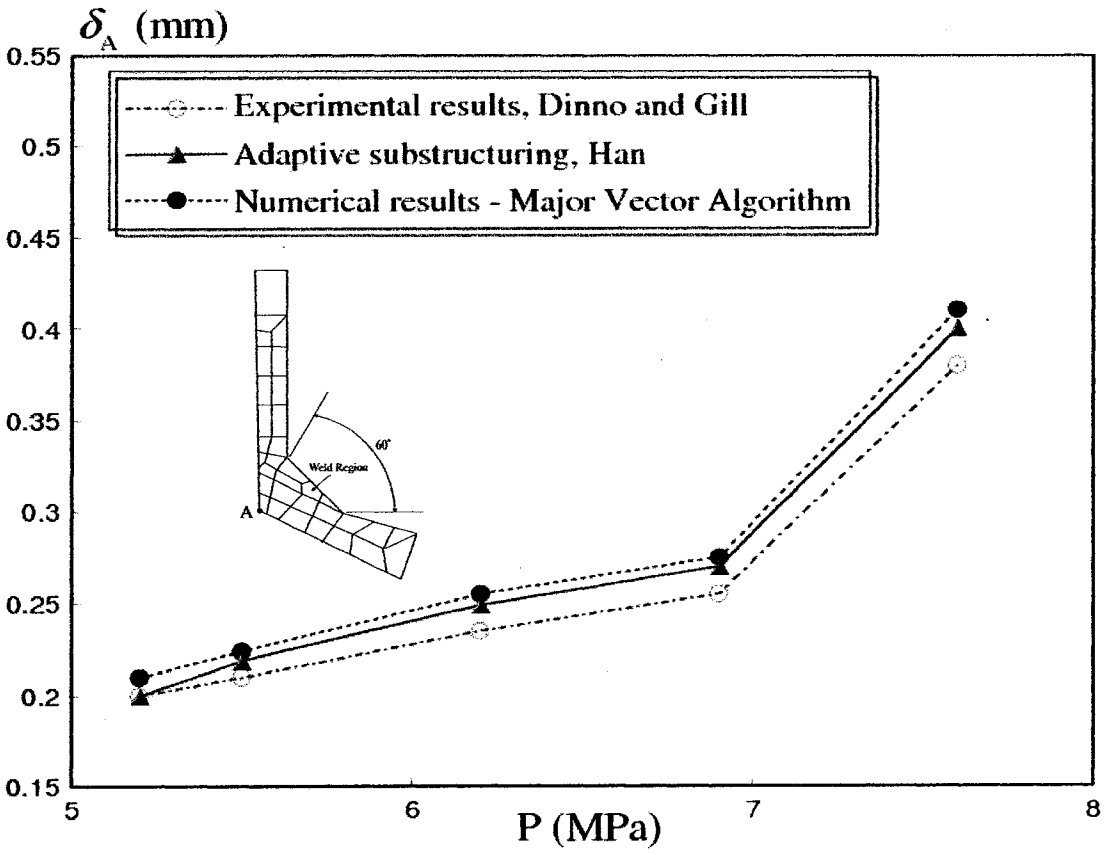

Figure 3.12: Deflection at point A of axisymmetric vessel with increasing pressure. Experimental results from Dinno and Gill (1965), adaptive substructuring results from Han (1984)

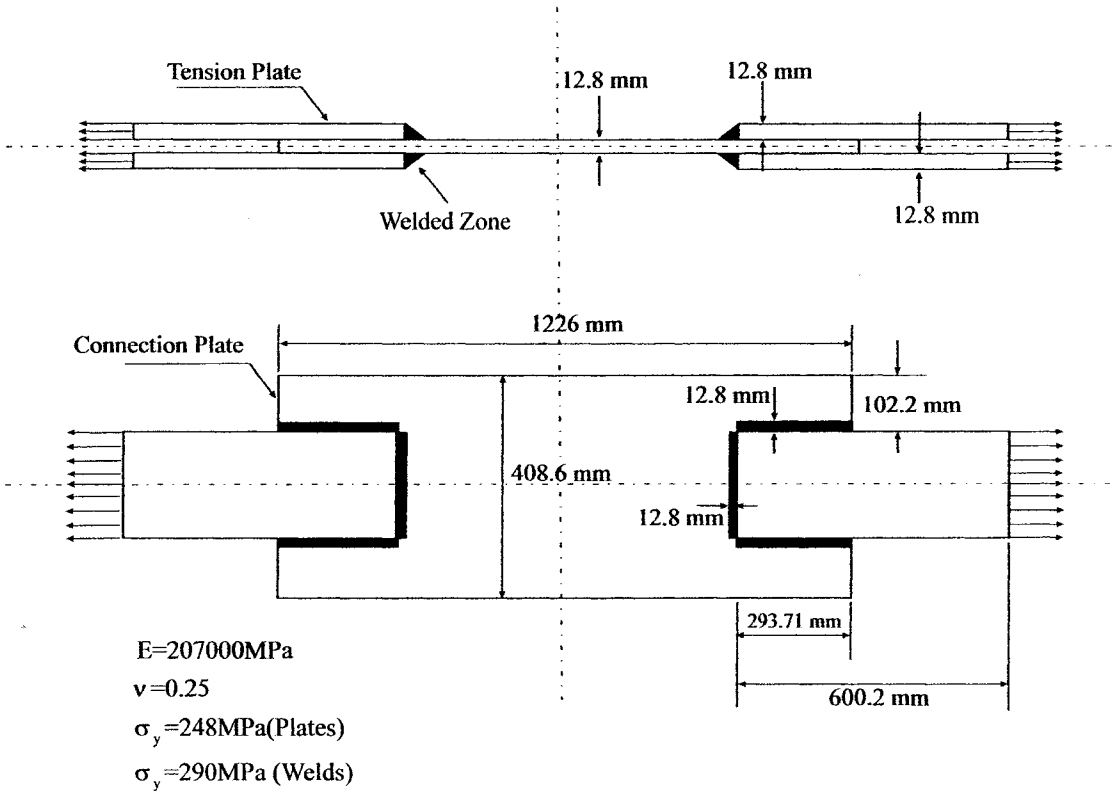

Figure 3.13: Welded tension plates, Han (1984)

Table 3.1: Statistics of analysis CPU time for axisymmetric pressure vessel

Analysis Approach	*S*	% Computational Savings
Adaptive Substructuring, Han (1984)	1.07	6
Major Vector Algorithm	3.18	68.5

Table 3.2: Statistics of analysis CPU time for welded tension plates

Analysis Approach	*S*	% Computational Savings
Adaptive Substructuring, Han (1984)	2.01	49
Major Vector Algorithm	2.82	64.6

Chapter 4

Validation of the Major Vector Algorithm on Sequentially Coupled Multiphysics FE Analysis of MEMS

This chapter presents the validation results for the application of the Major Vector algorithm in 3D sequentially coupled multiphysics FE problems. Two complicated multiphysics FE analysis of MEMS devices are discussed. The first case, presented in Section (4.1), deals with a sequentially coupled two-way electro-thermal FE analysis of micromachined MEMS gas sensors. This case represents a MEMS modeling that involve geometric complications and a large mesh size with a relatively simple sequential physics coupling. And, in Section (4.2), a multi-field coupled FE analysis of capacitive shunt RF MEMS switches is discussed. This analysis involves a two-way sequentially coupled electromagnetic (EM)-thermal analysis, a one-way sequentially coupled thermal-structural analysis, and finally a two-way sequentially coupled structural-electrostatic analysis. This case presents relatively simpler model geometry, where more sophisticated physical coupling analysis is investigated. In both multiphysics analysis cases, presented in this chapter, results from the

substructured coupled-field analyses were compared with experimental and numerical results published in the literature; and, the computational performance of the Major Vector algorithm is compared with the traditional-manual substructuring technique. Finally, some concluding remarks are presented in Section (4.3).

4.1 Coupled Electro-Thermal Analysis of MEMS Gas Sensor

The proposed MajorVector method has been utilized in modeling and evaluating the electro-thermal field in a MEMS gas sensor that was originally microfabricated by Mo *et al.* (2001). This case deals with the multiphysics modeling of the electro-thermal analysis within seven thin film layers of material that represents the full FE model of a microheater-based MEMS gas sensor. Due to the manufacturing uncertainties and material characterization problems at the micron scale, these micro devices have been reported to suffer from many reliability concerns during actual operation, such as detection sensitivity degradation and thermal fatigue failure, Mo *et al.* (2001), Puicorbe *et al.* (2003). In order to model the various design parameters of the MEMS gas sensors, a parametric analysis consisting of 625 total runs (n_{total}) is needed. The computational cost for each of these coupled electro-thermal analysis runs can reach up to 19.5 hrs on a Pentium IV 2.8 GHz processor station, which yields this study to be expensive and time consuming. In these cases, the utilization of

the substructuring technique can play a major role in reducing the total computational cost of the coupled-field FE analysis ($t_{Cpu_{Total}}$). To prove this argument, the Major Vector algorithm is utilized to solve the coupled electro-thermal FE model of the gas sensor. Also, a comparison between the applications of the Major Vector algorithm versus the traditional manual-substructuring is presented in this Section, where the identification and isolation of the substructures is achieved manually with full user-interaction.

4.1.1 Device Description

The modeled MEMS gas sensor is fabricated out of a silicon substrate that is followed by a thin film layer of SiO_2, as shown in Fig (4.1). The microheater/microsensor combination in the MEMS gas sensor is made of Pt/Ti alloy with ratio 5:1. A multilayer of $SiO_2/Si_3N_4/SiO_2$ is then deposited for insulation between the sensor/heater layers, while the top layer is made of SiO_2 thin film. A sensitive film used to detect the presence of hazardous pollution gases is deposited in the middle area (active area) of this SiO_2 top layer. The material type of the sensitive film is determined based on the gas type to be detected. In actual operation, an array of gas sensor cells is used to detect different types of gases. The optimum operation of the microsensor is achieved when the maximum temperature of the active area reaches approximately 400 ^{o}C, Mo *et al.* (2001).

4.1.2 Coupled Electro-Thermal FE Analysis

A three dimensional FE analysis is performed for the coupled electro-thermal problem in the MEMS gas senor. In a steady state, the thermal equilibrium within the sensor membrane is achieved by the balance between the heat generated in the electrical resistance, through the joule effect, and the heat loss by conduction, through the cooler supportive massive legs, and by convection, through air. The equations describing the electrical and steady state thermal conservation laws involve the 3D temperature distribution (T), the electric potential (E), as follows:

$$-\nabla[\frac{1}{R(T)}\nabla E]=0 \tag{4.1}$$

$$-\nabla[k(T)\nabla T]=\frac{1}{R(T)}[\nabla E]^2 \tag{4.2}$$

where, k and R denote the temperature dependent thermal conductivity and the electrical resistance, respectively. The equation describing the temperature dependence of the electrical resistance per unit area, $r_{res}(T)$ was reported for the heater material as, Mo *et al.* (2001)

$$r_{res}(T)=1.92(1+2.4\times10^{-3}T) \tag{4.3}$$

For boundary conditions (BC), the temperature at the external edges of the sensor is assumed to hold at room temperature, Puicorbe *et al.* (2003). On the upper surface of the membrane, the heat is dissipated through convective, conductive and thermal radiation exchange with the surrounding air. Due to the miniature scale of the heated

structures, the convection losses are considered negligible in this case. The air flow is very slow, and the air layer can then be modeled as a stagnant layer on top of the membrane. The conductive heat exchange with this air layer is calculated based on a layer thickness of (d = 0.3 μm) that is modeled on top of the membrane. The surfaces encountering heat exchange through radiation are considered as gray emitters with an emissivity of 0.5. Equation (4.4) describes the essential BC, while Equations (4.5) and (4.6) describe the natural BC described above.

$$T_s = T_r \tag{4.4}$$

$$q = -[\frac{k_{Air}}{d}(T - T_r) + \sigma_{SB}\varepsilon_r T^4] \tag{4.5}$$

$$q_i = -\sum_{j=1}^{4} \sigma_{SB} F_{ij} \varepsilon_{r,i} [T_i^4 - T_j^4], \quad i \neq j \tag{4.6}$$

where, T_s denote the surface temperature, q is the heat flux, k_{Air} is the thermal conductivity of air, σ_{SB} is the Stefan Boltzmann constant, ε_r is the emissivity , q_i is the heat flux from cavity wall (i), F_{ij} is the view factor between surfaces (i) and (j) and $\varepsilon_{r,i}$ is the emissivity of surface (i). The negative sign in Equations (4.5) and (4.6) denote the energy dissipation from the surface.

The FE model and temperature distribution on the top layer of the sensor are shown in Fig (4.2). For this case, an earlier FE mesh sensitivity analysis was carried out, and concluded that for a 3D model of the gas sensor, a minimum of 450,000 elements with 300,000 DOF is required to achieve mesh independent solution. This

large mesh size is often used in multiphysics problems that involves MEMS sensors and is usually attributed to the analysis complexity; which in this case, includes nonlinearities due to radiation, temperature dependence of the material properties and geometrical complications because of the sensor high geometrical aspect ratio.

4.1.3 Nonlinearity Classification

In this phase, nonlinearity criterions are set to identify elements belonging to the global linear domain. The nonlinearity criterions in the current gas sensor model include radiation effects and temperature dependence of the material properties of the composing thin films. However, the severity of each criterion depends on the operating temperature and the type of thin film material. This means that for each thin film layer, there is a certain temperature, defined as the linearity temperature (T_L) that identifies the status of linearity of the elements within this layer. Beyond T_L, the nonlinearity arising from the material properties temperature dependence has a significant effect on the solution accuracy. Therefore, all elements bounded by a contour with a value equal or higher than T_L should be reassigned to the nonlinear region, as shown in Fig (4.2-B) and (4.2-C).

To identify T_L, a non-linearity sensitivity run is conducted for each of the gas sensor seven layers. In each run, one of the thin film layers is treated as a substructure (i.e. linear zone) and the applied power (P) is then ramped up. The temperature at the

center of the layer is then calculated for each power load step and compared with the temperature experimentally obtained by Mo *et al.* (2001). The linearity temperature is identified for each thin film layer, once an absolute error percentage (ε), set for the analysis, is reached between the numerical and experimental temperature values. The outcomes of these sensitivity runs and error distribution are shown in Fig (4.3) and Fig (4.4), respectively. where, TNAS, refers to the total nonlinear analysis strategy, in which substructuring was only considered for the silicon substrate. The linearity temperatures for different thin film layers are listed in Table 4.1 for ε of 2, 4 and 5.

In this study, for example, the substructuring process can be partially extended to other regions, if ε = 3 percent is considered acceptable by the sensor designer. This strategy is referred to as the reduced nonlinear analysis strategy (RNAS), and is used to maximize the computational savings without exceeding a "designer specified" acceptable loss in the solution accuracy. A schematic representation of the nonlinearity zones calculated by using T_L for different thin film layers in RNAS is shown in Fig (4.5). where, $P_{Varient}$ represents the dependence of material properties on temperature, and reduced nonlinearity regions are calculated based on a 3 percent acceptable error

4.1.4 Parametric Study

A parametric study of the coupled electro-thermal problem in MEMS gas sensors is conducted to examine the efficiency of the Major Vector algorithm introduced earlier

in Chapter 3. This study is carried out using a single processor machine; where the substructuring performance of the MajorVector algorithm is evaluated against the traditional manual-substructuring technique. Computational parameters used in this evaluation include the isolation speed factor (*I.S.F*), which refers to the reduction in the linear zones isolation overhead time, and percentage reduction in the total computational cost of the runs conducted in the parametric study (t_{Cpu_R}). The study also identifies the effect of the aspect ratio threshold value (r) on the number of generated substructures (N_s), substructuring time (t_s), and the size of the interface problem (N_B). The *I.S.F* and t_{Cpu_R} are calculated using Equations (4.7) and (4.8), respectively.

$$I.S.F = \frac{t_{s_M}}{t_{s_{MV}}} \tag{4.7}$$

$$t_{Cpu_R} = \frac{t_{Cpu_{Total,ns}}}{t_{Cpu_{Total,s}}} \tag{4.8}$$

where, t_{s_M} and $t_{s_{MV}}$ refer to the linear-zones isolation overhead time using the traditional manual-substructuring and the MajorVector algorithm, respectively. And, the total computational cost of the parametric study runs with substructuring (manual or automated) and with direct analysis is referred to as $t_{Cpu_{Total,s}}$ and $t_{Cpu_{Total,ns}}$, respectively. In the current case, the value of the modeling time (t_m) was found to be negligible compared to the solution time of the coupled electro-thermal model of the

MEMS gas sensor. Therefore, $t_{Cpu_{Total,ns}}$ and $t_{Cpu_{Total,s}}$ are approximated using Equations (4.9) and (4.10), respectively.

$$t_{Cpu_{Total,ns}} \approx t_{sol,ns}(n_{total}) \ , \ t_m \ll t_{sol,ns} \tag{4.9}$$

$$t_{Cpu_{Total,s}} \approx t_{sol,s}(n_{total}) + t_s(n_s) \ , \ t_m \ll t_{sol,s} \tag{4.10}$$

where, $t_{sol,ns}$ and $t_{sol,s}$ refer to the solution time with direct analysis and with substructuring, respectively; while n_s refer to the number of runs, in which the previously generated substructures have to be updated.

4.1.5 Comparison between S_{MV} and S_M

A comparison between the automated substructuring process using the MajorVector algorithm (S_{MV}) and the traditional manual-substructuring (S_M) for both nonlinear analysis strategies, TNAS and RNAS, is shown in Tables (4.2) and (4.3), respectively. The following observations are presented based on these results:

(1) n_s represents only 4 percent of n_{total} with the TNAS. On the other hand, for RNAS, the substructuring is extended to regions within the thin film layers, having temperature values less than or equal to T_L, which increases n_s to 100 percent of n_{total}.

(2) The size of the interface problem (N_B) increases with the RNAS compared to TNAS due to the increase in the number of generated substructures. However,

N_B is higher with S_M due to the inaccuracy introduced during the process of the manual isolation of the linear regions.

(3) The isolation speed factor (*I.S.F*) is higher with the RNAS due to the increased substructuring overhead time in manual isolation with S_M.

(4) An additional savings of 48 percent in the solution time ($t_{sol,s}$) can be noticed for the RNAS over the TNAS with S_{MV}. However, this reduction in cost is only reduced to 44 percent saving in $t_{Cpu_{Total,s}}$; which is attributed to the multiplication of t_s by 100 percent of n_{total} in the RNAS case compared to only 4 percent of n_{total} in the TNAS case.

(5) The overall comparison between S_{MV} and S_M emphasize the superiority of the Major Vector algorithm over the traditional manual-substructuring technique. This is mainly obvious in the reduction in N_B, higher *I.S.F* ranging from 17 to 19, better solution accuracy (€) and an additional 46 percent reduction in t_{Cpu_R}.

4.1.6 Effect of Aspect Ratio Threshold Value

This section describes the utilization of the modified RSB algorithm to assess and update the substructures generated in the gas sensor model. Fig (4.6) shows the effect of varying (r) from 1, to 5 on the number of generated substructures, interface size problem and the substructuring time for the Si_3N_4 thin film layer. As shown in Fig

(4.6-A), (4.6-B), and (4.6-C), (r) is inversely proportional to N_s because the partitioning of the substructures is ramped up to achieve the required AR constraint. This increase in the N_s value will also result in an increase in the value of N_B. More results that highlight the effect of decreasing r on the individual components level and the whole system level, are listed in Tables (4.4), (4.5) and (4.6) for (r) values of 1, 3 and 5, respectively.

The effect of (r) on different computational parameters can be shown in Table (4.7) for (r) values of 1, 3 and 5 with both nonlinear analysis strategies (TNAS and RNAS). These results indicate that:

(1) The substructuring time (t_s) increases with the decrease in the value of (r) due to the additional overhead time taken by the modified RSB algorithm to partition the generated substructures with unacceptable AR.

(2) The $I.S.F$ increases with the reduction of the (r) value.

(3) The solution time increases with the decrease in (r), which can be attributed to the increase in N_B. It is also important to note the reduction in the solution error (Є) with the decrease in the value of (r).

(4) The total computational cost of the parametric study runs increases with the decrease in (r) due to the increase in t_s and $t_{sol,s}$.

(5) For this specific case study, the solution error using (r) values of 1 or 10 will defer by 2.3 percent with the application of RNAS. This error variation is considered less significant when compared to the reduction achieved in the

overall computational cost of the parametric analysis (76.87 percent for r =10, compared to 69.23 percent for r =1, using RNAS).

4.2 Coupled Multiphysics FE Analysis of RF MEMS Switches

The RF MEMS switch model, analyzed in this work, consists of fixed-fixed corrugated aluminum thin film membrane, mounted on a silicon substrate, and suspended over a bottom electrode insulated by a dielectric film, as shown in Fig (4.7). This switch is utilized in wireless communication and radar systems for carrying RF signals in the range from 0.1 to several thousands GHz, Goldsmith *et al.* (2001, 1998). When the switch is inactivated, a low capacitance state is exhibited between the aluminum membrane and the bottom electrode, and the device is in the off state. When a voltage is applied between the two conductors, an electrostatic force is created to pull the membrane down. At a certain voltage, referred to as the pull-in voltage (V_{PI}), the membrane collapses and makes contact with the dielectric layer, and the device is in the on state, Rebeiz (2003).

For RF MEMS switches, the long-term reliability is limited by two mechanisms, mainly the buckling failure and the membrane stiction with the dielectric layer, Jensen *et al.* (2003), Wang *et al.* (2006). The membrane buckling occurs, because of the compressive thermal stresses, induced at higher operating temperatures,

associated with high transmitting frequencies ($\omega > 0.1\text{GHz}$), Rizk *et al.* (2002). At these frequencies, self inductance of the conductor causes electrons crowding at the outside edges of the beam, a phenomenon commonly known as the skin effect. This phenomenon increases the heat dissipation to the beam; therefore higher temperatures are generated, which causes the switch to buckle. On the other hand, membrane stiction with the dielectric layer occurs at higher actuation voltages, because of the charge build-up in the dielectric layer, Pamidighantam *et al.* (2002).

In order to investigate different failure mechanisms in RF MEMS switches, a multi-field coupled FE analysis (see Fig (4.8)) is needed. This analysis involve a two-way, sequentially coupled-field, a harmonic EM-thermal analysis to calculate the temperature distribution in the switch membrane, at high operational frequencies; then, a one-way, sequentially coupled-field, thermal-structural analysis is conducted to calculate the induced compressive thermal stresses and the new deformation state of the switch; finally, the new deformation state of the switch, is used as a starting point for a two-way, sequentially coupled-field, structural-electrostatic analysis, to calculate the switch pull-in voltage. A schematic representation of the physical domains used in the RF MEMS switch, multi-field coupled analysis, is shown in Fig (4.9).

The computational cost, to solve the multi-field coupled FE analysis of the RF MEMS switch model is very expensive (31 hrs on a Pentium IV, single processor station). Therefore, the utilization of the substructuring to solve the RF switch model

can play a major role in analyzing this problem, more efficiently. Full details of the substructured coupled multi-field FE analysis, for the RF MEMS switch, the used boundary conditions (BCs) and validation examples are presented next.

4.2.1 EM-Thermal Fields Coupling

In the harmonic EM field, the analysis starts with the RF switch initially at room temperature (T_r). A current (I) load that varies harmonically with time, is applied at the edge ($x=0$) of the switch membrane. The electric field distribution is determined by solving the governing Maxwell's equations, Stewart (2001).

$$\nabla E = \frac{\rho_m(T)}{\varepsilon_o},\ \nabla_x E = -\frac{\partial B}{\partial t},\ \nabla B = 0,\ \text{and}\ \nabla_x B = \mu_o J + \varepsilon_o \mu_o \frac{\partial E}{\partial t} \qquad (4.11)$$
$$\text{BCs},\quad E = 0\big|_{x=l_m},\quad \vec{B}.\vec{s} = 0\big|_{x=l_m}$$

where, ∇, is the divergence operator; E, is the electrical field strength; $\rho_m(T)$, is the temperature dependant electrical resistivity of the switch membrane material; ε_o, is the permeability of free space; ∇_x, is the curl operator; B, is the magnetic field strength; and, μ_o is the permittivity of free space.

After solving for E, the current density (J) is calculated by, $J = E/\rho_m(T)$ and the analysis is switched to the thermal field to calculate the temperature distribution (T). For the frequencies considered in this study ($\omega \geq 0.1\text{GHz}$), the time constant for the thermal response is much longer than the period of variation of the input power.

Therefore, T is calculated using the steady state heat equation given by, Jensen *et al.* (2003).

$$\nabla(k_m \nabla T) = -\|J\|^2 \rho_m(T) \tag{4.12}$$

where, k_m is the thermal conductivity of the switch membrane material. The convection and radiation heat transfer mechanisms were negligible compared to the heat transfer by conduction [3]. The BCs, used in the thermal analysis, assume that the edges of the switch membrane ($x = 0, l_m$) are kept at room (T_r). Adiabatic BCs are assumed for the other four sides of the membrane ($z = g_0$, $g_o + t_m$ and $y = 0, W_m$). The value of the electrical resistivity is updated for the new temperature distribution, and the analysis is switched back to the EM field to calculate J . Iterations between the EM and thermal fields are executed in sequence until a convergence for the value of T is achieved. The current applied to the EM field is ramped up and the whole procedure is repeated until the value of the maximum current is reached.

In the substructured EM-thermal coupled-field FE analysis, the nonlinearity arises from the temperature dependence of the electrical resistivity. The temperature variation of the electrical resistivity is adjusted by the Wiedemann-Franz law given by, $\rho_m(T) = LT / k_m$. where, $L = 2.45 \times 10^{-8}$ W-Ω/K^2 is the Lorentz number, Zhu *et al.* (2004). However, this variation, only effect the solution accuracy at elevated temperatures, exhibited at the later stages of current loading. Therefore, the EM analysis starts by considering the whole switch aluminum membrane as a single

substructure. As the current loading increases, the nonlinearity zone expands and the substructure(s) is updated, to preserve the solution accuracy. A schematic representation of the expansion of the nonlinear zone during the loading stages in the EM-thermal field analysis is shown in Fig (4.10).

To assess the accuracy of the substructured EM-thermal coupled-field model, the following two examples were utilized:

- **Example 1**

In this example, the temperature distribution along the length of a fixed-fixed gold beam ($l_m = 400\mu m, W_m = 50\mu m, t_m = 2\mu m$), with an input power of 1W is calculated. The beam was analyzed at two operational frequencies, 40 MHz and 40 GHz. At low frequencies, the current is spread evenly through the beam. For higher frequencies, self inductance of the conductor causes electrons crowding at the outside edges of the beam, a phenomenon commonly known as the skin effect, Jensen *et al.* (2003). This phenomenon increases the heat dissipation to the beam; therefore higher temperatures are generated in the beam with higher operational frequencies. Results from the coupled EM-thermal model highlight this effect, and are compared with numerical model data reported by Jensen *et al.* in 2003, as shown in Fig (4.11). A good agreement between the two models is evident.

- **Example 2**

In this example, the spatial average temperature rise versus input power in a fixed-fixed gold beam ($l_m = 400\mu m$, $W_m = 20\mu m$, $t_m = 2\mu m$),is calculated. The beam

was analyzed at operational frequencies of 2, 13.5 and 18 GHz. The results from the substructured EM-thermal model were compared with numerical and experimental data reported by Wang *et al.* in 2006. The comparison is shown in Fig (4.12), where, EFE-BI refers to the finite element boundary integral method used to analyze the same problem by Wang *et al.* in 2006. The results from the Major Vector algorithm were calculated initially based on a linearity temperature of 115 °C. For an operational frequency of 13.5 GHz, the results start to diverge from the experimental measurements at an input power higher than 0.5 W. Therefore, the linearity temperature criteria were reduced to 95 °C for input power higher than 0.5 W, and the same criteria was used to calculate the spatial average temperature rise for frequencies above 13.5 GHz. As shown in Figure 4.12, the reduction of T_L, yields better solution accuracy, but this was on the expense of higher computational costs.

The performance results of the Major Vector algorithm (S_{MV}) versus the traditional manual-substructuring (S_M), for the EM-thermal coupled-field FE analysis of the RF MEMS switch, are listed in Table (4.8).

4.2.2 Thermal-Structural Fields Coupling

The temperature distributions calculated from the substructured EM-Thermal coupled-field analysis are applied to the structural field model as body loads. Due to the mismatch of the coefficient of thermal expansion between the switch membrane and the substrate, thermal stresses and new switch deformation state, results from the

applied T. The thermally induced axial strain ($\varepsilon_{th,x}$) and stress ($\sigma_{th,x}$) at a given position (x, z) are given by, Blendez *et al.* (2002).

$$\varepsilon_{th,x}(x,z) = -\Delta\alpha \int_{T_r}^{T(x,z)} dT, \qquad \sigma_{th,x}(x,z) = \overline{E_m}(\varepsilon_{th,x}(x,z)) \tag{4.13}$$

where, $\Delta\alpha$ is the difference in thermal coefficient expansion between the membrane and the substrate; $\overline{E_m}$ is the effective Young's modulus of the switch membrane, given by, $\overline{E_m} = E_m/(1-\nu_m^2)$ for $W_m > 5t_m$, Pamidighantam *et al.* (2002); E_m and ν_m, refer to the membrane material Young's modulus and Poisson's ratio, respectively. Once the thermal induced stress distribution is known, the new switch geometry is found by calculating the membrane deflection (D_m) from Karaman equation, with four known BCs, Doerner and Mix (1998).

$$\frac{d^4D_m}{dx^4} = \frac{1}{D}\left[\frac{E_m t_m}{2}\left(\frac{dD_m}{dx}\right)^2\left(\frac{d^2D_m}{dx^2}\right) + \sigma_{th,x}(x,z)(1-\nu_m)t_m\left(\frac{d^2D_m}{dx^2}\right)\right], \qquad D_m = 0\Big|_{x=\pm L_m/2} \quad and \quad \frac{dD_m}{dx} = 0\Big|_{x=\pm L_m/2} \tag{4.14}$$

where, D is the flexural rigidity of the membrane, given by, $D = E_m t_m^3/(12(1-\nu_m^2))$.

In the substructured thermal-structural coupled-field FE analysis, the nonlinearity in the structural domain is determined based on the state of the effective thermal stress. The state of stress is divided into four levels. The first level is the yield stress (σ_Y); the second is $F_1 \times \sigma_Y$; the third is $F_1 \times F_2 \times \sigma_Y$; and finally the fourth level is below $F_1 \times F_2 \times \sigma_Y$; where, F_1 and F_2 are factors less than unity and greater than 0.7,

Han (1984). At the initial stages of the temperature loading, the effective thermal stress values, at all the elements in the structural domain, lay within levels three and four; therefore, the whole switch membrane is considered as a single substructure at the beginning of the structural field analysis. As the temperature loading increase, elements reaching stress levels one or two are reassigned to the nonlinear region, and the reduced stiffness matrix and load vector of the new substructures are recalculated. If no elements belonging to a particular substructure need to be reassigned to the nonlinear domain, the reduced stiffness matrix and the load vector of this substructure, from the previous load step, are saved and used for the next loading step.

The performance results of the substructured thermal-structural coupled-field FE analysis, utilizing the Major Vector algorithm and the traditional manual-substructuring, are listed in Table (4.9).

4.2.3 Structural-Electrostatic Fields Coupling

The new switch geometry, calculated in the substructured thermal-structural coupled-field FE analysis, is shown in Fig (4.13). This geometry is used as a starting point for the structural-electrostatic analysis. In the electrostatic field, the essential BCs are the applied ramped voltages at the bottom and top conductors. Since the width (W_m) of the modeled switch membrane is greater than the initial gap length (g_o), the fringing field effects were neglected, Pamidighantam *et al.* (2002). The voltage distribution

(V) in the underlying medium was calculated by solving the governing Laplace equation with two known BCs, Peroulis *et al.* (2003).

$$\nabla^2 V = \frac{\partial^2 V}{\partial x^2} + \frac{\partial^2 V}{\partial y^2} + \frac{\partial^2 V}{\partial z^2} = 0, \qquad V = V_0\big|_{z=g_0} \text{ and } V = 0\big|_{z=t_e} \tag{4.15}$$

where, V_o refer to the applied ramped voltage at the bottom of the aluminum switch membrane. The electrostatic force distribution was then calculated, and the model is switched to the structural field. A new deformation state was obtained from the structural analysis and the model was switched back to the electrostatic field. The electrostatic domain mesh was updated and a new value for the electrostatic force distribution was calculated. Iterations between the structural and electrostatic fields are executed in sequence until a convergence in the membrane deflection was reached. The applied voltage is ramped up and the process is repeated for the new voltage value.

In the substructured structural-electrostatic coupled-field FE analysis, the nonlinearity in the structural domain arises from the geometric nonlinearity, associated with the large deflections induced in the switch membrane ($> 0.01 t_m$). Therefore, for the structural field analysis, the substructuring was only limited to the substrate. In the electrostatic domain (free space between two conductors), the nonlinearity arises from the mesh update associated with the deformation of the underlying medium with the membrane deflection. However, the pull-in voltage value

is reached when the maximum center membrane deflection reaches approximately $0.67g_o$. Therefore, for the electrostatic domain, all the elements lying above a distance $0.3g_o$ from the bottom electrode are assigned to the nonlinear domain from the beginning of the electrostatic analysis.

To assess the accuracy of the substructured structural-electrostatic coupled-field FE analysis, the following two examples were utilized:

- **Example 1**

In this example, results from the substructured structural–electrostatic model are compared with the closed-form analytical expression for the pull-in voltage given by, Pamidighantam *et al.* (2002).

$$V_{PI} = \sqrt{\frac{8K_{eff}g_o^3}{27\varepsilon_o A_{eff}}} \tag{4.16}$$

where, K_{eff} is the effective beam stiffness, and is given by Equation (4.17) for a uniform electrode, Pamidighantam *et al.* (2002); ε_o is the permittivity of free space; A_{eff} is the effective area, given by Equation (4.18), which mainly accounts for the fringing field effects and the charge redistribution effects, Chang (1994), Palmer (1937)

$$K_{eff} = \left[\frac{32\overline{E_m}W_m t_m^3}{l_m^3} + \frac{8.32N}{l_m}\right], \quad N = (\overline{\sigma_{res}} + \sigma_{NL})W_m t_m \tag{4.17}$$

$$A_{eff} = W_{m,eff} t_m$$
$$W_{m,eff}(\beta) = W_m \left(1 + 0.65 \frac{(1-\beta) g_o}{W_m} \right), \quad \beta = \frac{z_{\max}}{g_o} \tag{4.18}$$

where, $\overline{\sigma_{res}} = \sigma_{res}(1-\upsilon_m)$ is the residual film stress; $\sigma_{NL} = \pi^2 E_m z_{\max}^2 / 4l_m^2$ is an estimate of the induced axial stress due to the nonlinear stiffening; $z_{\max}$ is the center deflection of the beam at a given applied voltage.

The analytical and the FE simulation results, for the pull-in voltage versus beam length, for a fixed-fixed gold beam, at different microfabrication residual stresses are shown in Fig (4.14). In this example, a value of 0.4 was assumed for β_{PI}^{CC}, which reduces the effective area by 22.5 percent. The comparison shows a good agreement between the substructured structural-electrostatic model and the analytical solution.

- **Example 2**

In this example, the pull-in voltage versus gap length, for a fixed-fixed aluminum beam, was calculated using the substructured structural-electrostatic model, the analytical solution and compared to numerical results reported by Rebeiz in 2003. The comparison was conducted at residual stress values of 0, 30 and 60 MPa, as shown in Fig (4.15). In this example, β_{PI}^{CC} was assumed to be 1. As shown in Figure (4.15), results from the substructured structural-electrostatic FE analysis are in good agreement with the analytical and reported numerical solutions.

The performance results of the substructured structural-electrostatic coupled-field FE analysis, utilizing the Major Vector algorithm and the traditional manual-

substructuring, are listed in Table (4.10). It can be shown that the large deformations and geometric nonlinearity involved in the structural-electrostatic fields coupling limit the benefit of the substructuring technique because of the limited linear region in the FE domain. Therefore speed factors close to one were obtained, which indicate that the substructuring is not efficient in analyzing these types of problems.

4.3 Concluding Remarks

The validation results for the application of the Major Vector algorithm to substructure sequentially coupled multiphysics FE problems have been presented in this chapter. Two complicated multiphysics FE analysis of MEMS devices are discussed. The first case deals with a sequentially coupled two-way electro-thermal FE analysis of micromachined MEMS gas sensors. This case represents a MEMS modeling case that involve geometric complications and a large mesh size with a relatively simple sequential physics coupling. The second case deals with a multi-field coupled FE analysis of RF MEMS switches. This case presents relatively simpler model geometry, where more sophisticated physical coupling analysis is investigated. A good agreement has been found between the results from the substructured coupled-field analysis and those published from various studies in the literature. The computational performance of the Major vector algorithm has also been compared with the traditional manual-substructuring technique. The performance comparison results indicate the following:

(i) A considerable reduction in the overhead time of the linear region isolation phase was achieved by using the Major Vector algorithm compared to the traditional manual-substructuring technique. This result is evident in the higher isolation speed factors (*I.S.F*) that can reach up to 37, when using the Major Vector algorithm.

(ii) The Major Vector algorithm provides more flexibility to the FE analyst to use different approaches in analyzing coupled multiphysics problems. This was evident in analyzing the two multiphysics cases, presented in this chapter, where two nonlinear analysis strategies were utilized to analyze these problems.

(iii) Better solution accuracy and higher speed factors are achieved with the Major Vector algorithm compared to the traditional manual-substructuring technique.

(iv) The aspect ratio threshold value (r) is inversely proportional to N_s because the partitioning of the substructures is ramped up to achieve the required AR constraint, which also results in an increase in N_B. However, the modified

RSB algorithm minimizes this increase by ignoring the load balancing constraint.

(v) The solution error exhibited using larger (r) values is less significant when compared to the reduction in the total computational cost of the coupled-field FE analysis. This result was evident in the MEMS gas sensor problem, where increasing (r) values from 1 to 10 will defer the solution accuracy by an average of 2.31 percent; while and additional 8 percent reduction in the computational cost was achieved by increasing (r) from 1 to 10.

(vi) The substructuring does not improve the efficiency of FE problems that involve geometric nonlinearities. This was evident in the coupled structural-electrostatic analysis of RF MEMS switch, where a speed factor close to one was achieved. Therefore utilizing different approaches, such as FE meshless techniques might be more adequate in analyzing these types of problems, more efficiently.

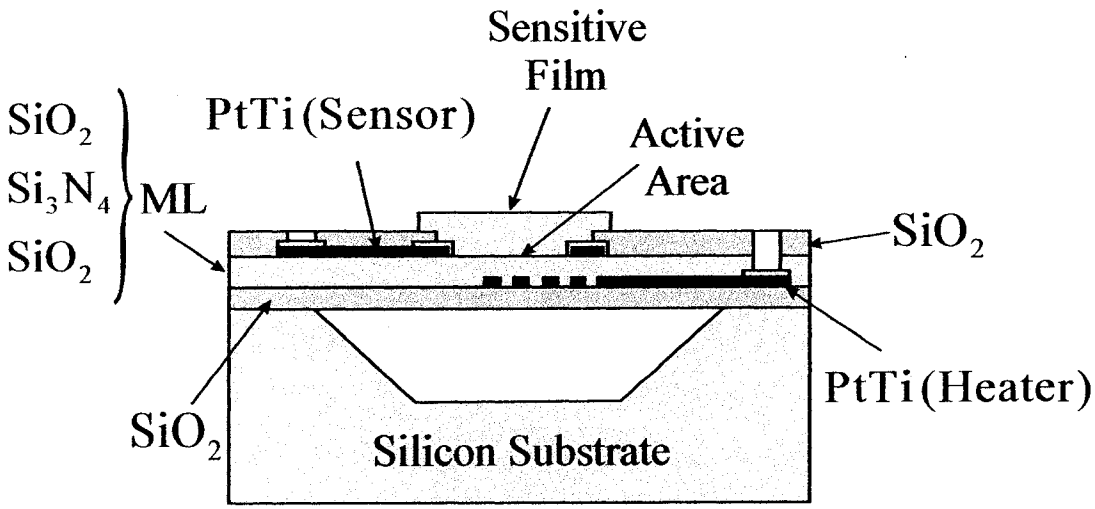

Figure 4.1: Microheater gas sensor cell, Mo *et al.* (2001)

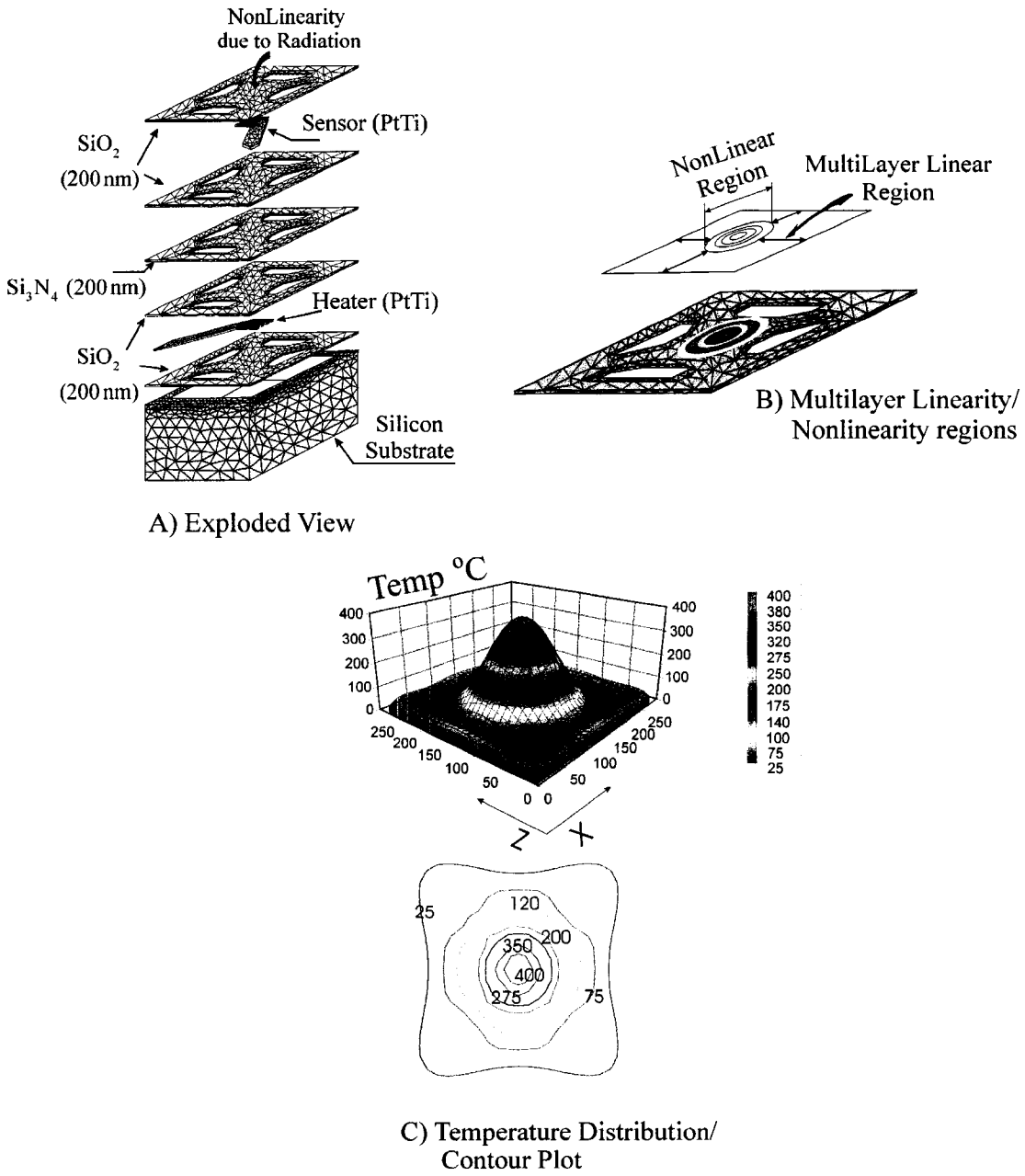

Figure 4.2: MEMS gas sensor model

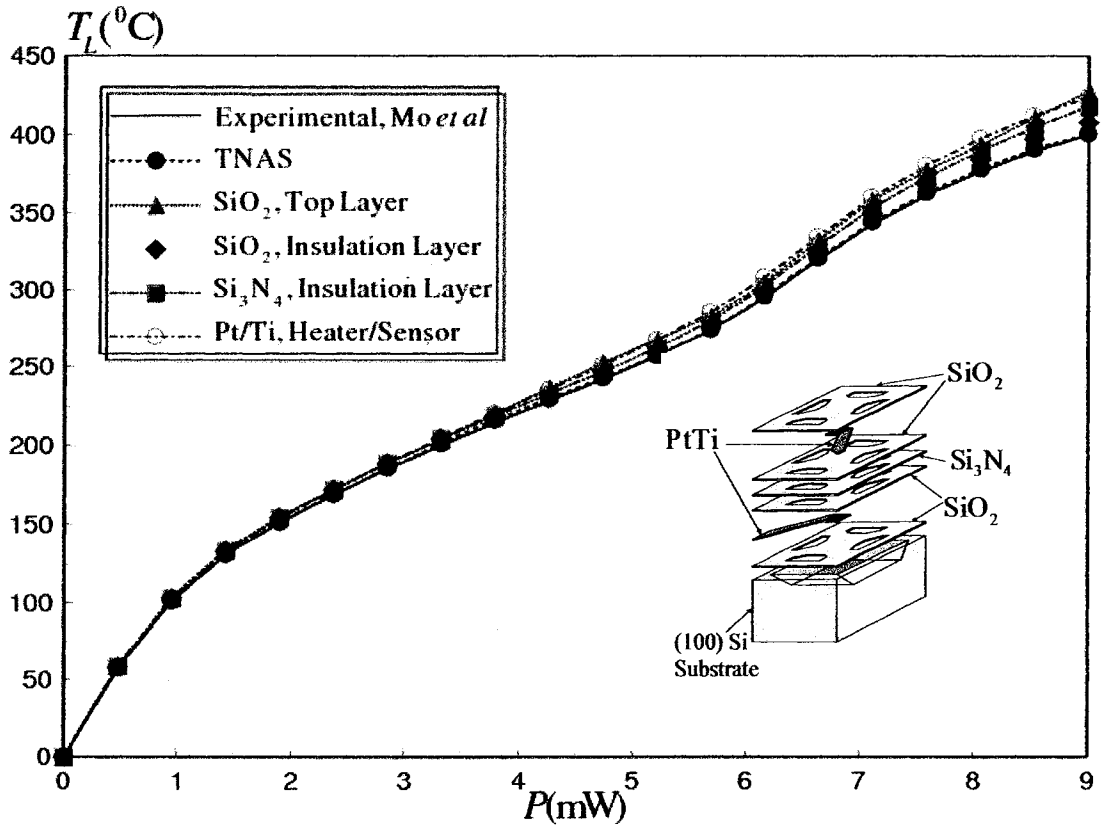

Figure 4.3: Linearity temperature versus input power for different sensor thin film layers, experimental results reported by Mo *et al.* (2001)

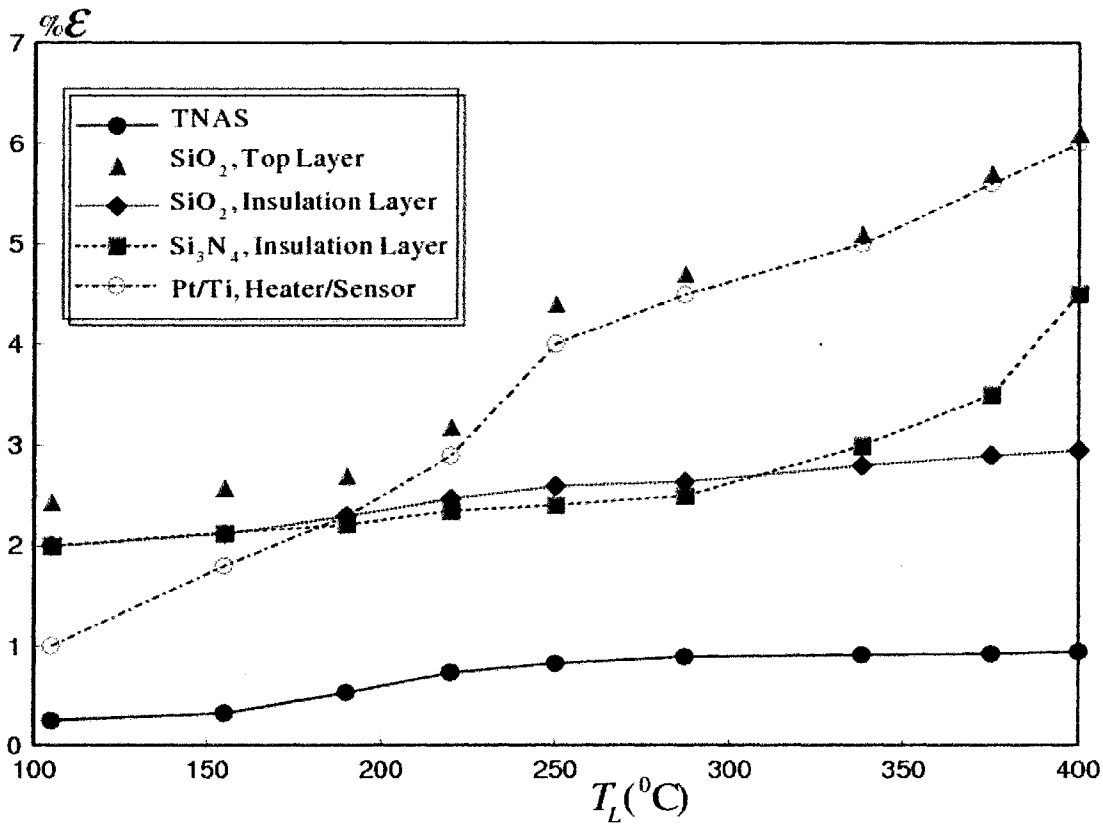

Figure 4.4: Percentage error distribution versus T_L for different sensor thin film layers, $\mathcal{E}$ calculated relative to experimental results reported by Mo *et al.* (2001)

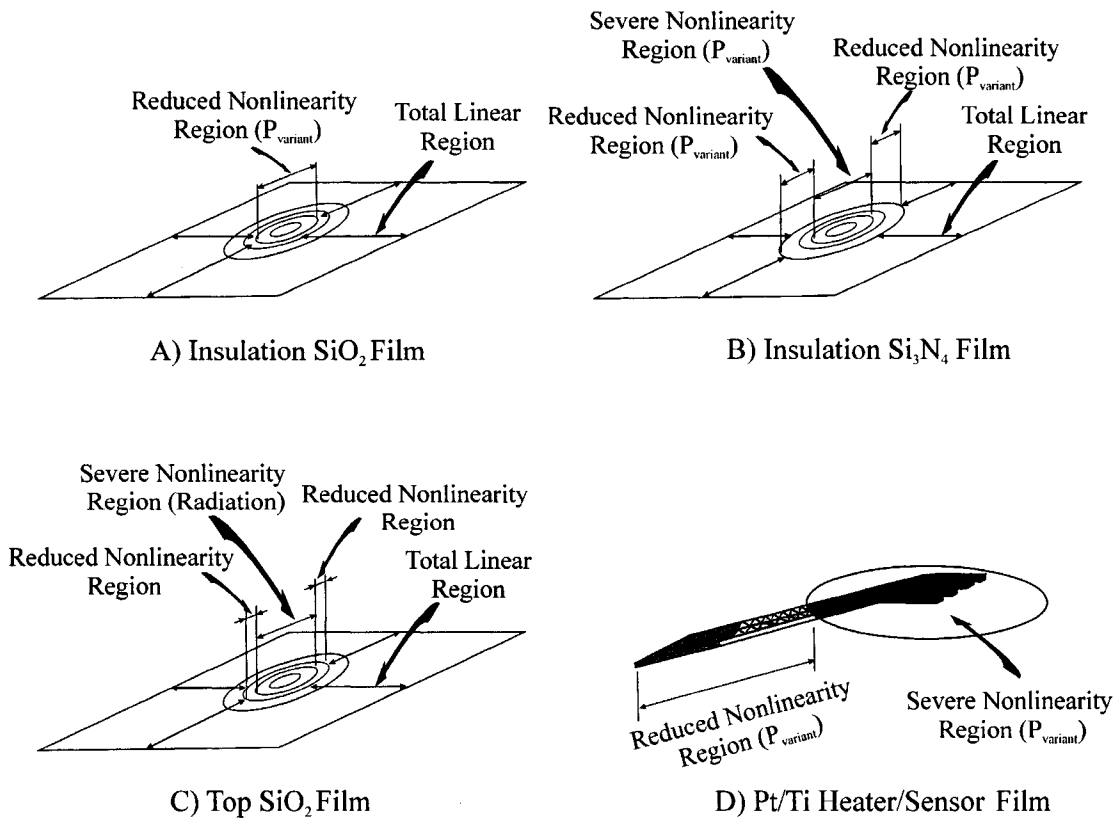

Figure 4.5: Linearity/nonlinearity zones for different gas sensor thin film layers bounded by T_L calculated from sensitivity analysis, with $\%\mathcal{E}$=3, RNAS

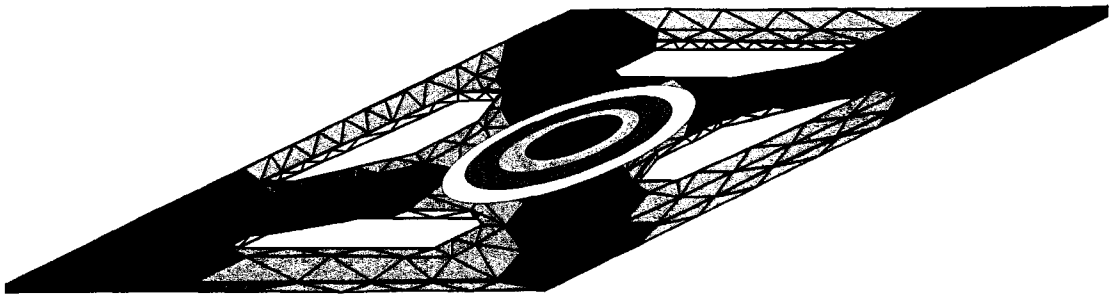

A) $r = 1,\ N_s = 8$

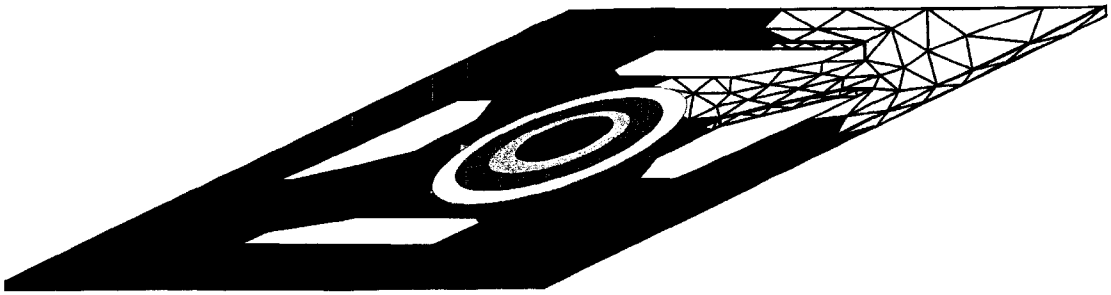

B) $r = 3,\ N_s = 4$

C) $r = 5,\ N_s = 2$

Figure 4.6: Effect of $AR_{Threshold}$ on the number of generated substructures, Si_3N_4 film, (RNAS)

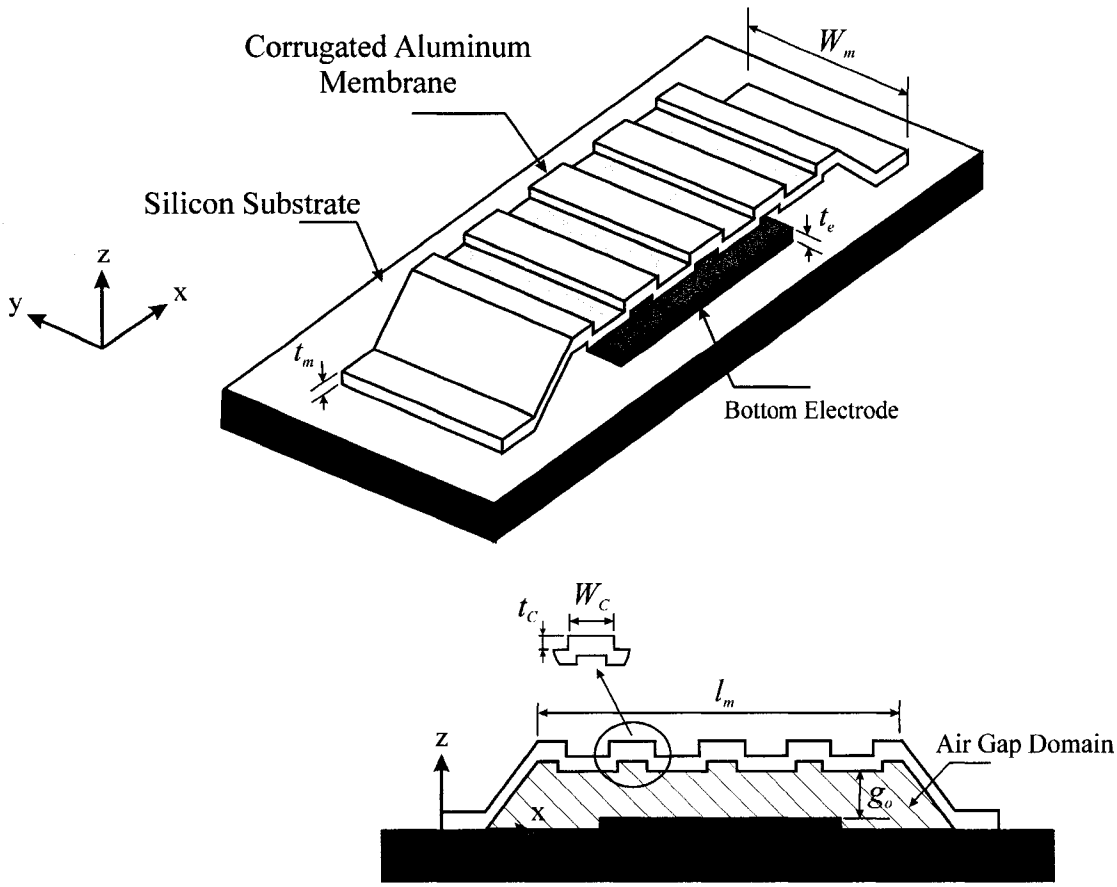

Figure 4.7: Corrugated capacitive shunt RF MEMS switch

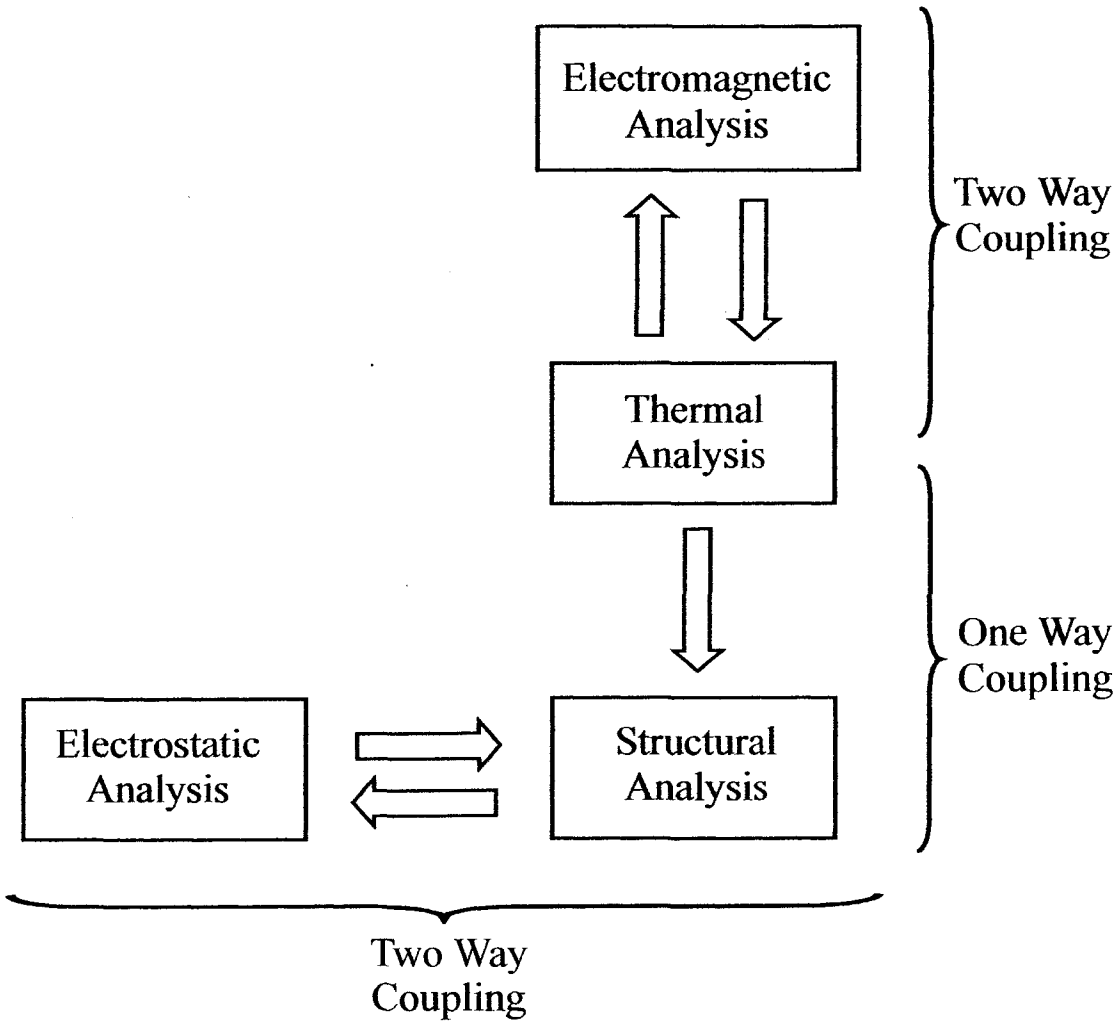

Figure 4.8: Flow chart for coupled field analysis procedure for RF MEMS switch

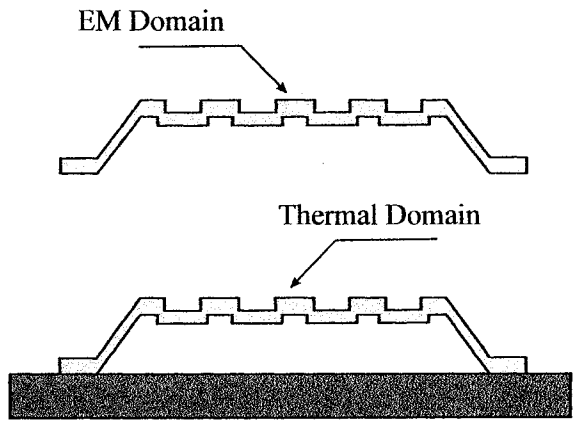

A) Coupled EM-Thermal Analysis

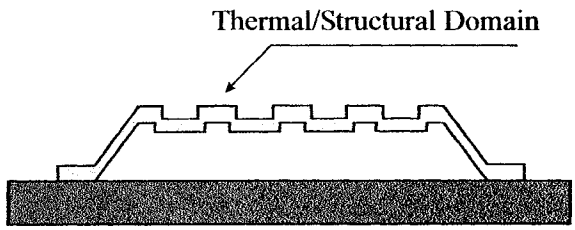

B) Coupled Thermal-Structural Analysis

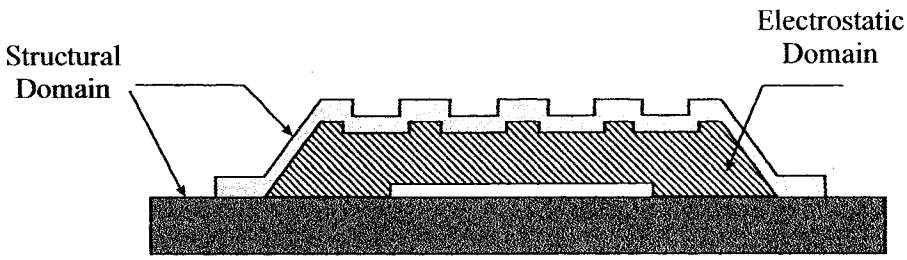

C) Coupled Structural-Electrostatic Analysis

Figure 4.9: Schematic of physical domains in multi-field coupled FE analysis of RF MEMS switch

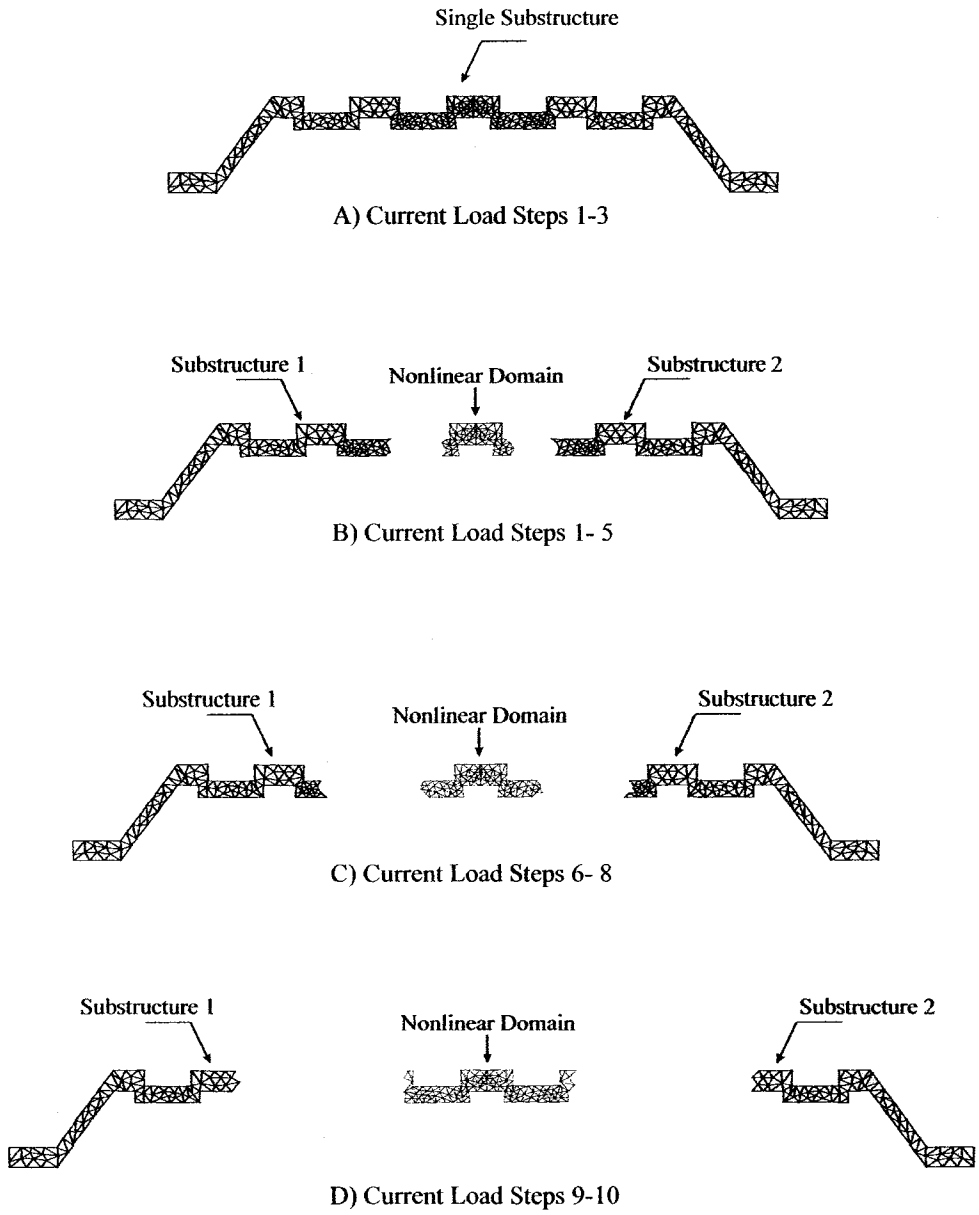

Figure 4.10: Expansion of nonlinear domain at different current load steps in the EM analysis of RF MEMS switch, substructuring conducted with Major Vector algorithm

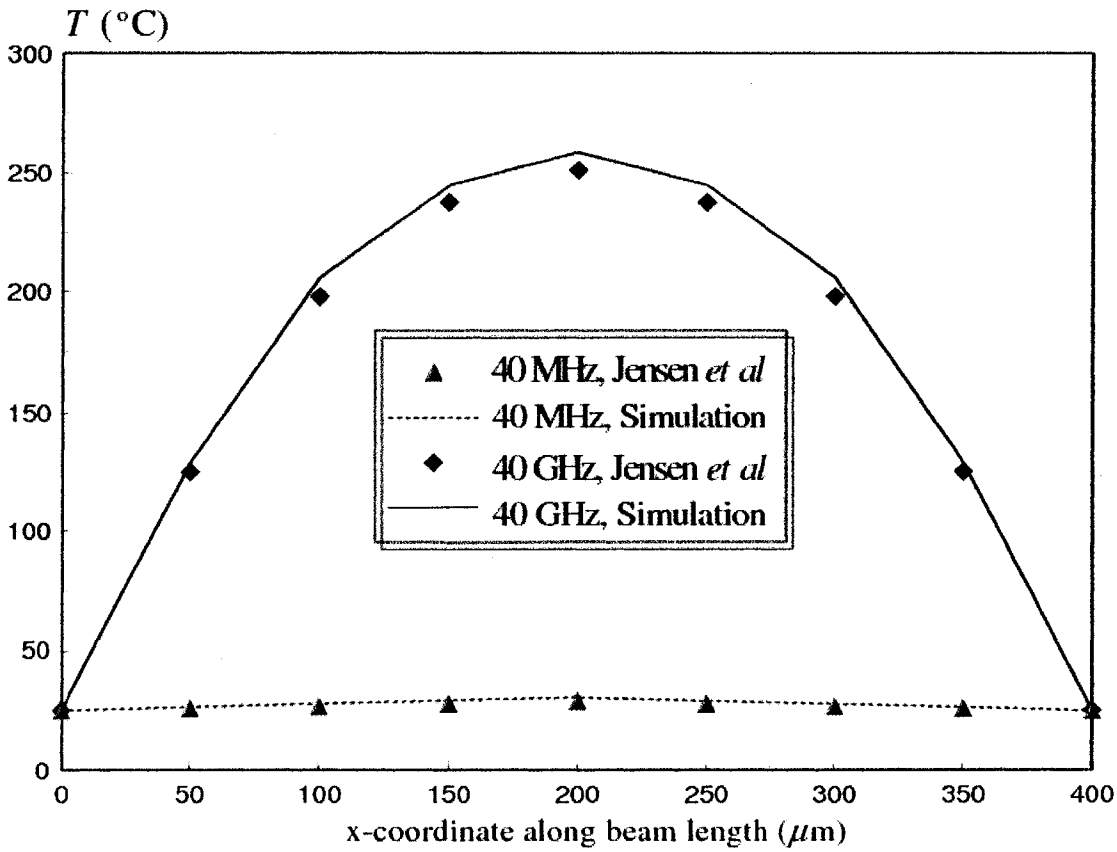

Figure 4.11: Substructured EM-thermal model predictions versus numerical model results reported by Jensen *et al.* of the temperature distribution versus coordinate along beam length for fixed-fixed gold beam at frequencies of 40 MHz and 40 GHz ($l_m = 400\mu m, W_m = 50\mu m, t_m = 2\mu m$, P=1W)

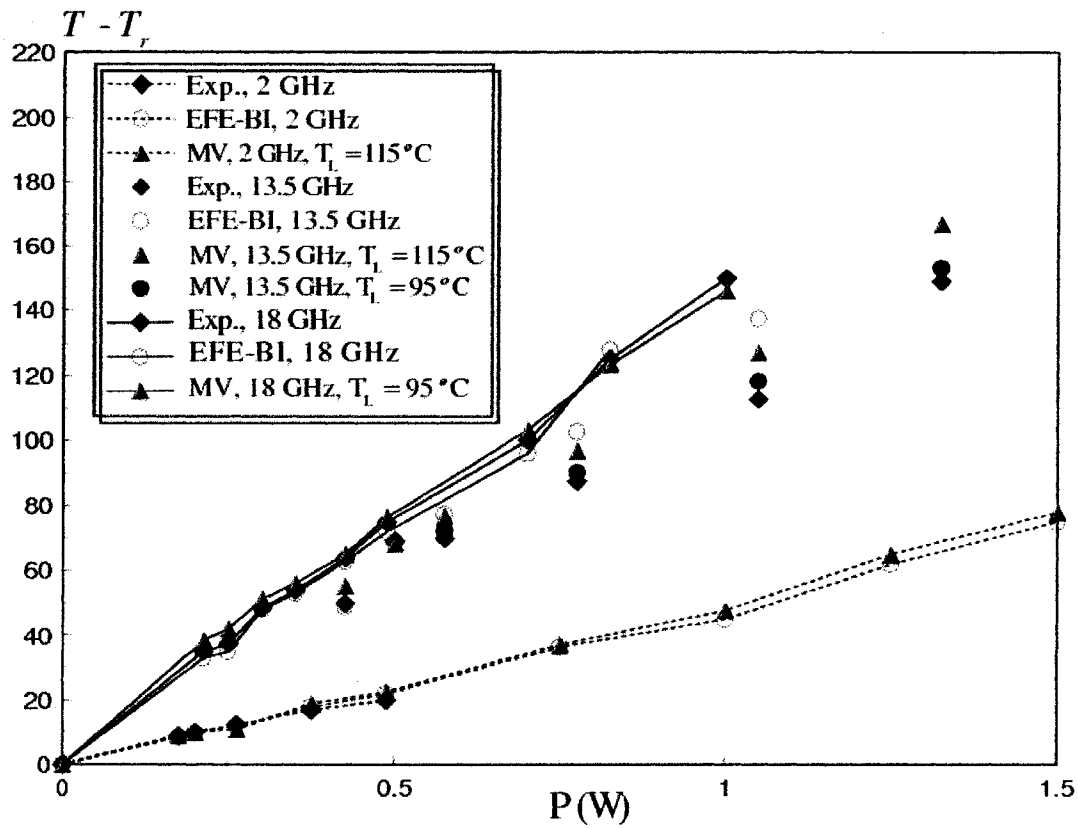

Figure 4.12: Substructured EM-thermal model predictions versus numerical model results and experimental data reported by Wang *et al.* of spatially average temperature rise versus input power for fixed-fixed gold beam at frequencies of 2 GHz, 13.5 GHz and 18 GHz. ($l_m = 400\mu m$, $W_m = 20\mu m$, $t_m = 2\mu m$)

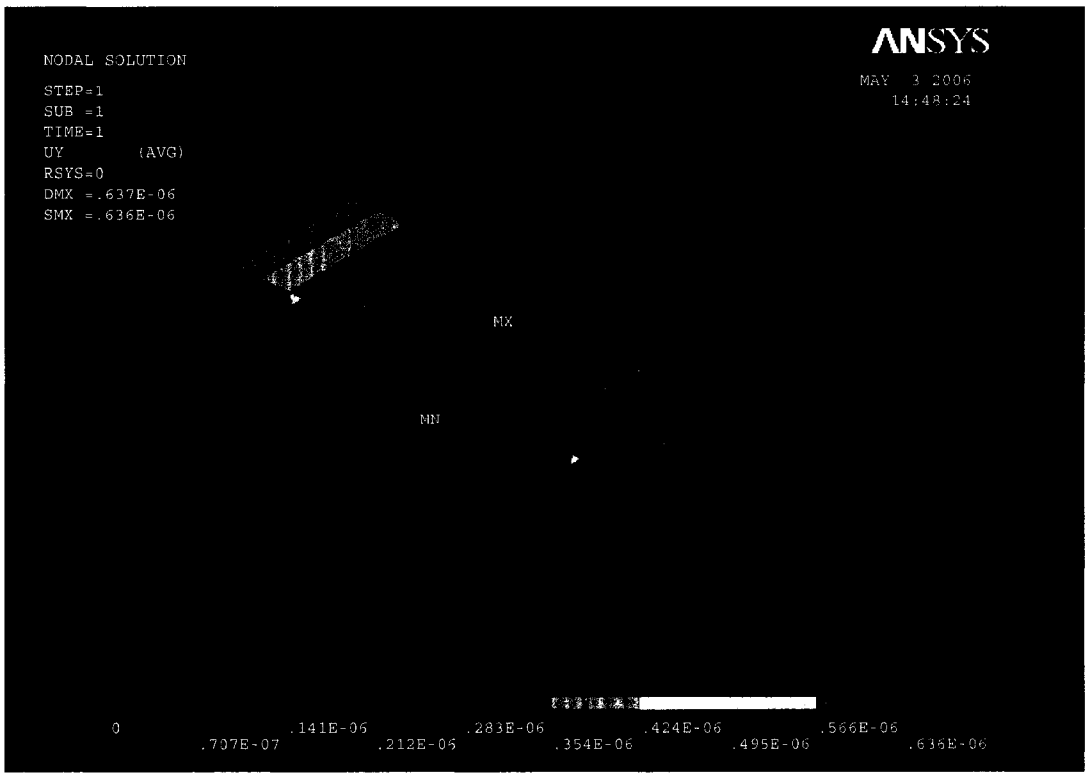

Figure 4.13: Distribution of displacement vertical component along x-coordinate predicted by coupled EM-thermal analysis followed by a coupled thermal-structural analysis for corrugated aluminum RF MEMS switch membrane ($l_m = 91\mu m, W_m = 20\mu m, t_m = 1\mu m$, $t_C = 0.9t_m$, , $\omega = 20\,\text{GHz}$, P=0.75 W)

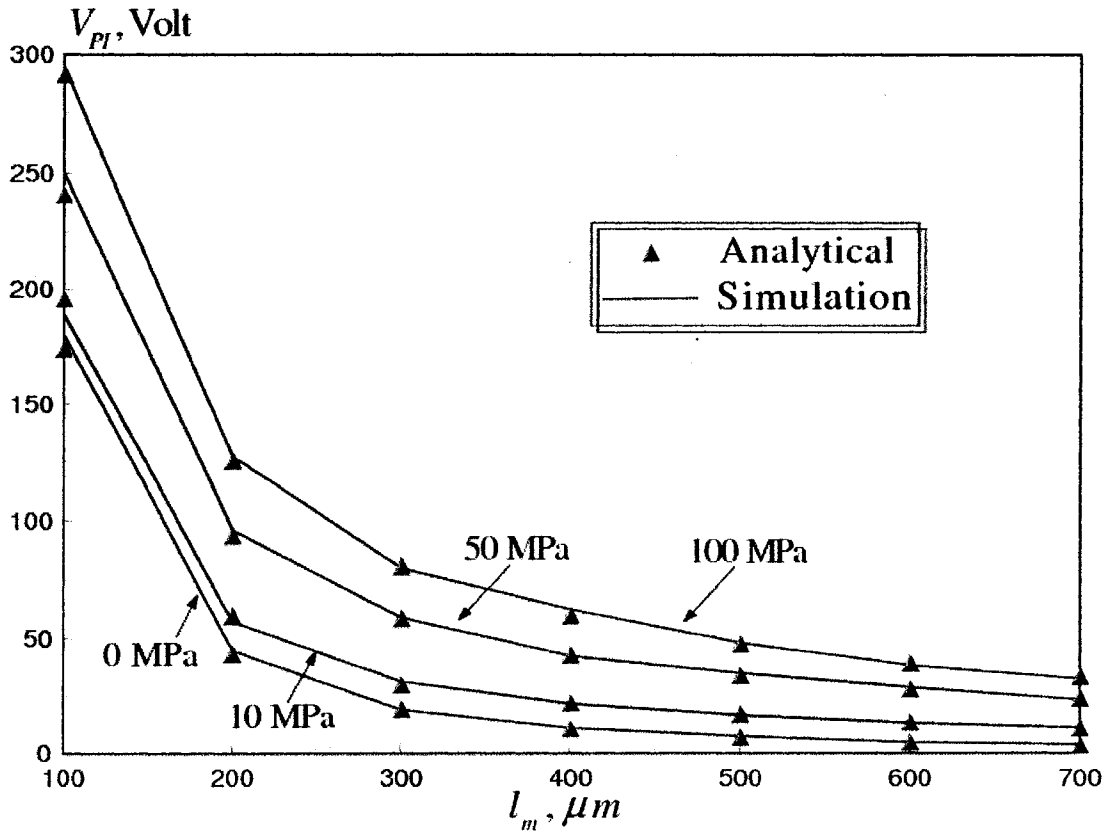

Figure 4.14: Substructured structural-electrostatic model predictions versus analytical results reported by Pamidighantam *et al.* of pull-in-voltage versus beam length for fixed-fixed gold beam at different values of microfabrication residual stresses, ($W_m = 50\mu m, t_m = 1\mu m, g_o = 2.5\mu m, \beta_{PI}^{CC} = 0.4, E_m = 77$ GPa)

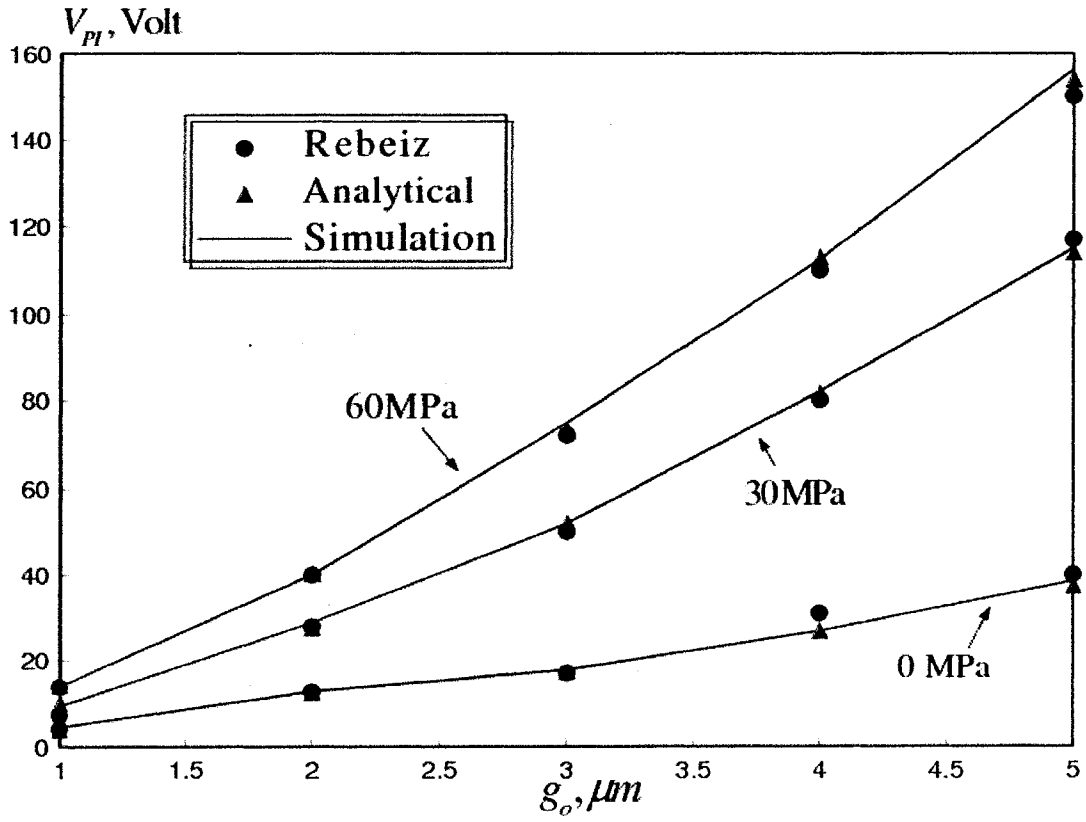

Figure 4.15: Substructured structural-electrostatic model predictions versus analytical results reported by Pamidighantam *et al.* and simulation results reported by Rebeiz of pull-in-voltage versus initial gap length for fixed-fixed aluminum beam at different values of microfabrication residual stresses.

Table 4.1: List of nonlinearity classification for material properties of various gas sensor layers

Layer	Location	$\mathcal{E}$	$T_L(^0C)$
SiO_2 film	Top Layer	2	≈ 57
		3	225
		5	350
Pt/Ti film	Sensor and Heater	2	175
		3	225
		5	340
Si_3N_4 film	Insulation Layer	2	110
		3	350
		5	400
SiO_2 film	Support and Insulation Layer	2	110
		3	400
		5	400

Table 4.2: Comparison between S_{MV} and S_M (TNAS, r=10), MEMS gas sensor

Parameter	S_{MV}	S_M
n_{total}	625	625
n_s	25	25
N_B	22150	21423
t_s (hr.)	0.33	5.78
$I.S.F$	17.52	1
$t_{sol,s}$ (hr.)	7.98	9.42
ϵ	1.2	1.32
$t_{Cpu_{Total,s}}$ (hr.)	4995	6032
t_{Cpu_R}	59.02	50.5
S	2.45	2.02

Table 4.3: Comparison between S_{MV} and S_M (RNAS, $r=10$), MEMS gas sensor

Parameter	S_{MV}	S_M
n_{total}	625	625
n_s	625	625
N_B	31542	32014
t_s (hr.)	0.4	6.52
$I.S.F$	19.76	1
$t_{sol,s}$ (hr.)	4.18	6.79
€	5.23	6.3
$t_{Cpu_{Total,s}}$ (hr.)	2818	8318.75
t_{Cpu_R}	76.87	31.74
S	4.4	1.28

Table 4.4: N_s and N_B for different gas sensor model components for RNAS ($r=1$)

Component	Parameter	RNAS
Insulation SiO_2 film	N_s	8
	N_B	11042
Pt/Ti heater/sensor film	N_s	8
	N_B	1007
Insulation Si_3N_4 film	N_s	8
	N_B	13243
Top SiO_2 film	N_s	8
	N_B	10352
Total Model	N_s	32
	N_B	35644

Table 4.5: N_s and N_B for different gas sensor model components for RNAS (r=3)

Component	Parameter	RNAS
Insulation SiO_2 film	N_s	4
	N_B	9005
Pt/Ti heater/sensor film	N_s	4
	N_B	861
Insulation Si_3N_4 film	N_s	4
	N_B	10952
Top SiO_2 film	N_s	4
	N_B	8263
Total Model	N_s	16
	N_B	29081

Table 4.6: N_s and N_B for different gas sensor model components for RNAS (r =5)

Component	Parameter	RNAS
Insulation SiO_2 film	N_s	2
	N_B	8235
Pt/Ti heater/sensor film	N_s	2
	N_B	501
Insulation Si_3N_4 film	N_s	2
	N_B	9265
Top SiO_2 film	N_s	2
	N_B	7239
Total Model	N_s	8
	N_B	25240

Table 4.7: Computational parameters with different r for TNAS and RNAS, MEMS gas sensor.

r	Parameter	TNAS	RNAS
1	t_s (hr.)	0.62	1.1
	$I.S.F$	35.94	37.12
	$t_{sol,s}$ (hr.)	9.23	5.3
	€	0.87	2.92
	$t_{Cpu_{Total,s}}$ (hr.)	5784.25	3750
	t_{Cpu_R}	52.54	69.23
3	t_s (hr.)	0.51	0.78
	$I.S.F$	23.22	27.62
	$t_{sol,s}$ (hr.)	8.971	5.031
	€	1.23	3.71
	$t_{Cpu_{Total,s}}$ (hr.)	5618.875	3500.625
	t_{Cpu_R}	53.9	71.27
5	t_s (hr.)	0.43	0.54
	$I.S.F$	21.21	24.47
	$t_{sol,s}$ (hr.)	8.53	4.42
	€	1.89	4.85
	$t_{Cpu_{Total,s}}$ (hr.)	5341.25	3025
	t_{Cpu_R}	56.2	75.17

Table 4.8: Statistics of EM-thermal two-way coupled-field FE analysis (for total analysis, N_B is the average number of boundary nodes for all load steps), RF MEMS switch.

	Analysis Approach	t_s (hr.)	N_B	t_{Cpu} (hr.)	S
Current Load Steps (1-5)	D-A	---	---	2	---
	S_M	0.4	187	1.2	1.25
	S_{MV}	0.15	221	0.83	2.1
Current Load Steps (6-8)	D-A	---	---	5	---
	S_M	0.4	187	2.1	2
	S_{MV}	0.1	142	1.5	3.2
Current Load Steps (9,10)	D-A	---	---	6	---
	S_M	0.4	187	2.5	2
	S_{MV}	0.05	98	2.1	2.7
Total EM-Thermal Coupled-Field FE Analysis	D-A	---	---	13	---
	S_M	1.2	187	5.8	1.85
	S_{MV}	0.3	154	4.43	2.75

Table 4.9: Statistics of thermal-structural one-way coupled-field FE analysis (for total analysis, N_B is the average number of boundary nodes for all load steps), RF MEMS switch.

	Analysis Approach	t_s (hr.)	N_B	t_{Cpu} (hr.)	S
Temperature Load Steps (1-5)	D-A	---	---	0.72	---
	S_M	0.28	1316	0.3	1.23
	S_{MV}	0.15	1113	0.25	1.8
Temperature Load Steps (6-8)	D-A	---	---	1.08	---
	S_M	0.28	1316	0.522	1.34
	S_{MV}	0.08	1120	0.38	2.3
Temperature Load Steps (9,10)	D-A	---	---	1.2	---
	S_M	0.28	1316	0.48	1.57
	S_{MV}	0.08	1049	0.43	2.3
Total Thermal-Structural Coupled-Field FE Analysis	D-A	---	---	3	---
	S_M	0.84	1316	1.302	1.4
	S_{MV}	0.31	1094	1.06	2.2

Table 4.10: Statistics of structural-electrostatic two-way coupled-field FE analysis, RF MEMS switch.

	Analysis Approach	t_s (hr.)	N_B	t_{Cpu} (hr.)	S
Total Structural-Electrostatic Coupled-Field FE Analysis	D-A	---	---	15	---
	S_M	0.24	1300	13.4	1.1
	S_{MV}	0.15	1257	12.9	1.15

Chapter 5

Reliability Analysis of MEMS Gas Sensors

This chapter presents the reliability analysis results of microheater-based MEMS gas sensors. The substructured sequentially coupled electro-thermal gas sensor model, validated in Chapter 4, is used here to study these devices performance, in response to variations within geometry, residual stresses and thin films material properties, generated at various stages of microfabrication. The obtained results are then utilized to predict the variation in the gas detection sensitivity performance and the onset of fatigue failure for the gas sensors under thermal cyclic loading. Section (5.1) presents a brief introduction to the MEMS gas sensor technology and the main reliability problems encountered during these sensors operation. The design framework and the applied variations in design parameters, utilized with the gas sensor case study, are presented in Sections (5.2) and (5.3), respectively. The effect of variations in the thermal, electrical properties of thin films and the dimensional tolerance on the gas detection sensitivity is discussed in Section (5.4). Next, the onset of fatigue failure under these variations and recommended modifications to the gas sensor design are presented in Section (5.5). Finally some concluding remarks on the reliability analysis results are presented in Section (5.6).

5.1 Problem Definition – MEMS Gas Sensors

Growing concern with the environment and the industry's need for operating under certain environmental measures raises the necessity of gas sensors to detect, monitor and control various chemical species, Puicorbe *et al.* (2003), Shen *et al.* (1996), Parameswaran *et al.* (1990). For these devices, the main reliability design issues of concern are the gas detection sensitivity (GDS) and the fatigue failure under the thermal cyclic loading encountered during operation, Mo *et al.* (2001). However, uncertainties introduced during the miniaturization process of the gas sensor can produce large deviations in the target value of the gas detection sensitivity and fatigue life. For example, without a sufficient control over the deposition process of thin films, some deviations in the thickness and other dimensional parameters can be introduced, which might affect the thermal response of the device, Callard and Talliarida (1998), Kleiner *et al.* (1996), Brotzen *et al.* (1992).

Another concern is the characterization of the thermal, electrical and mechanical properties of thin films. To date no systematic study can provide a precise value for characterizing these properties. Most of the current studies only provide these values for a certain range of thin films dimensions and for a specially designed micromechanical test structures within certain tolerance ranges, Branger *et al.* (1996). Even the method of fabrication (thermal, chemical vapor deposition, low pressure or plasma enhanced chemical vapor deposition) was reported to generate different characteristics for thin films, Sadek and Moussa (2005), Firebaugh *et al.* (1998),

Schneider *et al.* (1995). Therefore, most designers use bulk material data to characterize the properties of the considered thin film materials. However, since the microstructure of thin films usually differs strongly from that of bulk samples, this assumption often deviate the gas sensor performance from the design expectations. Consequently, in order to obtain an efficient gas sensor design, it is essential to understand how processing parameters can affect the dimensional and material variables for thin films.

In this chapter, a design framework is developed to study the effect of the variations in the thermal, electrical and mechanical characteristics of thin films on the operational performance of micromachined MEMS gas sensors. The MEMS gas sensor, manufactured by Mo *et al.* (2001), and modeled in Chapter 4, is used as a case study in this thesis. Details of the design framework and the main parameters studied will be presented next.

5.2 Design Framework

The proposed gas sensor design framework is shown in Fig (5.1). Starting from a preliminary design of the gas sensor, an investigation of different deposition process alternatives for various thin film layers is conducted. The data used at this stage, includes the ranges of the expected residual stresses and the variations in the material properties corresponding to different deposition processes and parameters. At this stage, a preliminary estimation is conducted for the necessity of reducing the residual

stresses by annealing. The preliminary assessment is based on the application of the device.

For example, for various applications in optical technology and applications that involve moving components, the control of the residual stresses to a desired value is essential for the successful operation of the device, Brown (2003), Ma (2002). On the other hand, for other applications like MEMS gas sensors (except for optical gas sensors), the annealing is not required, and might alter some desired mechanical, thermal and electrical properties of various thin films, Wrbanek and Laster (2005), Branger *et al.* (1996). However, a later assessment of the residual stresses is also conducted at the final stages of the framework, based on the final levels of the operational stresses and their combined effect on the reliability and fatigue life of the gas sensor.

Following the evaluation of the residual stresses, the expected variations in the material properties and geometric parameters are applied to various thin films and then an evaluation of their effect on the overall performance and the reliability of the device are conducted. At the final stage, various deposition/post deposition parameters are recommended. This is the most important stage of the proposed framework; since at this stage, correlating the microfabrication parameters to the device performance can be established before proceeding to the actual manufacturing process. In addition, variables that need a strict control over their manufacturing tolerance can be identified. This would mainly reduce or even eliminate the

probability of applying strict tolerance over less important variables and consequently reduce the overall microfabrication cost.

5.3 Dimensional Tolerances and Material Characterization

As reported by Madou (2002), dimensional uncertainties are of a great concern in surface micromachining processes. Relative tolerances are poor and can reach up to 1% in a length of 100-μm. For smaller sizes, the situation becomes much more critical. Using data reported by Madou (2002), a ± 20% was found to be a reasonable expectation for the thicknesses tolerance during surface micromachining of thin films used in our case study.

As discussed previously in Section (5.1), the characterization of the material properties is a major problem in the design of microelectromechanical systems (MEMS). Few works can be found in the literature that study the thermal/electrical material characterization for thin films, and most of them are limited to the characterization of SiO_2 thin films, Callard *et al.* (1999), Arx (1998), Kleiner *et al.* (1996), Paul and Baltes (1993), Brotzen *et al.* (1992). However, in the work reported by Callard *et al.* (1999), a ±20% change in the thickness of SiO_2 thin films was found to cause a variation in the thermal conductivity ranging between ±17%. Unfortunately, no similar information for other thin film materials, used in the current case study was available. Therefore, in the electrothermal model, bulk material values for thin film materials that could not be found in the literature for thin films thermal

and electrical material properties were initially used Brown (2003), Ma (2002), Stark (1999).

Unlike the thermal/electrical material properties, the link between the deposition parameters and the mechanical properties of thin films is better established. Many studies can be found that link the mechanical properties like the coefficient of thermal expansion (e) [Pan (2002)], Young's modulus (E) [Chaung (2004), Denhoff (2003), Sharpe *et al.* (1999), Yi and Kim (1999), Sharpe *et al.* (1997)], and the mechanical characteristics like the residual stresses (σ_{res}) [Denhoff (2003), Seok *et al.* (2002), Min and Kim (2000), Kim and Allen (1999)], to the deposition/annealing conditions. However, the variation in the mechanical characteristics, as reported in the literature, usually lies within ±12-18%. Therefore in the reliability analysis of the gas sensor, a variation in the range of ± 20% was applied for these properties.

5.4 Gas Detection Sensitivity Analysis

Gas detection sensitivity (GDS) analysis is conducted by correlating the thermal response of the gas sensor with the experimental results reported by Mo *et al.* (2001). The experimental results illustrate the relation between GDS of the sensor and the peak temperature in the active area. The gas detection sensitivity was defined as the change in the resistance of the sensitive resistor when absorbing a certain amount of the gas species relative to its resistance in the gas. The gas detection sensitivity was assessed for two different techniques of sensitive film deposition. The first technique

was the electron beam evaporization method (EBEM). As shown in Fig (5.2), the maximum GDS of the sensor was for the C_2H_5OH gas and was associated with a maximum temperature of 400 °C. However, even with this temperature the maximum GDS that could be reached was about 5.5. To further improve the GDS results, the radical oxygen assisted electron beam evaporization (ORM) method was used for sensitive film deposition. As shown in Fig (5.3), using this technique the GDS was considerably increased to about 170 with a shift of the required active area's maximum temperature to around 325 °C. The later reduction in the maximum temperature requirement is of a great advantage in terms of reduction in the required power consumption during the operation (6.5 mW in comparison to 9 mW required to reach 400 °C).

The effect of the manufacturing uncertainties on the sensitivity of the sensor is assessed for both techniques of sensitive film deposition. The results were calculated based on the resulted change in the thermal response and GDS-temperature correlation reported by Mo *et al.* (2001). The parameters investigated in the analysis include the variation in the thermal properties; electrical properties and the thickness of the CMOS thin films forming the insulation layer (ML). The average values of the thermal conductivity were taken as 1.4, 28 and 43 (W/m/ °C) for the SiO_2, Si_3N_4 and the Pt/Ti, respectively. While the nominal value for the electrical resistivity was taken as 15.5E-16 (Ω. m) for the Pt/Ti.

The active area's temperature was calculated after subjecting the gas sensor model to the expected variation in the value of the studied parameters. A non-dimensional parameter refereed to as the thermal response factor (α_T) represents the effect of varying the parameter of interest on the thermal response of the modeled micro heater gas sensor. The thermal response factor is defined as

$$\alpha_T = \frac{T_{Actual}}{T_o} \tag{5.1}$$

where, T_{Actual} is the actual maximum temperature in the active area after varying the physical property under investigation and T_o is the nominal temperature calculated from the original model. The thermal response results were later used with the experimental data reported by Mo *et al.* (2001), to estimate the GDS of the gas micro sensor for both techniques of sensitive film deposition. A non-dimensional parameter referred to as the GDS factor (ψ_{sen}), was used to express the percentage variation in GDS as follows

$$\psi_{sen} = \frac{\psi - \psi_o}{\psi_o} \times 100 \tag{5.2}$$

where, ψ is the actual GDS of the gas sensor and ψ_o is the GDS of the original model.

5.4.1 The Effect of the Variation in the Material Properties

The variation in the thermal response factor with the percentage variation in the value of the thermal conductivities of SiO_2, Si_3N_4 and Pt/Ti are shown in Fig (5.4). It can be seen that the variation in the thermal conductivity of Si_3N_4 has the most significant effect on the thermal response of the gas micro sensor. A reduction of 14% and a maximum increase of 13% in the maximum temperature can be noticed with a 20% increase and decrease in the thermal conductivity of Si_3N_4, respectively. On the other hand, the variations in the thermal conductivity of SiO_2 and Pt/Ti have minor effect that ranges between –1% and 2.5% on the thermal response factor of the micro sensor. A linear fit was used to express the relation between the thermal response and the thermal conductivity tolerance for the SiO_2, Si_3N_4 and Pt/Ti with an average root mean square error (RMS) of 0.0055 as follows

$$\alpha_T = c^P + d^P \kappa_p, \tag{5.3}$$

where, c^P and d^P are constants in Equation (5.3) and κ_p is tolerance percentage applied to the thermal conductivity value. A list of Equation (5.3) constants for Pt/Ti, SiO_2 and Si_3N_4 are shown in Table (5.1).

The thermal response was later used to evaluate the GDS of the gas sensor with both techniques of sensitive film deposition as shown in Fig (5.5) and Fig (5.6). For the EBEM method, the variation in the thermal conductivity of Si_3N_4 results in a large degradation in the gas sensor GDS that ranges between –25% to –20% with a 20% increase and decrease in the value of the design thermal conductivity, respectively. A

similar effect could be noticed when the value of GDS was evaluated for the ORM method. The degradation in the GDS results only when the thermal conductivity of Si_3N_4 was reduced, while a large improvement that could reach about 34% can be achieved with an increase in the value of the thermal conductivity of 20%. For both techniques of sensitive film deposition, the variations in the thermal conductivity of SiO_2 and Pt/Ti were found to have a negligible effect on the operational GDS of the sensor. Hence certain measures should be used to control and evaluate the thermal conductivity of the Si_3N_4 before proceeding to the actual micro machining process. Results shown in Fig (5.5) and Fig (5.6) were fitted using linear and polynomial fitting, respectively, with an average RMS of 2.5%. The fitted results were then used to express the relation between the sensitivity of the sensor and the thermal conductivity tolerance for the SiO_2, Si_3N_4 and Pt/Ti for both sensitive film deposition techniques as follows

$$\psi_{sen,EBEM} = c_0^P + c_1^P \kappa_p + c_2^P \kappa_p^2 \tag{5.4}$$

$$\psi_{sen,ORM} = d_0^P + d_1^P \kappa_p + d_2^P \kappa_p^2 \tag{5.5}$$

where, c_0^P, c_1^P, and c_2^P are Equation (5.4) constants and d_0^P, d_1^P, and d_2^P are Equation (5.5) constants. A list of Equations (5.4) and (5.5) constants for SiO_2, Pt/Ti and Si_3N_4 can be found in Tables (5.2) and (5.3), respectively.

The effect of characterization uncertainty in the value of the electrical resistivity for the heater and sensor material (Pt/Ti) on the thermal response and GDS factors for

the EBEM and ORM methods is shown in Fig (5.7) and Fig (5.8). The variation in the electrical resistivity value generates a large deviation in the thermal response of the sensor that ranges between –18% and 22%. This deviation in the thermal response results in a significant change in the operational GDS of the sensor. For the EBEM method a large degradation in the GDS can be noticed all over the applied tolerance range and could reach up to –44%. On the other hand, for the ORM, almost the same degradation results within the negative region of the applied tolerance. However, a large improvement in the GDS of the sensor can be noticed within the positive region of the applied tolerance. This improvement increases linearly to reach an improvement of about 48% with an increase of 20% to the design value of the electrical resistivity. Results shown in Fig (5.7) and Fig (5.8) were fitted using linear and polynomial fitting with average RMS errors of 0.1 and 3%, respectively. The fitted results were then used to express the relation between the thermal response, sensitivity of the sensor and the electrical resistivity tolerance for the sensor and heater material for both sensitive film deposition techniques as follows

$$\alpha_T = 1.011 - 0.01\gamma_{PtTi} \tag{5.6}$$

$$\psi_{sen,EBEM} = -1.35 - 0.473\gamma_{PtTi} - 0.124\gamma_{PtTi}^2 \tag{5.7}$$

$$\psi_{sen,ORM} = 3.6 + 2.24\gamma_{PtTi} \tag{5.8}$$

where, γ_{PtTi} is the applied tolerance percentage to the nominal value of the electrical resistivity of Pt/Ti.

5.4.2 Effect of Dimensional Tolerance

In this section, the effect of possible variations in the thickness of the insulation layers on the thermal response and the sensitivity of the gas sensor will be introduced. The current work investigates the variation in the thickness of the insulation layers individually and the total thickness of the insulation layer. The terms ML_1, ML_2, ML_3, and ML_{Layer} refer to the thickness of the bottom, upper SiO_2, middle Si_3N_4 and total insulation layer, respectively. As shown in Fig (5.9), Fig (5.10), Fig (5.11) and Fig (5.12), the variation in the thickness of the Si_3N_4 and the total insulation layer thickness has the most significant effect on the thermal response factor and consequently on the GDS of the gas sensor. The thermal response of the sensor varies considerably in the range of –15% to 18% within the assumed range of applied thickness tolerance. The predicted GDS of the sensor was found to degrade by about 30% with the EBEM method allover the range of the applied thickness variation. The gas detection sensitivity of the sensor had almost the same degradation with the ORM method allover the negative region of the applied thickness tolerance. However an improvement on the GDS can be noticed all over the positive region of the applied dimensional tolerance to reach about 44%.

Results shown in Fig (5.9), Fig (5.10) and Fig (5.11) were fitted using linear and polynomial fitting with average RMS errors of 0.2, 4% and 2%, respectively. The fitted results were then used to express the relation between the thermal response,

GDS of the sensor and the thickness tolerance for the thin films forming the insulation layer for both sensitive film deposition techniques as follows

$$\alpha_T = c^G + d^G \tau \tag{5.9}$$

$$\psi_{sen,EBEM} = c_0^G + c_1^G \tau + c_2^G \tau^2 \tag{5.10}$$

$$\psi_{sen,ORM} = d_0^G + d_1^G \tau + d_2^G \tau^2 \tag{5.11}$$

where, τ is the thickness tolerance, c^G, d^G, are Equation (5.9) constants, c_0^G, c_1^G, and c_2^G are Equation (5.10) constants and d_0^G, d_1^G, and d_2^G are Equation (5.11) constants. A list of Equations (5.9), (5.10) and (5.11) constants can be found in Tables (5.4), (5.5) and (5.6), respectively.

5.5 Thermal Fatigue Analysis

Although the fatigue failure of thin films have been rarely studied before, recent studies confirmed that micron-scale structural thin films, are susceptible to premature failure at stress amplitudes as low as half the fracture strength, Mönig *et al.* (2004), Muhlstein and Ritchie (2003). The MEMS gas sensor under investigation is subject to cyclic thermal loading ranging from the residual stresses generated during the fabrication process and the actual operational thermal stress. In this Section, the effect of thin film material property variations on the fatigue life of the gas sensor is presented. A list of the studied parameters, as well as the range of their applied

variations is shown in Table (5.7). The terms, p, T, G and D_R denote the deposition temperature, deposition pressure, the SiH_2Cl_2/NH_3 ratio and the deposition rate.

No reported value for the ultimate strength of Pt/Ti thin film material could be found in the literature. As reported by Strikar and Spearing (2003), in similar cases the value of the ultimate strength for the bulk material could be taken as a conservative limit for the ultimate strength. As will be shown in Section (5.4.1), the operational stress level for Pt/Ti (microheater/sensor material) was beyond the ultimate fracture strength. This would suggest rupture or delimitation of the Pt/Ti thin film, which was found to be in good agreement with previous experimental studies reported in the literature, Wrbanek and Laster (2005), Puicorbe *et al.* (2003). The replacement of the Pt/Ti with doped polysilicon, which is a well-studied material commonly, used for MEMS gas sensors microheater/sensor was suggested at this stage.

The power-temperature relationship for both Pt/Ti and polysilicon are shown in Fig (5.13). The main concern was the increase in the power consumption resulting from the use of the polysilicon as a microheater material. As shown in Fig (5.13), the increase in the power consumption (P) at the optimum operating temperature (T_{max}^{AA} = 400 °C) of the active area was found to be approximately 10% (increase of 1 mW). The other concern was the shifting in the thermal response (α_T) and the performance GDS (ψ_{sen}) of the gas sensor with the variation in the electrical resistivity of polysilicon. Using the same procedure described earlier in Section (5.4), the variation

in α_T and ψ_{sen} with the polysilicon resistivity variation was calculated. The numerical results confirmed a tighter variation in the thermal response and consequently a lower degree of performance sensitivity degradation (improvement of approximately 13% over Pt/Ti).

5.5.1 Effect on Maximum Stress

A structural analysis has been conducted to study the effect of the variations in the thermal, electrical and mechanical properties on the maximum generated stress in various thin film layers of the gas sensor. In the electro-thermal analysis, only the conductivity of Si_3N_4 and the resistivity of the heater material (Pt/Ti or polysilicon), were found to cause a significant effect on the thermal response of the gas sensor. Therefore, only the variations of these thermal/electrical parameters were considered at this stage. The variation of the maximum generated stress on various thin film layers versus the uncertainty in the thermal conductivity of Si_3N_4, the electrical resistivity of Pt/Ti and polysilicon can be shown in Fig (5.14), Fig (5.15) and Fig (5.16), respectively. The dimensionless term β_σ (stress factor) indicate the ratio between the actual maximum operational stress ($\sigma_{A_{max}}$) and the nominal maximum stress ($\sigma_{N_{max}}$), stress value before applying the property variation). The values for $\sigma_{N_{max}}$ and its ratio relative to the ultimate fracture strength (S_{ut}) of different thin film materials are listed in Table (5.8).

As shown in Fig (5.14), the variation in the thermal conductivity of Si_3N_4 generate a significant variation in the maximum operational stress level ranging from -12 to72% for SiO_2, -14 to 28% for Pt/Ti, and -24 to 46% for polysilicon. A less significant variation of ± 5% can be noticed for the maximum stress of Si_3N_4. This variation can be attributed to the great variation generated in α_T, and the combined effect of the coefficient of thermal expansion (e) of the thin film material and the thin film proximity to the active area. Results shown in Fig (5.14) were fitted using linear fitting (Equation (5.12)), for Si_3N_4, Pt/Ti and polynomial fitting (Equation (5.13)) for SiO_2 and polysilicon as follows

$$\beta_{\sigma}^{Si_3N_4,Pt/Ti} = a_o + a_1 \kappa^{Si_3N_4} \tag{5.12}$$

$$\beta_{\sigma}^{SiO_2,Poly} = b_o + b_1(\kappa^{Si_3N_4}) + b_2(\kappa^{Si_3N_4})^2 + b_3(\kappa^{Si_3N_4})^3 + b_4(\kappa^{Si_3N_4})^4 \tag{5.13}$$

where, a_o, a_1 are Equation (5.12) constants and b_o, b_1, b_2, b_3 and b_4 are Equation (5.13) constants. Equations (5.12) and (5.13) constants, as well as the average root mean square error (RMS) of curve fitting are listed in Tables (5.9) and (5.10), respectively.

A similar effect can be noticed for the variation of β_{σ} with the variation of the electrical resistivity of Pt/Ti and polysilicon, as shown in Fig (5.14). It can be seen that the variation in γ_{PtTi} generates a significant variation in the maximum operational stress level ranging from -40 to 88% for SiO_2, -32 to 42% for Pt/Ti, and ± 8% for Si_3N_4. Results shown in Fig (5.14) were fitted using linear fitting (Equation (5.14)) for Si_3N_4, Pt/Ti and polynomial fitting (Equation (5.15)) for SiO_2 as follows

$$\beta_{\sigma}^{Si_3N_4,Pt/Ti} = a_o + a_1\gamma_{PtTi} \tag{5.14}$$

$$\beta_{\sigma}^{SiO_2} = b_o + b_1(\gamma_{PtTi}) + b_1(\gamma_{PtTi})^2 + b_1(\gamma_{PtTi})^3 + b_1(\gamma_{PtTi})^4 \tag{5.15}$$

Equations (5.14) and (5.15) constants, as well as the average root mean square error (RMS) of curve fitting are listed in Tables (5.9) and (5.10), respectively. A less significant effect can be noticed for the variation in the maximum operational stress with γ_{Poly} due to the tighter variation in the thermal response, as shown in Fig (5.15). Results shown in Fig (5.15) was fitted using linear fitting (Equation (5.16)) for Si_3N_4 and polynomial fitting (Equation (5.17)) for SiO_2 and polysilicon as follows

$$\beta_{\sigma}^{Si_3N_4} = a_o + a_1\gamma_{Poly} \tag{5.16}$$

$$\beta_{\sigma}^{SiO_2,Poly} = b_o + b_1(\gamma_{Poly}) + b_1(\gamma_{Poly})^2 + b_1(\gamma_{Poly})^3 + b_1(\gamma_{Poly})^4 \tag{5.17}$$

Equations (5.16) and (5.17) constants, as well as the average root mean square error (RMS) of curve fitting are listed in Tables (5.9) and (5.10), respectively.

The dimensionless terms β_e and β_E indicate the ratios between the actual and nominal values of the coefficient of thermal expansion (e) and Young's modulus (E) for different thin film materials, respectively. The variation of the stress factor (β_σ) for different thin film materials with β_e of Si_3N_4 can be shown in Fig (5.16). The variation of $\beta_e^{Si_3N_4}$ was found to generate a significant variation in maximum stress of Si_3N_4 ranging from -13 to 33%. A less significant variation ranging from 0 to +5% can be noticed for other thin film materials. Similarly, the same effect can be noticed

for the variation of β_e for other thin film materials, as shown in Fig (5.17), Fig (5.18) and Fig (5.19).

The variation of the coefficient of thermal expansion of an individual thin film material generates a significant variation in its maximum generated stress and a reduced degree of variation for the other thin film materials. Equation (5.18) is a polynomial fitting of the numerical results expressing the relation between $\beta_\sigma^{Si_3N_4}$ and $\beta_e^{Si_3N_4}$. The relation between the stress factor (β_σ) for Pt/Ti, polysilicon and SiO_2 and β_e can be expressed linearly by Equation (5.19), where β_e refer to the variation in the coefficient of thermal expansion for different thin film materials.

$$\beta_\sigma^{Si_3N_4} = b_o + b_1(\beta_e^{Si_3N_4}) + b_1(\beta_e^{Si_3N_4})^2 + b_1(\beta_e^{Si_3N_4})^3 + b_1(\beta_e^{Si_3N_4})^4 \qquad (5.18)$$

$$\beta_\sigma^{Pt/Ti,Poly,SiO_2} = a_o + a_1\beta_e^{Pt/Ti,Poly,SiO_2} \qquad (5.19)$$

A list of Equation (5.18) constants, as well as the average RMS of curve fitting can be shown in Table (5.10); and, a list of constants in Equation (5.19) for Pt/Ti, polysilicon and SiO_2, as well as the average RMS of curve fitting can be shown in Table (5.9).

The variation of the stress factor (β_σ) with the β_E, are shown in Fig (5.20). In contrast to the coefficient of thermal expansion, the variation in Young's modulus only generates a variation in the maximum stress of thin film materials. As shown in Fig (5.20), the variation of β_E generates a variation in the maximum stress level ranging from –32 to 36% for Si_3N_4, -19 to 16% for SiO_2 and –20 to 14% for Pt/Ti.

Results shown in Fig (5.20) were linearly fitted to express the relation between β_σ and β_E for different thin film materials as follows

$$\beta_\sigma^{Si_3N_4,SiO_2,Pt/Ti} = a_o + a_1\beta_E^{Si_3N_4,SiO_2,Pt/Ti} \quad (5.20)$$

where, β_E refer to the variation in Young's modulus for different thin film materials. A list of Equation (5.20) constants for different thin film materials, as well as the average RMS of curve fitting can be found in Table (5.9).

5.5.2 Effect on Fatigue Life

As shown in Table (5.8), the value of $\sigma_{N_{max}}$ for Pt/Ti was approximately two times the ultimate fracture strength, which suggests rupture or delimitation of the Pt/Ti thin film. Based on this result, an investigation was conducted to replace the Pt/Ti with doped polysilicon as a heater/sensor material. The polysilicon has a higher fracture strength and a coefficient of thermal expansion, which is higher by an order of magnitude than Pt/Ti (more compatible with neighboring thin film materials). This clearly explains the great reduction in the operational stress of the heater material by using polysilicon rather than Pt/Ti. An investigation of other thin film materials reveals that the operating stress levels are safe enough with regard to static failure. The next step was to investigate the fatigue life for different thin film materials under thermal cyclic loading.

The microheater is subjected to a state of fluctuating stress ranging from a minimum value of the residual stress to a maximum value of the operating stress

level. An equivalent value for a completely reversed loading should be calculated to be able to estimate the fatigue life using the S-N curve. The value of the equivalent alternating stress can be calculated using Goodman's curve, the values for the actual mean and alternating stresses. The following equations were used to calculate the equivalent alternating stress.

$$\sigma_{\mathrm{m}} = \frac{\sigma_{A_{\max}} - \sigma_{res.}}{2} \tag{5.21}$$

$$\sigma_{\mathrm{a}} = \frac{\sigma_{A_{\max}} + \sigma_{res.}}{2} \tag{5.22}$$

$$\sigma_a^{eqv.} = \frac{\sigma_a S_u}{S_u - \sigma_m} \tag{5.23}$$

where, σ_{m} is the actual mean stress, σ_{a} is the actual alternating stress and $\sigma_a^{eqv.}$ is the equivalent alternating stress.

An initial investigation of different thin film materials at different values of residual stress, show a safe level of the equivalent alternating stress against fatigue failure except for Si_3N_4 ($\sigma_a^{eqv.} > 0.5 S_{ut}$). The largest variation of $\sigma_{A_{\max}}$ for Si_3N_4 was found to occur with $\beta_e^{Si_3N_4}$ and $\beta_E^{Si_3N_4}$, therefore only the variation of $\sigma_a^{eqv.}$ for Si_3N_4 with these parameters was studied. The dimensionless terms $\beta_{\sigma_a^{eqv.}}$, $\delta_{\sigma_{res}}$ denote the ratios of $\sigma_a^{eqv.}$ and $\sigma_{res.}$ to S_{ut}, respectively. The relation between $\beta_{\sigma_a^{eqv.}}$, N (fatigue life in number of cycles) and $\beta_e^{Si_3N_4}$ at different $\delta_{\sigma_{res}}$ can be shown in Fig (5.21) and Fig (5.22), respectively. Lower values for $\sigma_a^{eqv.}$ and higher N can be noticed with $\delta_{\sigma_{res}}$ of –

0.15 ($\sigma_{res.}$ = -60 MPa). The gas sensor is safe against fatigue failure at $\beta_e^{Si_3N_4}$ in the range of 0.8 to 0.87 regardless of the value of $\delta_{\sigma_{res}}$, while for other ranges it suffers from failure at relatively short operational life cycles. The same effect can be seen for the variation of $\sigma_a^{eqv.}$ and N with $\beta_E^{Si_3N_4}$ at different $\delta_{\sigma_{res}}$ as shown in Fig (5.23) and Fig (5.24), respectively. However a wider range of $\beta_E^{Si_3N_4}$ variation (0.8 to 0.95) provides a safe operation under cyclic thermal loading regardless of the value of $\delta_{\sigma_{res}}$.

5.6 Concluding Remarks

In this chapter, The Major Vector algorithm has been utilized to study the reliability of micromachined MEMS gas sensors. The effect of the uncertainties generated, during various stages of microfabrication, to the dimensional parameters and the thin film material properties on the operational performance of the gas sensor have been investigated. The performance of the MEMS gas sensor has been assessed for the gas detection sensitivity and the fatigue life of the sensor under thermal cyclic loading. Equations that relate this performance to the variation of different design variables in the gas sensor have been fitted from the calculated results to set design rules for the development process of the gas sensor. The results of the reliability study indicate the following:

(i) For the EBEM and ORM sensitive film deposition techniques, the variation of the thermal conductivity of Si_3N_4 and Pt/Ti electrical resistivity alters the GDS by a factor that could reach 45%.

(ii) The variations in the thermal conductivities of Pt/Ti and SiO_2 had a negligible effect on the gas sensor performance

(iii) On studying the dimensional parameters, the thickness of the Si_3N_4 middle layer and the total thickness of the insulation layer were found to have a significant effect on the thermal response and the sensitivity of the micro sensor. However a significant improvement on the sensitivity of the sensor was noticed allover the positive applied tolerance region of some parameters with the ORM sensitive film deposition technique

(iv) The results of the parametric study suggest the use of polysilicon as a heater/sensor material instead of the used Pt/Ti, which was proven to suffer from stress levels close to twice its ultimate fracture strength. The suggested design modification would result in an increase in the power consumption of only 10%. However, a considerable improvement of 13% in the performance GDS and a great reduction in the operational stress levels could be achieved.

(v) Except for Si_3N_4, all thin film materials are safe with regard to cyclic fatigue failure at different levels of residual stresses. This would suggest that annealing might not be required, especially that the application of the gas sensor does not require perfectly flat thin film layers for successful operation.

(vi) For Si_3N_4, the lowest equivalent alternating stress level was found at σ_{res} =-60 MPa. This value of the residual stress corresponds to a SiH_2Cl_2/NH_3 ratio of approximately 5.5 and a deposition temperature of 850 °C. Regardless of the value of the residual stress, the variation of the coefficient of thermal expansion and Young's modulus for Si_3N_4 should be kept with in –20% to 0%.

(vii) The variation of thermal/electrical parameters did not have a significant effect on the fatigue life of the sensor. However a strict control over the variations of these parameters with in ±5% is essential to prevent large degradations in the performance GDS of the device.

(viii) The current work emphasizes the greater role of modeling at the pre-microfabrication stage. The numerical results can be used at the design stage to set more careful control on some parameters that would alter the operation of the gas sensor if, otherwise not carefully measured and controlled.

(ix) Finally, the current lack in the characterization of thin films material properties adds a great disadvantage to the MEMS industry and is especially emphasized in this study. Therefore, finding appropriate means of materials testing and setting strict controls on the micromachining process, in a way that would help in a better characterization of material properties; and provide a better control over the dimensional parameters of thin films is strongly recommended.

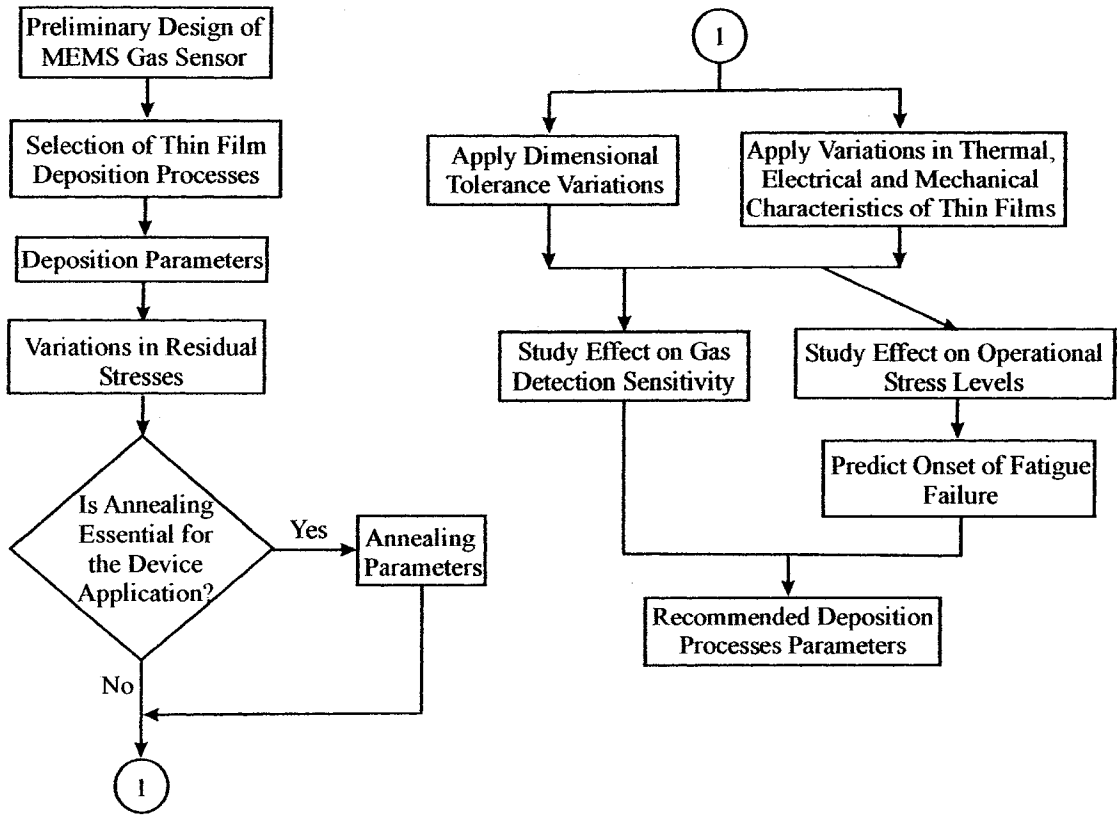

Figure 5.1: MEMS gas sensor design framework

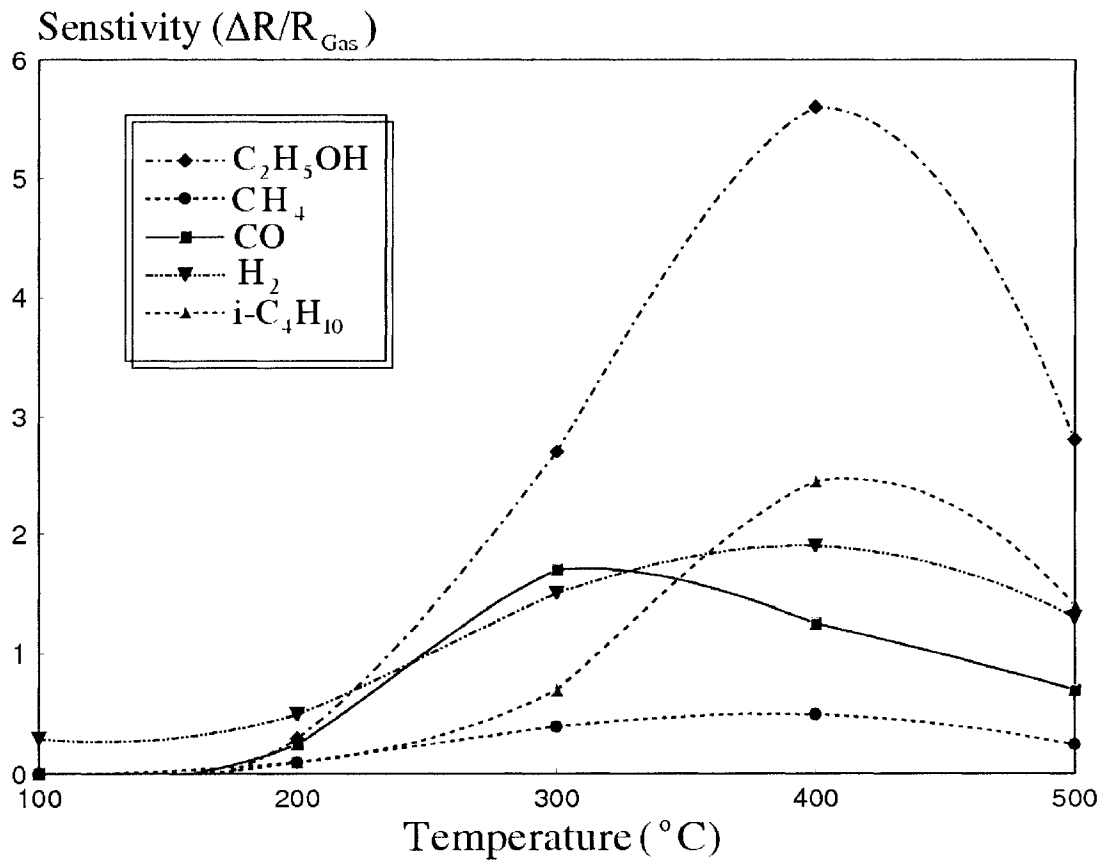

Figure 5.2: Dependence of the sensitivity on the heater temperature, Mo *et al.* (2001), (sensitive film deposited by EBEB method)

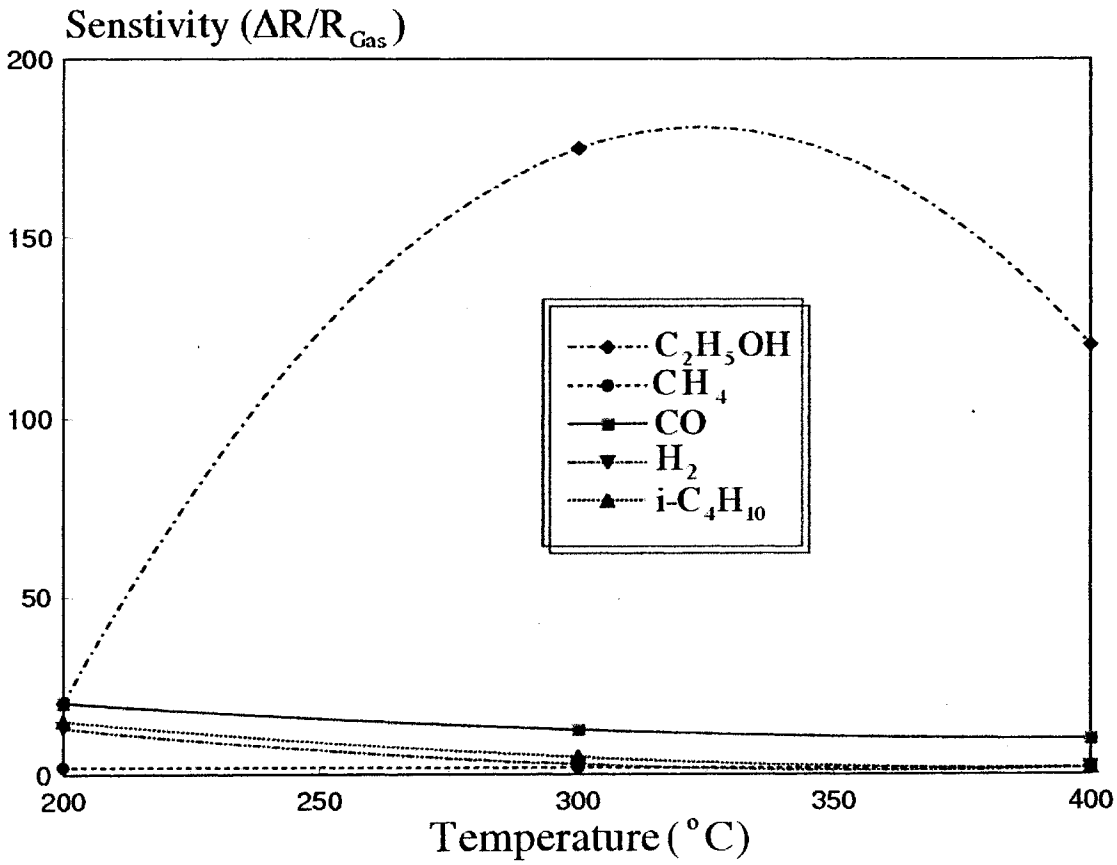

Figure 5.3: Dependence of the sensitivity on the heater temperature Mo *et al.* (2001), (sensitive film deposited by ORM method)

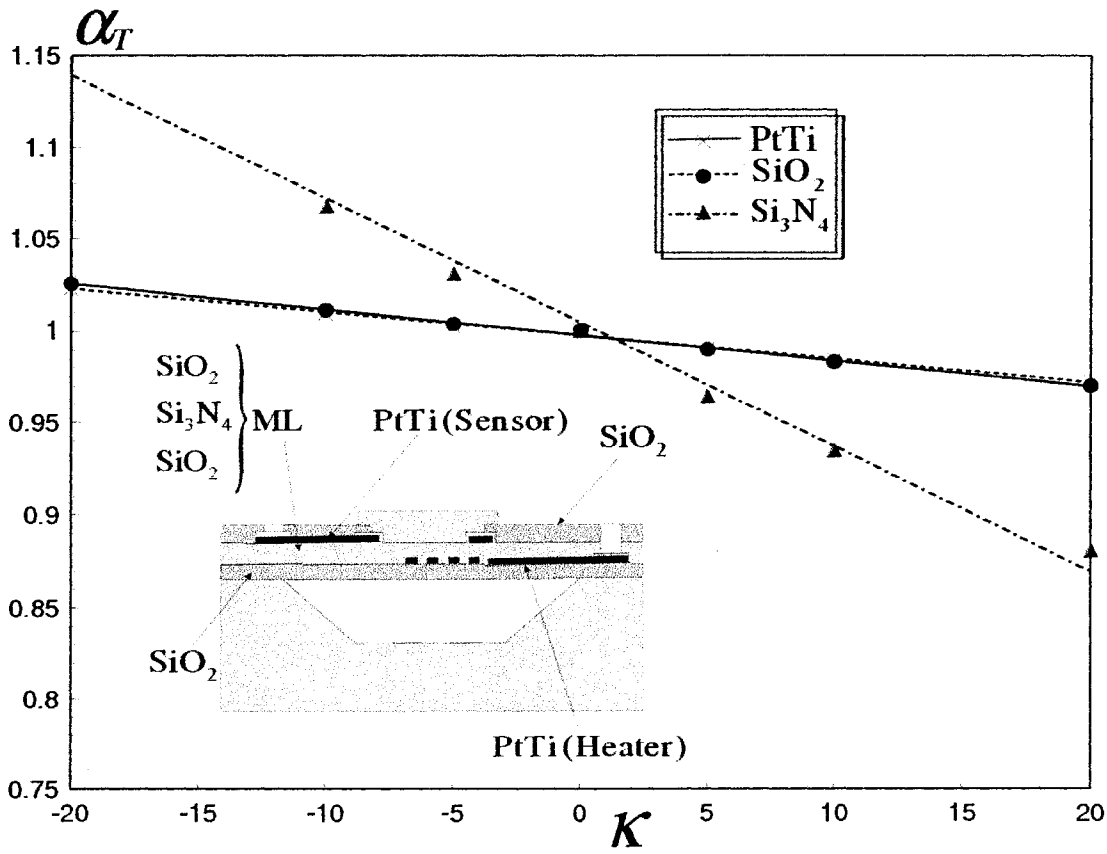

Figure 5.4: Effect of percentage variation in the thermal conductivity of Pt/Ti, SiO2 and Si_3N_4 on thermal response of the gas sensor

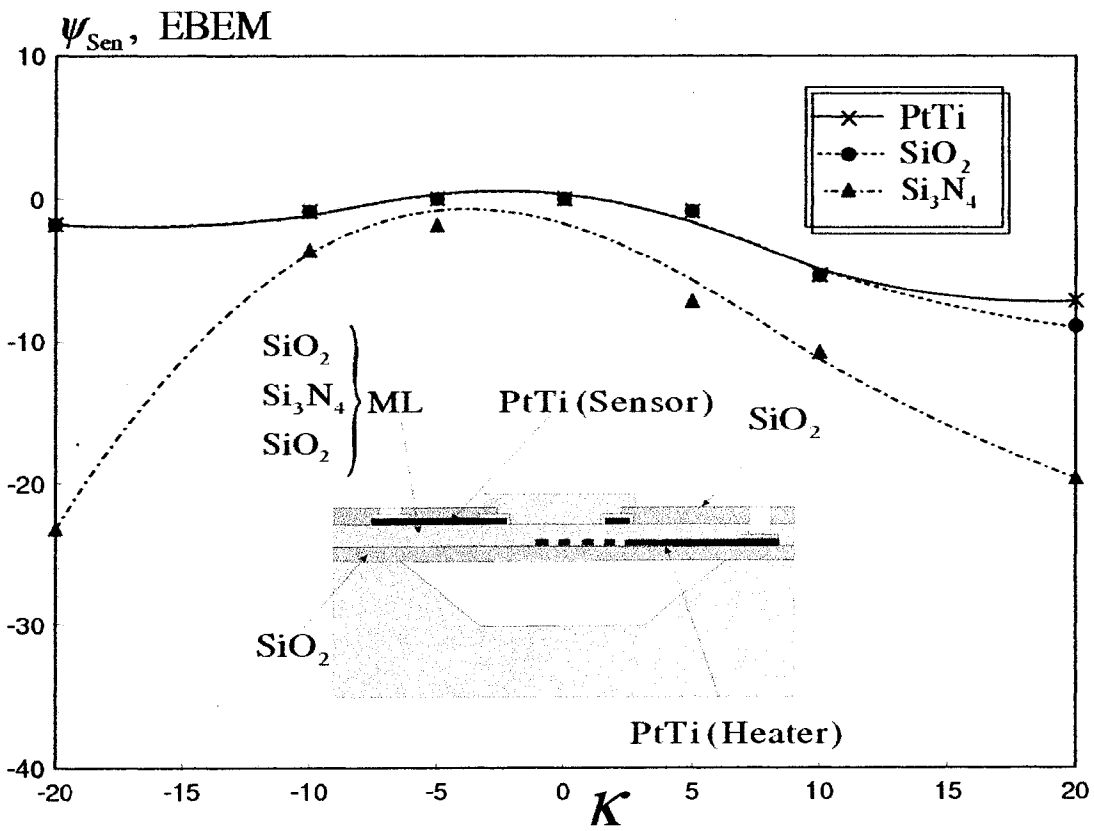

Figure 5.5: Effect of percentage variation in the thermal conductivity of Pt/Ti, SiO_2 and Si_3N_4 on sensor sensitivity (sensitive film deposited by EBEB method)

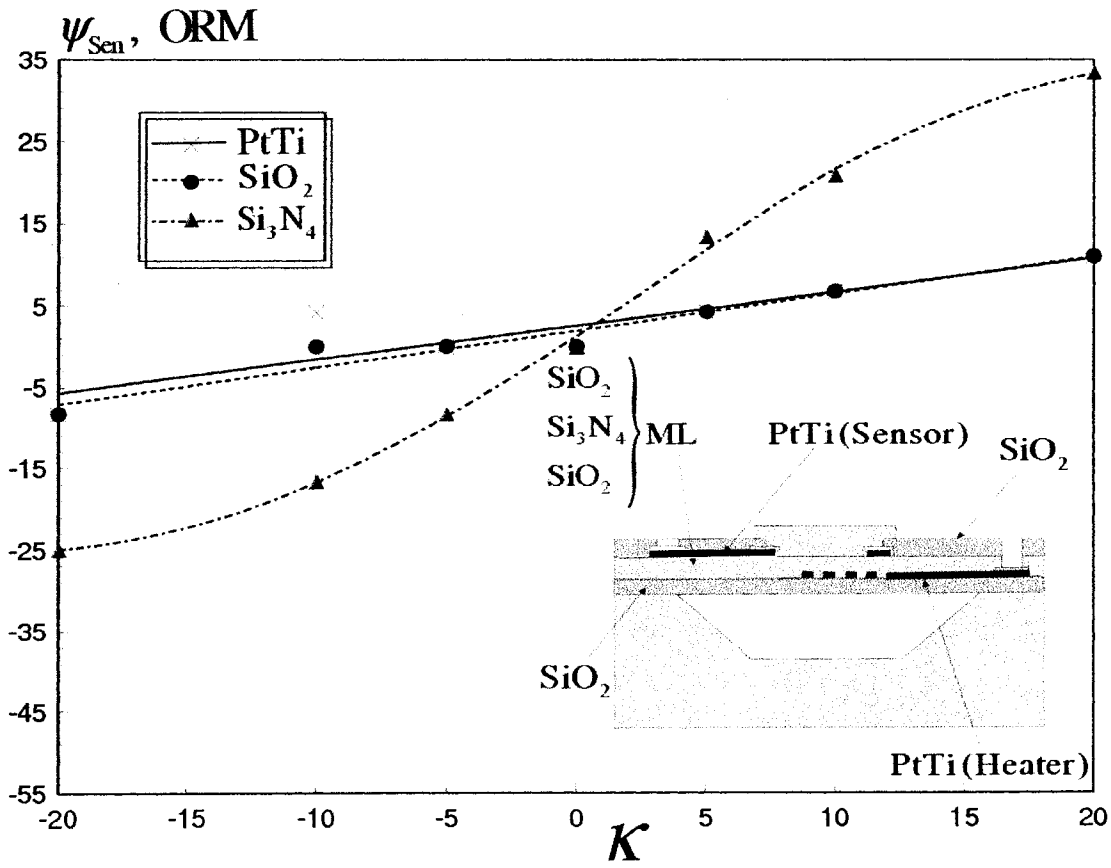

Figure 5.6: Effect of percentage variation in the thermal conductivity of Pt/Ti, SiO_2 and Si_3N_4 on sensor sensitivity (sensitive film deposited by ORM method)

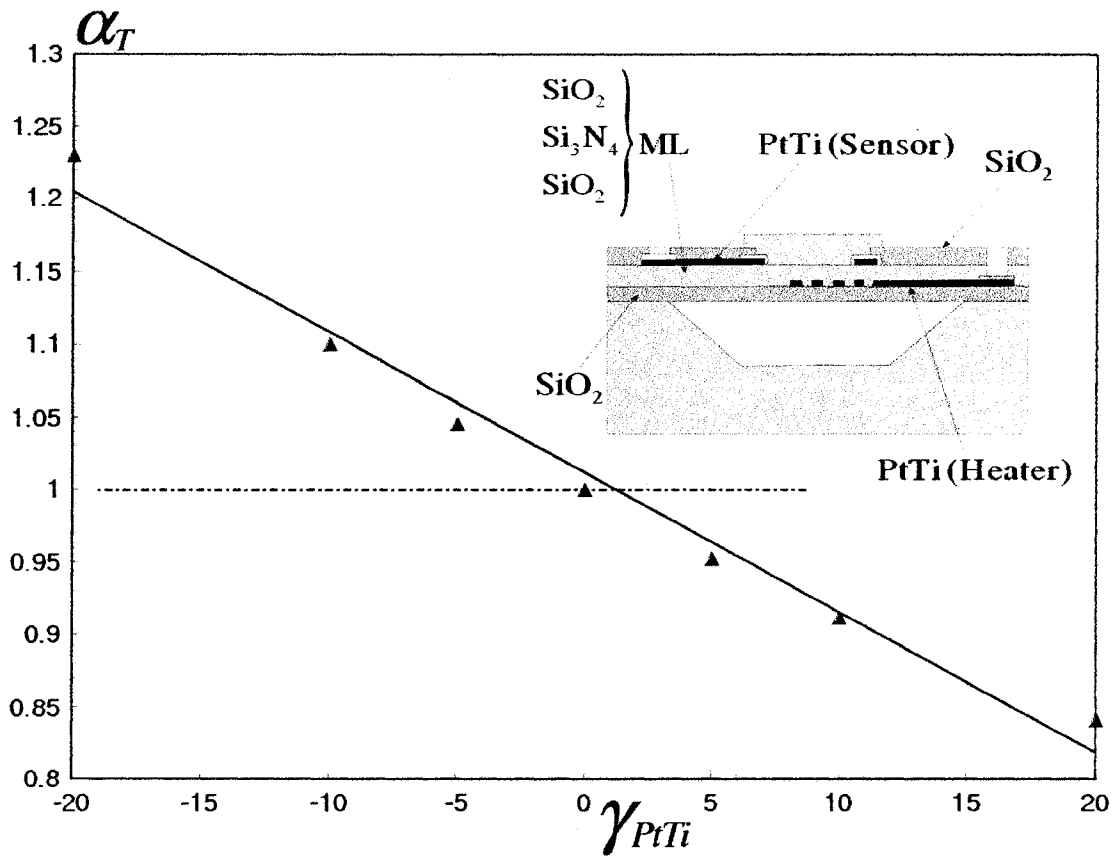

Figure 5.7: Effect of percentage variation in the electrical Resistivity of Pt/Ti on the thermal response of the gas sensor

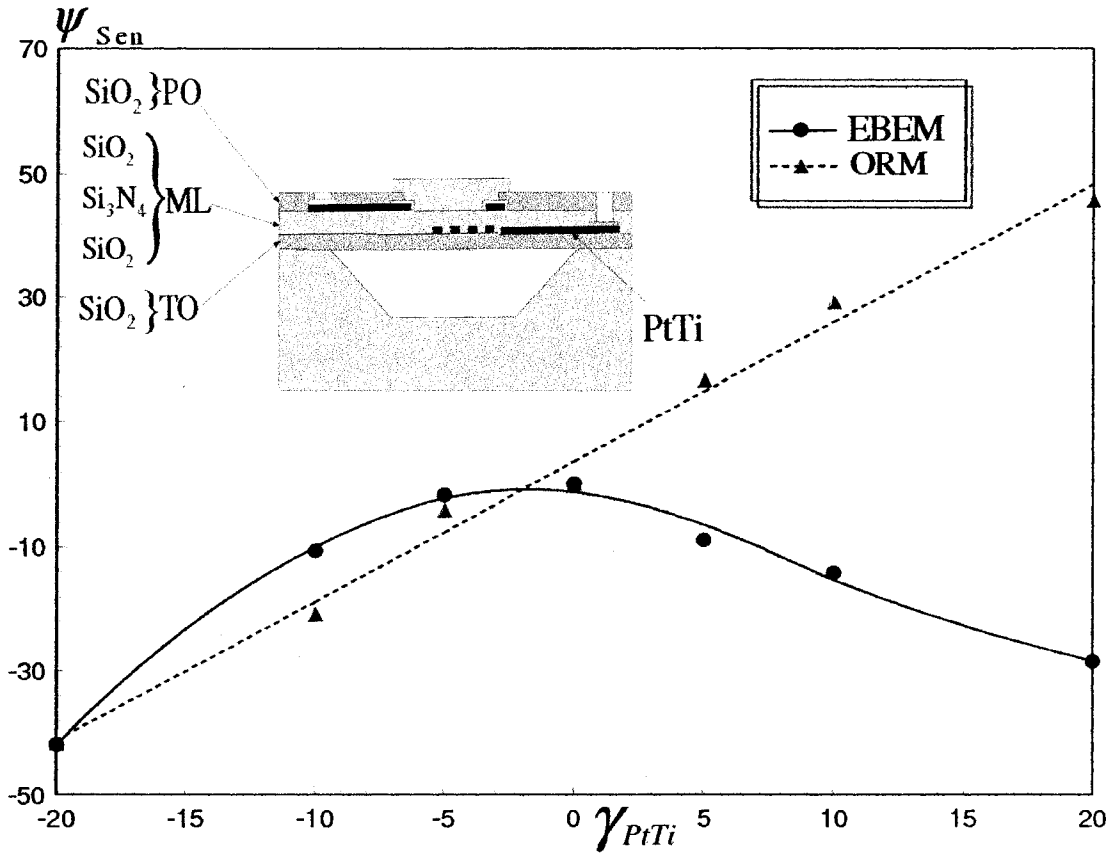

Figure 5.8: Effect of percentage variation in the electrical Resistivity of Pt/Ti on the sensitivity of the gas sensor

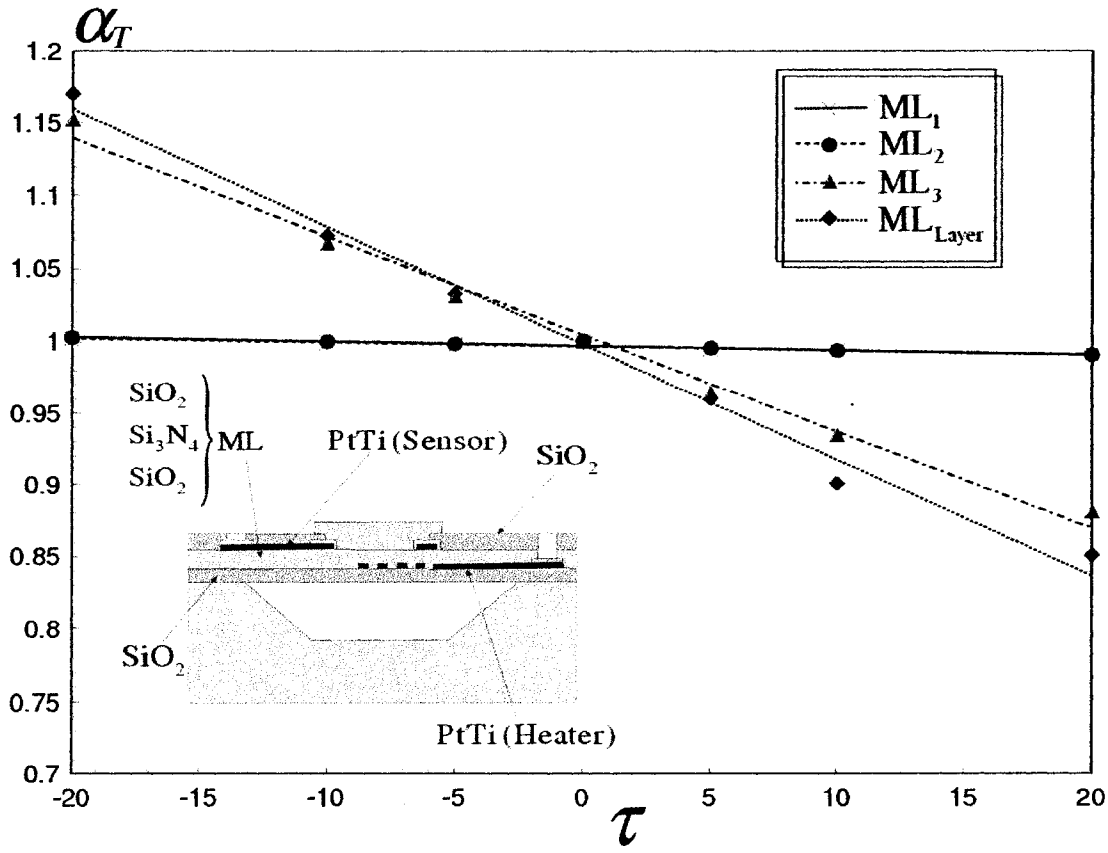

Figure 5.9: Effect of percentage variation in the insulation thickness of ML_1, ML_2, ML_3 and ML_{Layer} on the thermal response of the gas sensor

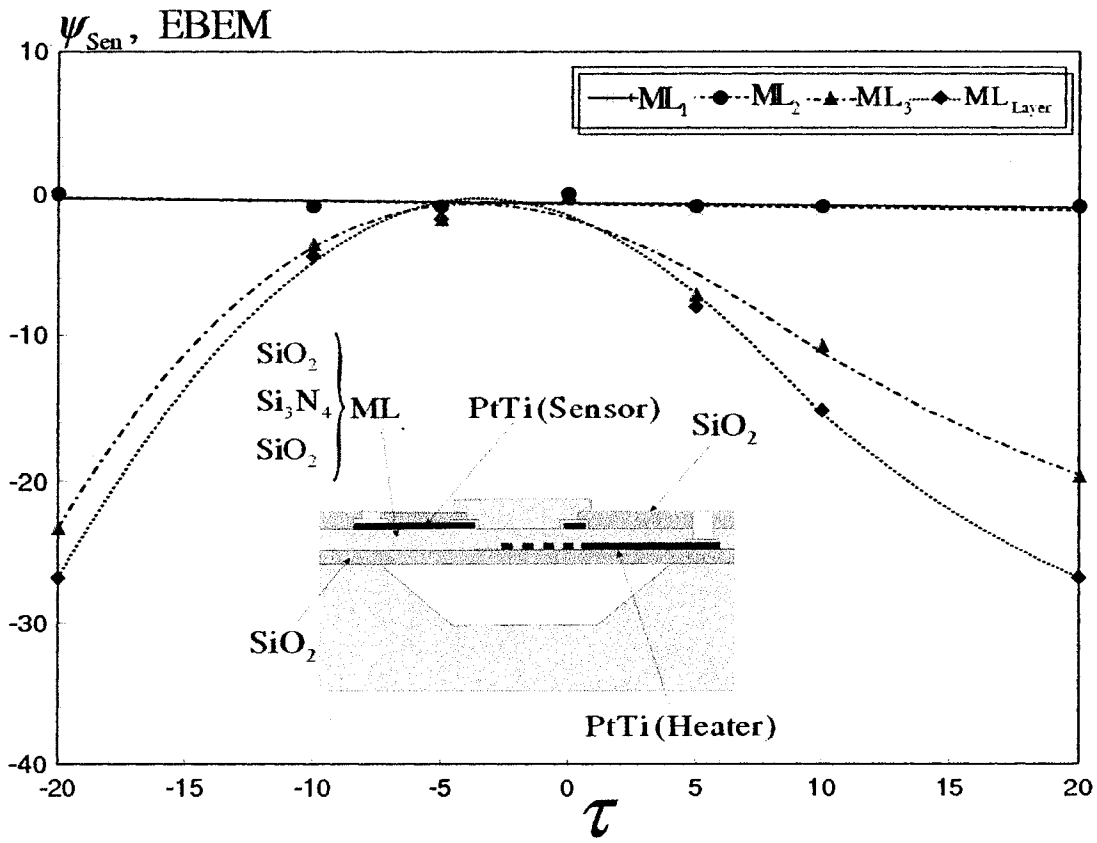

Figure 5.10: Effect of percentage tolerance in insulation thickness of ML_1, ML_2, ML_3 and ML_{Layer} on the sensitivity of the gas sensor (sensitive film deposited by EBEB method)

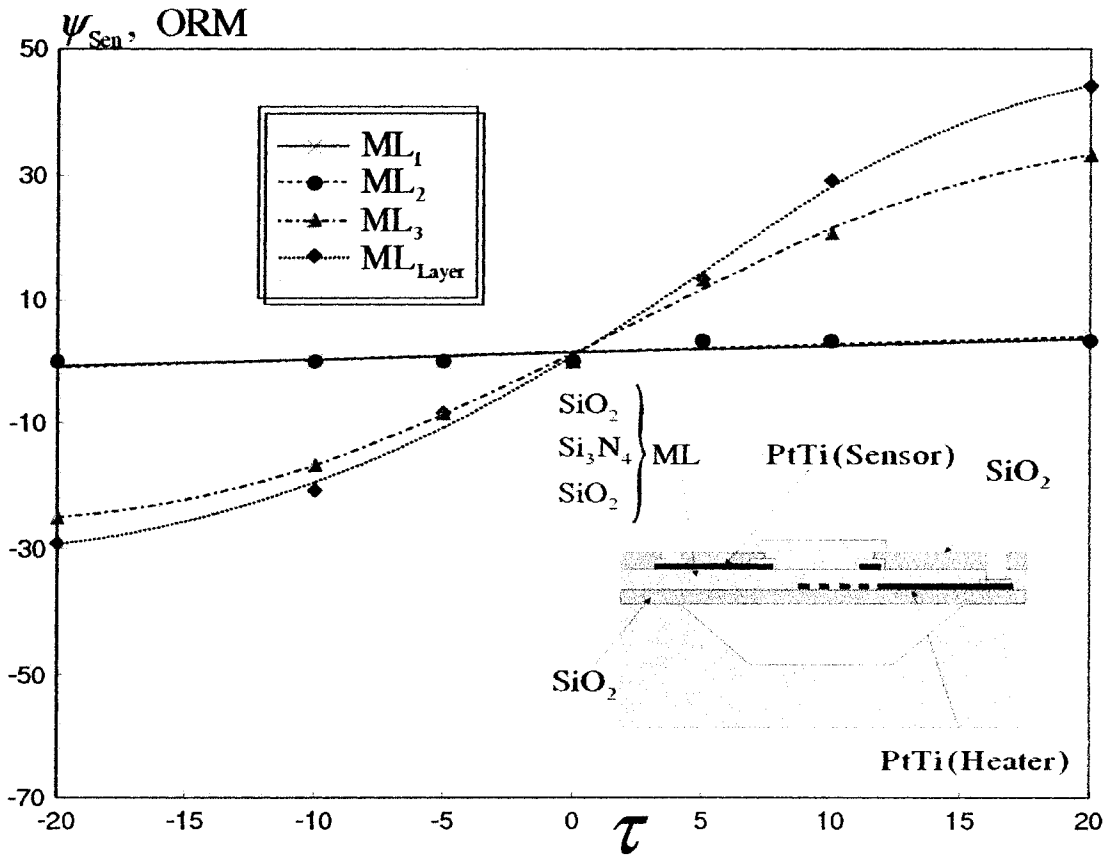

Figure 5.11: Effect of percentage tolerance in insulation thickness of ML_1, ML_2, ML_3 and ML_{Layer} on the sensitivity of the gas sensor (sensitive film deposited by ORM method)

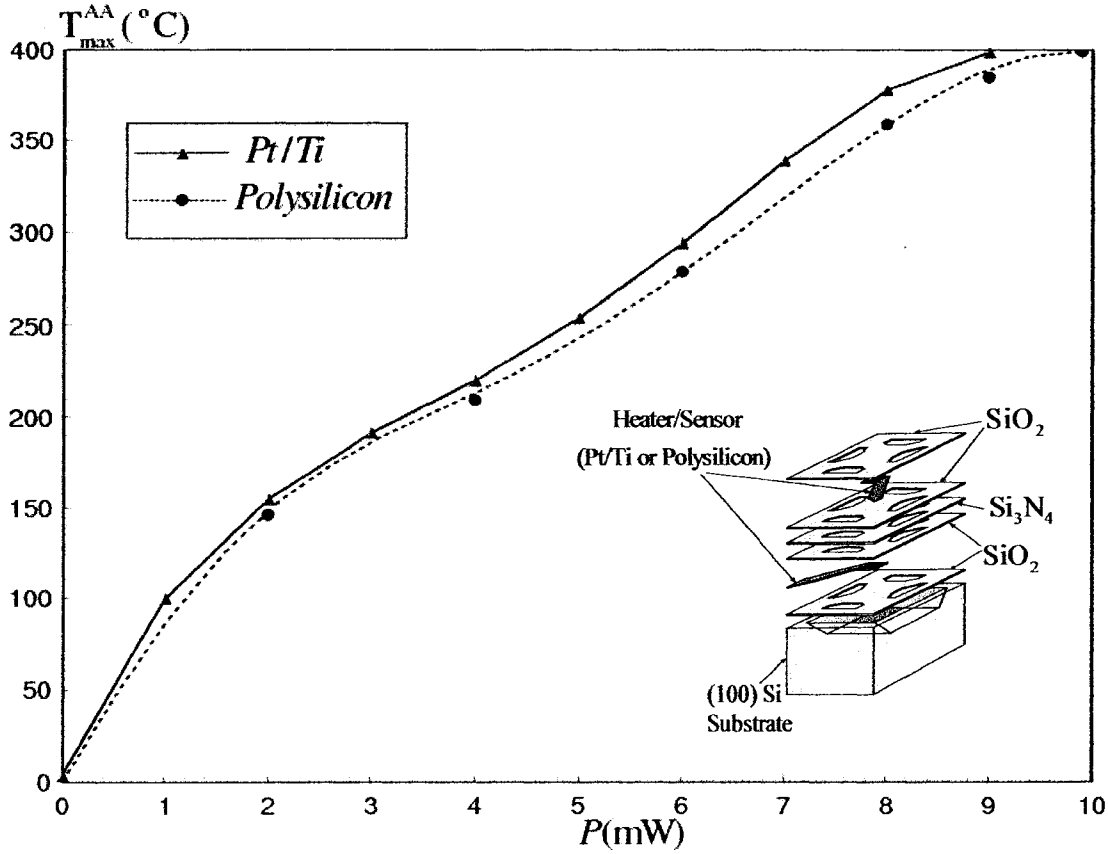

Figure 5.12: Power temperature relationship for different heater material

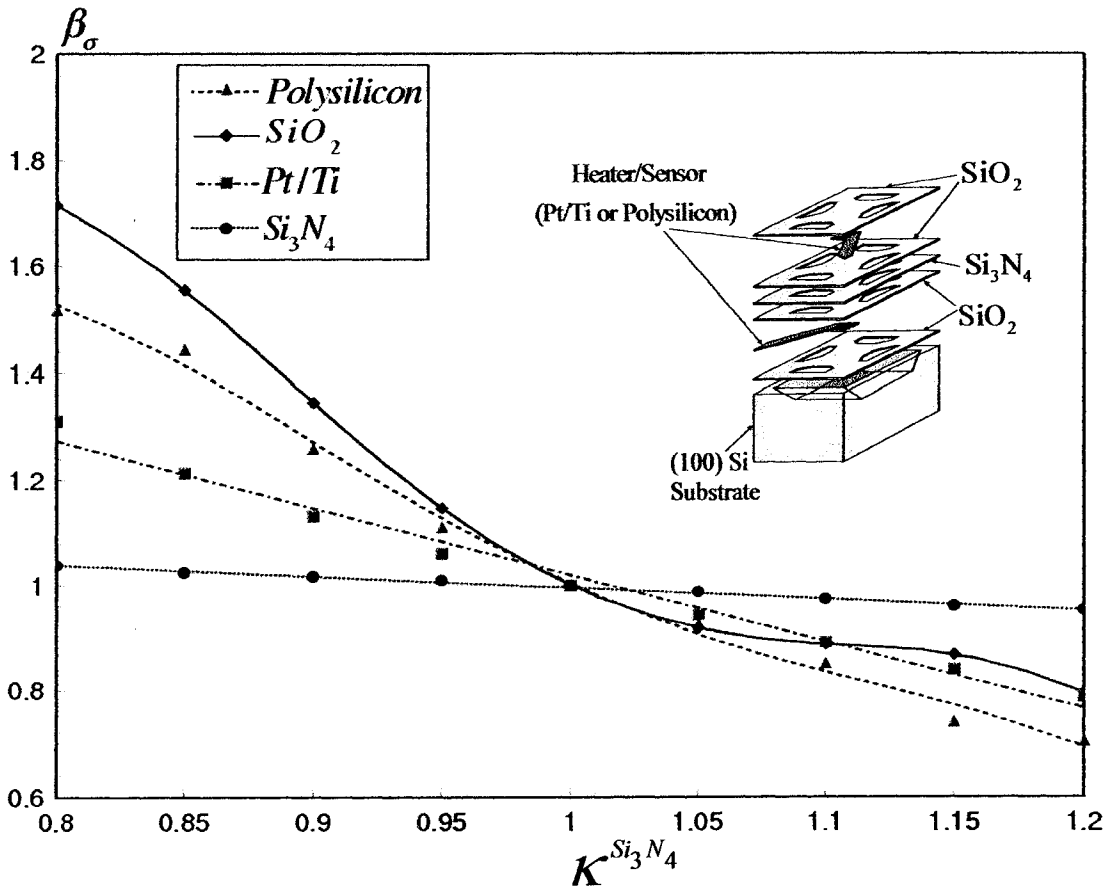

Figure 5.13: Effect of thermal conductivity variation of Si_3N_4 on the maximum thermal stress of different gas sensor materials

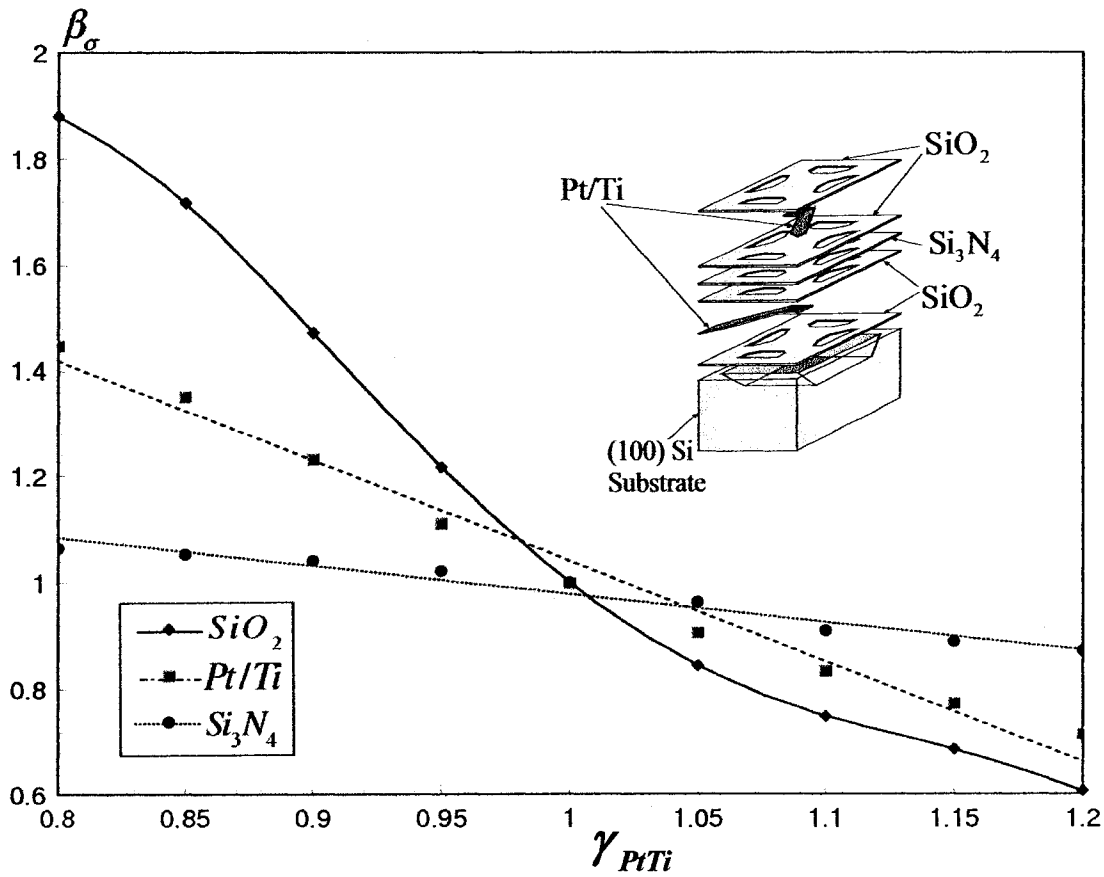

Figure 5.14: Effect of electrical resistivity variation of Pt/Ti on the maximum thermal stress of different gas sensor materials

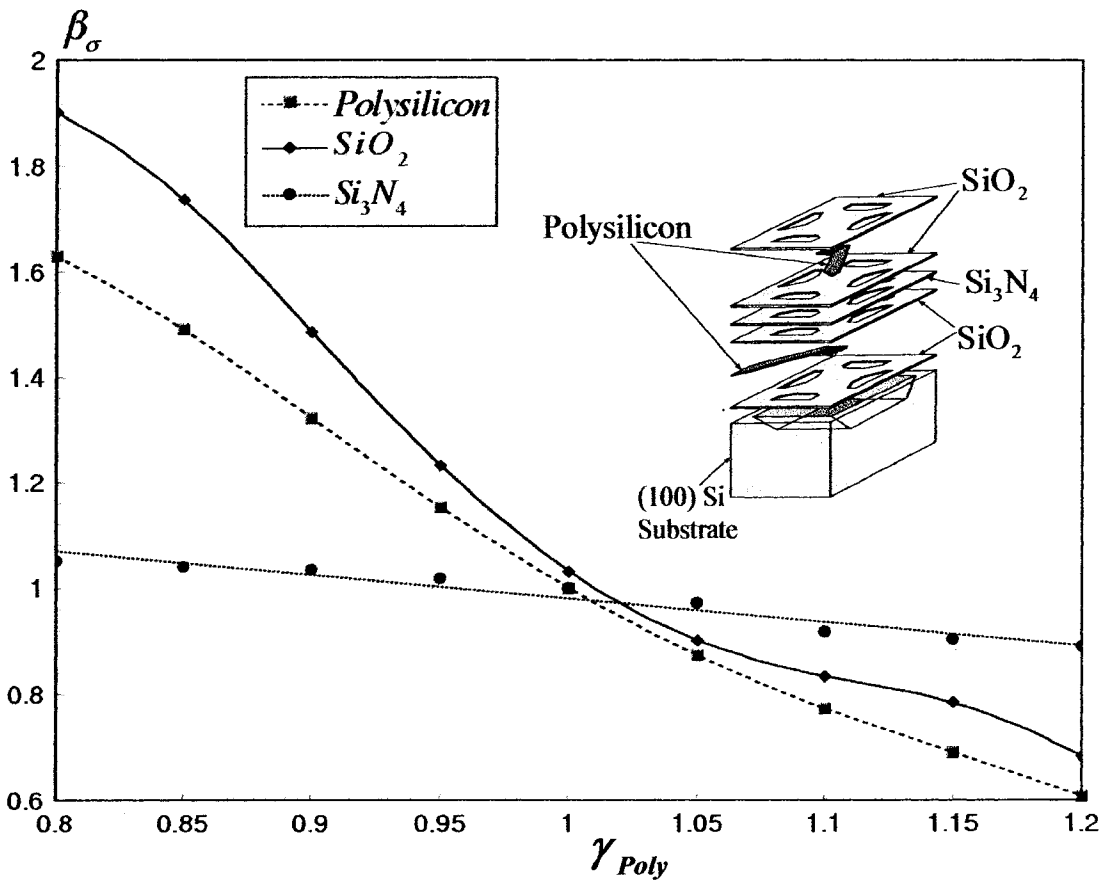

Figure 5.15: Effect of electrical resistivity variation of polysilicon on the maximum thermal stress of different gas sensor materials

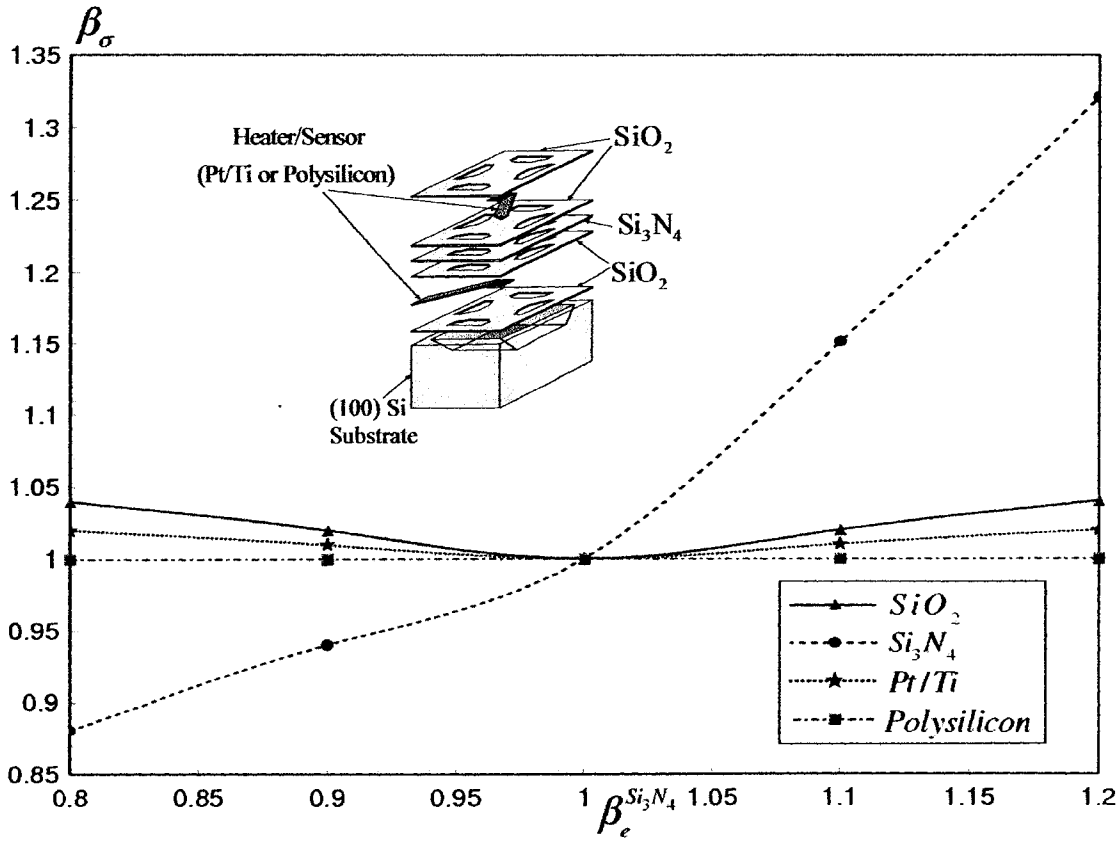

Figure 5.16: Effect of the variation of the coefficient of thermal expansion of Si_3N_4 on the maximum thermal stress of different gas sensor materials

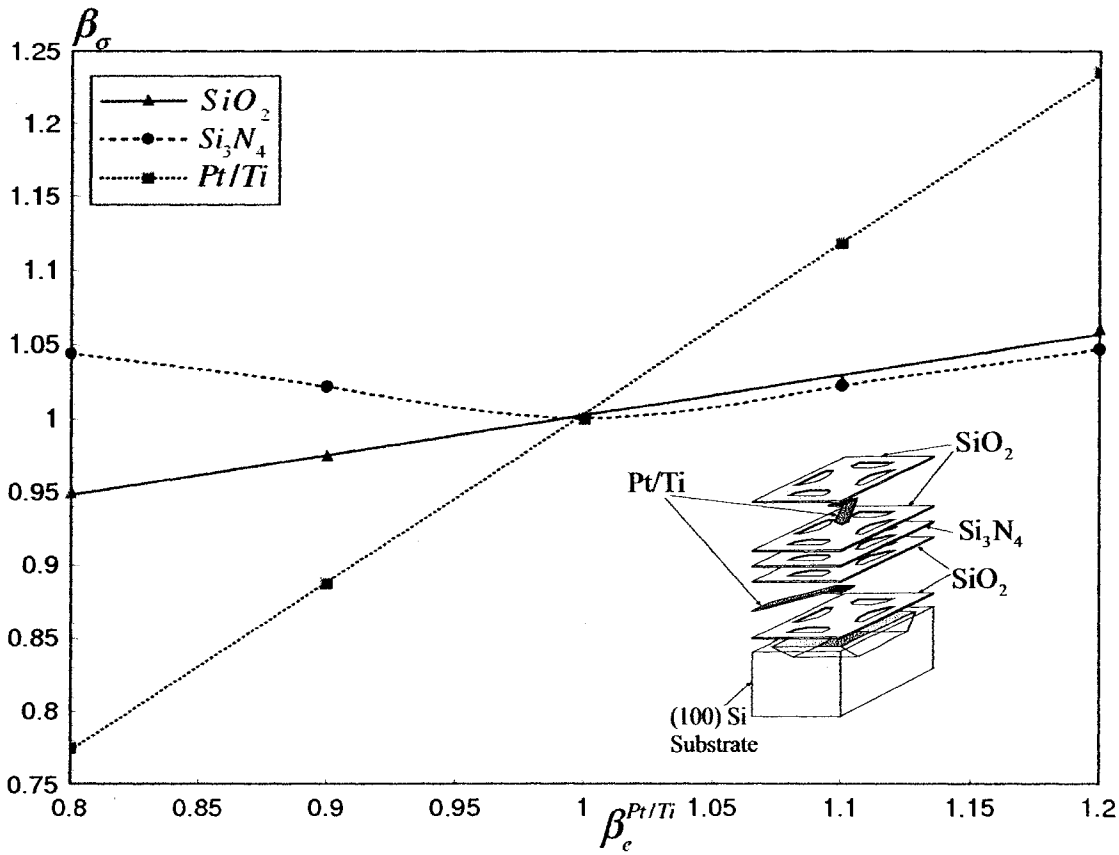

Figure 5.17: Effect of the variation of the coefficient of thermal expansion of Pt/Ti on the maximum thermal stress of different gas sensor materials

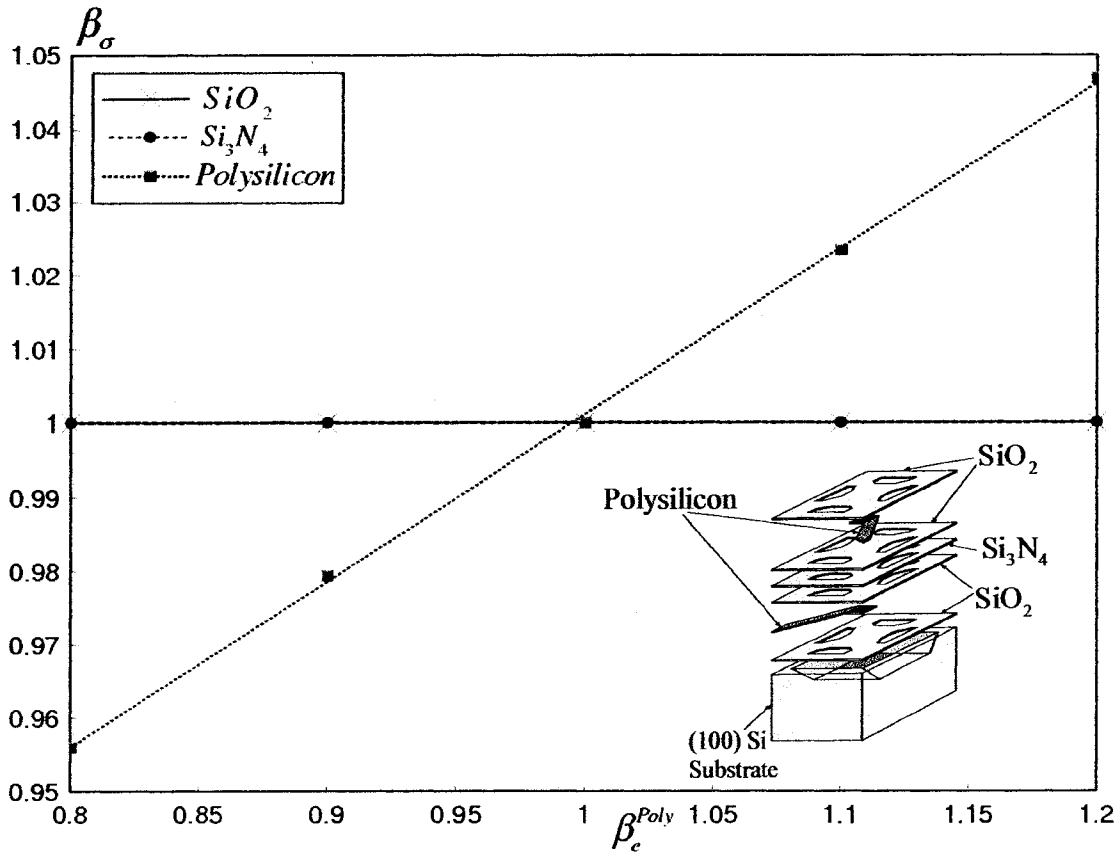

Figure 5.18: Effect of the variation of the coefficient of thermal expansion of polysilicon on the maximum thermal stress of different gas sensor materials

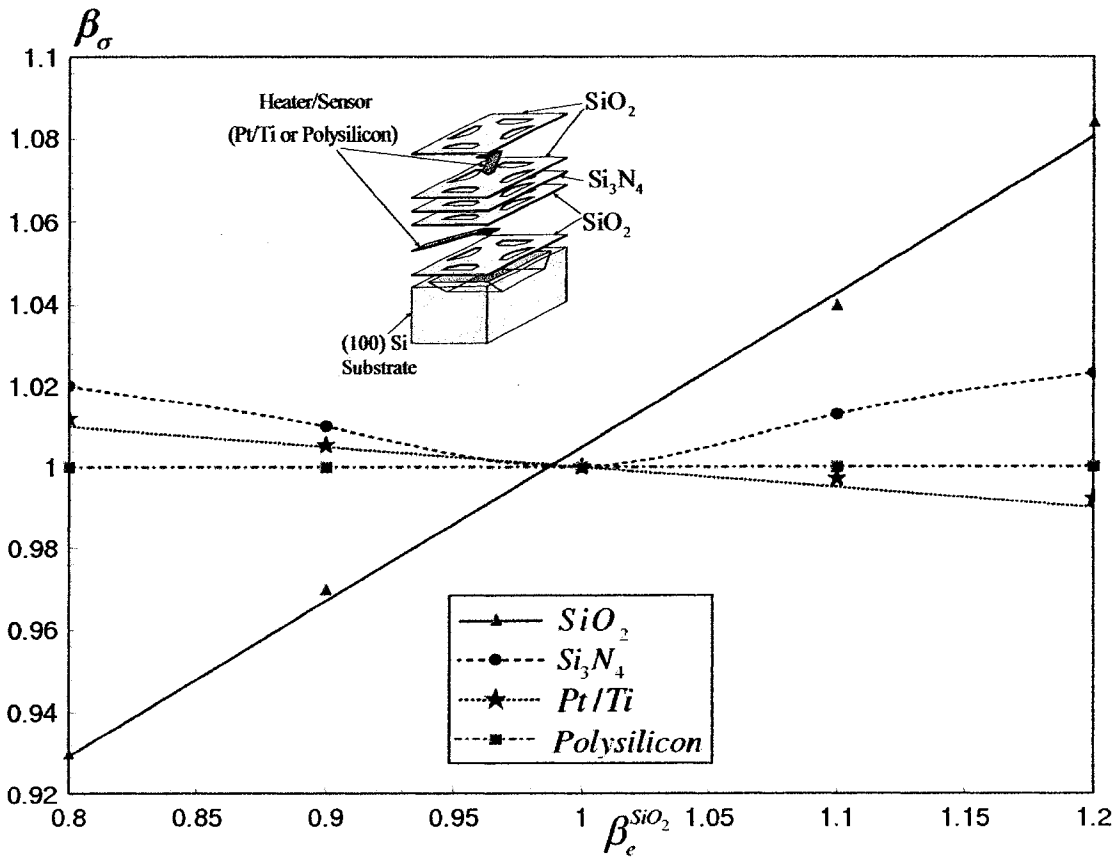

Figure 5.19: Effect of the variation of the coefficient of thermal expansion of SiO_2 on the maximum thermal stress of different gas sensor materials

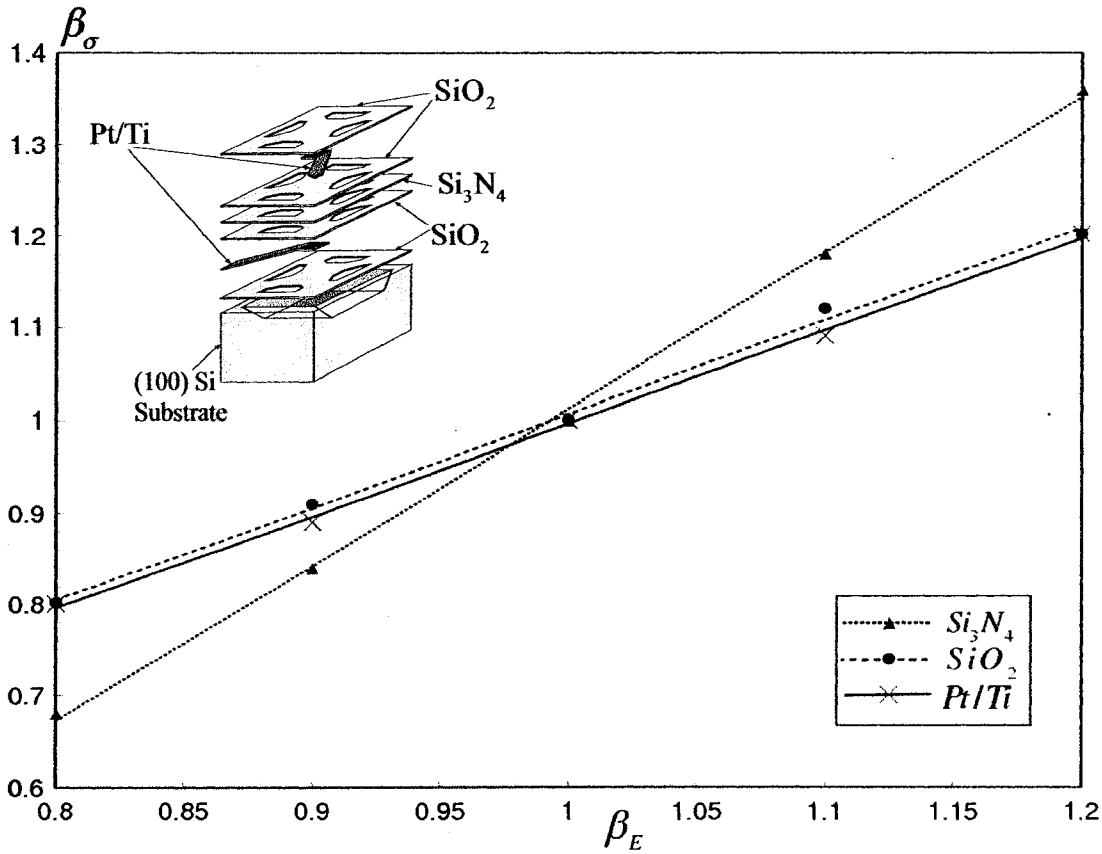

Figure 5.20: Effect of the variation of Young's modulus on the maximum thermal stress of different gas sensor materials

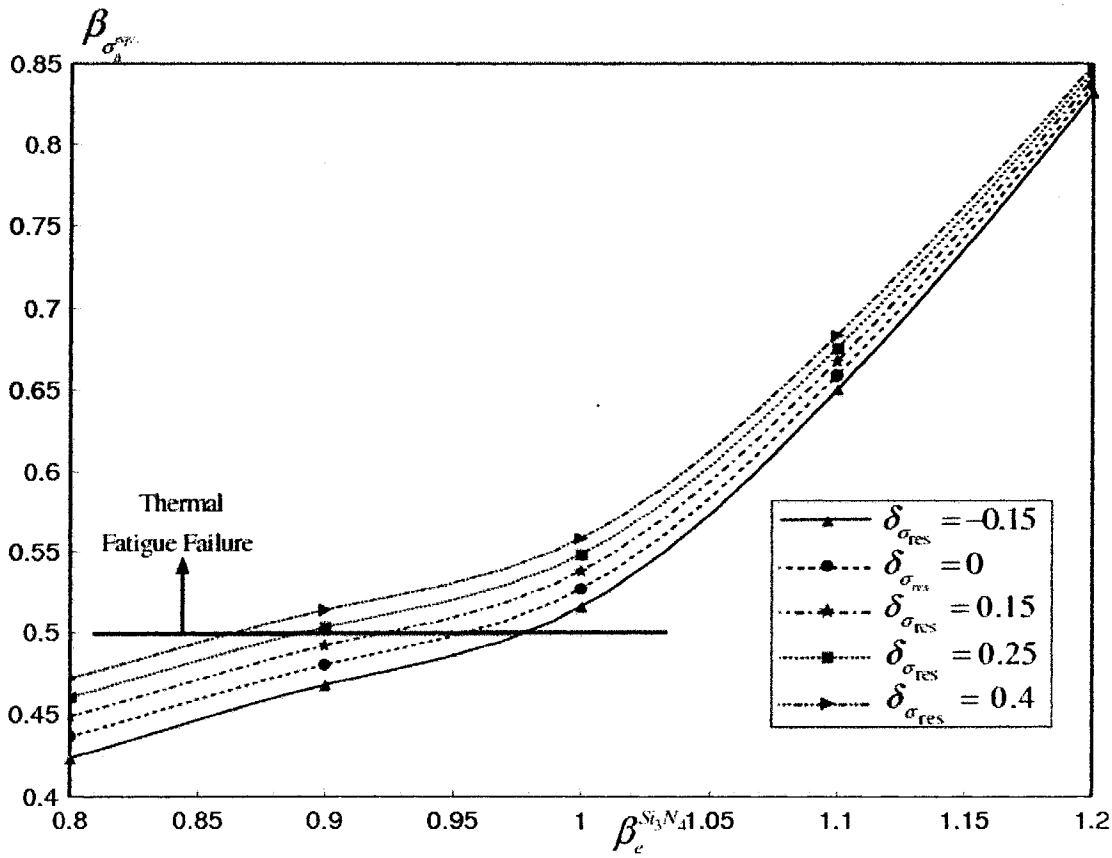

Figure 5.21: Effect of the variation of the coefficient of thermal expansion and deposition residual stress for Si_3N_4 on the equivalent alternating stress of Si_3N_4

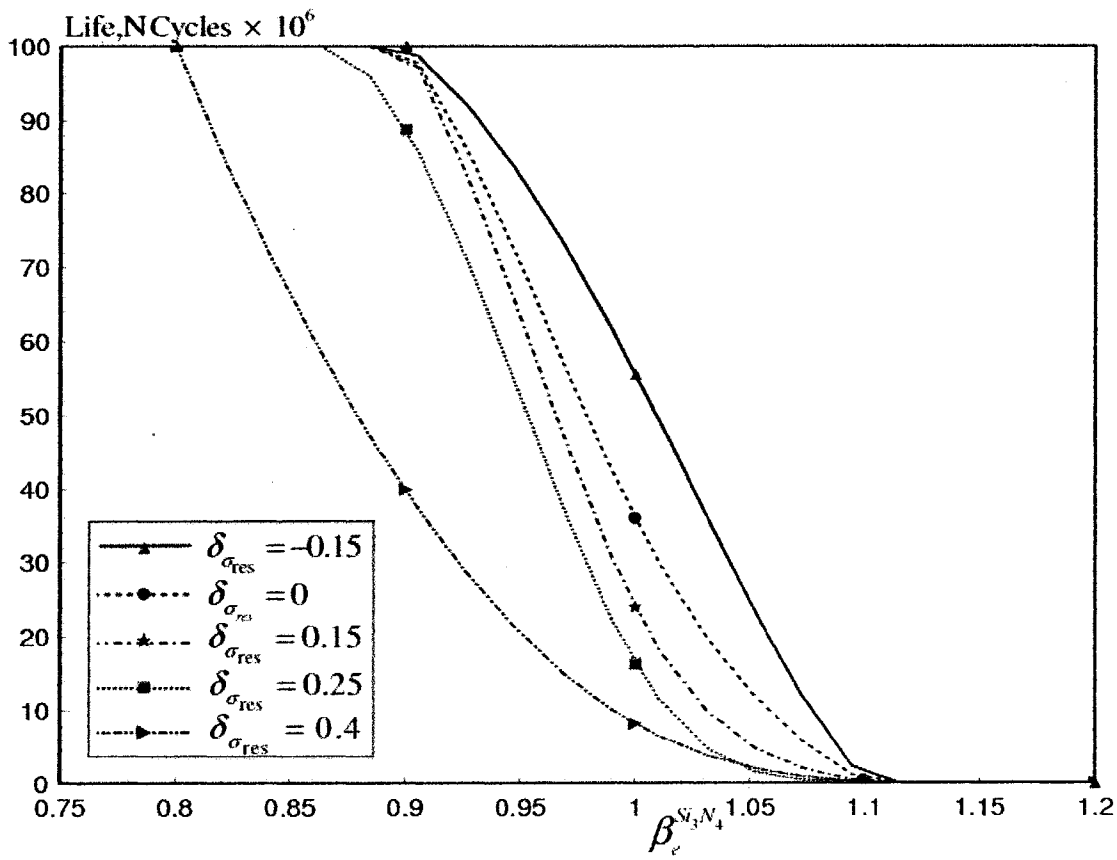

Figure 5.22: Effect of the variation of the coefficient of thermal expansion and deposition residual stress for Si_3N_4 on the expected fatigue life of the gas sensor

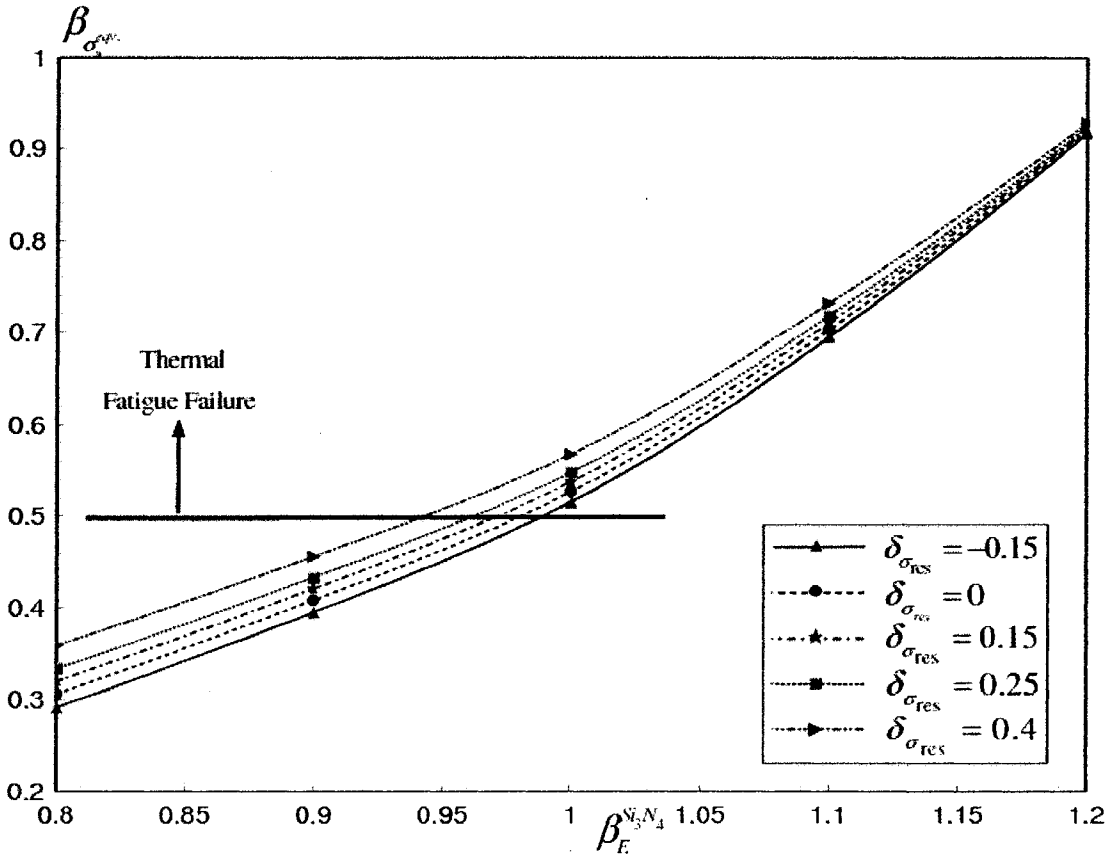

Figure 5.23: Effect of the variation of Young's modulus and deposition residual stress for Si_3N_4 on the equivalent alternating stress of Si_3N_4

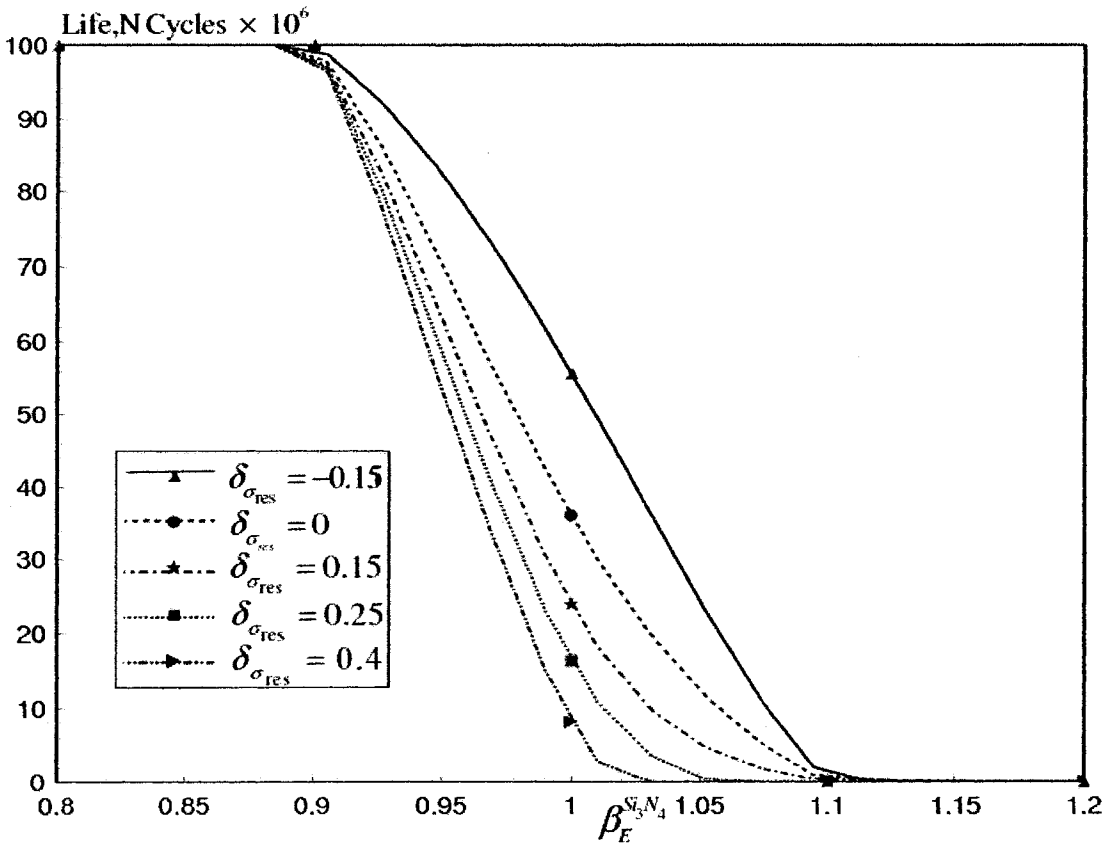

Figure 5.24: Effect of the variation of Young's modulus and deposition residual stress for Si_3N_4 on the expected fatigue life of the gas sensor

Table 5.1: A list of Equation (5.3) constants

	c^P	d^P
SiO_2	*0.997*	*-0.0014*
Si_3N_4	*1.0043*	*-0.007*
Pt/Ti	*0.997*	*-0.0013*

Table 5.2: A list of Equation (5.4) constants

	c_0^P	c_1^P	c_2^P
SiO_2	*0.31*	*-0.21*	-0.041
Pt/Ti	*0.3*	*-0.18*	-0.04
Si_3N_4	-1.7	-0.5	-0.06

Table 5.3: A list of Equation (5.5) constants

	d_0^P	d_1^P	d_2^P
SiO_2	*1.89*	*0.43*	0
Pt/Ti	*1.904*	*0.45*	0
Si_3N_4	1.3	2.1	0.012

Table 5.4: A list of Equation (5.9) constants

	c^G	d^G
ML_1	0.99	-0.0003
ML_2	0.996	-0.0004
ML_3	1.01	-0.006
ML_{Layer}	0.998	-0.008

Table 5.5: A list of Equation (5.10) constants

	c_0^G	c_1^G	c_2^G
ML_1	-0.25	-0.0125	0
ML_2	-0.23	-0.01	0
ML_3	-1.73	-0.53	-0.061
ML_{Layer}	-1.523	-0.7	-0.094

Table 5.6: A list of Equation (5.11) constants

	d_0^G	d_1^G	d_2^G
ML_1	1.43	0.11	0
ML_2	1.38	0.098	0
ML_3	1.28	2.1	0.015
ML_{Layer}	0.886	2.57	0.04

Table 5.7: A list of the studied parameters and their reported variations

	Coefficient of Thermal expansion (e) ($^{o}C^{-1}$)	Young's Modulus (E) (GPa)	Residual Stresses (σ_{res}) (GPa)	Major Contributing Deposition Parameters
SiO_2	$7\times10^{-6}\pm18\%$	75 ± 7.8	$-0.3\rightarrow0.3$	f(p,T)
Si_3N_4	$3.3\times10^{-6}\pm18\%$	310 ± 32	$-0.2\rightarrow0.8$	f(T, G)
Pt/Ti	$0.97\times10^{-5}\pm18\%$	140 ± 16	$0.2\rightarrow0.9$	$f(D_R)$
Polysilicon	$2.7\times10^{-6}\pm18\%$	162 ± 14	$-0.4\rightarrow0.3$	f(p,T)

Table 5.8: A list of $\sigma_{N_{max}}$ and $\sigma_{N_{max}} / S_{ut}$ for different thin film layers

	$\sigma_{N_{max}}$ (MPa)	$\sigma_{N_{max}} / S_{ut}$
SiO_2	343	< 0.3
Si_3N_4	265	~ 0.7
Pt/Ti	478	~ 2
Polysilicon	341	~0.08

Table 5.9: A list of linear equations constants and the average RMS of curve fitting

Equation	Material	a_o	a_1	RMS
5.12	Si_3N_4	1.21	-0.22	0.02
5.12	Pt/Ti	2.3	-1.27	0.04
5.14	Si_3N_4	1.51	-0.53	0.02
5.14	Pt/Ti	2.93	-1.90	0.05
5.16	Si_3N_4	1.43	-0.45	0.02
5.19	Pt/Ti	-0.15	1.15	0.001
5.19	Polysilicon	0.78	0.23	0.001
5.19	SiO_2	0.62	0.38	0.005
5.20	Si_3N_4	-0.68	1.7	0.05
5.20	SiO_2	-0.002	1.001	0.02
5.20	Pt/Ti	-0.005	1.002	0.01

Table 5.10: A list of polynomial equations constants and the average RMS of curve fitting

Equation	Material	b_o	b_1	b_2	b_3	b_4	RMS
5.13	SiO_2	-155.3	-660	-1019.5	690	-172.4	0.02
5.13	Polysilicon	-72.1	307.21	-470.81	314.5	-77.8	0.04
5.15	SiO_2	-162	674.1	-1020.4	674.9	-165	0.001
5.17	SiO_2	-199.2	833.6	-1247.7	852.7	-211.4	0.001
5.17	Polysilicon	-59.3	254.24	-386.8	255.1	-62.2	0.001
5.18	Si_3N_4	-46	192	-292.6	196.4	-48.7	0.002

Chapter 6

Reliability Analysis of RF MEMS Switches

This chapter presents the reliability analysis results of capacitive shunt RF MEMS switches. The substructured sequentially coupled multi-field model of capacitive RF MEMS switches, validated in Chapter 4, is used to study the switch performance, in response to variations within geometry, residual stresses and operational current frequency. The obtained results are then utilized to predict the onset of stiction and buckling with RF MEMS switches and its effect on these switches long term reliability. Section (6.1) presents a brief introduction to the RF MEMS switches technology and the reliability problems encountered during these switches operation. The outcomes of the reliability study for the capacitive shunt RF MEMS switches are presented in Section (6.2). The effects of the input power operational frequencies, the mean and the gradient residual stresses generated during microfabrication, are presented for flat RF switches in Sections (6.2.1) and (6.2.2), respectively. Some mechanical approaches, such as the utilization of corrugated switch membranes and through holes in the switch membrane are discussed in Section (6.2.3). Finally, some concluding remarks on the reliability analysis results are presented in Section (6.3).

6.1 Problem Definition – RF MEMS Switches

Radio Frequency (RF) Micro-Electro-Mechanical Systems (MEMS) capacitive shunt switches have demonstrated an enormous impact on the applications of wireless communication systems and satellite technology. These switches raise the performance of communication systems to a significant level over its solid-state counterpart such as Field Effect Transistors (FETs) and P-Type Intrinsic N-type (PIN) diodes. The prime reasons that these RF switches are currently under immense consideration includes, their wider capacity frequency range (from RF to mm-wave signal), lower power consumption, lower insertion loss, and lack of inter-modulation distortion, Peroulis *et al.* (2004), Rebeiz (2003), Goldsmith *et al.* (2001), Goldsmith *et al.* (1998). The reliability of these switches are reported to sustain up to 0.1-40 billion cycles, while only handling power with maximum capacity of 0.5 W, Jensen *et al.* (2003), Rizk *et al.* (2002), Thiel *et al.* (2002). The major failure modes of RF MEMS switches are shown to occur due to membrane stiction, buckling, and creep, Jensen *et al.* (2003).

The operation of RF MEMS switches requires an electrostatic force in order to actuate from the up, or "off" position, into the down, or "on" position. The voltage required to actuate the RF MEMS switch in this manner is referred to as the pull-in voltage. This voltage is dictated by the geometry and stiffness of the RF MEMS switch. A higher pull-in voltage will decrease the overall lifespan of the RF MEMS switch, as shown by Goldsmith *et al.* (2001).

As in all micromachined MEMS devices, residual stresses develop in the manufacturing process. The residual stresses can be separated into two specific stresses, thermal and intrinsic stresses, Chen *et al.* (2002), Doerner and Mix (1998), Stadtmueller (1992). Thermal stresses are generated through differences in thermal expansion coefficients in adjacent materials in the manufacturing process. The generation of intrinsic stresses is far more complicated. Generally, intrinsic stresses involve any stress generated from excess vacancies, crystal dislocations, grain boundary interactions, or phase transformations, Chen *et al.* (2002), Stadtmueller (1992). Overall, the residual stresses generated in RF MEMS switches ultimately affect the general state of stress, and therefore, failure mechanisms of the MEMS device.

While loaded with high frequency alternating current, the RF MEMS switch undergoes an electron crowding phenomena, otherwise known as the skin effect, Jensen *et al.* (2003). Due to self-inductance, the electrons flowing through the switch will be crowded on the edges of the conductor, creating a localized area of high temperature near the edges of the RF switch. Therefore, severe compressive thermal stresses develop due to this localized heating, causing the switch to buckle upwards. Depending upon the magnitude and direction of the residual stresses, this localized heating could potentially cause the RF MEMS switch to fail under severe buckling with sufficient load.

The geometry of the RF MEMS switch greatly affects the power handling and

frequency loads that each switch can experience. In addition, the actuation voltage of RF MEMS switches is affected by the geometry of these switches; for example, a mechanically stiffer switch will require a larger pull-in voltage. Mechanical approaches such as the addition of corrugations and holes can be introduced to control the membrane stiffness of the RF MEMS switch, in order to attain a specific design pull-in voltage.

6.2 Reliability Study

Given the good accuracy exhibited by the coupled multi-field FE model, as shown in Chapter 4, the reliability of aluminum RF MEMS switches is examined in this Section. Two candidate mechanisms are studied, mainly stiction problem at higher pull-in voltages and failure due to buckling. First, the effect of the operational frequency in the range of 0.1-100 GHz is studied, for flat switch membranes. Next, the effect of mean and gradient residual stresses, generated during different stages of microfabrication is evaluated. Finally, corrugated switch membranes and through holes in the switch membrane are presented, as alternative mechanical solutions for the RF switch reliability problem. The variation of the pull-in voltage (V_{PI}) and critical buckling strain (ε_{cr}) with switch length (l_m) at different membrane thicknesses ($t_m = 0.5-3\mu m$), are shown in Fig (6.1) and Fig (6.2), respectively. The pull-in voltage was calculated for a flat aluminum membrane, at room temperature, in the absence of residual stresses. It can be seen that V_{PI} decreases with the increase in

l_m due to the reduction in the bending stiffness of the switch membrane, Pamidighantam *et al.* (2002). The same effect can also be noticed for ε_{cr}, which varies proportionally with $\left(t_m / l_m\right)^2$.

6.2.1 Effect of Operational Frequencies

The steady state temperature distribution along switch membrane length, at an input power of 0.75 W, is plotted in Fig (6.3), as a function of operational frequency. The maximum temperature occurs at the mid span of the beam. However, the maximum steady state temperature at 0.1 GHz (29.5 °C) is considerably lower than at 100 GHz (320 °C). The temperature rise induces compressive thermal stresses in the switch membrane, which increases the initial gap between the membrane and the bottom electrode. Therefore, a coupled structural-electrostatic analysis of the switch membrane shows that V_{PI} increases dramatically with the increase in ω, because of the change in the initial deformation state of the switch, as shown in Fig (6.4). Moreover, thermally induced compressive stresses cause the switch to buckle at $\omega \geq 10\,\text{GHz}$.

6.2.2 Effect of Residual Stresses

Residual stresses are inherently generated during various stages of microfabrication. A general uniaxial residual stress field can be approximated by, Peroulis *et al.* (2003).

$$\sigma_{res}(z) \simeq \sigma_M + \sigma_{Gr}(z), \quad g_o \leq z \leq g_o + t_m \tag{6.1}$$

where, σ_M, $\sigma_{Gr}(z)$ refer to the mean and gradient (intrinsic) residual stresses generated in the thin film during microfabrication, respectively. Typical values reported in the literature, indicate an experimental measurements in the range of 0 to over 100 MPa for σ_M and 5-30 MPa for $\sigma_{Gr}(z)$, Chen *et al.* (2002).

Uniaxial tensile mean residual stresses (50-100 MPa), were applied to the flat aluminum RF switch, to examine its effect on V_{PI} and average axial strain (ε). The pull-in voltage-frequency curves predicted by the multi-field coupled model are shown in Fig (6.5), at different values of σ_M, for flat RF switch membrane, with dimensions ($l_m = 600\mu m, W_m = 20\mu m, t_m = 3\mu m$). It can be seen that the applied residual stresses, increase the pull-in voltage by 20-40 percent. This increase can be explained by the increased stiffening of the beam with the increase in the value of the applied residual stress. However, as shown in Fig (6.6), the tensile residual stresses counteract the compressive thermal stresses induced at higher operational frequencies, as depicted by Equation (6.2). It can be seen that ε, can be shifted above the value of the critical buckling strain, which increases the power handling capability of the switch, to higher operational frequencies. So, in a sense, the microfabrication tensile residual stresses can be utilized to eliminate the buckling failure, but the stiction problem, due to charge build-up in the dielectric layer,

associated with higher actuation voltages, can still cause switch failure at a limited number of operational cycles.

$$\varepsilon = -\Delta\alpha \int_{T_r}^{T(x,z)} dT + \frac{\sigma_{res}(z)}{E_m} \tag{6.2}$$

The effect of applied microfabrication gradient residual stresses on the performance of the switch is shown in Fig (6.7) and Fig (6.8). Two profiles (A and B), reported in the literature, are examined here, Lishchynska *et al.* (2005), Chen *et al.* (2002). In these analyses, a 50 MPa mean residual stress was considered. Profiles A and B, shown in Fig (6.9), can be described by the following functions:

Profile A

$$\sigma_{Gr}(z) = \left(\frac{-4\sigma_G}{t_m^2}\right)z^2 + \frac{\sigma_G}{t_m}\left(\frac{8g_o}{t_m^2}+4\right)z - \frac{4\sigma_G g_o}{t_m}\left(\frac{g_o}{t_m}+1\right) \tag{6.3}$$
$$g_o \le z \le g_o + t_m$$

Profile B

$$\sigma_{Gr}(z) = \left(\frac{2\sigma_G}{t_m}\right)z - \sigma_G\left(\frac{2g_o}{t_m}+1\right) \tag{6.4}$$
$$g_o \le z \le g_o + t_m$$

It can be seen that RF switches exhibiting profile A, requires higher pull-in voltages for actuation. However, a higher range of operational frequencies can be achieved with profile A, without buckling. In general, the effect of the applied gradient residual stresses is not as important as the effect of the mean residual stress, because of the

fixed-fixed switch configuration, considered in the current study. However, as reported in the literature, the effect of gradient residual stress is more dramatic in the case of fixed-free (cantilever) switch configurations.

6.2.3 Mechanical Approaches

As discussed in Section (6.2.2), a proper control of tensile residual stresses, generated during microfabrication, can be utilized to increase the power handling capabilities of RF MEMS switches. However, the higher actuation voltages exhibited; because of membrane stiffening is still a major problem. Therefore, to achieve reliable switch designs, much lower actuation voltages should be achieved. Three strategies have been proposed in literature to achieve this goal. The first one consists in modifying the out-of-plane geometry of the switch membrane, Zhu and Espinosa (2004). The second strategy consists in the use of corrugated switch membranes, Zhu and Espinosa (2004). The third strategy consists in the addition of holes to reduce the membrane effective Young's modulus, Peroulis *et al.* (2003). The second and third strategies are more achievable in microfabrication, Zhu and Espinosa (2004) ; hence, the combination of both strategies in RF MEMS switch design is examined in this Section, for an RF MEMS switch with dimensions ($l_m = 600\mu m, W_m = 20\mu m, t_m = 3\mu m$).

First, the effect of number of corrugations (N_C) and corrugation thickness (t_C), expressed by corrugation thickness ratio (t_C / t_m), was investigated. The pull-in

voltage versus N_C is shown in Fig (6.10). This analysis was conducted for σ_M range from 50-100 MPa, $t_C / t_m = 0.16$ and $\omega = 30\,\text{GHz}$. It can be seen that a 20-25 percent reduction in V_{PI}, was achieved with $N_C = 24$. The pull-in voltage versus t_C / t_m is shown in Fig (6.11). This analysis was conducted for σ_M range from 50-100 MPa, $N_C = 24$ and $\omega = 30\,\text{GHz}$. It can be seen that proper selection of t_C can dramatically reduce V_{PI}, up to 65 percent, at the studied range of microfabrication residual stresses. The average axial strain was also examined for RF switch ($N_C = 24, t_C / t_m = 0.5$), at range from 10-100 GHz, as shown in Fig (6.12). It can be seen that for $\sigma_M = 50\,\text{MPa}$, the buckling failure occurs at $\omega \simeq 50\,\text{GHz}$, while for $\sigma_M = 100$ MPa, the power handling capability of the RF switch can be increased beyond 100 GHz.

A very promising design is the addition of through holes in to corrugated switch membranes, Rebiez (2003). The holes total area can be up to 60 percent of the total surface area of the switch structure. The perforation pattern is mainly characterized by the ligament efficiency, $\mu_H = l_H / pitch$, defined as the ratio of the remaining link width to pattern pitch, as shown in Fig (6.13). The holes release part of the residual stresses in the membrane, and reduce the effective Young's modulus of the switch membrane. The reduction of the effective Young's modulus, yields lower values of actuation voltages. Moreover, this reduction increases the positive residual axial strain component, which counteracts the compressive strains generated at higher frequencies due to the skin effect. Therefore, the power handling capability of the RF

switch can be increased without buckling, while still at reliable ranges of actuation voltages. Fig (6.14) shows the average axial strain versus an operational frequency range 30-200 GHz. This analysis was conducted for μ_H range from 0.4-0.8, $\sigma_M = 100\,\text{MPa}$, $N_C = 24$ and $t_C / t_m = 0.5$. It can be seen that a higher operational frequency range is achievable for corrugated switch designs with holes ($\omega > 200\,\text{GHz}, \mu_H = 0.4$), compared to $\omega \simeq 100\,\text{GHz}$, for only corrugated switch design.

6.3 Concluding Remarks

The commercialization of RF MEMS switches is subject to the elimination of stiction problem, associated with higher actuation voltages and buckling failure at high RF power. In this chapter, a coupled multi-field model was utilized to examine the performance of RF MEMS switches at an operational frequency range 0.1-100GHz. The effect of microfabrication residual stresses and effectiveness of some mechanical approaches has been examined in detail. The coupled model, proposed in this chapter, represents the first effort to link an actual temperature distribution, associated with higher operational frequencies, to a coupled structural-electrostatic analysis of RF MEMS switches. Other studies reported in the literature, assume a uniform temperature distribution in the switch membrane, which might generate inaccurate predictions of the actual pull-in voltages. The main conclusions from the reliability analyses conducted in this case are summarized as follows:

(i) The temperature rise at higher operational frequencies induces compressive stresses in the switch membrane of flat RF MEMS switches. The induced compressive stresses lead to buckling and device failure for $\omega \geq 10\,\mathrm{GHz}$. Moreover, the change in the deformation state of the switch leads to a dramatic increase in the required actuation voltages.

(ii) In-plane tensile residual stresses generated during microfabrication counteract the induced compressive thermal stresses. In this sense, proper control of microfabrication residual stresses can increase the power carrying capacity of the RF switch. However, higher values of actuation voltages are exhibited because of the membrane stiffening effect.

(iii) Membrane corrugations, at a distance from the support area can be used to maintain the actuation voltages with in lower values. Therefore, using these membranes in conjunction with a proper control of microfabrication residual stresses, increase the reliable range of operation of the RF switch.

(iv) A better design can be achieved by introducing holes to corrugated switch membranes. These holes help in reducing the effective Young's modulus of the switch membrane. This mainly would yield lower actuation voltages. Moreover, this reduction increases the positive residual axial strain

component, which counteracts the compressive strains generated at higher frequencies. Therefore, the power handling capability of the RF switch can be increased considerably, without buckling, while maintaining a suitable actuation voltage. Analysis of corrugated switch membranes, with holes at a ligament efficiency of 0.4, shows that this design can increase the reliable operation of the RF switch to $\omega > 200\,\text{GHz}$.

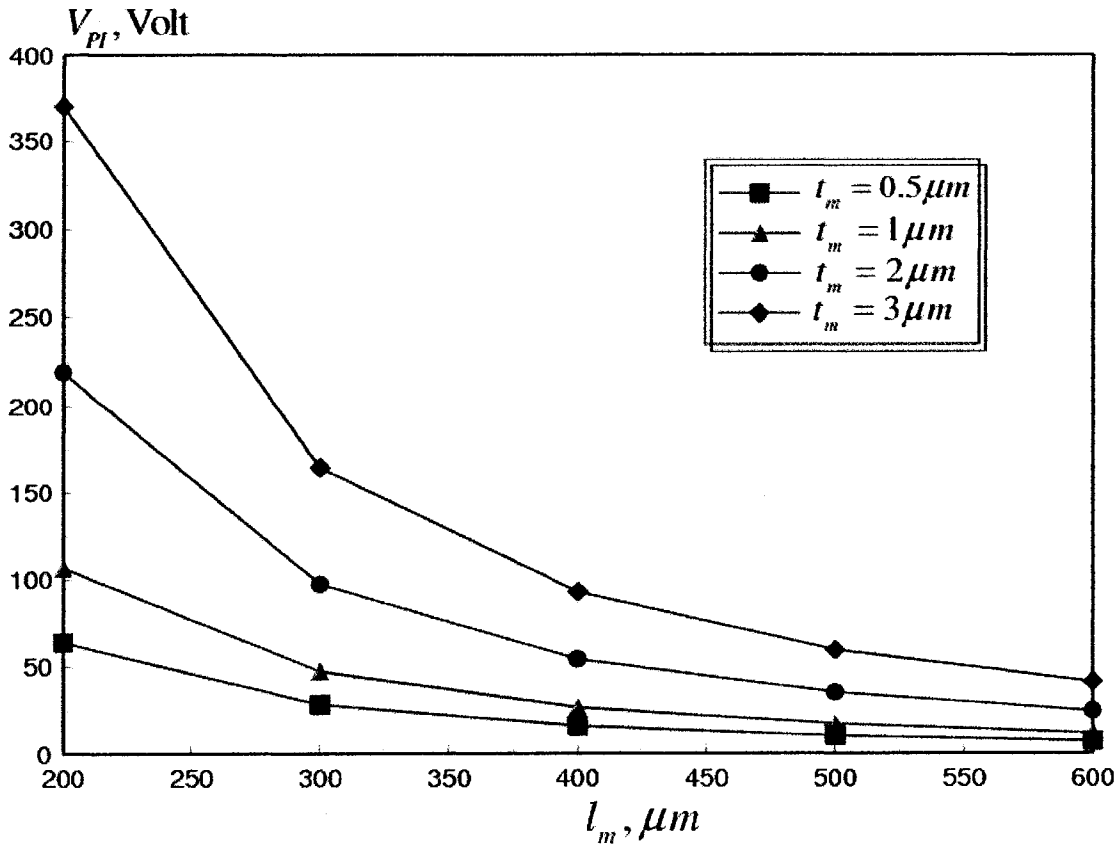

Figure 6.1: Pull-in-voltage versus membrane length at different membrane thickness of flat aluminum RF MEMS switch ($\sigma_M = \sigma_G = 0\,\text{MPa}, W_m = 20\mu m, T(x) = T_r$)

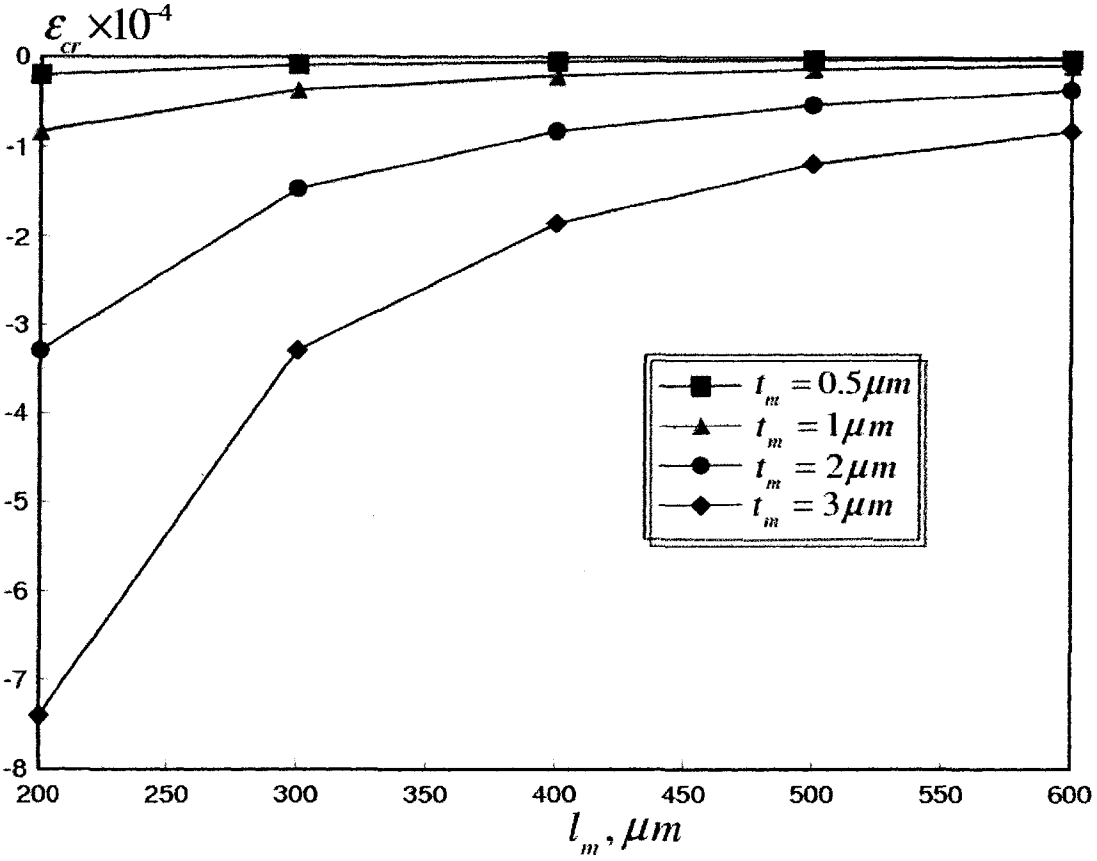

Figure 6.2: Critical buckling strain versus membrane length at different membrane thickness of flat aluminum RF MEMS switch

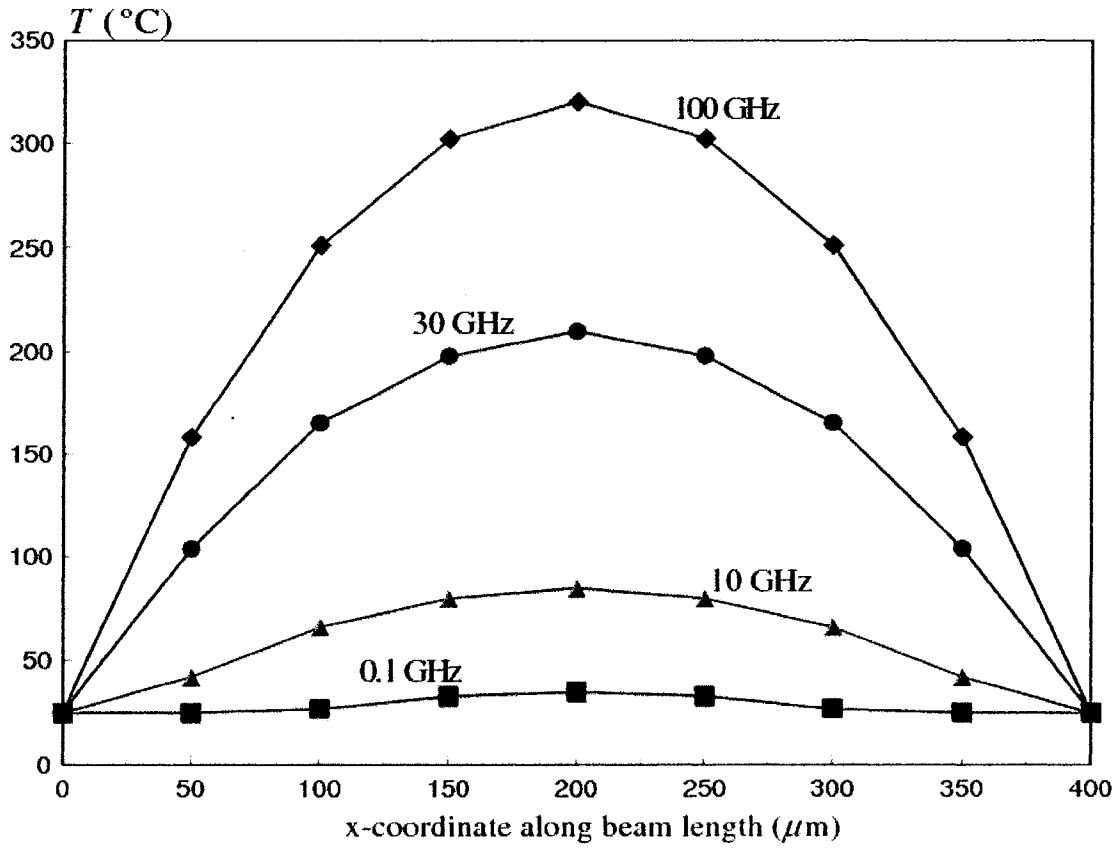

Figure 6.3: Temperature distribution along membrane length of flat aluminum RF MEMS switch at an operating frequency range of 0.1-100 GHz ($l_m = 400\mu m, W_m = 20\mu m$, $t_m = 3\mu m$, P=0.75W)

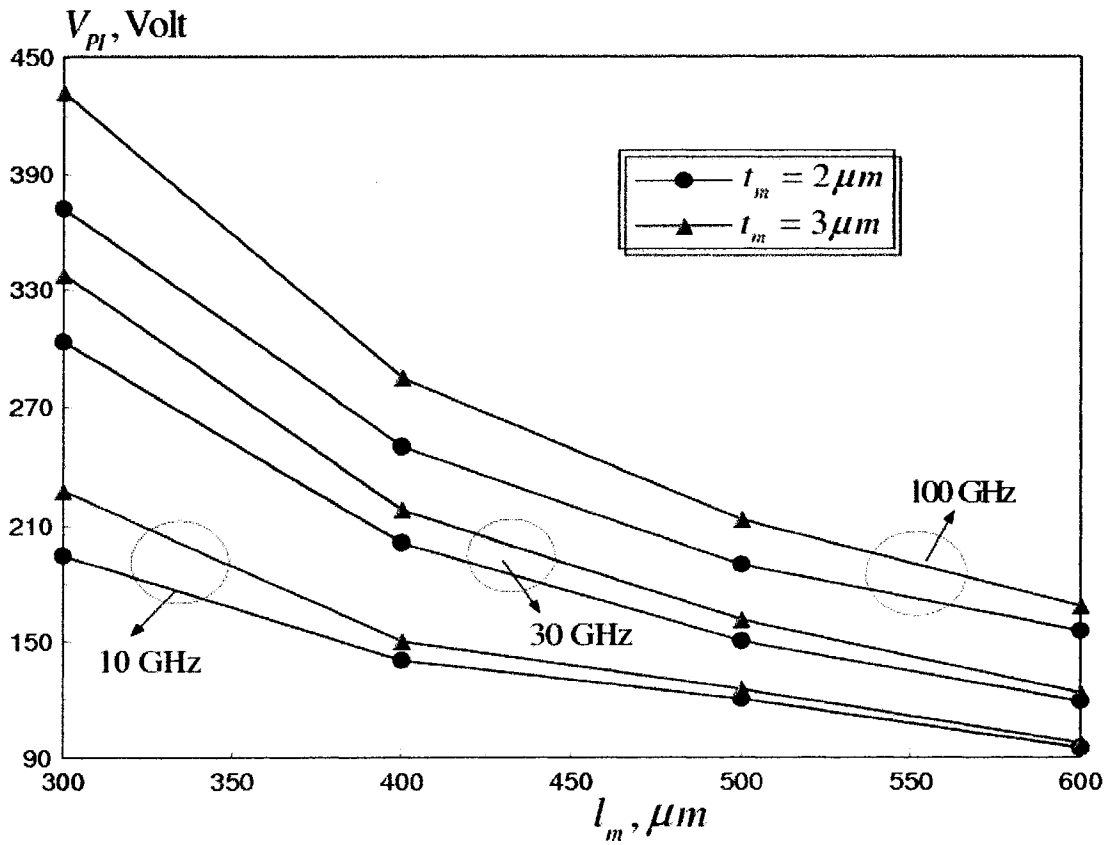

Figure 6.4: Pull-in voltage versus membrane length of flat aluminum RF MEMS switch at operating frequencies of 10, 30 and100 GHz ($W_m = 20\mu m$, $t_m = 2 \text{and} 3\mu m$)

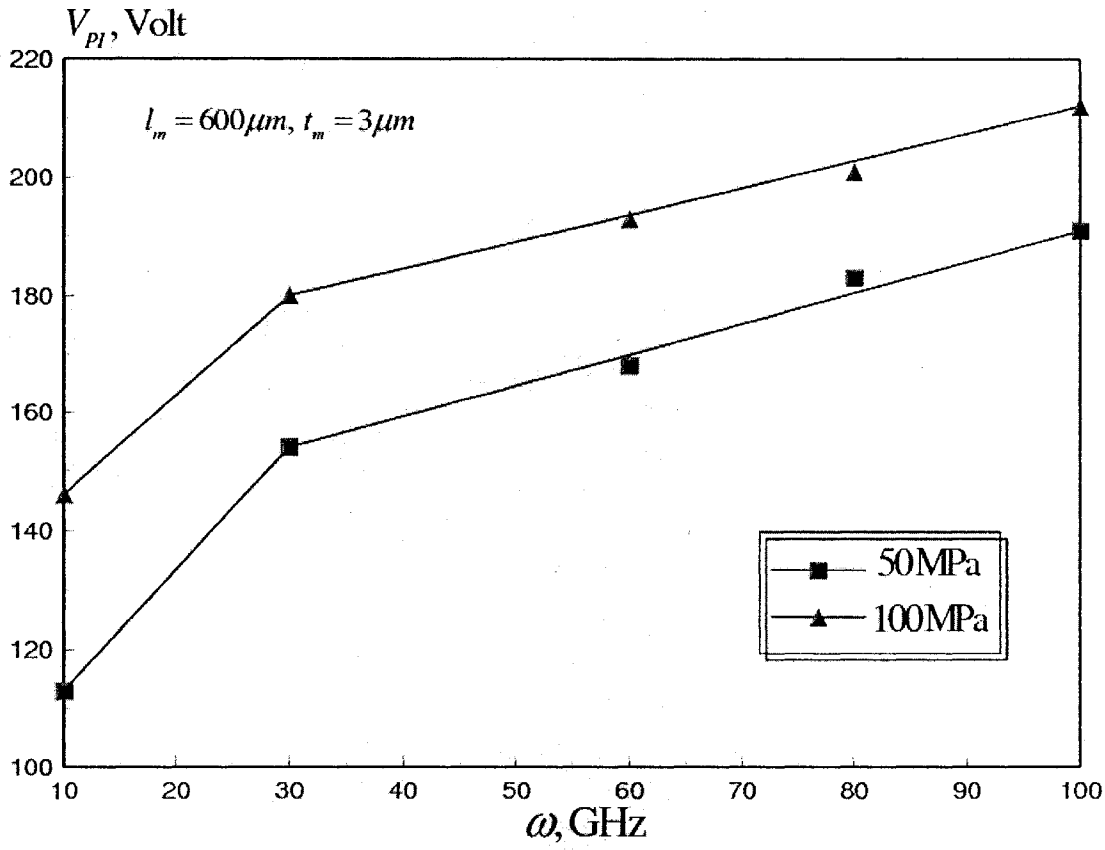

Figure 6.5: Effect of microfabrication mean residual stresses on V_{PI} of flat aluminum RF MEMS switch at operating frequency range of 10-100 GHz ($l_m = 600\mu m$, $W_m = 20\mu m$, $t_m = 3\,\mu m$)

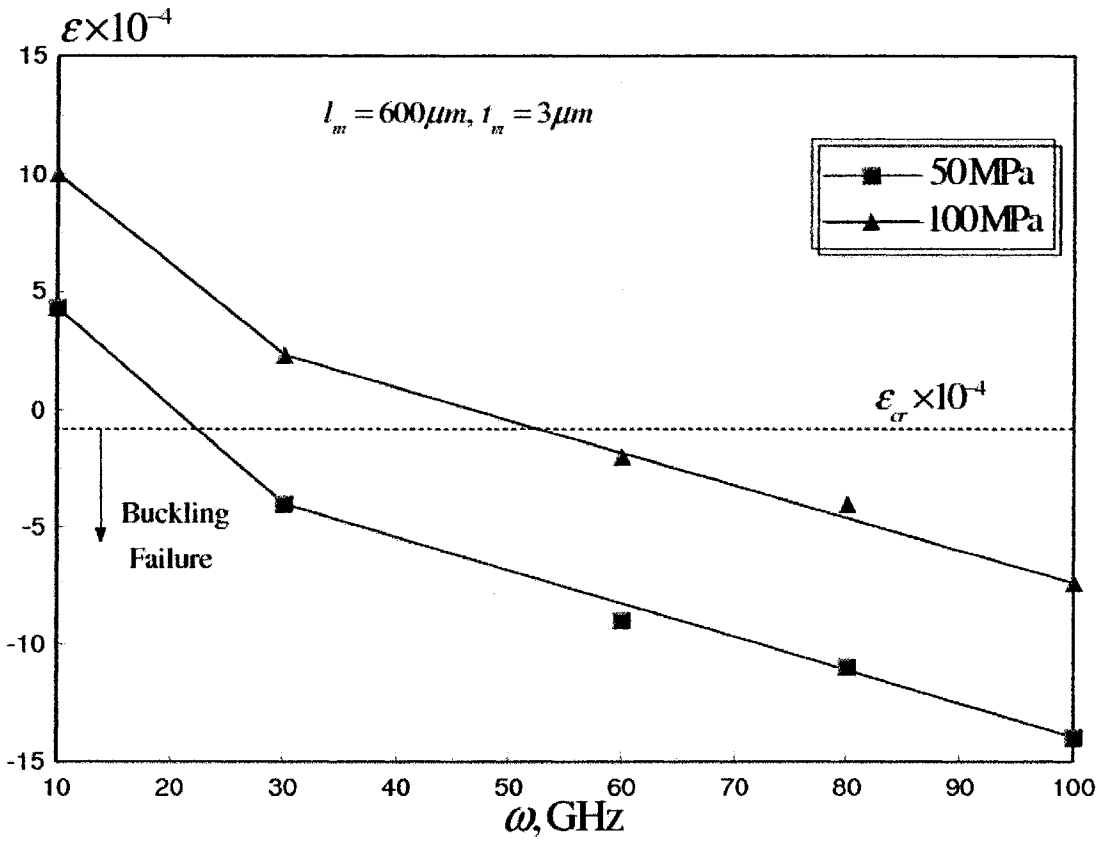

Figure 6.6: Effect of microfabrication mean residual stresses on ε of flat aluminum RF MEMS switch at operating frequency range of 10-100 GHz ($l_m = 600\mu m$, $W_m = 20\mu m$, $t_m = 3\mu m$)

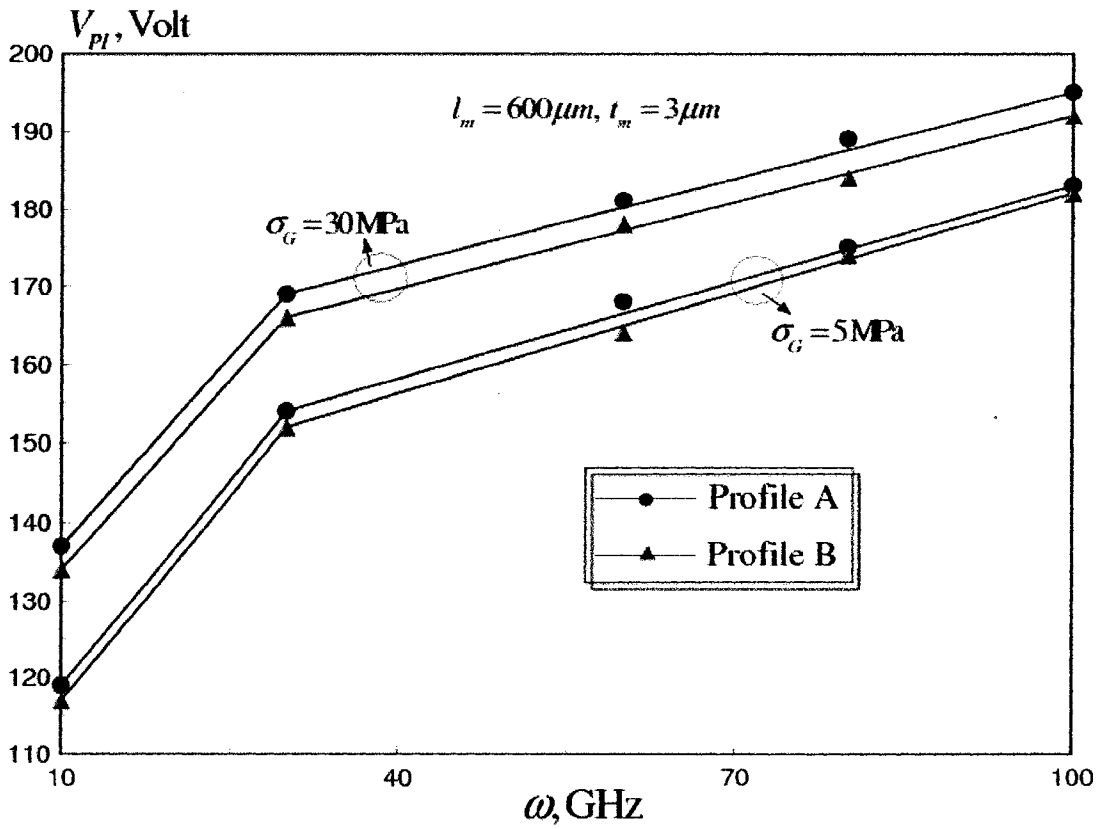

Figure 6.7: Effect of microfabrication gradient residual stresses on V_{PI} of flat aluminum RF MEMS switch at operating frequency range of 10-100 GHz ($l_m = 600\mu m$, $W_m = 20\mu m$, $t_m = 3\,\mu m$)

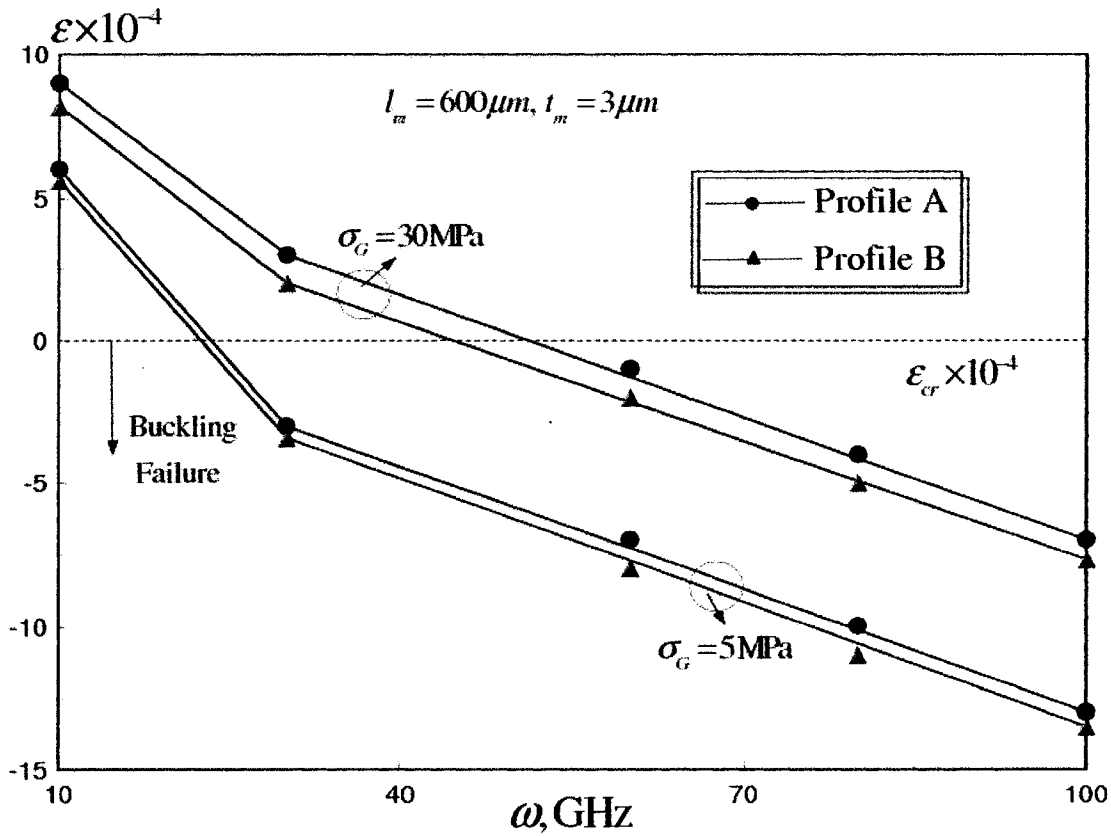

Figure 6.8: Effect of microfabrication gradient residual stresses on ε of flat aluminum RF MEMS switch at operating frequency range of 10-100 GHz ($l_m = 600\mu m$, $W_m = 20\mu m$, $t_m = 3\,\mu m$)

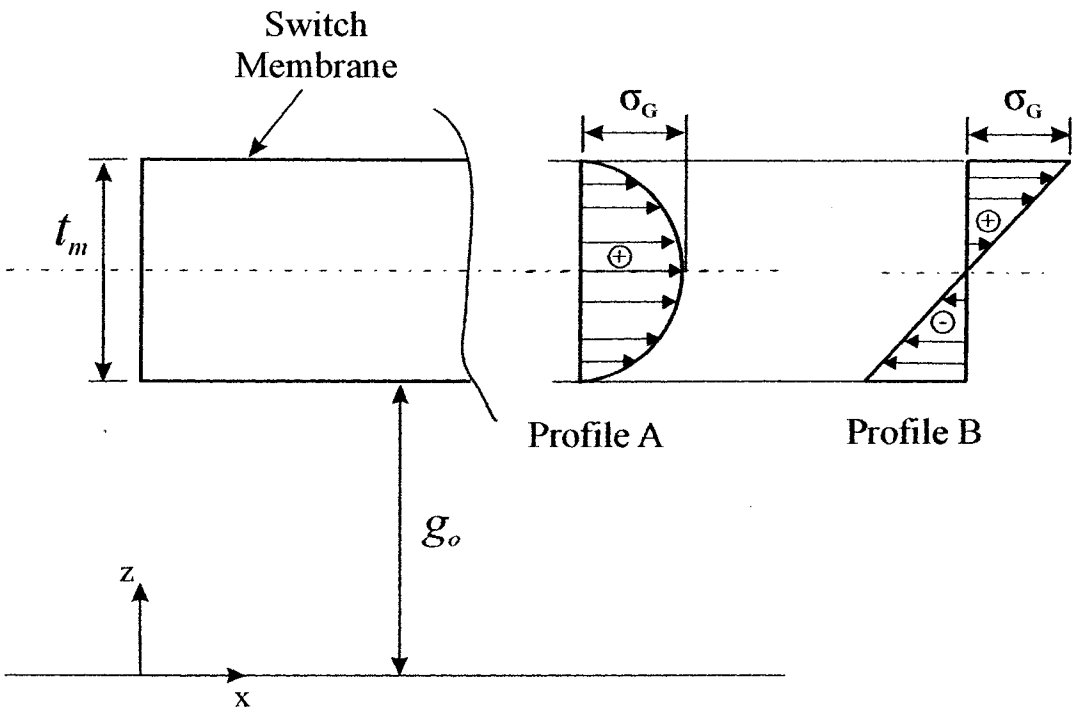

Figure 6.9: Profiles of applied gradient residual stresses

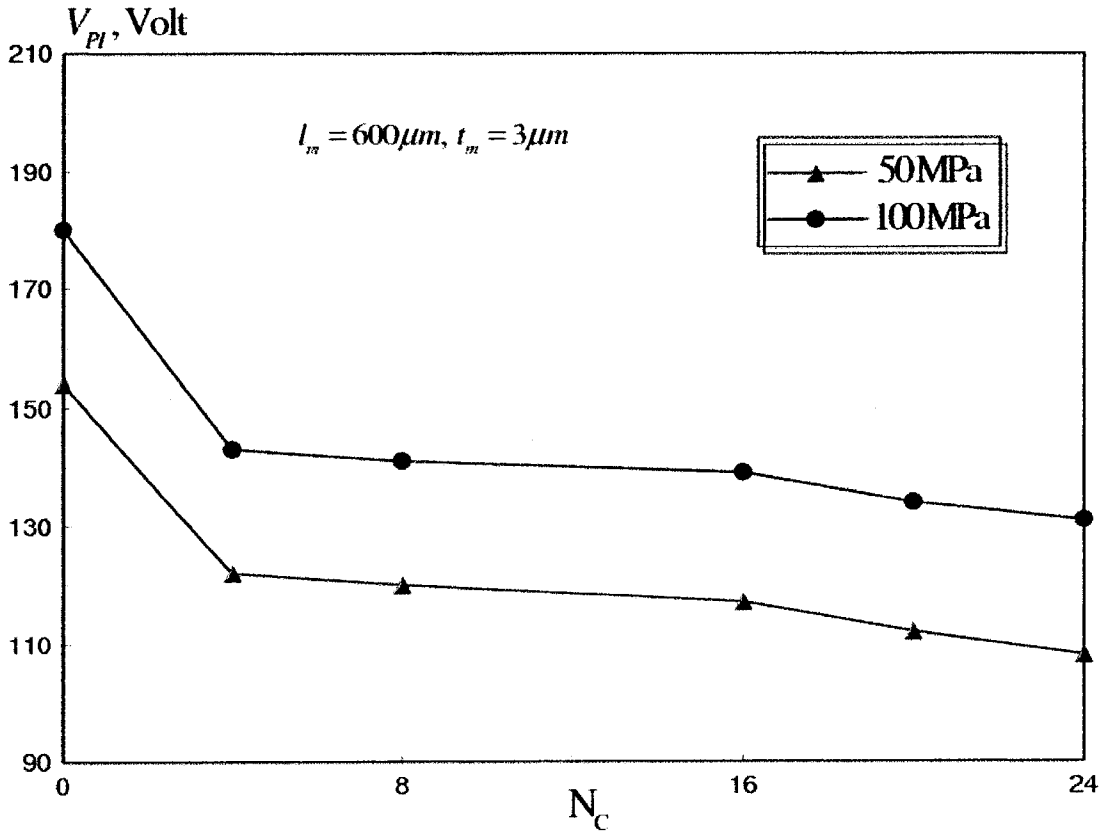

Figure 6.10: Effect of number of corrugations on V_{PI} of corrugated aluminum RF MEMS switch at σ_M range of 50-100 MPa ($l_m = 600\mu m, W_m = 20\mu m, t_m = 3\mu m, t_C / t_m = 0.16, \omega = 30\,\text{GHz}$)

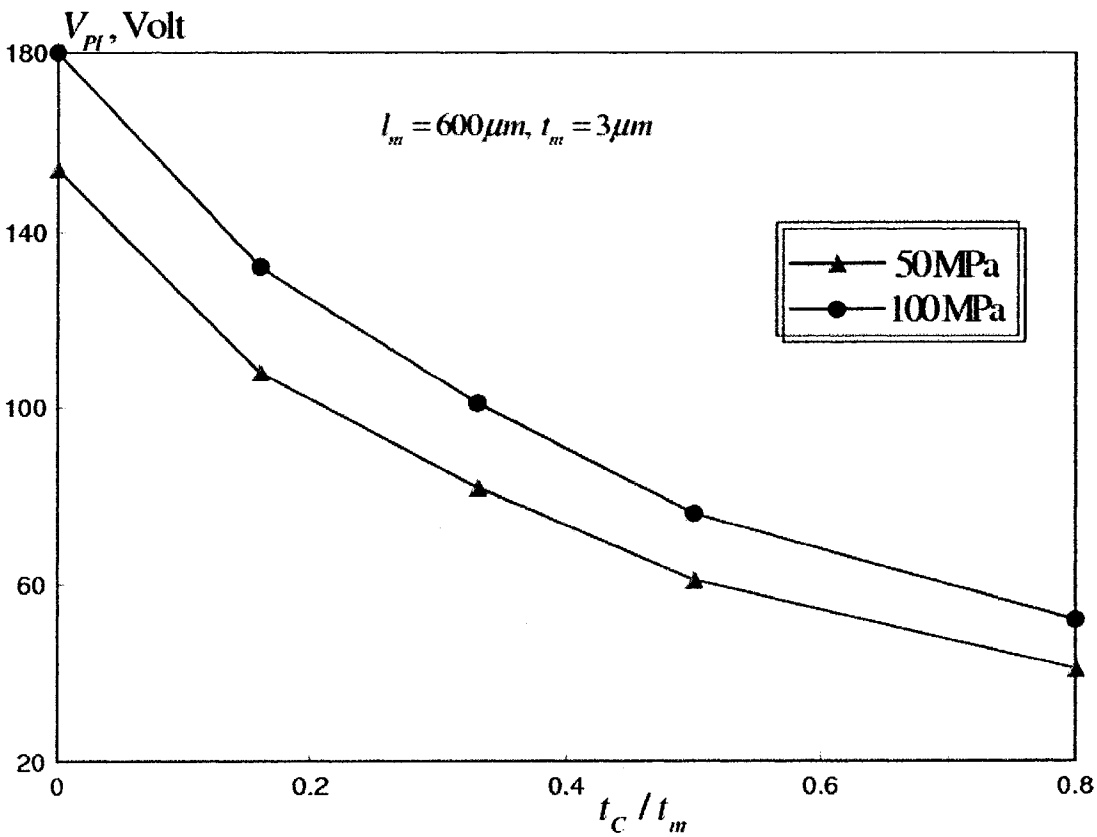

Figure 6.11: Effect of corrugation thickness ratio on V_{PI} of corrugated aluminum RF MEMS switch at σ_M range of 50-100 MPa ($l_m = 600\mu m$, $W_m = 20\mu m$, $t_m = 3\mu m$, $N_C = 24$, $\omega = 30$ GHz)

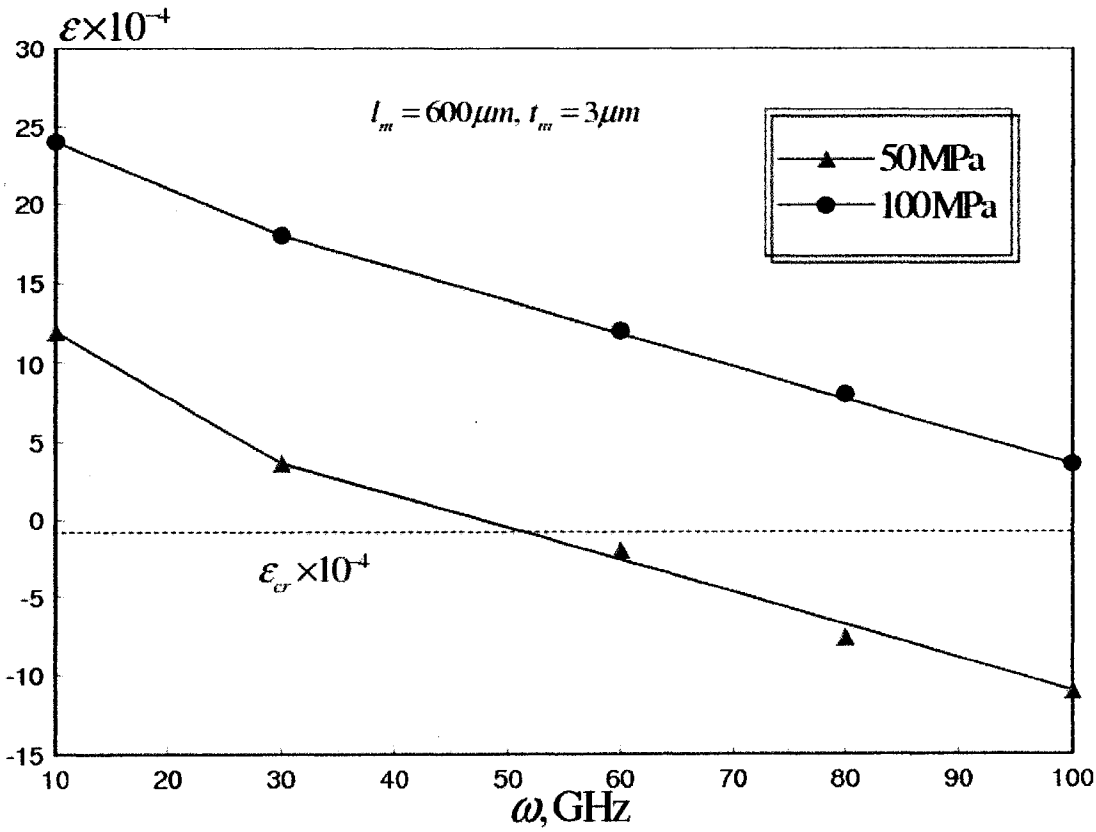

Figure 6.12: Average axial strain versus ω of corrugated aluminum RF MEMS switch at σ_M range of 50-100 MPa ($N_C = 24$, $t_C / t_m = 0.5$)

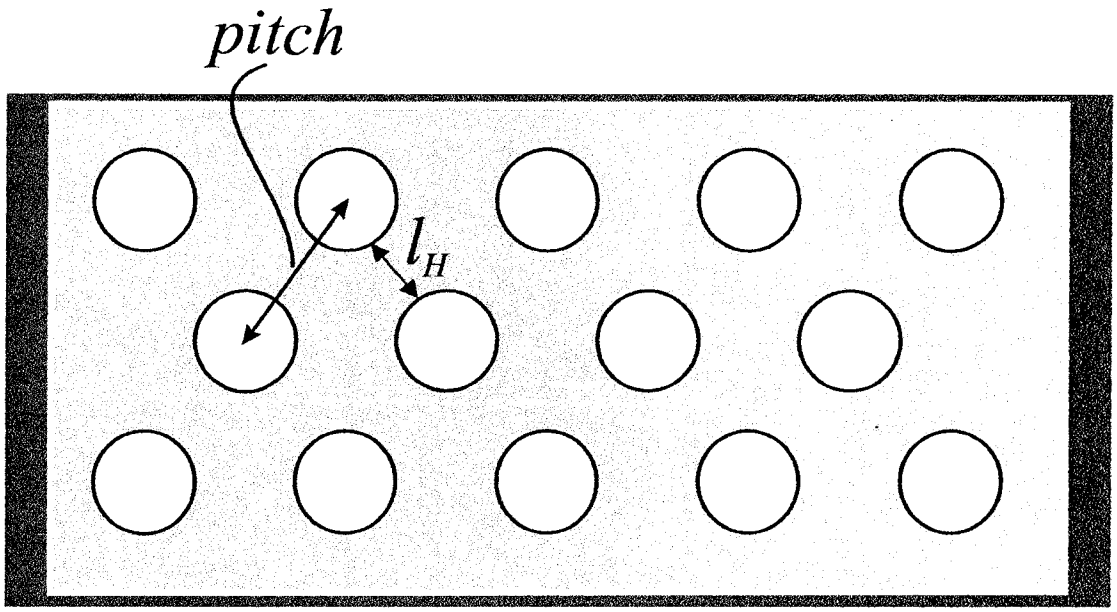

Figure 6.13: Parameters for the ligament efficiency in RF MEMS switch membrane with through holes

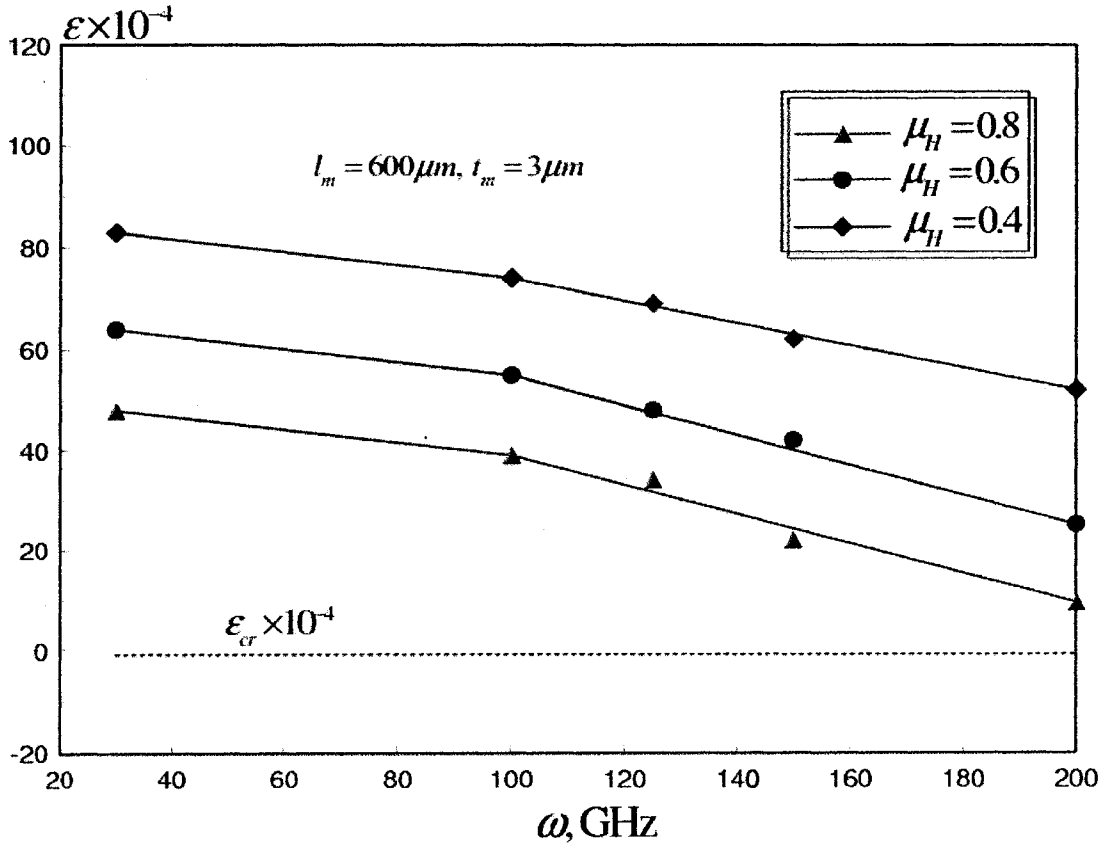

Figure 6.14: Effect of ligament ratio (μ_H) on average axial strain of corrugated aluminum RF MEMS switch at ω range of 30-200 GHz ($\sigma_M = 100\,\text{MPa}$, $N_C = 24$, $t_C / t_m = 0.5$)

Chapter 7

Conclusions and Recommendations for Future Work

7.1 Conclusions

The application of the substructuring technique to solve sequentially coupled multiphysics FE problems, emerging in the design and development cycle of MEMS has been investigated. The proposed substructuring methodology has been validated in several cases involving single physics, one-way and two-way sequentially coupled multiphysics FE analysis. The computational performance of the developed methodology has been compared with those of other computational saving techniques, utilized in previous studies, such as adaptive substructuring, and traditional manual-substructuring. The developed automated substructuring methodology was then utilized to conduct reliability studies of microheater-based MEMS gas sensors and RF MEMS switches.

To meet the objective of this thesis, an automated substructuring framework, written in MATLAB code, was developed to reduce the overhead cost involved in the preprocessing and processing stages of the substructuring, because of the extensive manual user interaction involved in the whole process. The backbone of the

developed automated substructuring framework is a novel algorithm referred to as the Major Vector. In this algorithm, the substructuring is treated as a graph partitioning problem, where, spectral techniques are utilized to automatically isolate the linear regions from a graphical representation of the FE mesh; and to automatically assess/modify the substructures aspect ratio. Moreover, a procedure was developed to map the load vectors between the overlapping substructures of the interacting physical domains and to systematically check the linearity state and update the generated substructures during loading within the analysis of each physical field.

The validation of the developed framework using various test cases involving single and multiphysics coupling shows a good agreement between the results from the substructured models and those obtained from studies, previously reported in the literature. On the structural analysis of axisymmetric pressure vessel case, a higher speed factor of 3.18 was achieved, compared to 1.07 speed factor achieved with the adaptive substructuring technique used by Han (1984). Also, in the structural analysis of the tension plates, a higher speed factor of 2.82 was achieved with the Major Vector algorithm compared to 2.01 speed factor with the adaptive substructuring algorithm used by Han (1984).

The computational performance of the developed Major Vector algorithm on multiphysics analysis test cases indicated that considerable reduction in the overhead time of the linear region isolation phase can be achieved compared to the traditional manual-substructuring technique. This result was shown based on the higher isolation

speed factors that can range from 19-37, when using the Major Vector algorithm. Moreover, better solution accuracy is achieved with the Major Vector algorithm compared to the traditional manual-substructuring technique, because of the elimination of the human error factor in the linear regions isolation phase. In addition, the Major Vector algorithm provides more flexibility to the FE analyst in using different approaches to analyze coupled multiphysics problems.

The analysis of the effect of other computational performance parameters indicated that the aspect ratio threshold value (r) is inversely proportional to the number of generated substructures (N_s) because the partitioning of the substructures is ramped up to achieve the required AR constraint, which also results in an increase in N_B. The solution error exhibited using larger (r) values is less significant when compared to the reduction in the total computational cost of the coupled-field FE analysis. This result was evident in the MEMS gas sensor case study, where increasing (r) values from 1 to 10 will defer the solution accuracy by an average of 2.31 percent; while an additional 8 percent reduction in the computational cost was achieved by increasing (r) from 1 to 10.

The results presented in the coupled structural-electrostatic FE analysis of the capacitive shunt RF MEMS switch indicate that substructuring does not improve the efficiency of FE problems that involve geometric nonlinearities. In this problem a speed factor close to one was achieved. Therefore utilizing different approaches, such

as FE meshless techniques might be more adequate in analyzing these types of problems more efficiently.

For the reliability study performed on the microheater-based MEMS gas sensor, the uncertainties generated in the microfabrication stage, with respect to some of the design parameters, were found to have considerable potential in altering the performance of the device. This underline the fact that the current lack in the characterization of thin films material properties can be a great source of uncertainty in MEMS reliability, which is emphasized in this study. Therefore, finding appropriate means of materials testing and setting strict controls on monitoring the micromachining process; in a way that would achieve a better characterization of material properties; and thus provide a better control over the geometrical parameters of thin films is strongly recommended.

The results of the reliability study of the RF MEMS switches indicate that the temperature rise at higher operational frequencies induces compressive stresses, which leads to buckling failure at $\omega \geq 10\,\text{GHz}$. In-plane tensile residual stresses generated during microfabrication were found to counteract these compressive stresses. In this sense, proper control of microfabrication residual stresses can increase the power carrying capacity of the RF switch. However, higher values of actuation voltages are exhibited because of the membrane stiffening effect.

Design modifications in the RF MEMS switch such as corrugations, at a distance from the support area can be used to maintain the actuation voltages at reasonable

values. Therefore, using these membranes in conjunction with a proper control of the microfabrication residual stresses, increase the reliable range of operation of the RF switch at higher operational frequencies. In addition, a better design can be achieved by introducing holes to corrugated switch membranes. These holes are proven to reduce the effective Young's modulus of the switch membrane. This mainly would yield lower actuation voltages. Moreover, this reduction increases the positive residual axial strain component, which counteracts the compressive strains generated at higher frequencies. Therefore, the power handling capability of the RF switch can be increased considerably, without buckling, while maintaining a suitable actuation voltage.

7.2 Achievements and Contributions

The achievements and contributions of this thesis toward the improvement on the use of the substructuring technique to solve sequentially coupled multiphysics FE problems, with the main focus on its application in MEMS design and development are summarized as follows:

(i) The development of an automated substructuring framework, using a MATLAB © written code, to automate the substructuring tasks at the preprocessing and processing stages.

(ii) At the preprocessing stage of the substructuring process, the overhead cost of the linear regions isolation phase and the substructures (*AR*) assessment/modification has been reduced considerably by eliminating the extensive manual user interaction previously involved in the substructuring process.

(iii) The developed Major Vector algorithm was used as a part of a procedure to check the linearity state of the substructures during loading and update these substructures once the nonlinearity expands to the locations of these substructures.

(iv) The work presented in the current research presents the first effort to treat the substructuring as a graph partitioning problem.

(v) The generic nature and the flexibility of the developed framework present a significant contribution to the substructuring of coupled-field problems. Since it mainly deals with a graphical representation of the FE mesh, therefore, various cases of coupled multiphysics problems can be analyzed.

(vi) The developed automated substructuring framework has been successfully implemented to reduce the computational cost of various cases involving one-way and two-way sequentially coupled multiphysics FE analysis for MEMS.

(vii) The developed automated substructuring framework was utilized to study the reliability of microheater-based MEMS gas sensors and RF MEMS switches.

7.3 Recommendations for Future Work

Finally, some suggestions for future work in the development of the automated substructuring framework and its possible applications in new areas are perhaps in order. They are as follows:

(i) The proposed substructuring framework can be extended to include an algorithm that implements the constrained substructuring technique. This would mainly contribute to a further reduction in the interface size problem of the generated substructures and improve on the efficiency of analyzing multiphysics problems.

(ii) The proposed substructuring framework can be extended to include an algorithm that couples the master nodes of neighboring substructures. This would reduce the number of parametric analysis runs that requires an

update of the previously generated substructures, especially if the parametric study includes variations in geometric parameters. However this is not applicable for parametric analysis runs that deal with variations in material property characteristics.

(iii) The work presented in the current research is focused on solving multiphysics problems on single processors. However, the developed substructuring framework can be easily extended to be applied in conjunction with Domain Decomposition (DD) techniques to solve the sub-domains distributed at each processor.

Bibliography

Al-Nasra M., Nguyen D. T., 1991, "An Algorithm for Domain Decomposition in Finite Element Analysis," Computers & Structures, Vol. 39, pp. 277-289.

ANSYS v10.1, 2005, "Coupled Field Analysis Guide, User's Manual," Analysis Systems, Inc., Houston, Pa.

Belendez T., Neipp C., Belendez A., 2002, "Large and Small Deflections of a Cantilever Beam," European Journal of Physics, Vol. 23, pp. 371-379.

Branger V., Pelosin V., Badawi K.F., Goudeau P., 1996, "Study of Mechanical and Microstructural State of Platinum Thin Films," Thin solid Films, Vol. 275, pp. 22-24.

Brotzen F. R., Loos P. J., Brady D. P., 1992, "Thermal Conductivity of Thin SiO_2 Films," Thin Solid Films, Vol. 207, pp. 197-201.

Brown K.B., 2003, "Optical Detection of Gases and Vacuum with CMOS Microstructures, Ph.D. Thesis, University of Alberta, Edmonton, Canada

Bustillo, J., Howe, R. T. and Muller, R. S., 1998, "Surface Micromachining for MEMS," Proceedings of IEEE, Vol. 86, pp. 1552-1574.

Callard S., Tallarida G., Borghesi A., Zanotti L., 1999, "Thermal Conductivity of SiO_2 Films by Scanning Thermal Microscopy," Journal of Non-Crystalline Solids, Vol. 245, pp. 203-209.

Chang K., 1994, "Microwave solid-state circuits and applications," Wiley-Interscience, New York, USA.

Chaung W.H., Luger T., Fettig R.K., Ghodssi R., 2004, "Mechanical Property Characterization of LPCVD Silicon Nitride Thin Films at Cryogenic Temperatures," Journal of Microelectromechanical Systems, Vol. 13, pp. 870-879.

Chen S., Baughn T.V., Yao Z. J., Goldsmith C. L., 2002, "A New In Situ Residual Stress Measurement Method for a MEMS Thin Fixed-Fixed Beam Structure," Journal of Microelectromechanical Systems, Vol. 11, pp. 309-316.

Denhoff M.W., 2003, "A Measurement of Young's Modulus and Residual Stress in MEMS Bridges using a Surface Profiler," Journal of Micromechanics and Microengineering, pp. 686-692.

Deo N., 1974, "Graph Theory with Applications to Engineering and Computer Science," Prentice-Hall, New York, USA

Dinno K. S., Gill S. S., 1965 "An Experimental Investigation into the Plastic Behavior of Flush Nozzles in Spherical Pressure Vessels," International Journal of Mechanical Science, Vol. 7, pp. 817-839.

Dodds R.H., 1980, "Substructuring in Linear and Non-Linear Analysis," International Journal for Numerical Methods in Engineering, Vol. 15, pp. 583-597.

Doerner M., Nix W., 1998, "Stresses and Deformation Processes in Thin Films on Substrates" CRC Circuit. Rev. Solid States Material Science, Vol. 14, pp. 225-268.

Escaig Y., Martin P., 1999, "Examples of Domain Decomposition Methods to Solve Non-Linear Problems Sequentially," Advanced Engineering Software, Vol. 30, pp. 847-855.

Farhat C., 1988, "A Simple and Efficient Automatic FEM Domain Decomposer," Computers & Structures, Vol. 5, pp. 579-602.

Farhat C., Lesoinne M., 1991, "Automatic Partitioning of Unstructured Meshes for the Parallel Solution of Problems in Computational Mechanics," International Journal for Numerical Methods in Engineering, Vol. 36, pp. 745-764.

Feynman, R. P., 1992, "There's Plenty of Room at the Bottom," Journal of Microelectromechanical systems, Vol. 1, pp 60-66.

Firebaugh S. L., Jensen K.F., and Schmidt M.A., 1998, "Investigation of High-Temperature Degradation of Platinum Thin Films with an *In Situ* Resistance Measurement Apparatus," Journal of Microelectromechanical Systems, Vol.7, pp. 128-135.

Gad El Hak, M., 2001, "The MEMS Handbook," CRC Press, Boca Raton, USA

Giridharan, M. G., Stout, P., Yang, H. Q., Athavale, M., Dionne, P. and Przekwas, A., 2001, "Multi-Disciplinary CAD System for MEMS," Journal of Modeling and Simulation of Microsystems, Vol. 2, pp. 43-50.

Goldsmith C., Ehmke J., Malczewski A., Pillans B., Eshelman S., Yao Z., Brank J., Eberly M., 2001, "Lifetime characterization of capacitive RF MEMS switches," IEEE International Micorwave Symposium, Vol. 1.

Goldsmith C. L., Yao Z. M., Eshelman S., Denniston D., 1998, "Performance of Low-Loss RF MEMS Capacitive Switches," IEEE Microwave and Guided Wave Letters, Vol. 8, pp. 269-271.

Haemers W.H., 1980, "Eigenvalue Techniques in Design and Graph Theory," Mathematisch Centrum, Amsterdam, Holland.

Han T.Y., Abel J.F., 1985, "Adaptive Substructuring Techniques in Elasto-Plastic Finite Element Analysis," Computers & Structures, Vol. 20, pp. 181-192.

Han T. Y., 1984, "Adaptive Substructuring and Interactive Graphics for Three-Dimensional Elasto-Plastic Finite Element Analysis," Ph.D. Thesis, Cornell University, USA.

Harary F., 1972, "Graph Theory," Addison-Wesley, Massachusetts, USA

Hendrickson B., Leland R., 1993, "An Improved Spectral Partitioning Algorithm for Mapping Parallel Computations," Sandia Report SAND92-1460, Sandia National Laboratories, USA

Hsieh S. H., 1997, "Evaluation of Automatic Domain Partitioning Algorithms or Parallel Finite Element Analysis," International Journal for Numerical Methods in Engineering, Vol. 40, pp. 1025-1051.

Hsieh S. H., 1993, "Parallel Processing for Nonlinear Dynamics Simulations of Structures Including Rotating Blade-Disk Assemblies," Ph.D. Dissertation, Cornell University

Hsieh S.H., Paulino G.H., Abel J.F., 1995, "Recursive Spectral Algorithms for Automatic Domain Partitioning in Parallel Finite Element Analysis," Computer Methods in Applied Mechanics and Engineering, Vol. 121, pp. 137-162.

Jensen B. D., Saitou K., Volakis J. L., Kurabayashi K., 2003, "Fully Integrated Electrothermal Multidomain Modeling of RF MEMS Switches," IEEE Microwave and Wireless Components Letters, Vol. 13, pp. 364-366.

Jensen B. D., Saitou K., Volakis J. L., Kurabayashi K., 2003, "Impact of Skin Effect on Thermal Behavior of RF MEMS Switches," Proceedings of the 6th ASME-JSME Thermal Engineering Joint Conference.

Jonsson J., Krenk S., Damkilde L., 1995, "Recursive Substructuring of Finite Elements," Computers & Structures, Vol. 54, pp. 395-404.

Judy, W. J., 2001, "Microelectromechanical Systems (MEMS): Fabrication, Design and Applications," Smart Materials and Structures, Vol. 10, pp. 1115-1134.

Kaveh A., Davaran A., 1999, "Spectral Bisection of Adaptive Finite Element Meshes for Parallel Processing," Computers & Structures, Vol. 70, pp. 315-323.

Kaviany M., "Principles of Heat Transfer," Wiley-Interscience, New York, USA

Kim Y.K., Allen M.G., 1999, "In Situ Measurement of Mechanical Properties of Polyimide Films Using Micromachined Resonant String Structures," IEEE Transactions on Components and Packaging Technology, Vol. 22, pp. 282-290.

Kleiner M. B., Kühn S.A., Weber W., 1996, "Thermal Conductivity Measurements of Thin Silicon Dioxide Films in Integrated Circuits," IEEE Transactions of Electron Devices, Vol. 43, pp. 1602-1608.

Kovacs, G. T., 1998, "Micromachined Transducers Sourcebook," McGraw-Hill, New York, USA

Leplan H., Geenen B., Robic J.Y., Pauleau Y., 1995, "Residual Stresses in Evaporated Silicon Dioxide Thin Films: Correlation with Deposition Parameters and Aging Behavior," Journal of Applied Physics, Vol. 78, pp. 962-968.

Lin L.Y., Goldstein E.L., 2002, "Opportunities and Challenges for MEMS in Light wave Communications," IEEE Journal on Selected Topics in Quantum Electronics, Vol. 8, pp. 163-172.

Lishchynska M., Cordero N., Slatery O., O'Mahony C., 2005, "Modeling Electrostatic Behavior of Microcantilevers Incorporating Residual Stress Gradient and non Ideal Anchors," Journal of Micromechanics and Microengineering, Vol. 15, pp.10-14.

Ma Y., 2002, "CMOS Optical Micro-Radiator Sensor," Ph.D. Thesis, University of Alberta, Edmonton, Canada.

Madou, M. J., 2002, "Fundamentals of Microfabrication: The Science of Miniaturization," CRC Press, Boca Raton, USA.

Malone J. G., 1990, "Parallel Nonlinear Dynamic Finite Element Analysis of Three-Dimensional Shell Structures," Computers & Structures, Vol. 35, pp. 523-539.

Malone J. G., 1988, "Automatic Mesh Decomposition and Concurrent Finite Element Analysis for Hypercube Multiprocessor Computers," Computer Methods in Applied Mechanics and Engineering, Vol. 70, pp. 27-58.

Miller G. L., Teng S. H., Thurston W., Vavasis S. A., 1992, "Automatic Mesh Partitioning," Technical Report CTC92TR112, Cornell Theory Center, Cornell University.

Min Y.H., Kim Y.K., 2000, "*In Situ* Measurement of Residual Stresses in Micromachined Thin films Using a Specimen with Composite-Layered Cantilevers," Journal of Micromechanics and Microengineering, Vol. 10, pp. 314-321.

Mo Y., Okawa Y., Tajima M., Nakai T., Nobuyuki, Natukawa K., 2001, "Micro-Machined Gas Sensor Array Based on Metal Film Microheater," Sensors and Actuators B, Vol. 79, pp. 175-181.

Mönig R., Keller R.R., Volkert C.A., 2004, "Thermal Fatigue Testing of Thin Metal Films," Review of Scientific Instruments, Vol. 75, pp. 4997-5004.

Muhlstein C.L., Ritchie R.O., 2003, "High-Cycle Fatigue of Micron-Scale Polycrystalline Silicon Films: Fracture Mechanics Analyses of the Role of Silica/Silicon Interface," International Journal of Fracture, Vol. 119/120, pp. 449-474.

Nathenson, H. C., Newell, W. E., Wickstrom, R. A., Davis, J. R. Jr., 1967, "The Resonant Gate Transistor," IEEE Transactions in Electronic Devices, Vol. 14, pp. 117-124.

Nix W. D., 1989, "Mechanical Properties of MEMS Materials," Metallurgical Transactions, Vol. 20A, pp. 2217-2245.

Noor A.K., Kamel H.A., Fulton R.E., 1978, "Substructuring Techniques Status and Projections," Computers & Structures, Vol. 8, pp. 621-632.

Owen D.R., Goncalves O.J.A., 1982, "Substructuring Techniques in Material Non-Linear Analysis," Computers & Structures, Vol. 15, pp. 205-313.

Palmer H. B., 1937, "The Capacitance of a Parallel Plate Capacitor by the Schwartz-Christoffel Transformation," Journal of Electrical Engineering, Vol.56, pp. 363-366.

Pamidighantam S., Puers R., Baert K., Tilmans H. A.C., 2002, "Pull-in Voltage Analysis of Electrostatically Actuated Beam Structures with Fixed-Fixed and Fixed-Free end conditions," Journal of Micromechanics and Microengineering, Vol. 12, pp. 458-464.

Pan C.H., 2002, "A Simple Method for Determining Linear Thermal Expansion Coefficients of Thin Films," Journal of Micromechanics and Microengineering, Vol. 12, pp. 548-555.

Parameswaran M., Robinson A.M., Ristic L., Chau K., Allegretto W., 1990, "A CMOS Thermally Isolated Gas Flow Sensor," Sensors Materials, Vol. 2 , pp.17–26.

Arx M., 1998, "Thermal Properties of CMOS Thin Films," Ph.D. Thesis, ETH Zurich.

Paul O., Baltes H., 1993, "Thermal Conductivity of CMOS Materials for the Optimization of Microsensors," Journal of Micromechanics and Microengineering, Vol. 3, pp. 110-112.

Peroulis D., Pacheo S. P., Sarabandi K., Katehi L. P. B., 2003, "Electromechanical Considerations in Developing Low-Voltage RF MEMS Switches," IEEE Transactions on Microwave Theory and Techniques, Vol. 51, pp.259-270.

Peroulis D., Pacheo S. P., Sarabandi K., Katehi L. P. B., 2001, "Tunable Lumped Components with Applications to Reconfigurable MEMS Filter," IEEE MIT-S International Microwave Symposium, Vol. 1, pp.341-344.

Peterson, K. E., 1982, "Silicon as a Mechanical Material," Proceedings of IEEE, Vol. 70, pp. 420-457.

Powell S., Kennedy M., D., Williams F.W., 1997, "Efficient Multilevel Substructuring with Constraint for Buckling and Vibrations Analysis of Prismatic Plate Assemblies," International Journal of Mechanical Science, Vol. 39, pp. 795-805.

Puicorbe J., Vogel D., Michel B., Vila A., Garcia I., Cane C., Morante J. R., 2003, "Thermal and Mechanical Analysis of Micromachined Gas Sensors," Journal of Micromechanics and Microengineering, Vol. 13, pp. 548-556.

Rebeiz G. M., 2003 "RF MEMS: Theory, design and technology," Wiley-Interscience, New York, USA

Rizk J., Chaiban E., Rebeiz G., 2002, "Steady State Thermal Analysis and High-Power Reliability Considerations of RF MEMS Capacitive Switches," IEE MTT-S International Microwave Symposium, Vol. 1, pp. 239-242.

Rodriguez J., Sun J., 1992, "A Domain Decomposition Study for a Parallel Finite Element Code," Computers in Engineering, Vol. 2, pp. 83-90.

Roux F.X., 1989, "Acceleration of the Outer Conjugate Gradient by Reorthogonalization for a Domain Decomposition Method for Structural Analysis Problems," Proceedings of Third International Conference on Supercomputing.

Sadek K., Moussa W., 2005, "Investigating the Effect of Deposition Variation on the Performance Sensitivity of Low- Power Gas Sensors," Sensors and Actuators B, Vol. 107, pp. 497-508.

Sadek K., Moussa W., 2003, "Application of Adaptive Multilevel Substructuring Technique to Model CMOS Micromachined Thermistor Gas Sensor, Part (I): A Feasibility Study," Proceedings of ICMENS 2003 Conference.

Sadek K., Moussa W., 2003, "Application of Adaptive Multilevel Substructuring Technique to Model CMOS Micromachined Thermistor Gas Sensor, Part (II): Effect of Manufacturing Uncertainties in the Reliability of MEMS," Proceedings of ICMENS 2003 Conference.

Schneider D.M., Maibach J., Obermeier E., Schneider D., 1995, "Variations in Young's Modulus and Intrinsic Stress of LPCVD-Polysilicon due to High-Temperature Annealing," Journal of Micromechanics and Microengineering, Vol. 5, pp. 121-124.

Senturia, S. D., 2004, "Microsystem Design," Springer, New York, USA

Seok S., Lee B., Chun K., 2002, "A New Electrical Residual Stress Characterization Using Bent Beam Actuators," Journal of Micromechanics and Microengineering, Vol. 12, pp. 562-566.

Sharpe W.N., Turner K.T., Edwards R.L., 1999, "Tensile Testing of Polysilicon," Experimental Mechanics, Vol. 39, pp. 162-170.

Sharpe W.N., Yaun B., Vaidyanathan R., 1997, "Measurements of Young's Modulus, Poisson's Ratio and Tensile Strength of polysilicon," Proceedings of the Tenth IEEE International Workshop on Microelectromechanical Systems, Nagoya, Japan.

Shen B., Allegretto W., Hu M., B. Yu, Robinson A.M., Lawson R., 1996, "Simulation and Physical Response of Negative Temperature Coefficient of Resistance of Polysilicon Micromachined Structures," Canadian Journal of Physics, Vol. 74, pp. 147–150.

Simon H.D., 1991, "Partitioning of Unstructured Problems for Parallel Processing," Computer Systems Science & Engineering, Vol. 2, pp.135-148.

Stadtmueller M., 1992, "Mechanical Stress of CVD-Dielectrics," Journal of Electrochemical Society, Vol.139, pp. 3269-3274.

Stark B., 1999, "MEMS Reliability Assurance Guidelines for Space Applications," JPL Publication, 99-1.

Stewart J. V., 2001, "Intermediate Electromagnetic Theory," World Scientific, Singapore, Singapore

Strikar V.T., Spearing S.M., 2003, "Materials Selection in Micromechanical Design: An Application of the Ashby Approach," Journal of Microelectromechanical Systems, Vol. 12, pp. 3-10.

Tas N., Sonnenberg T., Jansen H., Lagtenberg R., Elwenspoek M., 1996, "Stiction in Surface Micromachining," Journal of Micromechanics and Microengineering, Vol. 6, pp. 385-397.

Thiel W., Tornquist K., Reano R., Katehi L. P. B., 2002, "A Study of Thermal Effects in RF-MEMS Switches Using a Time Domain Approach," IEE MTT-S International Microwave Symposium, Vol. 1, pp. 235-238.

Thouless M. D., 1994, "Fracture Mechanics for Thin-Film Adhesion," IBM Journal of Resources Development, Vol. 38, pp. 367-377.

Uma S., McConnell A.D., Asheghi M., Kurabayashi K., Goodson K.E., 2001, "Temperature-Dependent Thermal Conductivity of Undoped Polycrystalline Silicon Layers," International Journal of Thermophysics, Vol. 22, pp. 605-616.

Wan K.T., Kogut L., 2005, "The Coupling Effect of Interfacial Adhesion and Tensile Residual Stress on a Thin Membrane Adhered to a Flat Punch," Journal of Micromechanics and Microengineering, Vol. 15, pp. 778-784.

Wang Z., Jensen B. D., Chow L. L. W., Volakis J. L., Saitou K., Kurabayashi K., 2006, "Full-Wave Electromagnetic and Thermal Modeling for the Prediction of Heat-Dissipation-Induced RF-MEMS Switch Failure," Journal of Micromechanics and Microengineering, Vol. 16, pp. 157-164.

Williams F.W., Liu X., Zhong W., 1995, "Investigation of the Accuracy of the Solution of the Constrained Substructuring Method, Computers & Structures, Vol. 58 917-923.

Wrbanek J.D., Laster K.L., 2005, "Preparation and Analysis of Platinum Thin Films for High Temperature Sensor applications," NASA/TM-2005-213433, pp. 1-19.

Yi T., Kim C.J., 1999, "Measurement of Mechanical Properties for MEMS Materials," Measurement Science and Technology, Vol. 10, pp. 706-716.

Zhu Y., Espinosa H. D., 2004, "Effect of Temperature on Capacitive RF MEMS Switch Performance, a Coupled Field Analysis," Journal of Micromechanics and Microengineering, Vol. 14, pp. 1270-1279.

Zienkiewicz O. C., 1977, "The Finite Element Method," McGraw Hill, New York, USA

Appendix A

List of Contributed Publications

To the current date, the research work done has contributed the following list of publications.

1) Sadek K., Moussa W., 2006a, "Automated Substructuring by Spectral Techniques to Solve Large 3-D Finite Element Models on Single Processors," Computer Methods in Applied Mechanics and Engineering, Submitted.

2) Sadek K., Moussa W., 2006b, "Automated Spectral Isolation of Substructures to Solve Sequentially Coupled-Field FE Problems," Finite Elements in Analysis and Design, Submitted.

3) Sadek K., Moussa W., 2006c, "A Coupled Field Multiphysics Modeling Approach to Investigate RF MEMS Switch Failure Modes at Various Operational Conditions," Microelectronics Reliability, Submitted.

4) Sadek K., Moussa W., 2005a, "Investigating the Effect of Deposition Variation on the Performance Sensitivity of Low- Power Gas Sensors," Sensors and Actuators B, Vol. 107, pp. 497-508.

5) Sadek K., Moussa W., 2005b, "MEMS Design for Fabrication," Proceedings of ICMENS 2005 Conference.

6) Sadek K., Moussa W., 2004, "Assessment of the Effect of Micro-Fabrication Uncertainties on the Sensitivity of Gas Sensors Using 3-D Finite Element Modeling," Proceedings of ICMENS 2004 Conference.

7) Sadek K., Bhattacharyya A., Moussa W., 2003a, "Effect of Variable Material Properties and Environmental Conditions on Thermomechanical Phase Transformations in Shape Memory Alloy Wires," Computational Materials Science, Vol. 27, pp. 493-506.

8) Sadek K., Moussa W., 2003b, "Application of Adaptive Multilevel Substructuring Technique to Model CMOS Micromachined Thermistor Gas Sensor, Part (I): A Feasibility Study," Proceedings of ICMENS 2003 Conference.

9) Sadek K., Moussa W., 2003c, "Application of Adaptive Multilevel Substructuring Technique to Model CMOS Micromachined Thermistor Gas Sensor, Part (II): Effect of Manufacturing Uncertainties in the Reliability of MEMS," Proceedings of ICMENS 2003 Conference.

Appendix B

Automated Substructuring MATLAB © Code

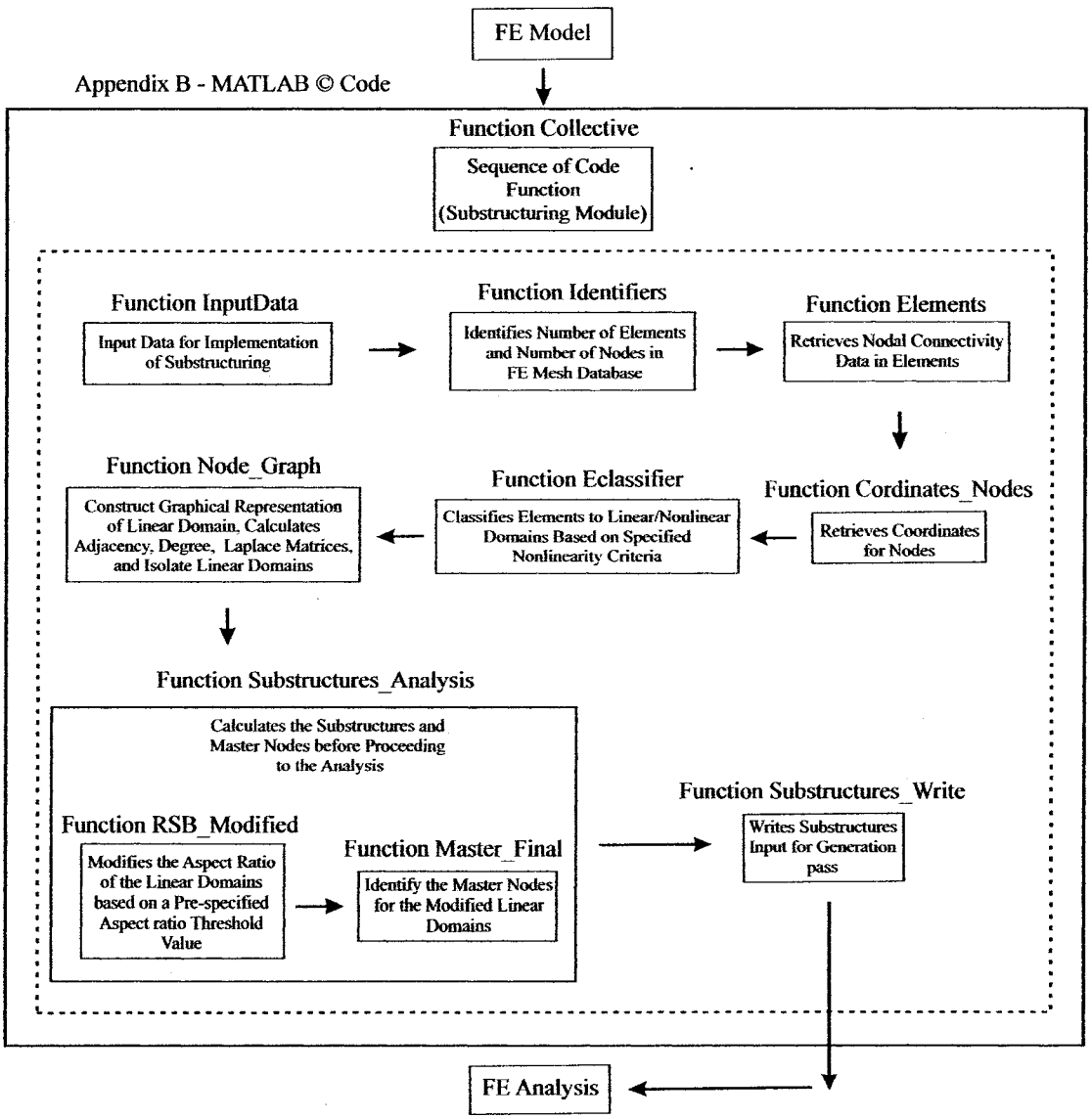

Figure B.1: Substructuring MATLAB © Code Index Chart

B.1 Function Collective

Function [ELEMENTS, ELinear, DomainsNumber, MajorVector, DomainsNodes, MasterNodes, AspectRatio, MajorVector_Values, DomainsNodes_Analysis, Master_Nodes_Analysis, AR_Threshold] = Collective;

[FileName, NodeFileName, StressFileName, SigmaYield, Permission, Ratio, AR_Threshold] = InputData;

[NumberofNodes, ElementStart, ElementEnd] = Identifiers (FileName, Permission);

[ELEMENTS, NumberofElements] = Elements (ElementStart, ElementEnd, FileName, Permission);

[ELinear] = EClassifier (ELEMENTS, StressFileName, Permission, SigmaYield, NumberofElements, Ratio);

[Cordinates] = Cordinates_Nodes (NumberofNodes, NodeFileName, Permission);

[DomainsNumber, MajorVector, DomainsNodes, MasterNodes, AspectRatio, MajorVector_Values] = NodeGraph (ELinear, Cordinates);

[DomainsNodes_Analysis, Master_Nodes_Analysis] = Substructures_Analysis (DomainsNumber, AR_Threshold, AspectRatio, DomainsNodes, MasterNodes, ELinear, Cordinates);

[End] = Substructures_Write (DomainsNodes_Analysis, Master_Nodes_Analysis);

B.2 Function Input Data

```
function [FileName, NodeFileName, ResultsFilename, Non_Linearity_Criteria,
Permission, Ratio, AR_Threshold] = InputData

FileName = 'JobName.cdb'

NodeFileName = 'Node_List.lis'

ResultsFilename='Substep_.lis'

Non_Linearity_Criteria = 'NonLinearity

Permission = 'r'

Ratio = 'Ratio'

AR_Threshold = 'AR'
```

B.3 Function Identifiers

```
function [NumberofNodes, ElementStart, ElementEnd] = Identifiers (FileName,
Permission);


fid = fopen (FileName, Permission);
z = 0;
x = 0;
while ~feof (fid)
   Tline = fgets (fid);
   m = findstr (Tline, 'NBLOCK');
   s = findstr (Tline, 'N,');
   K1 = any (m);
   K2 = any (s);
   if K1 == 0
      z = z+1;
   end
   if K1 == 1
      INodeStart = z+1;
   end
```

```
    if s == 1
        x = x+1;
        if x == 1
        INodeEnd = z;
        end
    end
end
INodeStart = INodeStart+1;
INodeEnd = INodeEnd;
NumberofNodes = INodeEnd - INodeStart;
fclose (fid);
fid = fopen (FileName, Permission);
s = 1;
for I = 1:INodeEnd+4
    fgets (fid);
end
ElementStart = I+1;
while ~feof (fid)
    tline = fgets (fid);
    k = findstr (tline, '-1');
```

```
 if k == 7
    ElementEnd = I+s-1;
 end
 s = s+1;
end
ElementStart = ElementStart;
ElementEnd = ElementEnd;
NumberofNodes
ElementStart
ElementEnd
fclose (fid);
idd = 'file1'
```

B.4 Function Elements

```
function [ELEMENTS, NumberofElements] = Elements (ElementStart, ElementEnd,
FileName, Permission);

fid = fopen (FileName, Permission);
NumberofElements = ElementEnd - ElementStart +1;
ELEMENTS = zeros (NumberofElements, 7);
L = 0;
for I = 1: ElementStart-1
   fgets (fid);
end
for s = 1:NumberofElements
   L = L+1
   Material = fscanf (fid, '%s', 1);
   Type = fscanf (fid, '%s', 1);
   skip8 = fscanf (fid, '%s', 8);
   EId = fscanf (fid, '%s',1);
   Type = sscanf (Type, '%e');
   Material = sscanf (Material, '%e');
   EId = sscanf (EId, '%e');
```

```
        Node1 = fscanf (fid, '%s',1);
        Node2 = fscanf (fid, '%s',1);
        Node3 = fscanf (fid, '%s',1);
        skip = fscanf (fid, '%s', 1);
        Node4 = fscanf (fid, '%s',1);
        skip3 = fscanf (fid, '%s',3);
        Node1 = sscanf (Node1, '%e');
        Node2 = sscanf (Node2, '%e');
        Node3 = sscanf (Node3, '%e');
        Node4 = sscanf (Node4, '%e');
        ELEMENTS (L, 1:7) = [EId, Material, Type, Node1, Node2, Node3, Node4];
    end
ELEMENTS;
fclose (fid);
```

B.5 Function Cordinates_Nodes

```
function [Cordinates] = Cordinates_Nodes (NumberofNodes, NodeFileName,
Permission);

fid = fopen (NodeFileName, Permission);
Cordinates = zeros (NumberofNodes,4);
L=1;
V = 0;
while V < 1000000
  k = fscanf (fid, '%s', 1);
  I='NODE';
  R = ismember (k, I);
  R = sum (R);
  if R ~= 0
    fgets (fid)
  end
  if R == 0
  ID= sscanf (k, '%e');
  X = fscanf (fid, '%s', 1);
  Y = fscanf (fid, '%s', 1);
```

```
    Z = fscanf (fid, '%s', 1);
    X= sscanf (X, '%e');
    Y= sscanf (Y, '%e');
    Z= sscanf (Z, '%e');
    Cordinates (L, 1:4) = [ID, X, Y, Z];
   L = L+1
   if L > NumberofNodes
      V = 1000001
   end
   end
end
fclose (fid)
```

B.6 Function EClassifier

```
function [ELinear] = EClassifier (ELEMENTS, ResultsFilename, Permission,
Non_Linearity_Criteria, NumberofElements, Ratio);

Stresslevel = Non_Linearity_Criteria
VV = length (ELEMENTS);
ELinear = zeros (VV, 5);
fid = fopen (StressFileName, Permission)
for s = 1:7
   fgets (fid)
end
L=0
n = 0
while n < 100000
   Stars = '*****'
   MIN = 'MINIMUM'
   ID = fscanf (fid, '%s',1);
   K1 = ismember (ID, Stars);
   K1 = sum (K1)
   K2 = ismember (ID,MIN)
```

```
    K2 = sum (K2)
    if K1 == 5
      fgets (fid);
      for z = 1:4
        fgets (fid)
      end
      ID = fscanf (fid, '%s',1);
    end
    if K2 == 7
      n = 1000001
    end
    Stress = fscanf (fid, '%s',1);
    ID = sscanf (ID, '%e');
    Stress = sscanf (Stress, '%e');
    if Stress < Stresslevel
     L=L+1
     Nodes_1 = ELEMENTS (ID, 4:7);
     ELinear (L, 1:5) = [ID, Nodes_1];
    end
  end
  ELinear (L+1:VV, :) = [];
```

B.7 Function NodeGraph

```
Function [DomainsNumber, MajorVector, DomainsNodes, MasterNodes,
AspectRatio, MajorVector_Values] = NodeGraph (ELinear, Cordinates);


D = length (ELinear);
NodesElinear = [];
for I = 1:D
   for s = 2:5
      x = ELinear (I, s);
      w = ismember (x, NodesElinear);
      if w == 0
         NodesElinear = [NodesElinear; x];
      end
   end
end
kk =2
NodesElinear = sort (NodesElinear);
F = length (NodesElinear);
NodesElements = zeros (F, 20);
```

```
ELinearReduced = ELinear (:, 2:5);
for I = 1:F
   x = NodesElinear (I);
   ee = ismember (ELinearReduced, x);
   [u w] = find (ee);
   u = sort (u);
   g =length (u);
   for ff = 1:g
      d = u (ff);
      NodesElements (I,1) = x;
      NodesElements (I,ff+1) = ELinear (d,1);
   end
   I
end
NodeNumber = NodesElements (:, 1);
for I = 1:F
   PseudoNodeNumber (I, 1) = I;
end
NodeNumberCorrespondance = [PseudoNodeNumber, NodeNumber];
```

```
[m n] = size (NodesElements);
Adjacency = zeros (F, F);
NodesReducedElements = NodesElements (:, 2:n);
for I = 1:F
  x = 1;
  g = 1;
  tt = [];
  while g < 2
    vv = NodesReducedElements (I,x);
    if vv == 0
      g = 2;
    end
    if vv ~= 0
      tt (x) = vv;
      x = x+1;
    end
    if x == n
      g =2;
    end
  end
```

```
    ww = ismember (NodesReducedElements, tt);
    for s = 1:F
        K = ww (s,:);
        K1 = any (K);
        if K1 == 1
            Adjacency (I, s) = 1;
        end
    end
    Adjacency (I, I) = 0;
    I
end
Deg = zeros (F,F);
for x = 1:F
    Deg (x, x) = sum (Adjacency(x,1:F));
end
Laplace = Deg - Adjacency;
[Vector, LANDA] = eig (Laplace);
x = 1;
D = length (Laplace);
```

```
while x <= D
   LANDA_Check = LANDA (x, x);
   if LANDA_Check <= 1e-5
     DomainsNumber = x;
     x = x+1;
   end
   if LANDA_Check > 1e-5
      x = D+1;
   end
end
DomainsNumber;
D = length (Vector);
MajorVector = zeros (D,1);
weights = 1.55;
for s = 1:DomainsNumber
   Columns = weights * Vector (1:D, s);
   MajorVector = MajorVector + Columns;
   weights = weights +weights
end
MajorVector;
```

```
L = 1
MajorVector_Fake = MajorVector;
V = length (MajorVector);
DomainsNodes = zeros (V, DomainsNumber);
Number_Check = MajorVector (1);
MajorVector_Values (1,1) = Number_Check;
for n = 1:V
   K = MajorVector (n,1)
   gg = K - Number_Check;
   gg = abs (gg);
   if gg < 1e-6
      Index = n;
      DomainsNodes (L, 1)= NodeNumberCorrespondance (n,2);
      L = L+1;
      MajorVector_Fake (n,1) = 33333;
   end
end
for s = 2:DomainsNumber
   L = 1;
   r = 1;
```

```
while r <= V
  Number_Check = MajorVector_Fake (r, 1);
  if Number_Check == 33333
    r=r+1;
  end
  if Number_Check ~= 33333
    MajorVector_Values (1,s) = Number_Check;
    m = r;
    r = V+1;
  end
end
for n = 1:V
K = MajorVector (n,1);
gg = K - Number_Check;
gg = abs (gg);
 if gg < 1e-6
  Index = n;
  DomainsNodes (L, s) = NodeNumberCorrespondance (n, 2);
  L = L+1;
  MajorVector_Fake (n,1) = 33333;
 end
```

```
  end
end
V = length (DomainsNodes)
for x =1:DomainsNumber
  s = 1
  while s <= V
    ee = DomainsNodes(s,x)
    if ee ==0
      I (x,1) = s
      s = V+1
    end
    s=s+1;
  end
end
A = max (I)
DomainsNodes (A:V,:) = [ ];
Y = length (DomainsNodes)
Z = length (NodeNumberCorrespondance)
MasterNodes = zeros (Y, DomainsNumber)
for r = 1:DomainsNumber
  s=1
```

```
    n=1
    while s <= Y
      x = DomainsNodes (s,r)
      if x == 0
        s = Y+1
      end
      if x~=0
        [ee, loc] = ismember (x, NodeNumberCorrespondance)
        RowNumber = loc-Z
        Degreex = Deg (RowNumber, RowNumber)
        if Degreex <= 7
          MasterNodes (n ,r) = x
          n = n+1;
        end
      end
      s=s+1;
    end
end
V = length (MasterNodes);
```

```
for x =1:DomainsNumber
   s = 1;
   while s <= V
      ee = MasterNodes(s, x);
      if ee ==0
         I (x,1) = s;
         s = V+1;
      end
      s=s+1
   end
end
A = max (I)
MasterNodes (A:V,:) = [ ];
AspectRatio = zeros (1, DomainsNumber);
Y = length (MasterNodes);
for s = 1:DomainsNumber
   x = 2;
   L = 1;
   while x <= Y
      X2 = MasterNodes (x,s)
```

```
    if X2 == 0
      x=Y+1
    end
    if X2~=0
      X1 = MasterNodes (x-1, s);
      Cordinate2 = Cordinates (X2, 2:4);
      Cordinate1 = Cordinates (X1, 2:4);
      distance = Cordinate2-Cordinate1;
      distance = distance.^2;
      distance = sum (distance);
      distance = distance.^0.5;
      I (L,1) = distance;
      L=L+1;
    end
    x=x+1;
  end
    A = max(I);
    B = min (I);
    C = A/B;
    AspectRatio (1,s) = C;
end
```

```
EE = ELinear (:,2:5);

V = length (EE);

x = MasterNodes (1,1);

[ee, loc] = ismember (EE, x);

L=1;
```

B.8 Function RSB_Modified

```
function [Domain1,Domain2] = RSB_Modified (NodesElinear_Domain, ELinear,
Cordinates);

F = length (NodesElinear_Domain);
NodesElements_Domain = zeros (F, 20);
ELinearReduced = ELinear (:, 2:5);
for I = 1:F
   x = NodesElinear_Domain (I);
   ee = ismember (ELinearReduced, x);
   [u w] = find (ee);
   u = sort (u);
   g =length (u);
   for ff = 1:g
      d = u (ff);
      NodesElements_Domain (I,1) = x;
      NodesElements_Domain (I,ff+1) = ELinear (d,1);
   end
end
NodeNumber = NodesElements_Domain (:,1);
```

```
PseudoNodeNumber=[];
NodeNumberCorrespondance=[];
for I = 1:F
   PseudoNodeNumber (I,1) = I;
end
NodeNumberCorrespondance = [PseudoNodeNumber, NodeNumber];
 [m n] = size (NodesElements_Domain);
Adjacency = zeros (F,F);
NodesReducedElements =[];
NodesReducedElements = NodesElements_Domain (:,2:n);
for I = 1:F
   x = 1;
   g = 1;
   tt = [];
   while g < 2
      vv = NodesReducedElements (I,x);
      if vv == 0
         g = 2;
      end

      if vv ~= 0
```

```
        tt (x) = vv;
        x = x+1;
      end
      if x == n
        g =2;
      end
    end
    ww = ismember (NodesReducedElements, tt);
    for s = 1:F
      K = ww (s,:);
      K1 = any (K);
      if K1 == 1
        Adjacency (I, s) = 1;
      end
    end
    Adjacency (I,I) = 0;
    I;
end
Deg = zeros (F,F);

for x = 1:F
```

```
   Deg (x, x) = sum (Adjacency(x,1:F));
end
 Laplace = [];
Laplace = Deg - Adjacency;
 [Vector, LANDA] = eig (Laplace);
x = 1;
D = length (Laplace);
while x <= D
   LANDA_Check = LANDA (x, x);
   if LANDA_Check <= 1e-5
     DomainsNumber = x;
     x = x+1;
   end
   if LANDA_Check > 1e-5
      x = D+1;
   end
end
DomainsNumber;
Fiedler_Vector = Vector (:, 2);
Lengthof_Fiedler = length (Fiedler_Vector);
Sum_Fiedler = sum (Fiedler_Vector);
```

```
Median_Fiedler = Sum_Fiedler/Lengthof_Fiedler
n1=0;
n2=0;
for s=1:Lengthof_Fiedler
   X = Fiedler_Vector (s,1);
   if X <=Median_Fiedler
      n1 = n1+1;
      Domain1 (n1,1) = NodeNumberCorrespondance (s,2);
   end
   if X > Median_Fiedler
      n2 = n2+1;
      Domain2 (n2,1) = NodeNumberCorrespondance (s,2);
   end
end
```

B.9 Function Master_Final

```
function [DomainMasterNodes] = Master_Final (NodesElinear_Domain, ELinear,
Cordinates);


F = length (NodesElinear_Domain);
NodesElements_Domain = zeros (F,20);
ELinearReduced = ELinear (:,2:5);
for I = 1:F
   x = NodesElinear_Domain (I);
   ee = ismember (ELinearReduced, x);
   [u w] = find (ee);
   u = sort (u);
   g =length (u);
   for ff = 1:g
      d = u (ff);
      NodesElements_Domain (I,1) = x;
      NodesElements_Domain (I,ff+1) = ELinear (d,1);
   end
   I;
end
```

```
NodeNumber = NodesElements_Domain (:,1);
PseudoNodeNumber=[];
NodeNumberCorrespondance=[];
for I = 1:F
   PseudoNodeNumber (I,1) = I;
end
NodeNumberCorrespondance = [PseudoNodeNumber, NodeNumber];
 [m n] = size (NodesElements_Domain);
Adjacency = zeros (F,F);
NodesReducedElements =[];
NodesReducedElements = NodesElements_Domain (:,2:n);
for I = 1:F
   x = 1;
   g = 1;
   tt = [];
   while g < 2
      vv = NodesReducedElements (I,x);
      if vv == 0
         g = 2;
      end
```

```
    if vv ~= 0
      tt (x) = vv;
      x = x+1;
    end
    if x == n
      g =2;
    end
  end
  ww = ismember (NodesReducedElements, tt);
  for s = 1:F
    K = ww (s,:);
    K1 = any (K);
    if K1 == 1
      Adjacency (I, s) = 1;
    end
  end
  Adjacency (I,I) = 0;
  I;
end
Deg = zeros (F,F);
```

```
for x = 1:F
   Deg (x,x) = sum (Adjacency(x,1:F));
end
Y = length (NodesElinear_Domain)
Z = length (NodeNumberCorrespondance)
MasterNodes = zeros (Y,1)
   s=1;
   n=1;
   while s <= Y
      x = NodesElinear_Domain (s,1);
      if x~=0
         [ee, loc] = ismember (x, NodeNumberCorrespondance)
         RowNumber = loc-Z
         Degreex = Deg (RowNumber, RowNumber)
         if Degreex <= 7
            MasterNodes (n,1) = x
            n = n+1
         end
      end
      s=s+1;
   end
```

```
V = length (MasterNodes)
   s = 1
   while s <= V
      ee = MasterNodes(s,1)
      if ee ==0
         I  = s
         s = V+1
      end
      s=s+1
   end
end
A = max (I)
MasterNodes (A:V,:) = [ ]
DomainMasterNodes = MasterNodes;
```

B.10 Function Substructures_Analysis

```
function [DomainsNodes_Analysis, Master_Nodes_Analysis] = Substructures_Analysis (DomainsNumber, AR_Threshold, AspectRatio, DomainsNodes, MasterNodes, ELinear, Cordinates);

ELinear = ELinear;
Cordinates = Cordinates;
FFF = length (DomainsNodes);
RRR = length (MasterNodes);
X_AR = AR_Threshold;
if X_AR < 3
   n = 8*DomainsNumber
   DomainsNodes_Analysis = zeros (FFF, n);
   Master_Nodes_Analysis = zeros (RRR, n);
end
if (X_AR >= 3)&(X_AR < 5)
      n = 4*DomainsNumber
      DomainsNodes_Analysis = zeros (FFF, n);
      Master_Nodes_Analysis = zeros (RRR, n);
end
```

```
if (X_AR >= 5)&(X_AR < 8)
   n = 2*DomainsNumber
   DomainsNodes_Analysis = zeros (FFF, n);
   Master_Nodes_Analysis = zeros (RRR, n);
end
if X_AR >= 8
DomainsNodes_Analysis = DomainsNodes;
Master_Nodes_Analysis = MasterNodes;
end
if X_AR < 8
lll = 1;
for xxx = 1:DomainsNumber
   NodesElinear_Domain = [];
   www = AspectRatio (1,xxx);
   if www <= AR_Threshold
      DomainsNodes_Analysis (1:FFF,lll)= DomainsNodes (1:FFF,xxx);
      Master_Nodes_Analysis (1:RRR,lll)= DomainsNodes (1:RRR,xxx);
      lll = lll+1;
      xxx=xxx+1;
   end
```

```
if www > AR_Threshold
  yyy = length (DomainsNodes)
  zzz = 0;
  nnn = 1
  while nnn <= yyy
    aaa = DomainsNodes (nnn,xxx);
    if aaa == 0
      nnn = yyy+1
    end
    if aaa ~= 0
      zzz = zzz+1;
      NodesElinear_Domain_Fake (zzz,1) = aaa;
    end
    nnn = nnn+1;
  end
  NodesElinear_Domain = NodesElinear_Domain_Fake;
  NodesElinear_Domain_Fake = [];
  if X_AR < 3
[Domain1,Domain2] = RSB_Modified (NodesElinear_Domain, ELinear,
Cordinates);
```

```
Domain11 = Domain1;

Domain12 = Domain2;

NodesElinear_Domain = Domain11;

[Domain1, Domain2] = RSB_Modified (NodesElinear_Domain, ELinear,
Cordinates);

Domain111 = Domain1;

Domain112 = Domain2;

NodesElinear_Domain = Domain111;

[Domain1, Domain2] = RSB_Modified (NodesElinear_Domain, ELinear,
Cordinates);

Domain1111 = Domain1;

ggg = length (Domain1111)

DomainsNodes_Analysis (1:ggg,lll)= Domain1111;

lll = lll+1

Domain1112 = Domain2;

ggg = length (Domain1112)

DomainsNodes_Analysis (1:ggg,lll)= Domain1112;

lll = lll+1

NodesElinear_Domain = Domain112;
```

```
[Domain1, Domain2] = RSB_Modified (NodesElinear_Domain, ELinear,
Cordinates);
    Domain1121 = Domain1;
    ggg = length (Domain1121)
    DomainsNodes_Analysis (1:ggg,lll)= Domain1121;
    lll = lll+1
    Domain1122 = Domain2;
    ggg = length (Domain1122)
    DomainsNodes_Analysis (1:ggg,lll)= Domain1122;
    lll = lll+1
    NodesElinear_Domain = Domain12;
[Domain1, Domain2] = RSB_Modified (NodesElinear_Domain, ELinear,
Cordinates);
    Domain121 = Domain1;
    Domain122 = Domain2;
    NodesElinear_Domain = Domain121;
[Domain1, Domain2] = RSB_Modified (NodesElinear_Domain, ELinear,
Cordinates);
    Domain1211 = Domain1;
    ggg = length (Domain1211)
    DomainsNodes_Analysis (1:ggg, lll)= Domain1211;
```

```
        lll = lll+1
        Domain1212 = Domain2;
        ggg = length (Domain1212)
        DomainsNodes_Analysis (1:ggg,lll)= Domain1212;
        lll = lll+1
        NodesElinear_Domain = Domain122;
[Domain1, Domain2] = RSB_Modified (NodesElinear_Domain, ELinear,
Cordinates);
        Domain1221 = Domain1;
        ggg = length (Domain1221)
        DomainsNodes_Analysis (1:ggg,lll)= Domain1221;
        lll = lll+1
        Domain1222 = Domain2;
        ggg = length (Domain1222)
        DomainsNodes_Analysis (1:ggg,lll)= Domain1222;
        lll = lll+1
    end
    if (X_AR >= 3)&(X_AR < 5)
```

```
[Domain1, Domain2] = RSB_Modified (NodesElinear_Domain, ELinear,
Cordinates);
    Domain11 = Domain1;
    Domain12 = Domain2;
    NodesElinear_Domain = Domain11;
[Domain1, Domain2] = RSB_Modified (NodesElinear_Domain, ELinear,
Cordinates);
    Domain111 = Domain1;
    ggg = length (Domain111)
    DomainsNodes_Analysis (1:ggg,lll)= Domain111;
    lll = lll+1
    Domain112 = Domain2;
    ggg = length (Domain112)
    DomainsNodes_Analysis (1:ggg,lll)= Domain112;
    lll = lll+1
    NodesElinear_Domain = Domain12;
[Domain1, Domain2] = RSB_Modified (NodesElinear_Domain, ELinear,
Cordinates);
    Domain121 = Domain1;
    ggg = length (Domain121)
    DomainsNodes_Analysis (1:ggg,lll)= Domain121;
```

```
        lll = lll+1
        Domain122 = Domain2;
        ggg = length (Domain122)
        DomainsNodes_Analysis (1:ggg,lll)= Domain122;
        lll = lll+1
      end
      if (X_AR >= 5)&(X_AR < 8)
[Domain1, Domain2] = RSB_Modified (NodesElinear_Domain, ELinear,
Cordinates);
        Domain11 = Domain1;
        ggg = length (Domain11)
        DomainsNodes_Analysis (1:ggg,lll)= Domain11;
        lll = lll+1
        Domain12 = Domain2;
        ggg = length (Domain12)
        DomainsNodes_Analysis (1:ggg,lll)= Domain12;
        lll = lll+1
      end
   end
end
```

```
[RowN ColN]= size (DomainsNodes_Analysis);
rr = 0;
ii = 1;
while ii < 1000000000
   rr = rr+1;
   fff = DomainsNodes_Analysis (1,ii);
   if (rr == ColN) | (fff ==0)
      DomainsNumber_Analysis = rr;
      nn = ii;
      ii = 2000000000;
   end
   if fff ~= 0
      ii = ii+1;
   end
end
if rr == ColN
   DomainsNodes_Analysis=DomainsNodes_Analysis
end
if rr ~= ColN
   DomainsNodes_Analysis (:,rr:ColN) = [];
```

```
   DomainsNumber_Analysis = DomainsNumber_Analysis -1;
end
V = RowN;
for x =1:DomainsNumber_Analysis
   s = 1
   while s <= V
      ee = DomainsNodes_Analysis(s,x)
      if (ee ==0) | (s==RowN)
         I (x,1) = s
         s = V+1
      end
      s=s+1;
   end
end
A = max (I)
if A == RowN
   DomainsNodes_Analysis=DomainsNodes_Analysis;
end
if A ~= RowN
DomainsNodes_Analysis (A:V,:) = [ ];
```

```
end
[m n] = size (DomainsNodes_Analysis);
Master_Nodes_Analysis = zeros (m,n);
for ssssss = 1:n
  NodesElinear_Domain = [];
  yyy = m
    zzz = 0;
    nnn = 1
    while nnn <= yyy
      aaa = DomainsNodes_Analysis (nnn,ssssss);
      if aaa == 0
        nnn = yyy+1
      end
      if aaa ~= 0
        zzz = zzz+1;
        NodesElinear_Domain_Fake (zzz,1)=aaa;
      end
      nnn = nnn+1;
    end
    NodesElinear_Domain = NodesElinear_Domain_Fake;
    NodesElinear_Domain_Fake =[]
```

```
[DomainMasterNodes] = Master_Final (NodesElinear_Domain, ELinear, Cordinates)

    ggg = length (DomainMasterNodes)

    Master_Nodes_Analysis (1: ggg, ssssss)= DomainMasterNodes;

end

end
```

B.11 Function Substructures_Write

```
Function [End] = Substructures_Write (DomainsNodes_Analysis,
Master_Nodes_Analysis);

[K L]= size (DomainsNodes_Analysis);
[m n]= size (Master_Nodes_Analysis);
fid = fopen ('Substructures.txt','w');
fprintf (fid, 'FILNAME,JOBNAME_GEN\n');
fprintf (fid, 'RESUME,JOBNAME,DB\n');
s = 1
while s <= L
   fprintf (fid, '/SOLU\n');
   fprintf (fid, 'ANTYPE,7\n');
   fprintf (fid, 'SEOPT,Substructure%1.0f,1,,,\n',s);
   x = 1
   while x <= K
      aa = DomainsNodes_Analysis (x,s);
      if x == 1
         fprintf (fid, 'NSEL,S,,,%1.0f\n',aa);
```

```
    end
    if aa == 0
       x = K+1
    end
    if (aa ~=0)& x~=1
       fprintf (fid, 'NSEL,A,,,%1.0f\n',aa);
    end
    x=x+1;
end
g = 1
while g <= m
     aa = Master_Nodes_Analysis (g, s);
    if aa == 0
       g = m+1
    end
    if aa ~=0
       fprintf (fid, 'NSEL,U,,,%1.0f\n',aa);
    end
    g = g+1;
end
```

```
fprintf (fid, 'ESLN,S,0,ALL\n');
g = 1
while g <= m
    aa = Master_Nodes_Analysis (g,s);
  if g == 1
     fprintf (fid, 'NSEL,S,,,%1.0f\n',aa);
  end
  if aa == 0
     g = m+1
  end
  if (aa ~=0) & (g ~= 1)
     fprintf (fid, 'NSEL,A,,,%1.0f\n',aa);
  end
  g = g+1;
end
fprintf (fid, 'M, ALL, ALL, , , , , , ,\n');
fprintf (fid, 'NSLE, S, ALL,\n');
fprintf (fid, 'SOLVE\n');
fprintf (fid, 'FINISH\n');
fprintf (fid, 'ALLSEL,ALL\n');
```

```
   s = s+1
end
fclose (fid);
End = 'End'
```